CONTRIBUTORS

Isao Ando
International Research Center of Macromolecular Science, Tokyo Institute of Technology, Ookayama, Meguro-ku, Tokyo, Japan; Department of Materials Science and Engineering, Shonan Institute of Technology, Tsujido Nishikaigan, Fujisawa-shi, Kanagawa, Japan

Masaki Kakiage
Department of Applied Chemistry, Graduate School of Science and Engineering, Saitama University, Shimo-Ookubo, Sakura-ku, Saitama, Japan

Kazuhiro Kamiguchi
Magnetic Research Analysis Team, Structure Analysis Group, Research Department, Nissan Arc, Ltd., Natsushima-cho, Yokosuka-shi, Kanagawa, Japan

Hassan Kassassir
Centre of Molecular and Macromolecular Studies, Polish Academy of Sciences, Łódź, Poland

Sławomir Kaźmierski
Centre of Molecular and Macromolecular Studies, Polish Academy of Sciences, Łódź, Poland

Shigeki Kuroki
Department of Organic and Polymeric Materials, Tokyo Institute of Technology, Ookayama, Meguro-ku, Tokyo, Japan

Beata Miksa
Centre of Molecular and Macromolecular Studies, Polish Academy of Sciences, Łódź, Poland

Marek J. Potrzebowski
Centre of Molecular and Macromolecular Studies, Polish Academy of Sciences, Łódź, Poland

Mitsuru Satoh
Department of Chemistry and Materials Science, Tokyo Institute of Technology, Ookayama, Meguro-ku, Tokyo, Japan; International Research Center of Macromolecular Science, Tokyo Institute of Technology, Ookayama, Meguro-ku, Tokyo, Japan

Hiroki Uehara
Department of Chemistry and Chemical Biology, Gunma University, Tenjin-cho, Kiryu, Gunma, Japan

Dušan Uhrín
School of Chemistry, University of Edinburgh, Edinburgh, United Kingdom

K. Yamada
Department of Chemistry and Materials Science, Graduate School of Science and Engineering, Tokyo Institute of Technology, Ookayama, Megruo, Tokyo, Japan

Yuji Yamane
Silicone-Electronics Materials Research Center, Shin-Etsu Chemical Co., Ltd., Hitomi Matsuida-machi, Annaka-shi, Gunma, Japan

Takeshi Yamanobe
Department of Chemistry and Chemical Biology, Gunma University, Tenjin-cho, Kiryu, Gunma, Japan

PREFACE

It is my pleasure to welcome readers to Volume 70 of Annual Reports on NMR. In common with other members of this series, this volume consists of reports from many areas of science where NMR plays a vital role. The volume commences with a report on 'Recent Developments in Liquid-State INADEQUATE Studies' by D. Uhrín; following this is an account of 'Phosphorus-31 NMR Spectroscopy of Condensed Matter' by S. Kaźmierski, H. Kassassir, B. Miksa and M.J. Potrzebowski; K. Yamada reports on 'Recent Applications of Solid-Sate ^{17}O NMR'; K. Kamiguchi, S. Kuroki, Y. Yamane, M. Satoh and I. Ando provide an account on 'Spatial Inhomogeneity of Cavities in Polymer Network Systems as Characterised by Field-Gradient NMR Using Probe Diffusant Molecules and Polymers with Different Sizes'. The volume concludes with review of 'Practical NMR Analysis of Morphology and Structure of Polymers' by T. Yamanobe, H. Uehara and M. Kakiage. I express my thanks to all of these authors for their interesting coverage of developments in their areas of expertise.

G. A. Webb
Royal Society of Chemistry
Burlington House
Piccadilly
London, UK

CHAPTER 1

Recent Developments in Liquid-State INADEQUATE Studies

Dušan Uhrín

Contents

Abstract

This chapter covers the development and application of INADEQUATE (ADEQUATE) in high-resolution NMR spectroscopy during the period 2003–2009. Starting with the introduction of the basic concept of the technique, this

School of Chemistry, University of Edinburgh, Edinburgh, United Kingdom

Annual Reports on NMR Spectroscopy, Volume 70
ISSN 0066-4103, DOI: 10.1016/S0066-4103(10)70004-1

chapter highlights issues related to the increasing sensitivity of INADEQUATE including the use of ^{1}H and ^{13}C optimised, cryogenically cooled probes, single-transition INADEQUATE methods, post-acquisition processing and elimination of off-resonance effects. Various implementations of ^{1}H-detected INADEQUATE methods are compared, followed by the discussion of the techniques employed for the measurement of carbon–carbon coupling constants with an emphasis on long-range couplings. Recent applications of ^{13}C- and ^{1}H-detected INADEQUATE to primary structure determination of small molecules in studies of biosynthetic pathways as well as studies of fullerenes and polymers are presented. The chapter concludes with the examination of several recent examples of the use of INADEQUATE to ^{29}Si, ^{15}N and ^{77}Se.

Key Words: High-resolution NMR, INADEQUATE, ADEQUATE, Carbon–carbon coupling constants, Long-range couplings, Double-quantum coherence, ^{13}C NMR, ^{15}N NMR, ^{29}Si NMR, ^{77}Se NMR, Fullerenes, Polymers, Review.

1. INTRODUCTION

The incredible natural abundance double quantum transfer experiment (INADEQUATE) was proposed by Ray Freeman in 1980.[1,2] The acronym of this remarkable technique sat high among the many NMR acronyms since, at the time of its birth, it accurately described all its attributes. INADEQUATE was seen as an *incredible* experiment with vast potential; its widespread applications are dwarfed only by its *inadequate* sensitivity. Depending on the equipment available, an overnight-to-weekend INADEQUATE experiment on a medium-sized molecule would typically require hundreds of milligrams of sample. Only recently have such unfavourable requirements been addressed with advent of cryogenically cooled probes. Now, INADEQUATE experiments using samples of 5–10 mg have become realistic propositions.

The inherently low sensitivity of INADEQUATE means it will always remain less sensitive than many other NMR experiments. However, this has not restricted researchers improving the original experiment and, during the last 30 years, INADEQUATE has appeared in many different guises. Designed originally to trace out the carbon skeleton of organic molecules in liquid-state NMR, INADEQUATE has now found applications in several different areas. As the name implies, INADEQUATE is intended for molecules with natural abundance of a rare NMR active isotope or molecules that have been partially enriched with such an isotope, for example ^{13}C, ^{15}N or ^{29}Si, ^{77}Se, etc. The following discussion mainly deals with ^{13}C INADEQUATE; applications to other nuclei are also presented.

The last comprehensive review of INADEQUATE appeared in 2002.[3] Drawing on seminal papers, the current account presents recent developments and applications of INADEQUATE in high-resolution NMR with an emphasis on the last 7 years. Some earlier developments that stood the test of time are also discussed.

2. INADEQUATE—THE BASIC CONCEPT

In contrast to the standard NMR paradigm, where the structure of a molecule is implied indirectly, based on the interpretation of networks of homo- and heteronuclear coupling constants, INADEQUATE maps the carbon skeleton of molecules *directly* by identifying the bonded carbon atoms. This is why INADEQUATE is conceptually such an appealing experiment, often providing the ultimate proof for a primary structure of a small organic molecule.

Mapping of carbon–carbon connectivity can in principle be achieved via measuring $^{1}J_{CC}$ coupling constants (1D INADEQUATE[2]) or by using the frequency of the double-quantum coherences as the criterion of connectivity (2D INADEQUATE[1]). 1D INADEQUATE spectrum is in essence a superposition of many anti-phase (AP) doublets arising from pairs of coupled carbon spins. Identification of connected carbons through 1D INADEQUATE therefore requires matching of the signals with identical splitting, which is often hampered by spectral overlap. The majority of INADEQUATE experiments are therefore performed in a 2D manner.

At the heart of the INADEQUATE is a double-quantum (DQ) filter, which selects signals arising from molecules containing pairs of rare spins, while eliminating much larger signals from molecules with only one such spin. This is achieved by the use of phase cycling[1,2,4] or pulsed filed gradients.[5] For a description of the INADEQUATE experiment using product operator formalism, the reader is referred to Ref. 3. In brief, the pulse sequence of a phase-cycled 2D ^{13}C-detected INADEQUATE (Figure 1) starts with the creation of an AP carbon–carbon coherence. This is then converted into a mixture of zero-quantum (ZQ) and DQ coherences by the second 90° ^{13}C pulse. The efficiency of this process depends on the match between the J coupling constant and the evolution interval τ, which can be optimised for one-bond or long-range couplings. Fortunately, passive spins are not a concern in this experiment, as two rare spins only produce AX (AB) spin systems and the transfer efficiency is given by $\sin(\pi J_{CC}\tau)$. During the subsequent incrementable t_1 period, the DQ coherences are frequency labelled and converted by the third 90° pulse into AP carbon–carbon coherence. This is detected during the acquisition time, t_2, as it evolves into an observable magnetisation.

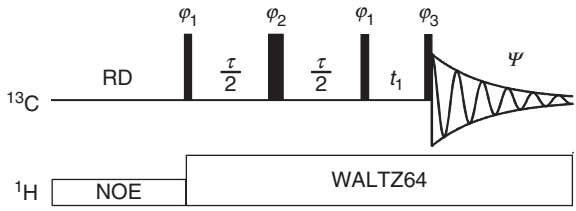

Figure 1 Pulse sequence of a 2D INADEQUATE experiment. The narrow and wide rectangles represent the 90° and 180° pulses, respectively. RD, relaxation delay, $\tau = 1/2\,J_{CC}$. The phase cycling is given in Table 1.

TABLE 1 Phase cycling of 2D INADEQUATE given in Figure 1.[a]

$\varphi_1 = (8)$	0 0 4 4 0 0 4 4 2 2 6 6 2 2 6 6
	4 4 0 0 4 4 0 0 6 6 2 2 6 6 2 2
$\varphi_2 = (8)$	4 0 0 4 4 0 0 4 6 2 2 6 6 2 2 6
	0 4 4 0 0 4 4 0 2 6 6 2 2 6 6 2
$\varphi_3 =$	0 1 2 3 1 0 3 2 2 3 0 1 3 2 1 0
$\varphi_4 =$	2 3 0 1 3 2 1 0 0 1 2 3 1 0 3 2[b]
$\psi =$	0 3 2 1 3 0 1 2

[a] The phase increment is equal to 90°, except for when symbol (8) is used, where the phase increment is equal to 45°.
[b] Applicable to the pulse sequence of Figure 9 B.

Due to the inherent low sensitivity, INADEQUATE must be carefully executed to eliminate potential artefacts. It has been shown that rapid pulsing in combination with the conventional selection of DQ coherences can produce artefacts in INADEQUATE spectra.[4] Their sources have been analysed and attributed, in part, to molecules containing only a single rare spin. Efficient phase cycling, given in Table 1, has been devised to produce artefact-free spectra. In addition, this phase cycling reduces the subtraction artefacts to a minimum, as it suppresses the signals from the abundant molecules containing only one rare spin. Overall, this phase cycling has been observed to provide a 30–40% improvement in signal-to-noise ratio.[4] An example of a 2D ^{13}C-detected INADEQUATE spectrum of a small molecule is given in Figure 2. The spectrum contains AP doublets along the directly detected single-quantum axis which are spread in the indirectly detected dimension according to DQ frequencies of coupled carbons. Signals are symmetry-related along the INADEQUATE diagonal. The carbon skeleton of the molecules is easily mapped out as outlined for fragments C5a, C6, C7, C7a, C7b and C15, C14a, C14, C13.

3. INCREASING THE SENSITIVITY OF INADEQUATE

3.1. Detection limits and cryogenically cooled probes

Two examples are cited here that should give the reader appreciation of how much compound and time is needed to obtain an INADEQUATE spectra using the latest generation of NMR equipment. The first example concerns ^{13}C detection. Using a Varian 500 MHz spectrometer equipped with a cryogenically cooled probe optimised for ^{13}C detection, a ^{13}C-detected INADEQUATE spectrum was acquired using 10 mg or 77 mM sample of 2,3:5,6-di-*O*-isopropylidine-α-D-mannofuranose ($M_w = 260$ g/mol) in $CDCl_3$ in only 9 h.[7] This reflects approximately a 10-fold increase in sensitivity over the equivalent standard NMR probe. Such level of sensitivity has allowed INADEQUATE to be made a part of ''all-in-one'' NMR experiment[7] designed to determine the structure of a small molecule from a single NMR experiment.

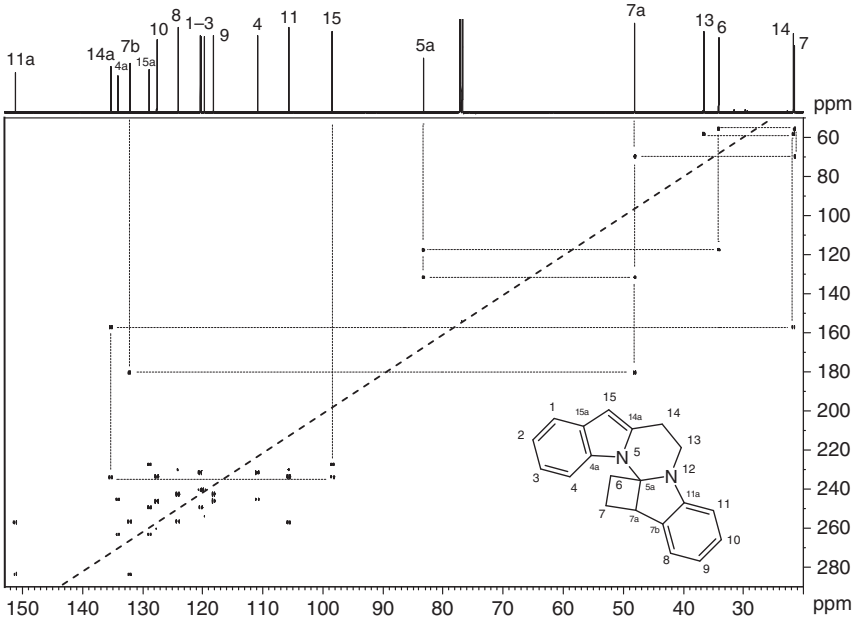

Figure 2 A 2D ^{13}C-deteced INADEQUATE spectrum of 7,7a,13,14-tetrahydro-6*H*-cyclobuta[*b*] pyrimido[1,2-*a*:3,4-*a*′]diindole given in the inset. The diagonal is shown as a dashed line. From Ref. 6, reproduced by permission of the Royal Society of Chemistry.

^{1}H-detection was used in the second example. A Bruker Avance 600 NMR spectrometer with a 5-mm TCI cryoprobe was used to acquire a 1,1-ADEQUATE (a variation of INADEQUATE) spectrum of a 21 mg or 133 mM sample of monobromophakellin ($M_w = 322$ g/mol) in 6 h.[8] To demonstrate the application and general feasibility of the ADEQUATE pulse sequence for metabolites, a smaller sample of 5.5 mg of monobromophakellin was prepared (35 mM). Sufficient signal-to-noise ratios were shown for seven out of nine possible correlations in 38 h. The two remaining correlations were barely larger than the noise level since the $^{1}J_{CH}$ and $^{1}J_{CC}$ coupling constants of the involved carbons were the largest (194 and 77 Hz) and smallest (135 and 38 Hz), respectively, and deviated from values (155 and 55 Hz) used to optimise the evolution intervals.

3.2. Addition of relaxation agents

One of the main advantages of ^{13}C-detected INADEQUATE is that, unlike ^{1}H-detected INADEQUATE, it provides information about connectivity of quaternary carbons. However, quaternary carbons are handicapped by slow spin-lattice relaxation. In order to improve their sensitivity, the addition of relaxation agents has been proposed.[9] It should be noted, however, that this procedure should be carried out with caution, as it may degrade signal strength by quenching the nuclear Overhauser effect.[10] One study showed that a moderate

enhancement of relaxation was achieved by dissolving oxygen under pressure at a low temperature and by adding substances that increases oxygen solubility.[11]

3.3. Single-transition INADEQUATE

The original efforts in increasing the sensitivity of INADEQUATE exploited the possibility of obtaining signal from both real and imaginary components of the DQ coherence. By using a 135° instead of a 90° ^{13}C pulse, DQ coherences are converted into observable single-quantum (SQ) coherences with a gain of 20–30% in signal intensity.[12] Introducing gradient selection with echo–anti-echo selection leads to a similar level of signal enhancement.[5] By realising the maximum efficiency that corresponds to the upper bound predicted for the DQ→SQ coherence transfer, the INADEQUATE CR (composite refocusing) experiment increased the sensitivity twofold relative to the regular phase-cycled INADEQUATE experiment.[5] Despite the fact that the INADEQUATE CR pulse sequence contains additional spin echoes, it has been shown to be robust against *J* mismatch[13] and amenable to implementation of off-resonance-effect compensating pulses.[14] The spin physics behind this remarkable experiment is discussed in detail Ref. 15.

Further developments along similar lines have been reported recently, initially in the context of 1D INADEQUATE.[16] The proposed pulse sequence (Figure 3) involves linear and bilinear spin rotations and is termed INADEQUATE LBR.

This pulse sequence aims to transfer the *y*-DQ coherence into a transition-selective signal. This is achieved by converting one part of the *y*-DQ coherence into SQ AP coherence by a 45° pulse, which is later refocused generating the in-phase (IP) magnetisation. The other part of the DQ coherence, which does not evolve during the second spin echo, is converted into an AP magnetisation. When combined with the IP part, a transition selective signal is obtained.

1D INADEQUATE LBR pulse sequence generates a theoretical sensitivity enhancement of 41% compared to a regular 1D INADEQUATE. The same gain is also provided by 1D INADEQUATE CR.[5] As the latter pulse sequence contains more delays, 1D INADEQUATE LBR is more robust when it comes to the mismatch between the set and actual *J* values. An experimental comparison, based on 11 sucrose signals, of all three 1D INADEQUATE pulse sequences

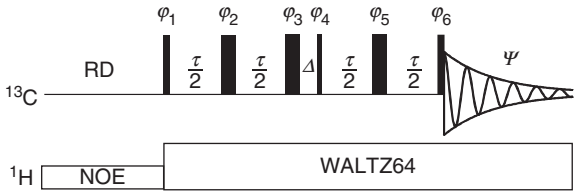

Figure 3 Pulse sequence of a 1D INADEQUATE LBR. The narrow, wider and wide rectangles represent 45°, 90° and 180° pulses, respectively. $\tau = 1/2J_{CC}$, $\Delta = 3$ μs. The following phase cycling applies: $\varphi_1 = \varphi_3 = 4x, 4y, 4(-x), 4(-y)$; $\varphi_1 = 4x, 4y, 4(-x), 4(-y), 4(-x), 4(-y), 4x, 4y$; $\varphi_4 = x, -y, -x, y$; $\varphi_5 = 8(x, -y, -x, y), 8(-x, y, x, -y)$; $\varphi_6 = -y, -x, y, x$; $\psi = x, y, -x, -y, -x, -y, x, y$.

demonstrated only a modest sensitivity improvement over the standard 1D INADEQUATE (15% and 24% for INADEQUATE CR and INADEQUATE LBR, respectively).

Carbon–carbon coupling constants cannot be determined from a single 1D INADEQUATE CR or 1D INADEQUATE LBR single-transition spectra. A remedy proposed by the authors is to mistune one of the pulses, which partially restores the other line in the spectrum while marginally decreasing the intensity of the main signal. This is not practical in noisy INADEQUATE spectra where a poor signal-to-noise ratio could introduce errors in J coupling determination. The acquisition of both single-transition spectra would be required. The pulse sequence of 1D INADEQUATE LBR is applicable also to spin-1 system (e.g. ^{2}H), and it was suggested that it can be used to distinguish between the isotropic and ordered phases.

As a building block, 1D INADEQUATE LBR has been utilised as an alternative approach for 2D homonuclear correlation of rare spins.[17] This experiment uses DQ filtration of INADEQUATE LBR followed by evolution of SQ coherences and ZQ planar mixing (Figure 4). SQ transition correlation spectrum with a suppressed diagonal is produced. It is referred to as low-abundance single-transition correlation spectroscopy (LASSY, or CLASSY for ^{13}C applications). SQ coherences evolving during t_1 relax slightly slower (factor of 0.75 under extreme narrowing limit) than the DQ coherences. For long t_1 acquisition times, this will translate into improved sensitivity of the experiment compared to standard INADEQUATE that utilises DQ coherences. The transfer between coupled carbons can be

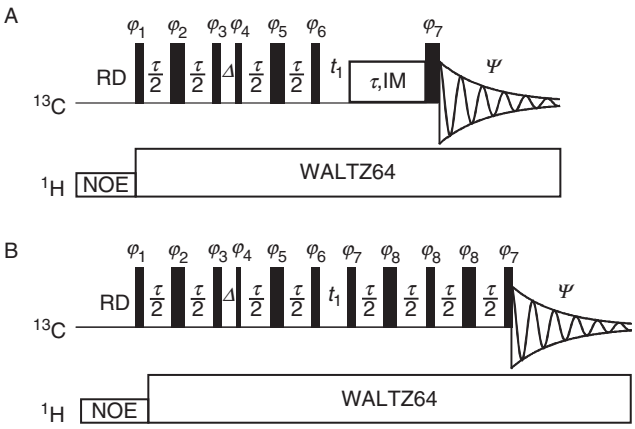

Figure 4 Pulse sequences 2D LASSY (or CLASSY) experiments. (A) CLASSY IM pulse sequence with isotropic mixing (IM). The narrow, wider and wide rectangles represent the 45°, 90° and 180° pulses, $\tau = 1/2J_{CC}$, $\Delta = 3$ μs. The following phase cycling was used: $\varphi_1 = \varphi_3 = 4x, 4y, 4(-x), 4(-y)$; $\varphi_2 = 4x, 4y, 4(-x), 4(-y), 4(-x), 4(-y), 4x, 4y$; $\varphi_4 = x, (-y), (-x), y$; $\varphi_5 = 8(x, -y, -x, y), 8(-x, y, x, -y)$; $\varphi_6 = -y, -x, y, x$; $\varphi_7 = 64x, 64(-x)$; $\psi = -x, y, x, -y, x, -y, -x, y$. (B) CLASSY DBR pulse sequence. $\varphi_1 = \varphi_3 = 4x, 4y, 4(-x), 4(-y)$; $\varphi_2 = 4x, 4y, 4(-x), 4(-y)$; $\varphi_4 = x, (-y), (-x), y$; $\varphi_5 = 4(x, -y, -x, y), 4(-x, y, x, -y)$; $\varphi_6 = -y, -x, y, x$; $\varphi_7 = 32y, 32(-x), 32(-y), 32(x)$; $\varphi_8 = 32x, 32y, 32(-x), 32(-y)$; $\psi = 4(-x, y, x, -y, x, -y, -x, y), 4(x, -y, -x, y, -x, y, x, -y)$.

achieved either via isotropic mixing (CLASSY IM, Figure 4 A) or double bilinear rotation (CLASSY DBR, Figure 4 B). The use of the former is limited by the spread of ^{13}C resonances that can be effectively spin-locked at higher fields. Variations in carbon–carbon couplings will also degrade the sensitivity of the experiment. The DBR implementation contains four spin echoes and is more prone to signal losses due to the J mismatch. Nevertheless, the authors have reported 19–25% enhancement of signal intensities compared with INADEQUATE CR using a sucrose sample. As this compound has rather uniform values of $^{1}J_{CC}$ coupling constants, more realistic samples need to be tested. Phase-alternated composite pulses[18] were implemented into CLASSY DBR pulse sequence and illustrated on a 500-MHz spectrum of camphor with a spread of resonances close to 200 ppm.

It should be noted that single-transition INADEQUATE spectra are generally not suitable for the determination of coupling constants. This is because the readout of the couplings in F_2 is affected by the isotope shifts. The combined use of F_2 and F_1 dimensions, which yields, in principle, the values of coupling constants, is problematic due to limited digital resolution in F_1. A possible solution is to acquire two spectra with the selection of one transition at the time. This should still be a factor of $\sqrt{2}$ more sensitive compared to regular INADEQUATE on an equal time basis.[5]

The applications of single-transition INADEQUATE experiments such as INADEQUATE CR remain rare today.[19] This is likely caused by the necessity of using composite pulses, the implementation of which is not straightforward for the average NMR user.

3.4. Post-acquisition processing

Several approaches to post-acquisition manipulation of INADEQUATE spectra that improve the signal-to-noise ratio have been proposed, as reviewed previously.[3] These either utilise the global and local symmetry of phase-sensitive INADEQUATE spectra containing large AP doublets[20,21] or perform non-linear least-square fits of AB spectral line shape patterns.[22–24] Despite their potential, the use of these procedures by NMR spectroscopists is limited, which could be due to the fact that the programs that perform such analysis are not widely available. The symmetry principles have been recently applied to the processing of the INADEQUATE spectrum acquired in a time-shared mode with other NMR experiments.[7] Authors have observed the expected twofold gain in sensitivity for AX spin systems and have incorporated into their algorithm a procedure that deals with strong coupling effects in AB systems. The line-fitting method was used to analyse INADEQUATE spectra of terreinol, uncovering some crucial carbon–carbon correlations.[25] An algorithm incorporating harmonic inversion signal processing has been proposed for the analysis noisy 1D INADEQUATE spectra.[26] DQ biased covariance spectroscopy converts a ^{13}C–^{13}C 2D INADEQUATE spectrum into a symmetric ^{13}C–^{13}C COSY-like 2D spectrum without a diagonal.[27] However, it should be noted that this procedure does not improve the signal-to-noise ratio of INADEQUATE spectra.

3.5. Elimination of the off-resonance effects

Typical ^{13}C rectangular pulses with $\gamma B_{1max} = 20$ kHz (12.5 and 25 μs for 90° and 180° pulses) generate large off-resonance effects for chemical shift range of 200 ppm required for ^{13}C. These effects can lead to a significant attenuation or complete loss of signal in multi-pulse INADEQUATE pulse sequences. Practical implementations of INADEQUATE pulse sequences must, therefore, include some sort of compensation of off-resonance effects. Several approaches have been reported to date.

Composite pulses that include global compensation of phase shifts[18] have been implemented into 2D INADEQUATE and 2D INADEQUATE CR pulse sequences with a dramatic signal recovery[14,15] (Figure 5). Pulses with all nominal angles were replaced by phase-alternating composite pulses that have a bandwidth $\Delta\omega/\omega_1$ of ± 0.65.[16] Such off-resonance-compensated pulse sequences, therefore, cover the complete range of ^{13}C chemical shifts on spectrometers up to ^{1}H frequency of 500 MHz.

The 180° inversion and refocusing pulses are particularly critical. When applied as simple rectangular pulses, these fail to cover the complete range of ^{13}C frequencies even at lower field instruments. Smoothened chirp pulses show much better inversion profiles (Figure 6 A) and have been implemented into the ADEQUATE pulse sequence.[28] These pulses are not suitable as refocusing pulses

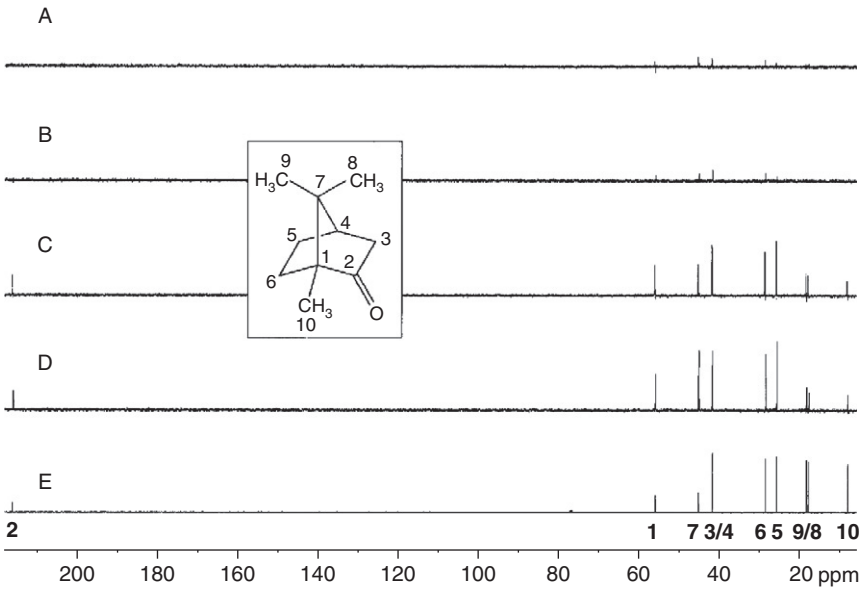

Figure 5 Natural-abundance 1D ^{13}C INADEQUATE CR spectra of camphor at 500 MHz: (A) and (B) left and right line of uncompensated INADEQUATE CR, respectively. (C) and (D) left and right line of off-resonance compensated INADEQUATE CR, respectively. (E) a one-scan single-pulse 1D ^{13}C spectrum for comparison. From Ref. 15, reproduced by permission of John Wiley and Sons.

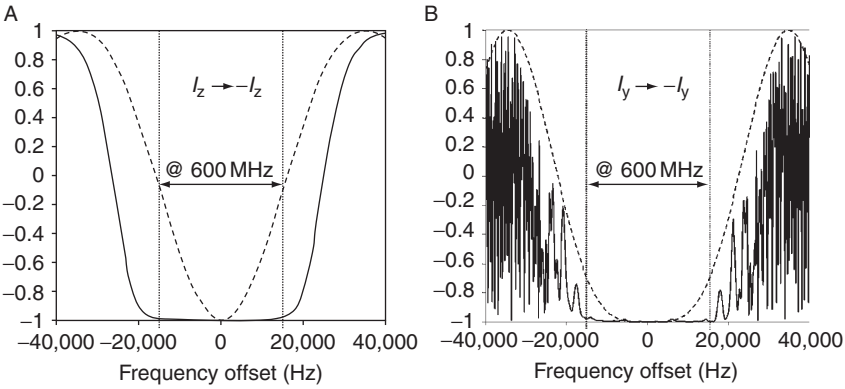

Figure 6 Frequency profiles of 180° ^{13}C pulses: (A) inversion of I_z magnetisation with a 25-μs rectangular pulse (dashed line) and the smoothed 500-μs chirp pulse applied at $\gamma B_{1max} = 10$ KHz; (B) frequency profile of a 25-μs refocusing rectangular pulse (dashed line) and the composite smoothed chirp pulse (solid line). 200-ppm ^{13}C range at 600 MHz is shown using dotted lines. Adapted from Ref. 28.

but can be arranged as composite adiabatic pulses presenting improved phase profile (Figure 6 B).

The combined use of adiabatic inversion and composite adiabatic pulses can have a dramatic effect on the sensitivity of 1,1-ADEQUATE on a 600-MHz NMR spectrometer as illustrated on spectra of cholesteryl acetate in Figure 7.[28]

Chirp pulses have also been used in a double-*J*-modulated INEPT-INADEQUATE.[29] Universal rotators constructed by combining two point-to-point rotations[30] have been recently used in ^{1}H- and ^{13}C-detected IPAP-INADEQUATE experiments.[31,32]

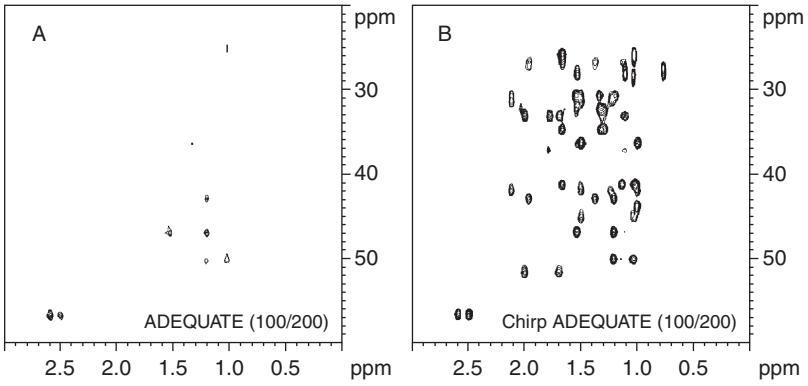

Figure 7 Parts of 1,1-ADEQUATE spectra of cholesteryl acetate acquired with ^{13}C offset at 100 ppm and covering the sweep with of 200 ppm. (A) rectangular (B) inversion and composite chirp pulses. From Ref. 28, reproduced by permission of John Wiley and Sons.

3.6. Utilising the ACCORDION principle

Excluding the carbon–carbon couplings across a triple bond, which could be as large as 240 Hz, a typical range of $^{1}J_{CC}$ coupling constants is 30–80 Hz.[33] Setting of the evolution intervals in INADEQUATE experiments to the average coupling constant of 55 Hz will therefore lead to some sensitivity losses. In ^{13}C- and ^{1}H-detected experiments, the signal intensity is typically affected by the setting of one and two evolution intervals according to $\sin(\pi\ J\tau)$ and $\sin^2(\pi\ J\tau)$, respectively. This results in a loss of 25% and 43% when $^{1}J_{CC}$ of 30 or 80 Hz are involved. When the evolution intervals are changed within a certain range during the incrementation of t_1, a more even distribution of signal intensities is achieved. Implementation of this accordion principle was proposed in an ACCORD-ADEQUATE experiment.[34]

3.7. ^{1}H detection

Quantifying the relative sensitivity of ^{1}H- and ^{13}C-detected INADEQUATE is not straightforward. One can start by considering the factor $(\gamma_{^1H}/\gamma_{^{13}C})^{5/2} = 32$, which takes into account the nucleus generating the initial polarisation and the nucleus used for the signal detection. Additional factors such as the heteronuclear NOE in ^{13}C-detected INADEQUATE (factor of $\sim$0.33), leakage of the signal into to ZQ coherences in ^{1}H-detection (0.5) and the use of pulsed field gradients (PFGs) in ^{1}H detection (factor of 0.71), all decrease the sensitivity advantage of ^{1}H-detected methods. Depending on a particular implementation of ^{1}H- or ^{13}C-detected INADEQUATE experiments, the above considerations can reduce the 32-fold sensitivity advantage of ^{1}H-detection approximately four- to sixfold.[3,5]

In practice, however, such considerable sensitivity gain is rarely realised by ^{1}H detection mainly due the complicated nature of ^{1}H multiplets. ^{13}C detection is performed under low-power ^{1}H decoupling allowing acquisition times of $\sim$400 ms, while the acquisition times of ^{1}H-detected experiments under high-power ^{13}C decoupling is limited to $\sim$100 ms. ^{13}C detection yields AP doublets with natural linewidths of few hertz, while ^{1}H detection leads to the detection of broad, unresolved proton multiplets with much wider lines.

In addition, the sensitivity of ^{1}H-detected INADEQUATE is degraded by the mismatch between the actual $^{1}J_{CH}$ and $^{1}J_{CC}$ coupling constants and the average ones used to optimise the evolution intervals ($\tau = 1/2\ ^{1}J_{CHav}$ and $\Delta = 1/2\ ^{1}J_{CCav}$). Neglecting the relaxation effects, the efficiency of the ^{13}C-detected INADEQUATE (pulse sequence of Figure 1) is given by $\sin(\pi^{1}J_{CC}\Delta)$, while the ^{1}H-detected INADEQUATE (pulse sequence of Figure 8 A) shows potentially more substantial signal losses according to $\sin^2(\pi^{1}J_{CH}\tau) \times \sin^2(\pi^{1}J_{CC}\Delta)$. These factors degrade the signal-to-noise ratio achievable in ^{1}H-detected experiments considerably, generally leaving only a small advantage over ^{13}C detection.

Numerous implementations of ^{1}H-detected INADEQUATE exist and, depending on the investigated molecule, it is therefore possible to choose the most appropriate experiment. Considering the H↔C↔C↔H pathway only, sensitivity of different ^{1}H-detected INADEQUATE experiments has been analysed.[35]

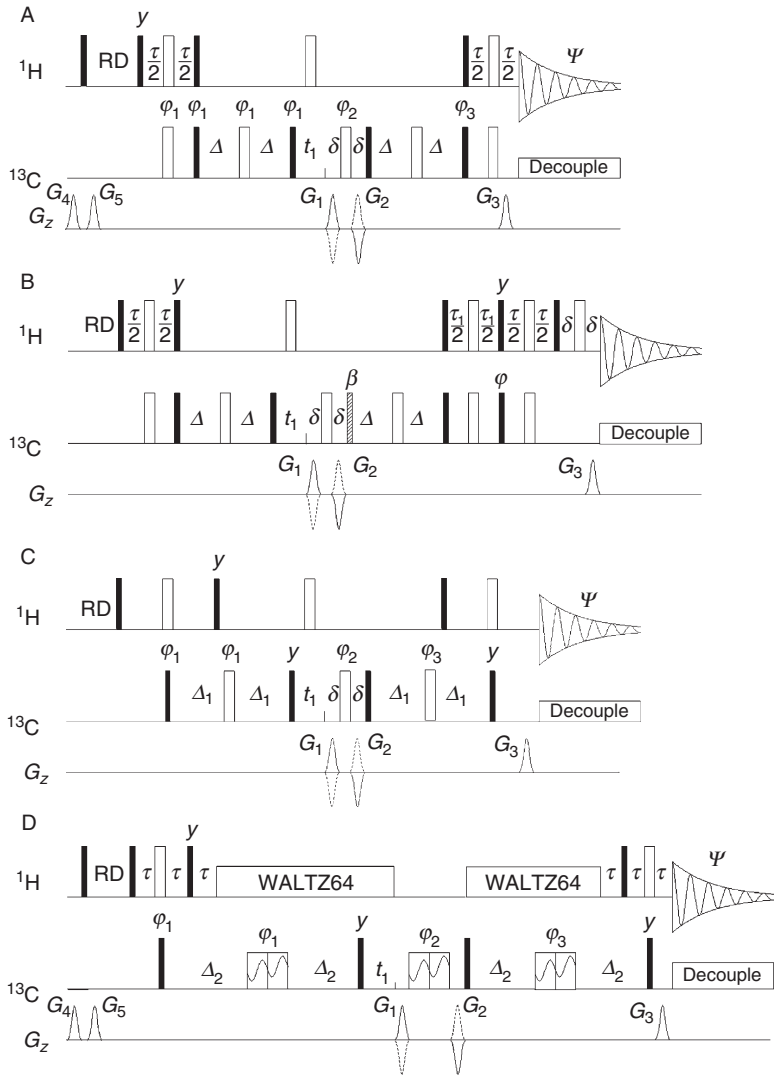

Figure 8 Various implementations of the H↔C↔C↔H pathway in INADEQUATE experiments. Filled and empty rectangles represent 90° and 180° rectangular pulses, $\tau = 1/2^1J_{CH}$, $\Delta = 1/4^1J_{CC}$ or $\Delta = 1/4^nJ_{CC}$, $\Delta_1 = 1/4^1J_{CC}$, $\Delta_2 = 1/4^nJ_{CC}$, $\Delta = 1.2$ ms. PFGs expressed as a percentage of 50 G cm^{-1} were $G_4 = 57\%$, $G_5 = 77\%$, $G_1 = 40\%$, $G_2 = -40\%$, $G_3 = 40.16\%$. (A) ^{1}H-detected INEPT-INADEQUATE, $\varphi_1 = x, y, -x, -y$; $\varphi_2 = x, y, -x, -y, -x, -y, x, y$; $\varphi_3 = 8x, 8(-x)$; $\psi = 2(x, -x, x, -x), 2(-x, x, -x, x)$; (B) INEPT-COS-INADEQUATE $\tau_1 = 1/2^1J_{CH}$ (CH), $\tau_1 = 1/4^1J_{CH}$ (CH_2) or $\tau_1 = 1/6^1J_{CH}$ (CH_3). In combination with the gradients for echo $\beta = \pi/3$, $\varphi = -y$ or $\beta = 2\pi/3$, $\varphi = y$ and for anti-echo $\beta = \pi/3$, $\varphi = y$ or $\beta = 2\pi/3$, $\varphi = -y$. (C) DEPT2-INADEQUATE for HCCH and HCC fragments, (D) DEPT2-INADEQUATE for long-range correlation of HCCH and HCC fragments. Dashed rectangle represents 90° ^{1}H pulse. Phase cycling for (C) and (D) is as follows: $\varphi_1 = x, -x$; $\varphi_2 = 2x, 2(-x)$; $\varphi_3 = 4x, 4y$; $\psi = 2(x, -x), 2(-x, x)$.

The authors compared the relative sensitivity of various implementations of INEPT or DEPT for the proton–carbon polarisation transfer steps including the pulse sequences utilising the coherence-order-selective (COS) transfers. By considering H_n protons in a general H_nCCH_m fragment, where $n = 1, 2, 3$ and $m = 0, 1, 2, 3$ refer to the number of attached protons, the authors concluded that the experiment of choice for general use is the 2D INEPT2-INADEQUATE (Figure 8 A). This experiment, initially proposed by Weigelt and Otting,[36] gives a uniform relative sensitivity of 0.25 for all n, m combinations.

The pulse sequence of the INEPT2-INADEQUATE starts with a $^1J_{CH}$-optimised INEPT transfer and finishes with a $^1J_{CH}$-optimised reverse INEPT step. The created carbon–carbon DQ coherences are frequency labelled using the gradient-enhanced echo–anti-echo selection. The carbon–carbon evolution delays, Δ, can be optimised for either one-bond or long-range carbon–carbon coupling constants. This experiment, therefore, is also the most general ^{1}H-detected method for establishing the long-range carbon–carbon correlations.

The INEPT-COS-INADEQUATE (Figure 8 B), which is in terms of sensitivity equivalent to the 1,1-ADEQUATE,[37] outperforms (relative sensitivity of 0.325) the INEPT-INADEQUATE experiments only for H_1CCH_m ($m = 0, 1, 2, 3$) segments. Particularly encouraging theoretical predictions for HCCH and HCC segments were obtained for the COS-DEPT pulse sequence[35] (not shown) with double the relative sensitivity (0.65) for HCCH segments and the same sensitivity (0.325) for HCC moieties. These results, however, were not confirmed experimentally by the authors.

For the HCCH and HCC segments, which are of particular interest to polyaromatic compounds, high relative sensitivity (0.5 and 0.25) was also predicted for the DEPT2-INADEQUATE pulse sequence (Figure 8 C). The main reason why this pulse sequence performs so well is that it incorporates refocusing of AP proton–carbon coherences prior to the creation of DQ carbon coherences. Its performance is also boosted by a smaller number of pulses (6 ^{1}H and 7 ^{13}C vs. 11 ^{1}H and 10 ^{13}C) and delays compared to those of the COS-INADEQUATE pulse sequence.

The DEPT2-INADEQUATE is also the experiment of choice for long-range carbon–carbon correlation in HCCH and CCH moieties. In this particular application, it is advantageous to apply ^{1}H decoupling during the long carbon–carbon evolution intervals, Δ_2, after refocusing of the one-bond proton–carbon couplings (Figure 8 D). This ensures that the proton longitudinal relaxation is eliminated as was illustrated in Ref. 31.

A simple modification of 2D 1,1-ADEQUATE and chemical shift ω_1-refocused 2D 1,1-ADEQUATE has been proposed recently.[38] An insertion of a 180° ^{1}H pulse into the initial ^{13}C–^{13}C spin-echo yields cross peaks edited by the CH_x multiplicity: the cross peaks of CH and CH_3 groups display opposite phase to those of CH_2 groups leading to distinct phase patterns facilitating spectral analysis. Although the length of the pulse sequence is not affected by this modification, losses of sensitivity can occur due to a mismatch between the set and actual value of $^1J_{CH}$ coupling constants.

4. MEASUREMENT OF $^{13}C–^{13}C$ COUPLING CONSTANTS

The one-bond and long-range carbon–carbon coupling constants are a rich source of structural information[33]; however, they are not yet widely used because of the inherent low sensitivity of INADEQUATE. This is a particular problem for the long-range couplings. The one-bond and long-range carbon–carbon coupling constants can in principle be measured using both ^{13}C- and ^{1}H-detected INADEQUATE experiments, although ^{1}H-detected methods require some modification of the basic chemical shift correlation techniques.

The signal-to-noise ratio of 10:1 is generally required for accurate measurement of coupling constants. This is more than what is needed to establish reliably the existence of a cross peak, and therefore the measurements of coupling constants will require more compound than is needed for basic correlation experiments. As a way of example, the long-range carbon–carbon coupling constants of Me-β-D-lactoside ($M_w = 356$ g/mol) were measured using 25 mg of sample dissolved in 350 μl of D_2O (Shigemi tube, 200 mM sample). Both ^{1}H- and ^{13}C-detected experiments (~42 h) yielded the same values of couplings, and although different spectrometers were used, it was implied that the ^{1}H detection was, in this particular instance, up to two times more sensitive than the ^{13}C detection.[31]

4.1. ^{13}C-detected methods

Most of the carbon–carbon coupling constants published recently have been measured using 2D ^{13}C-detected INADEQUATE spectra.[39–44] 1D INADEQUATE experiments were used less frequently[43,45] due to potential overlap problems. The measured coupling constants are usually used to resolve stereochemical problems and also compared with theoretical values.

Frequency separation between the two lines of AP doublets in ^{13}C-detected INADEQUATE spectra corresponds to $^{1}J_{CC}$ coupling constants, which are simply read out from the spectra. However, accurate determination of $^{n}J_{CC}$ coupling constants is more problematic due to possible partial cancellation of closely spaced AP doublets. The peak-to-peak distance in such doublets does not correspond to actual value of the coupling constant. A solution to this problem was proposed recently in the form of IPAP-INADEQUATE experiment (Figure 9).[32]

In this method, the accurate values of $^{n}J_{CC}$ coupling constants are obtained by editing of IP and AP carbon doublets. The AP doublets are acquired using the standard INADEQUATE pulse sequence (Figure 9 A). Due to the large spread of $^{n}J_{CC}$ couplings, purging of residual AP magnetisation is required to obtain pure IP doublets (Figure 9 B). This is achieved by the combination of an adiabatic inversion and a low-level pulsed field gradient. An estimate of the scaling factor between the long-range IP and AP doublets is required for the determination of coupling constants (Figure 10 A, B). This scaling factor can be obtained from the analysis of INADEQUATE spectra and measured ^{13}C relaxation times as described in Ref. 32.

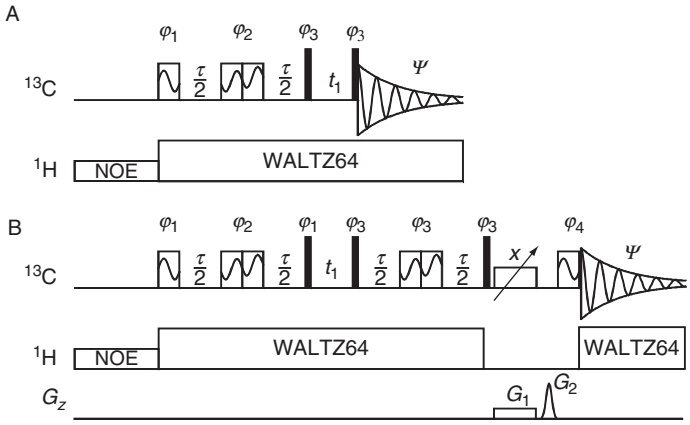

Figure 9 ^{13}C-detected IPAP INADEQUATE: (A) non-refocused (AP) and (B) refocused (IP) INADEQUATE: $\tau = 0.5/{}^nJ_{CC}$, the 90° rectangular pulses are shown as filled rectangles; 90° BEBOP and 180° BIBOP pulses are indicated as narrow and wide rectangles, respectively; the adiabatic inversion pulse is designated by an inclined arrow. Phase cycling is given in Table 1. From Ref. 32, reproduced by permission of John Wiley and Sons.

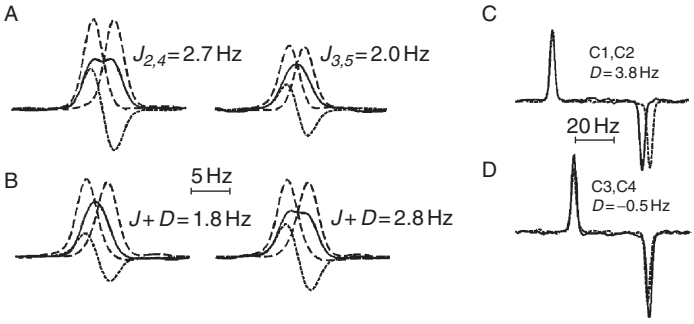

Figure 10 Examples of the analysis of long-range cross peaks in (A) isotropic and (B) aligned sample of Me-β-D-xylopyranoside. Short-dashed and solids lines show anti-phase (AP) and in-phase (IP) multiplets. Long-dashed singlets were obtained by the addition and subtraction of the IP and AP multiplets using appropriate scaling factors. (C) Overlay of two one-bond cross peaks from isotropic (solid line) and aligned (dashed line) samples. The multiplets were shifted to overlay on one line of the doublet in order to accentuate the difference between *J* and *D*.

Although the evolution intervals, τ, of the IPAP-INADEQUATE experiment are optimised for ${}^nJ_{CC}$ couplings, the one-bond correlation cross peaks appear in the spectra with random intensities. However, by recording two spectra with setting $\tau = 0.5/{}^nJ_{CC}$ and $\tau = 0.5/{}^nJ_{CC} + 0.5/{}^1J_{CC}$, the one-bond cross peaks will appear at least in one spectrum. The long-range correlations will appear with practically unchanged intensities in both spectra and are analysed from the spectrum which is their sum.

The carbon–carbon residual dipolar coupling constants (RDCs) are of particular interest for the structural investigation of small organic molecules in aligned

media. Since only two ^{13}C spins are selected in each molecule by the INADEQUATE pulse sequence, the extraction of carbon–carbon RDCs is not different from the measurement of J_{CC} coupling constants. An example of the determination of $^{n}D_{CC}$ and $^{1}D_{CC}$ coupling constants of Me-β-D-xylopyranoside from IPAP-INADEQUATE is given in Figure 10.

4.2. ^{1}H-detected methods

^{1}H-detected experiments for the measurement of $^{1}J_{CC}$ and $^{n}J_{CC}$ coupling constants are simple modifications of standard INADEQUATE/ADEQUATE experiments. These enable modulation of the signal either by $\sin(\pi J_{CC}t_1)$ or $\cos(\pi J_{CC}t_1)$ yielding AP[46–49] or IP[50] carbon–carbon doublets in the indirectly detected dimension. When performed as *J*-resolved experiments,[46–48] their applicability is limited to compounds with well-resolved proton multiplets. This limitation is removed when the *J*-modulation is superimposed on the evolution of DQ[47,48] or SQ[49] coherence. Such experiments also allow the scaling up of the coupling constants, which is particularly useful when measuring small long-range coupling constants.

In the regime of a limited digital resolution, which is typical for the indirectly detected dimension, the IP rather than AP doublets can provide more accurate values of coupling constants. This observation led to the design of a *J*-modulated ADEQUATE experiment (Figure 11 A)[50,51] that yields IP doublets in the F_1 dimension. This is achieved by simultaneously incrementing a carbon–carbon spin-echo period and the DQ labelling period t_1. In this arrangement, the coupling constants can be scaled up by an arbitrary scaling factor (Figure 12).

In order to cover the full range of ^{13}C chemical shifts, it is necessary to replace rectangular 180° pulses by adiabatic 180° pulses as discussed above. It was shown that in *J*-modulated ADEQUATE a partial evolution of $^{1}J_{CC}$ coupling constants during a composite 180° ^{13}C pulse in the middle of the incrementable spin-echo interval leads to inaccurate values of coupling constants.[51] The proposed solution employs a pair of shorter (<200 μs) broad-band inversion pulses. Such an arrangement compensates for off-resonance phase errors and covers an increased bandwidth compared to simple rectangular pulses.

For small long-range coupling constants and/or faster relaxing spin systems where sufficient resolution in F_1 cannot be achieved, editing of IP and AP doublets obtained in ^{1}H-detected IPAP DEPT-INADEQUATE or IPAP RINEPT-INADEQUATE[31] (Figure 13) is required. These ^{1}H-detected experiments are analogous to the ^{13}C-detected IPAP INADEQUATE[32] discussed above. The difference is that in ^{1}H-detected experiments the coupling constant modulates the cross peaks in the indirectly detected F_1 dimension.

These experiments use ^{1}H decoupling during most parts of the pulse sequence, which increases the lifetime of coherences.[31] The purging of the residual AP component of doublets is achieved by a combination of an adiabatic inversion and a low-level pulsed field gradient.

Long-range carbon–carbon coupling constants are a useful tool in the conformational analysis of glycosidic linkages of carbohydrates.[52] Figure 14 shows the

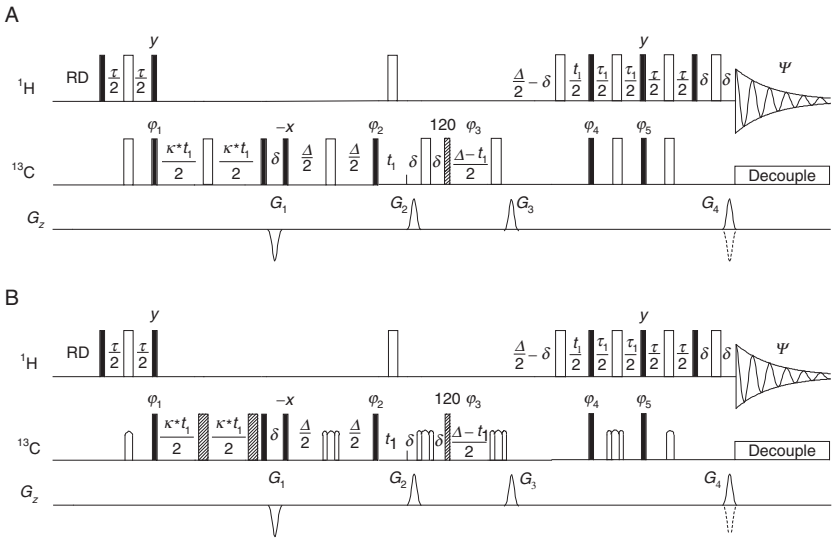

Figure 11 Pulse sequences of the *J*-modulated ADEQUATE experiment. Filled and empty rectangles represent 90° and 180° rectangular pulses with phase *x*, unless stated otherwise. The pulse with phase φ_3 is a 120° pulse. The following phase cycling was used: $\varphi_1 = x, -x$; $\varphi_2 = 4x, 4(-x)$; $\varphi_3 = 8x, 8(-x)$; $\varphi_4 = 2x, 2(-x)$; $\varphi_5 = y, -y$; $\psi = x, 2(-x), x, 2(-x, 2x, -x), x, 2(-x), x$. (A) Pulse sequence according to Ref. 50. In (B),[51] the inversion and refocusing pulses were chirp pulses as stated in Ref. 28. The shaded pulses were BIB pulses. Echo–anti-echo selection is achieved by the pulsed field gradients: $G_2 = 78.4\%$, $G_3 = 77.4\%$ and $G_4 = \pm 59\%$; $G_1 = -31\%$. $\tau = 1/2{}^1J_{CH}$, $\tau_1 = 1/2{}^1J_{CH}$ for CH and $1/4{}^1J_{CH}$ for all multiplicities, $\Delta = 1/2{}^1J_{CC}$, κ is the scaling factor for *J* evolution.

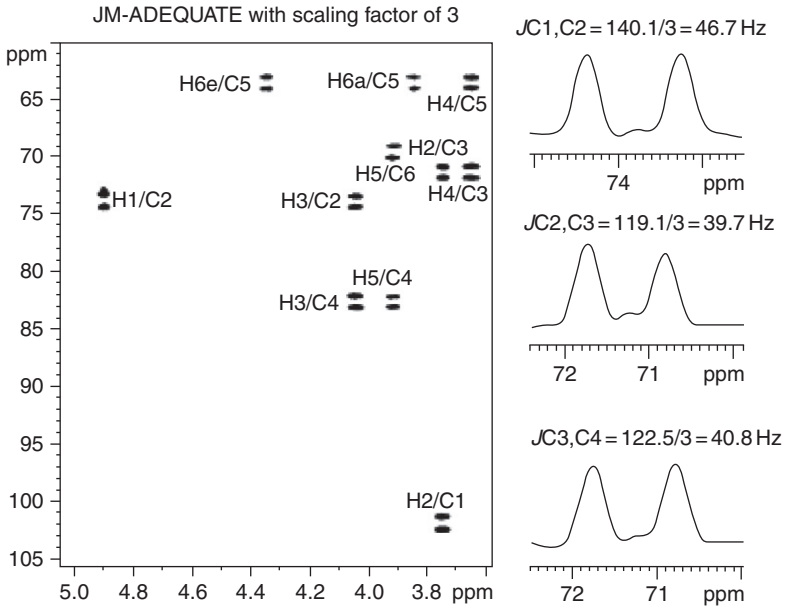

Figure 12 Measurement of ${}^1J_{CC}$ couplings of 4,6-benzylidene-1-metoxy-α-D-glucose using the pulse sequence of Figure 11 A. From Ref. 50, reproduced by permission of Elsevier.

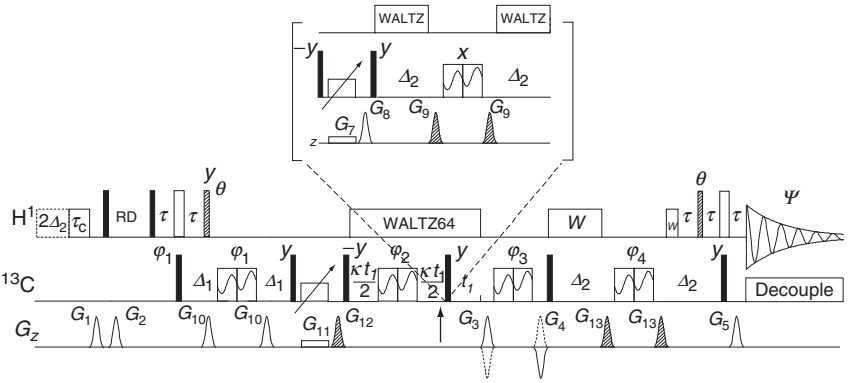

Figure 13 Pulse sequences of ^{1}H-detected IPAP DEPT-INADEQUATE. The insert is used when in-phase doublets are acquired. The filled and open rectangles represent 90° and 180° rectangular pulses, respectively, applied from the *x*-axis unless stated otherwise. The dashed rectangles of the DEPT pulse sequence represent rectangular pulses with flip angle $\theta = 90°$ or 45°. The 180° BIBOP pulses are indicated as wide rectangles with a sine wave. The ^{13}C adiabatic inversion pulses are designated by an inclined arrow. The following delays were used: $\tau = 0.5/{}^{1}J_{CH}$, $\Delta_1 = 0.25/{}^{1}J_{CC}$, $\Delta_2 = 0.25/{}^{n}J_{CC}$. For other parameters see Ref. 31. Reproduced by permission of Elsevier.

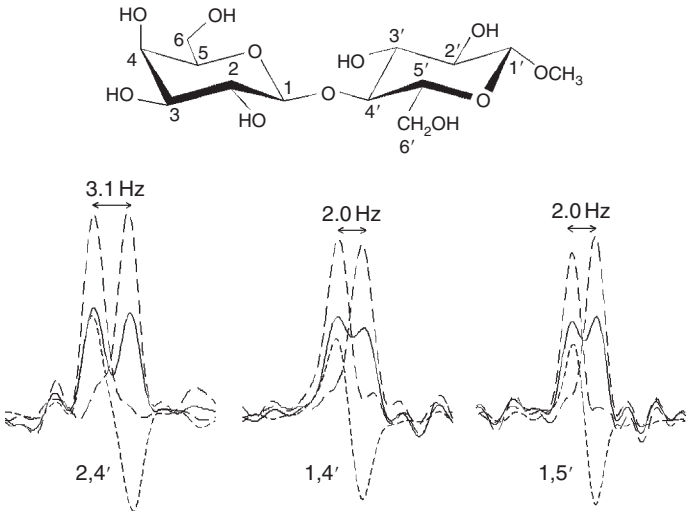

Figure 14 Determination of interglycosidic coupling constants of Me-β-D-lactoside, shown in the inset, using F_1 traces from IPAP DEPT-INADEQUATE spectra. The long-dashed lines are the sum or the difference of the in-phase (solid line) and anti-phase doublets (short-dashed line). From Ref. 31, reproduced by permission of Elsevier.

determination of coupling constants from IP and AP doublets extracted from the F_1 dimension of IPAP DEPT-INADEQUATE of Me-β-D-lactoside.

None of the above ^{1}H-detected experiments measures both the one-bond and long-range carbon–carbon couplings at the same time, as these require the evolution and refocusing delays to be optimised separately for each class of couplings. A simple modification of the 2D INEPT-INADEQUATE[36] (Figure 8 A), which turns both its fixed evolution intervals, τ, into incrementable ones was proposed. In such ^{1}H-detected double-J-modulated INEPT-INADEQUATE experiment,[29] the cross peaks are modulated by $\sin^2(\pi\ J_{CC}\kappa\ t_1)$ factor (κ is a scaling factor), yielding triplets with $-1{:}2{:}-1$ intensities in F_1 (Figure 15).

Compared to single J-modulated experiments, the sensitivity of double J-modulated INEPT-INADEQUATE is reduced by a factor of 2. Nevertheless, it offers the possibility of measuring both one-bond and long-range coupling constants from a single spectrum, which is achieved by a computer-assisted analysis of the cross peaks (Figure 15). The multiplets are extracted from F_1 traces of 2D spectra and inverse Fourier transformed. The high-frequency DQ modulation is removed from the reconstructed free induction decays (FIDs). These are then fitted using an appropriate transfer function to yield the values of coupling constants.

5. APPLICATIONS OF HIGH-RESOLUTION INADEQUATE TO ^{13}C

This section highlights the typical applications of ^{13}C- and ^{1}H-detected INADEQUATE and details a selection of examples from different areas of chemistry. These include primary structure determination of small molecules, the use of partially ^{13}C-enriched compounds in biosynthetic studies, the recent structural analysis of fullerenes and the latest development in NMR hardware that promises to advance the use of high-resolution INADEQUATE experiments for polymers.

5.1. Structure determination of small molecules

The elucidation of the primary structure of small organic molecules by tracing their carbon skeletons was, traditionally, the main focus of INADEQUATE experiments. It is not the first NMR experiment to be considered for such a task; typically a standard set of NMR spectra, that is COSY, TOCSY, NOESY, HSQC and HMBC, are performed and analysed first. If ambiguities remain after inspection of standard spectra, the tracing of carbon–carbon connectivities is embarked on. Nevertheless, an example is presented below where carbon–carbon connectivities are included at an earlier stage in order to reduce the number of computer-generated structures compatible with the experimental data.

5.1.1. ^{13}C-detection

This approach is exemplified by the structure determination of an allosteric ligand of G-protein-coupled receptor MT_2.[6] Self-condensation of 2-(1*H*-indol-2-yl)ethyl tolsylate, **1**, has initially been reported to yield product **3** (Figure 16).

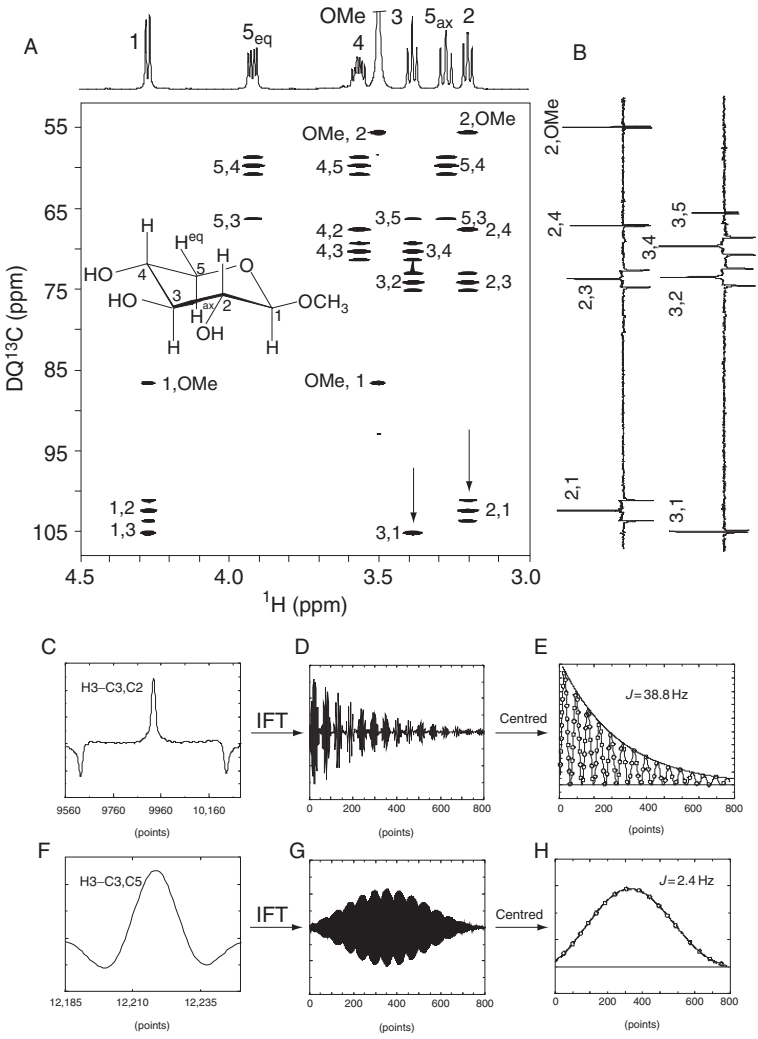

Figure 15 (A) A 2D DJM-INEPT-INADEQUATE spectrum of Me-β-D-xylopyranoside. (B) F_1 traces at ^{1}H chemical shifts of H_2 and H_3 protons as indicated by vertical arrows in (A) showing one-bond (2,1 and 2,3; 3,2 and 3,4) and long-range (2,4 and 2,OMe; 3,1 and 3,5) correlations. C_3C_2 and C_3C_5 cross peaks (C) and (F) were analysed. (D) and (G) show 800 real points of FIDs obtained after inverse Fourier transformation of the multiplets. The centred FIDs obtained by deconvolution with DQ frequencies are shown in (E) and (H) together with the results of the fitting. From Ref. 29, reproduced by permission of Elsevier.

However, the analysis of NOESY spectra yielded several interactions that were not compatible with the proposed structure. A ^{13}C-detected INADEQUATE spectrum (Figure 2) was therefore acquired, which showed several crucial connectivities between the carbons of the aliphatic chains, namely C5a, C6, C7, C7a, C7b and C15, C14a, C14, C13, revealing the existence of a cyclobutane ring in compound **2**, 7,7a,13,14-tetrahydro-6*H*-cyclobuta[*b*]pyrimido[1,2-*a*:3,4-*a*′]diindole.

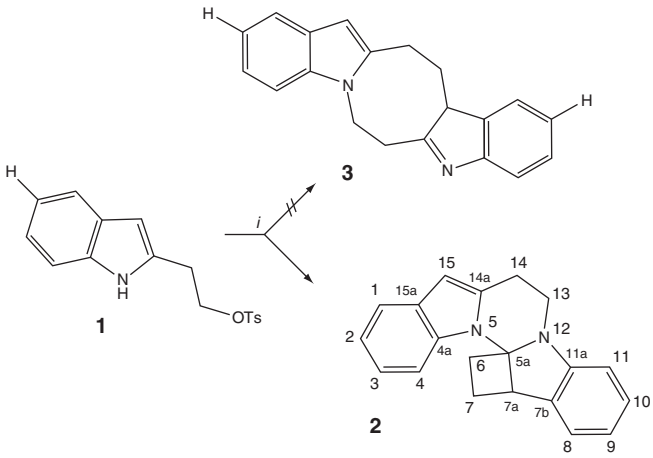

Figure 16 Two possible outcomes of the self-condensation of 2-(1*H*-indol-2-yl)ethyl tolsylate, compounds **2** and **3**.

Several structures have been corrected and elucidated with the aid of ^{13}C-detected INADEQUATE. For example, the ^{1}H and ^{13}C assignment of *trans*-3,4′,5-trihydroxystilbene was corrected.[53] The structure of a dimeric meroterpenoid, tridentorubin, was also investigated by ^{13}C-detected INADEQUATE,[54] while the structure of A-74528, an inhibitor for 20,50-phosphodiesterase isolated from *Streptomyces* sp., was elucidated on the basis of several crucial carbon–carbon connectivities that could not be determined from the analysis of its HMBC spectrum.[55] Additional examples of the use of ^{13}C-detected INADEQUATE to aid structure determination of small molecules can be found in the literature.[25,56–61]

5.1.2. ^{1}H-detection

A recent study of brominated pyrrole-imidazole alkaloids[8] illustrates the usefulness of additional carbon–carbon connectivities provided by 1,1-and 1,*n*-ADEQUATE spectra when analysed in conjunction with a ^{1}H–^{13}C HMBC experiment. 1,1-ADEQUATE allows the distinction to be made between the $^{2}J_{CH}$- and $^{3,4}J_{CH}$-mediated correlations seen in the HMBC spectrum, while the 1,*n*-ADEQUATE extends the ^{1}H–^{13}C HMBC correlations by another carbon atom, effectively providing pseudo-$^{4,5}J_{CH}$ correlations. This is illustrated in Figure 17 using monobromophakellin (**4**). The ADEQUATE experiments required ca 20 h in total of the acquisition time using 21 mg of **4** on a 600-MHz NMR instrument equipped with a BRUKER TCI cryoprobe.

The HMBC spectrum of **4** contains five cross peaks showing the correlations of H12 with carbons C2, C3, C10, C11 and C14. Correlation of H12 with carbon at 81 ppm seen in the 1,1-ADEQUATE spectrum overlaps with an HMBC cross peak. Thus, this is a $^{2}J_{CH}$-mediated cross peak. Also, C11 is the only carbon linked to C12. Comparison of HMBC and 1,*n*-ADEQUATE spectra identified three extra carbon atoms C4, C8 and C9 that are four, five and four bonds away, respectively, from proton H12.

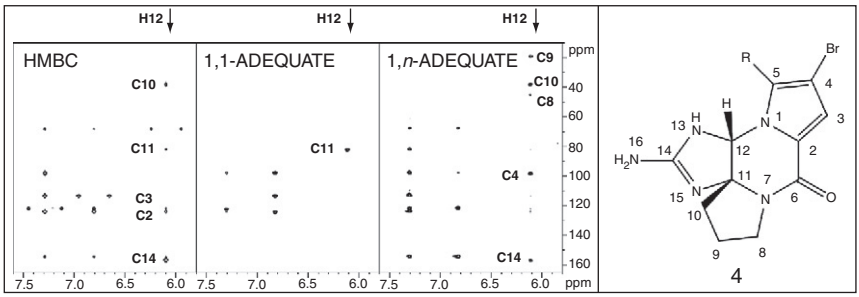

Figure 17 ^{1}H, ^{13}C HMBC, 1,1-ADEQUATE and 1,*n*-ADEQUATE spectra and the structure of **4**, From Ref. 8, reproduced by permission of the American Chemical Society.

These additional correlations significantly reduced the number of possible structures generated by an NMR-based structure generator used in this work. When only ^{1}H,^{1}H-COSY and ^{1}H,^{13}C-HMBC spectra were analysed, 1310 possible solutions were produced. When the ^{1}H, ^{15}N-HMBC and 1,1-ADEQUATE spectra were included, this number was reduced to four.

^{1}H-detected INEPT-INADEQUATE has been used to investigate the structures and aggregation trends of the intermediate π complexes of 4,4a,5,6,7,8-hexahydro-4a-methyl-naphthalen-2(3*H*)-one (**5**) and $Me_2CuLi{\cdot}LiI$ (**6**) in diethyl ether at 180 K[62] (Figure 18).

Compound **6**, but not **5**, was isotopically enriched. For the first time, carbon–carbon scalar coupling interactions across copper, between the cuprate moiety and an enone, without ^{13}C labelling of the enone were detected in these complexes.

Cytosporacin, a highly unsaturated polyketide, has been investigated[63] using an ACCORD-ADEQUATE experiment.[34] The same techniques helped to determine the structure of phormidolide, metabolite from the marine cyanobacterium *Phormidium* sp.[64] Other examples of the use of 1,1-ADEQUATE can be found in Refs. 65–67.

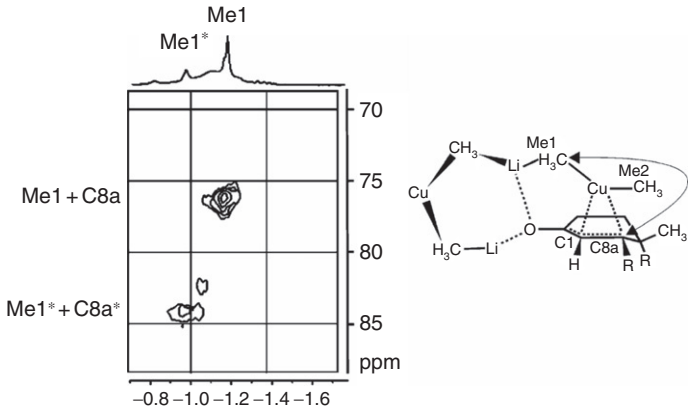

Figure 18 Section of a ^{1}H,^{13}C INEPT-INADEQUATE spectrum of **5** at natural abundance and ^{13}C-labeled **6**. From Ref. 62, reproduced by permission of the American Chemical Society.

5.2. Studies of biosynthetic pathways

When metabolites are grown in the presence of ^{13}C-labelled precursors, labelled in adjacent positions such as [$^{13}C_2$]acetate, the presence or absence of pairs of labelled carbon atoms and their mutual orientation in the final compound report on the biosynthetic pathway. For example, the biosynthesis of knipholone, an axially chiral phenylanthraquinone found in higher plants,[68] was investigated using this method. The compound was isolated from whole sterile plants after [$^{13}C_2$]acetate was fed by administration to the roots for a period of 2 months. Although ^{13}C detection limits were improved substantially by partial enrichment by ^{13}C, the overall amount of compound available was low (~1 mg). The ^{13}C NMR spectrum of the isolated knipholone showed partly overlapping signals and an insufficient signal-to-noise ratio, obscuring some of the ^{13}C doublets. It was impossible to draw the conclusions by measuring the $^{1}J_{CC}$ coupling constants. The problems were overcome by using ^{13}C-detected INADEQUATE (Figure 19) acquired on a spectrometer equipped with a cryoprobe, which permitted identification of the $^{13}C_2$ units as shown in the inset.

In the antraquinone part of the molecule, the only atom without a coupling partner was C2, which revealed the site of decarboxylation. Combined with the fact that the first (''western'') ring contained two and not three intact [$^{13}C_2$] units,

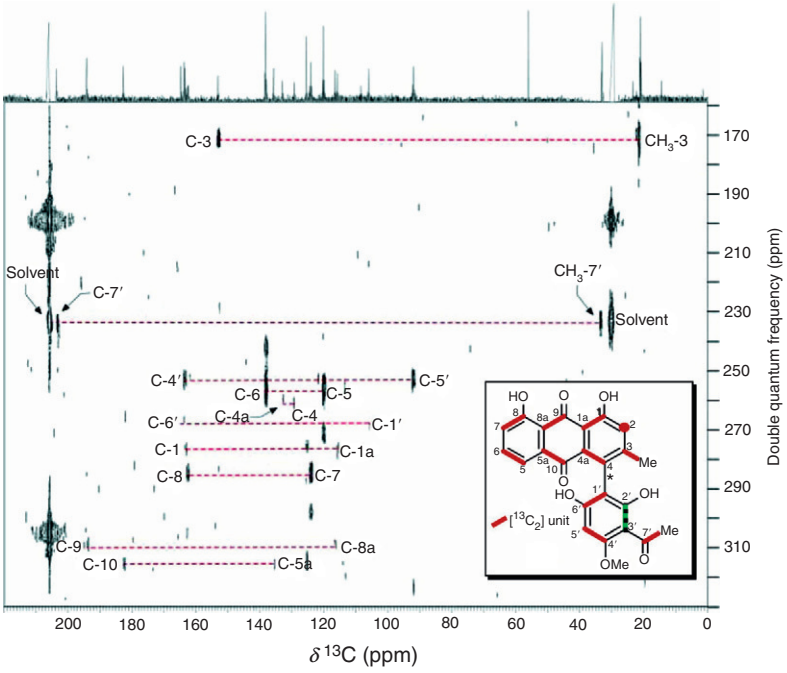

Figure 19 2D INADEQUATE NMR spectrum of knipholone in $(CD_3)_2CO$ isolated after administration of [$^{13}C_2$]-labelled acetate to *Kniphofia pumila*. The incorporation pattern of the intact [$^{13}C_2$] units is marked by thick lines; the only such unit that has remained unproven is marked by a dashed thick line. From Ref. 68, reproduced by permission of the American Chemical Society.

it was concluded that this part of the molecule is biosynthesised via the so-called F folding mode. The acetophenone part of the molecule, which does not undergo a decarboxylation reaction, originates from four acetate units. The surprising lack of randomisation of the intact [$^{13}C_2$] units in this ''southern'' part reveals the absence of a free symmetric intermediate as initially anticipated. This was also confirmed by the analysis of the data using more complex ^{13}C precursors.

Further examples of the use of INADEQUATE in biosynthetic studies include biosynthesis of naphthylisoquinoline alkaloids,[69] blepharismin C, toxic pigments of the ciliate *Blepharisma japonicum*,[70] lambertellols A and B and lambertellin and metabolites of Ascomycete fungi.[71]

5.3. Studies of fullerenes

^{13}C-detected INADEQUATE has been applied to ^{13}C-enriched C_{60} and C_{70} chemically modified fullerenes, yielding assignment of carbon resonances and values of carbon–carbon coupling constants, as reviewed previously.[3] More recently, ^{13}C-detected INADEQUATE underpinned the study of trends in chemical shift dispersion in fullerene derivatives[72] and was used in the structure determination of several adducts of C_{60} molecules.[73] The use of ^{13}C-detected INADEQUATE experiment has shown that the addition of *N*-(diphenylmethylene)glycinate esters to [60]fullerene under Bingel conditions gave [60]fullerenyldihydropyrroles[74] and not methano[60]-fullerenyl iminoesters as reported previously.

Two other selected examples of the application of INADEQUATE to fullerenes focus on endohedral metallofullerenes. The first is based on the reported mapping of the bond connectivity in the carbon cage of La@C_{82} anion, [La@C_{82}A]$^-$.[75] The ^{13}C NMR spectrum of [La@C_{82}A]$^-$ showed 17 distinct lines of near-equal intensity and 7 lines of half the intensity. This is expected ($17 \times 4 + 2 \times 7 = 82$) for a molecule with a C_{2v} symmetry.

The carbon signals were assigned through the analysis of a 2D ^{13}C-detected INADEQUATE spectrum acquired on a 13% ^{13}C-enriched sample. Once the assignment was known, carbon–carbon coupling constants were inspected. It is well known that the $^1J_{CC}$ increase with shortening bond length and increasing π-bond character. The 5,6 and 6,6 ring-fusion bonds of empty fullerenes, such as C_{60} and C_{70}, are considered to have single- and double-bond character, respectively, which is reflected in the values of carbon–carbon coupling constants as shown in Figure 20.

However, for [La@C_{82}A]$^-$ it was found that plots of these two types of couplings overlap, which was attributed to the shortening and elongation of the 5,6 and 6,6 ring-fusion bonds in [La@C_{82}A]$^-$, respectively. Calculation showed that the C–C bonds in the vicinity of La are elongated because of the electron transfer from La to C_{82}. The interpretation of coupling constants helped to establish the position of La in [La@C_{82}A]$^-$, which was further confirmed by the measurement of ^{13}C relaxation times.

The second example describes the determination of the position of the Ce atom in Ce@C_{82} by means of paramagnetic NMR spectral analysis of the ^{13}C signals of

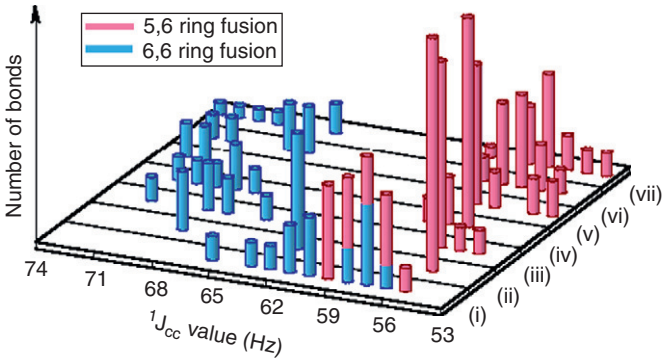

Figure 20 Histogram of $^1J_{CC}$ values compiled from seven fullerenes of (i) $[La@C_{82}\text{-}A]^-$, (ii) C_{70}, (iii) $C_{60}OsO_4$, (iv) $C_{60}H_2$, (v) $C_{60}H_6$, (vi) C_{60} trans-3 adduct and (vii) C_{60} trans-4 adduct. Copyright Wiley-VCH Verlag GmbH & Co. KGaA. Reproduced with permission from Ref. 75

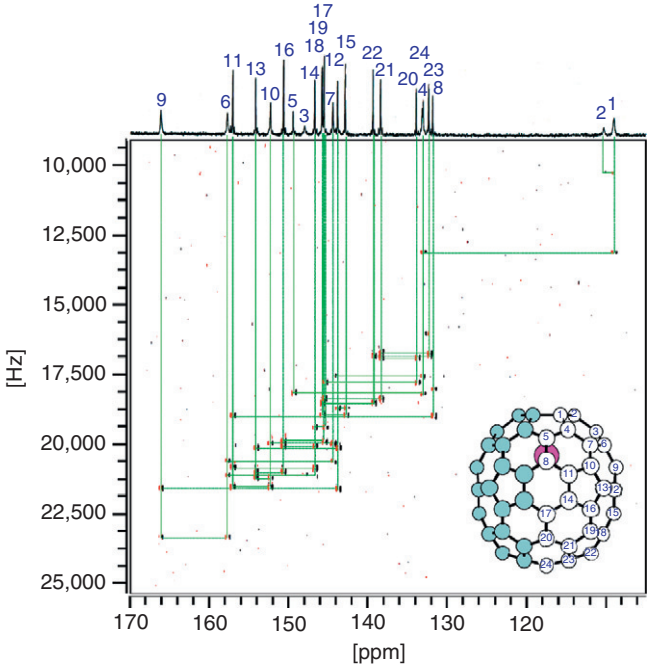

Figure 21 2D ^{13}C INADEQUATE spectrum of 9% ^{13}C-enriched $[Ce@C82]^-$ at 288 K and 125 MHz. The inset shows the schematic structure of Ce@C82. From Ref. 76, reproduced by permission of the American Chemical Society.

$Ce@C_{82}$ anion, $[Ce@C_{82}A]^-$.[76] Crucial to this investigation was the full assignment of all carbon signals provided by the 2D ^{13}C-detected INADEQUATE (Figure 21).

^{13}C NMR spectrum of $[Ce@C_{82}A]^-$ shows 24 lines and confirms the existence of C_{2v} symmetry. The spread of the resonances in this anion is, however, larger compared with the diamagnetic $[La@C_{82}\text{-}A]^-$ in Ref. 75. All carbon chemical shifts

showed considerable temperature dependence originating from the f electron remaining on Ce. Extrapolating the chemical shifts according to their T^{-2} dependency to $T^{-2} \rightarrow 0$ yielded values that were close to ^{13}C spectrum of the diamagnetic $[La@C_{82}]^-$. This indicates that the changes of ^{13}C chemical shifts compared to $[La@C_{82}]^-$ are largely due to pseudo contact shift, that is there is no significant connection between Ce atom and the cage that would give rise to contact shifts. Full geometry optimisation of $Ce@C_{82}$ anion using density functional theory followed. By comparing the calculated and experimental pseudo-contact shifts the Ce atom was shown to be located at an off-centred position adjacent to the hexagonal ring and 2.063 Å from its plane. Once again, assignment of the carbon resonances using INADEQUATE spectrum was crucial to this investigation.

5.4. Polymers

^{13}C NMR spectroscopy is a powerful method for analysing the structure of copolymers providing detailed information about their constitution, sequences, stereo- and regio-errors and chain-end structures. The presence of various microstructures influences the polymeric properties and provides an insight into the mechanism by which the polymerisation catalyst operates. However, because some structures occur in very low concentrations, early application of 2D INADEQUATE to polymers[77] found very few follow-up studies.[3]

A substantial boost in sensitivity for this field was provided by the recent development of a high-temperature, 10-mm, 400-MHz, ^{13}C-optimised cryoprobe.[78] The large NMR tube diameter is beneficial for polymer NMR studies due to increased sample volume in the active region of the probe. Equally important is the ability of this probe to perform experiments at high temperatures (120–135 °C).

Overall, a 5.5-fold sensitivity increase was observed for this cryoprobe at 125 °C compared to a conventional 400-MHz broad-band 10-mm probe. Its performance is illustrated by the investigation of the 2,1-inverse insertion in isotactic propylene[78,79] which exists in four diasteroisomeric forms depending on the position of the methyl groups, as shown in Figure 22.

2D ^{13}C-deteced INADEQUATE spectrum of poly(propylene-*co*-1-octene) (P/O) was acquired in 2.6 days using phase cycling with the suppression of rapid pulsing artefacts.[4] Once the ^{13}C assignment was made, protons were assigned using the ^{1}H–^{13}C HOESY experiments, which led to the identification of this regio-error as RE_3, which was present only in 0.55 mol%. The other two region-errors RE_1 and RE_2 were identified in samples prepared using different catalysts.[79]

6. APPLICATIONS OF INADEQUATE TO NUCLEI OTHER THAN ^{13}C

This section contains some recent applications of INADEQUATE to three non-^{13}C nuclei, that is ^{29}Si, ^{15}N and ^{77}Se. More examples can be found in Ref. 3.

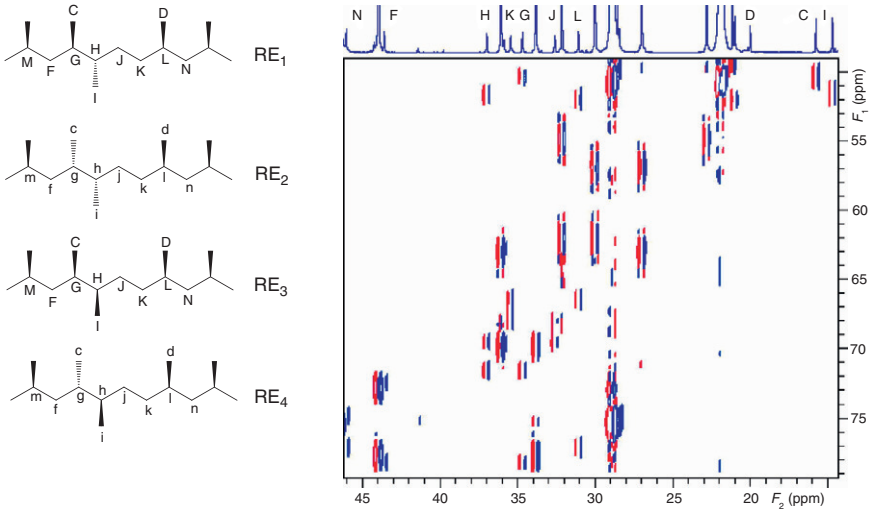

Figure 22 Stereochemical structures of 2,1-insertion regio-errors in isotactic polypropylene on the left and partial 2D INADEQUATE spectrum showing the 2,1-inverse insertion in P/O. The carbon atoms of the RE_3 regio-error are labelled in the ^{13}C spectrum shown at the top. From Ref. 78, reproduced by permission of Elsevier.

6.1. ^{29}Si

^{29}Si-detected INEPT-INADQUATE has been applied to confirm the structure of heptasilanortricyclene $MeSi(SiMe_2SitBu)_3$.[80] Small $^2J(^{29}Si–O–^{29}Si)$ couplings constants (1–4 Hz) in model siloxanes were measured[81] by a *J*-resolved INADEQUATE[82] that does not require optimisation of the evolution interval for a particular coupling constant. The ^{29}Si 2D INADEQUATE-CR[5] spectrum of dendritic polysilane tris[2,2,5,5-tetrakis(trimethylsilyl)hexasilyl]-methylsilane yielded a complete assignment of ^{29}Si resonances and the Si–Si connectivity for the entire molecule.[19]

The analysis of ^{29}Si INADEQUATE spectra of aqueous silicate solutions produced the most complete silicate oligomer speciation available to date.[83] Enrichment at 19% of ^{29}Si resulted in 15-fold sensitivity enhancement relative to the natural-abundance samples. Furthermore, the consequent 200-fold reduction of the required measurement time made these experiments possible. Figure 23 shows a 2D ^{29}Si INADEQUATE NMR spectrum of sodium silicate containing 35 g/l SiO_2 and 17.5 g/l Na_2O.

The analysis of the spectra is aided by the fact that the silicon chemical shifts are, to some extent, dependent on the number, $n = 0, 1, 2, 3$, of the nearest-neighbour tetrahedrons, Q^n (or $Q^{n\Delta}$, where Δ represent a tricyclic arrangement). As an example, the connectivity b–n–j observed in the INADEQUATE spectrum of Figure 23 identifies a species that corresponds to the connectivity $Q^{2\Delta}$–$Q^{3\Delta}$–Q^2 or $Q^{2\Delta}$–$Q^{3\Delta}$–$Q^{3\Delta}$. Each of these can be represented by several different structures. The candidate structures were computed using silicon anions containing up to 11 Si atoms and are, for this particular species, shown in Figure 24 as structures **7a–7e**.

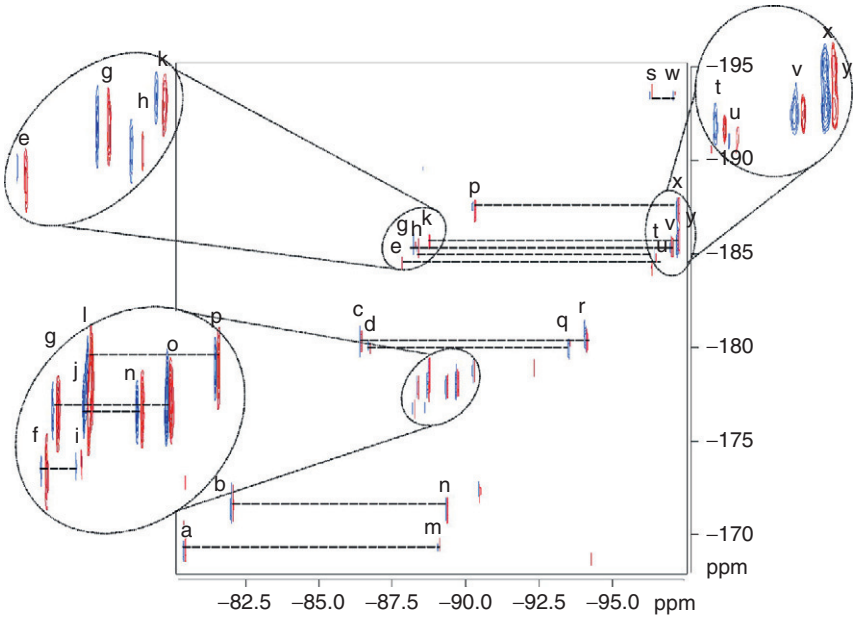

Figure 23 Room-temperature 99.4-MHz ^{29}Si 2D INADEQUATE NMR spectrum of sodium silicate recorded in 1.5 days. Dashed lines show connectivities between pairs of spins. From Ref. 83, reproduced by permission of the American Chemical Society.

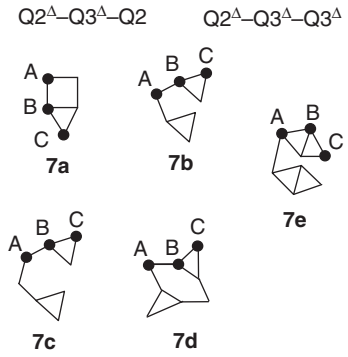

Figure 24 Representation of possible silicate anion structures for the species identified by b–n–j connectivites deduced from the 2D ^{29}Si INADEQUATE spectrum. The solid lines represent silicon–oxygen–silicon linkage and closed circles (A, B and C) are inequivalent site within each anion illustrating connectivities.

Because the structure of silicates oligomers tend to be as condensed as possible, structures with long linear chains and large cyclic rings are less plausible. On the basis of this statement, structures containing three-membered rings and threefold substituted Si sites appear the most likely candidates. Therefore, the most probable structure of the analysed species is **7e**. In combination with two other samples

with different concentrations of SiO_2 and Na_2O, altogether 14 species were unequivocally identified by the INADEQUATE experiments. It should be noted that symmetrical structures with only one unique Si atom cannot be identified by INADEQUATE.

6.2. ^{15}N

Direct observation of hydrogen bonds through the measurement of nitrogen–nitrogen coupling constants, $^{2h}J_{NN}$, pioneered using ^{15}N-labelled nucleic acids and proteins is much less explored in synthetic systems. One such example is provided by the study of ureidopyrimidinone heterocyclic unit, which forms very stable dimers held together by a linear array of four hydrogen bonds (see inset of Figure 25).[84] The sample contained a single ^{15}N label randomly distributed between nitrogens N^a, N^b and N^c. The 1D ^{15}N INADEQUATE spectrum (Figure 25 A) shows the signal from dimers that have pairs of ^{15}N atoms at positions *a* and *c*. This spectrum confirms the existence of an intermolecular $^{2h}J_{NaNc}$ coupling constant.

With decreasing temperature from +10 to −20 °C, splitting of AP doublets due to coupling between N^a and N^c increased from 2.2 to 5 Hz. The splitting is effected by the dissociation and re-association of the dimer and is therefore not equal to $^{2h}J_{NaNc}$ coupling constant unless a limiting value is achieved. This was not possible in this particular instance because of solubility problems at lower temperatures. Nevertheless, as the magnitude of the $^{2h}J_{NN}$ coupling constant depends on the hydrogen-bond length, experiments like this can, in principle, give very precise structural information on hydrogen-bonded complexes in solution.

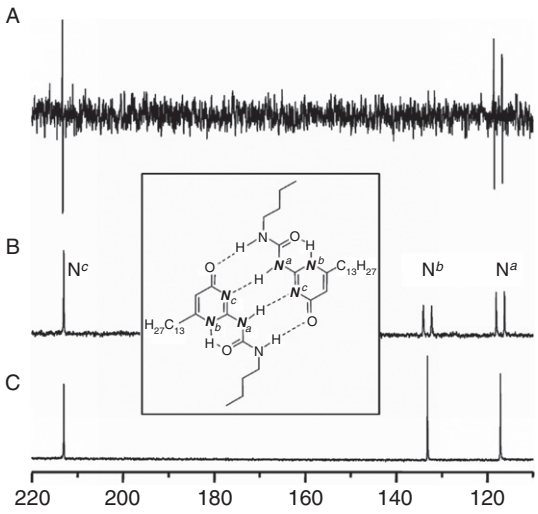

Figure 25 ^{15}N spectra of singly ^{15}N-labeled 2-butylureido-4[1*H*]-pyrimidinone. (A) One-dimensional ^{15}N INADEQUATE spectrum. (B) ^{1}H-coupled ^{15}N NMR spectrum. (C) Inverse-gated ^{1}H-decoupled ^{15}N NMR spectrum. From Ref. 84, reproduced by permission of the American Chemical Society.

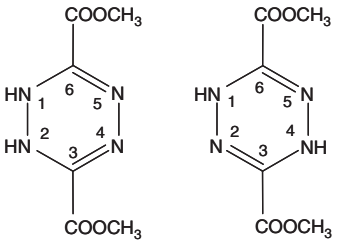

Figure 26 Dimethyl 1,2- and 1,4-dihydro-1,2,4,5-tetrazine-3,6-dicarboxylates.

Tautomerism of tetrazines was investigated by 1D ^{15}N INADEQUATE.[85] Dimethyl dihydro-1,2,4,5-tetrazine-3,6-dicarboxylate can exist either in 1,2- (**8**) or 1,4-dihydro (**9**) tautomeric forms (Figure 26). Both of these forms yielded two signals in ^{15}N NMR spectrum corresponding to N1, N2 and N4, N5 in tautomer **8** or N1, N4 and N2, N5 in tautomer **9**. Much smaller $^{2}J(^{15}N,^{15}N)$ between N1 and N5 (N2 and N4) would be expected for **8**.

In order to establish which form is present in the solution, $J(^{15}N,^{15}N)$ coupling constants were measured using 1D ^{15}N INADEQUATE on a compound that was 20% ^{15}N-labelled uniformly in all four nitrogen positions. Values of 12.1–12.3 Hz in different solvents were obtained. These correspond to the $^{1}J(^{15}N,^{15}N)$ between N1 and N2 (N4 and N5) and prove that this compound exists exclusively in the 1,4-dihydro tautomeric form **9**.

Another example where the $J(^{15}N,^{15}N)$ coupling constants were measured using 1D ^{15}N INADEQUATE is given in Ref. 86. This time, the ^{15}N enrichment was not uniform and $J(^{15}N,^{15}N)$ coupling constants between the ^{15}N(enriched) and ^{15}N(natural abundance) sites were measured.

6.3. ^{77}Se

Selenium-77 is a spin-1/2 nucleus with a natural abundance of 7.58% and a very broad chemical shift range, making it an ideal probe of local chemical environments. The following example details the use of 1D INADEQUATE for the measurement and interpretation of ^{2}J(Se–M–Se) (M: metal) coupling constants in an octahedral cluster $[Re_5OsSe_8(CN)_6]^{3-}$ with C_{4v} symmetry.[87] As can be seen in Figure 27, the eight selenium atoms of this compound are separated into two chemically non-equivalent sites, four and four near osmium and rhenium, respectively.

The 1D INADEQUATE spectrum Figure 28, optimised for the measurement of $J \sim 60$ Hz, reveals two AP doublets corresponding to ^{2}J(Se–M–Se) = 67.0 and 10.5 Hz.

Considering the Se atom in the front upper left corner of a cube, shown in Figure 27 B as a black sphere, there are four sites in the bottom half of the cluster that could give rise to these *J*-coupling interactions (dashed lines in Figure 27 B). One of these sites is directly beneath the highlighted Se atom along an edge of the Se8 cube. This ^{2}J(Se–M–Se) coupling is referred to as an E (edge) interaction. Two sites across a face diagonal from the highlighted Se atom, referred to as FD (face diagonal), also give rise to a ^{2}J(Se–M–Se) coupling. Finally, the last site across the

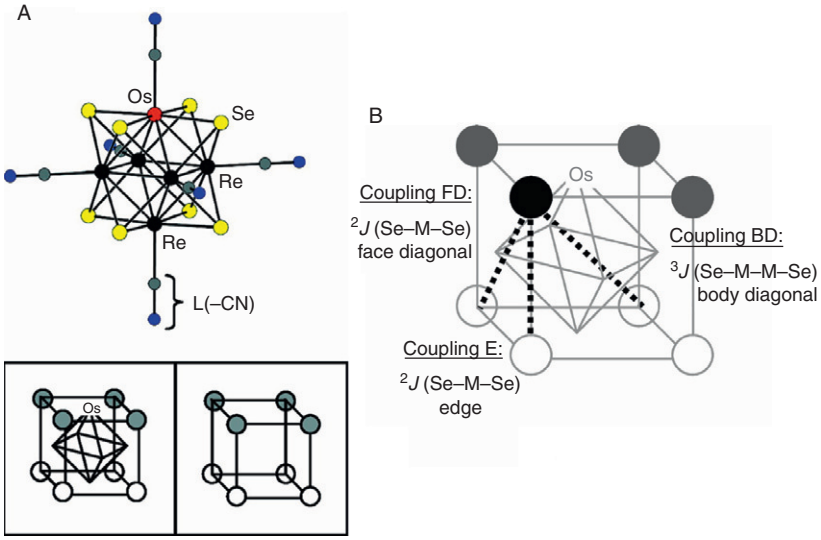

Figure 27 (A) Structure and schematic representations of the face-capped octahedral cluster $[Re_5OsSe_8(CN)_6]^{3-}$ with C_{4v} symmetry. The eight inner selenium ligands form a cube with two types shown as grey or white spheres (bottom drawing). (B) Possible Se–M–Se *J*-coupling interactions. From Ref. 87, reproduced by permission of the American Chemical Society.

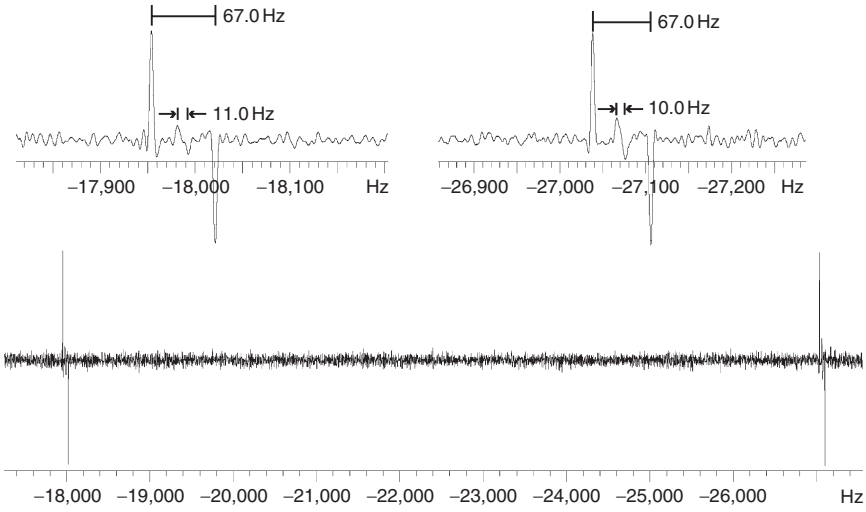

Figure 28 1D INADEQUATE ^{77}Se spectrum of $[Re_5OsSe_8(CN)_6]^{3-}$ with a 4.1-ms fixed evolution period. Expanded spectra contain multiplets centred at −188.6 and −284.0 ppm. From Ref. 87, reproduced by permission of the American Chemical Society.

body diagonal gives rise to a ^{3}J(Se–M–M–Se) interaction and is referred to as BD (body diagonal). Based on the analysis of the intensities of the main and satellite lines in 1D ^{77}Se spectrum of $[Re_5OsSe_8(CN)_6]^{3-}$, two observed ^{2}J(Se–M–Se) couplings of 67.0 and 10.5 Hz were assigned to FD and E interaction, respectively. The BD requires a long-range interaction via two different metals and is very likely too small to be observed. Knowledge of these Se–Se *J*-couplings could be a key for the interpretation of ^{77}Se data from different geometric isomers in systems with multiple selenium sites.

7. OUTLOOK

The closing decade has seen incremental improvements of INADEQUATE pulse sequences and gradual positioning of this experiment for a more general use in high-resolution NMR spectroscopy. This would not have been possible without the recent introduction of cryogenic probes that substantially increased the sensitivity of many NMR experiments. When concluding their review of the INADEQUATE, Buddrus and Lambert[3] wrote in 2002: ''The day will come when a few milligrams of a completely unknown compound from a plant or a microorganism, measured overnight, will yield the secret of its constitution by daybreak.'' Today we are much closer to achieving this aim.

Improved sensitivity of NMR instruments has enabled the development of methods for the measurement of carbon–carbon coupling constants, particularly the long-range coupling constants, which are expected to complement the proton–proton and proton–carbon coupling constants in the configurational and conformational analysis of compounds.

INADEQUATE in the field of high-resolution NMR is still mainly applied to the establishment of carbon–carbon connectivities, but its application to other nuclei continue to appear in the literature sporadically. Improvements in the sensitivity comparable to those offered by ^{1}H- or ^{13}C-optimised cryogenically cooled probes would undoubtedly increase the usage of INADEQUATE for non-carbon nuclei significantly.

REFERENCES

1. A. Bax, R. Freeman and T. A. Frenkiel, *J. Am. Chem. Soc.*, 1981, **103,** 2102–2104.
2. A. Bax, R. Freeman and S. P. Kempsell, *J. Am. Chem. Soc.*, 1980, **102,** 4849–4851.
3. J. Buddrus and J. Lambert, *Magn. Reson. Chem.*, 2002, **40,** 3–23.
4. M. Bourdonneau and B. Ancian, *J. Magn. Reson.*, 1998, **132,** 316–327.
5. N. C. Nielsen, H. Thogersen and O. W. Sorensen, *J. Am. Chem. Soc.*, 1995, **117,** 11365–11366.
6. M. I. Attia, D. Guclu, B. Hertlein, J. Julius, P. A. Witt-Enderby and D. P. Zlotos, *Org. Biomol. Chem.*, 2007, **5,** 2129–2137.
7. E. Kupce and R. Freernan, *J. Am. Chem. Soc.*, 2008, **130,** 10788–10792.
8. S. W. Meyer and M. Kock, *J. Nat. Prod.*, 2008, **71,** 1524–1529.
9. G. N. Lamar, *Chem. Phys. Lett.*, 1971, **10,** 230.
10. R. Freeman, K. G. R. Pachler and G. N. Lamar, *J. Chem. Phys.*, 1971, **55,** 4586.
11. D. L. Mattiello and R. Freeman, *J. Magn. Reson.*, 1998, **135,** 514–521.

12. T. H. Mareci and R. Freeman, *J. Magn. Reson.*, 1982, **48,** 158–163.
13. N. C. Nielsen and O. W. Sorensen, *J. Magn. Reson. Ser. A*, 1996, **123,** 135–139.
14. J. Bunkenborg, N. C. Nielsen and O. W. Sorensen, *Magn. Reson. Chem.*, 2000, **38,** 58–61.
15. A. Meissner and O. W. Sorensen, *Concepts Magn. Reson.*, 2002, **14,** 141–154.
16. V. Ramesh and N. Chandrakumar, *Magn. Reson. Chem.*, 2006, **44,** 936–942.
17. V. Ramesh, C. George and N. Chandrakumar, *Chem. Phys. Lett.*, 2009, **474,** 375–380.
18. M. H. Levitt, *in*: *Encyclopaedia of Nuclear Magnetic Resonance*, D. M. Grant and R. K. Harris (eds.) Wiley, Chichester, 1996, pp. 1396–1411.
19. J. B. Lambert and H. W. Wu, *Magn. Reson. Chem.*, 2000, **38,** 388–389.
20. J. Lambert and J. Buddrus, *J. Magn. Reson. Ser. A*, 1993, **101,** 307–312.
21. T. Nakazawa, H. Sengstschmid and R. Freeman, *J. Magn. Reson. Ser. A*, 1996, **120,** 269–273.
22. R. Dunkel, C. L. Mayne, J. Curtis, R. J. Pugmire and D. M. Grant, *J. Magn. Reson.*, 1990, **90,** 290–302.
23. R. Dunkel, C. L. Mayne, R. J. Pugmire and D. M. Grant, *Anal. Chem.*, 1992, **64,** 3133–3149.
24. M. P. Foster, C. L. Mayne, R. Dunkel, R. J. Pugmire, D. M. Grant, J. M. Kornprobst, J. F. Verbist, J. F. Biard and C. M. Ireland, *J. Am. Chem. Soc.*, 1992, **114,** 1110–1111.
25. F. C. de Macedo and A. J. Marsaioli, *Magn. Reson. Chem.*, 2005, **43,** 251–255.
26. S. D. Kunikeev and H. S. Taylor, *J. Phys. Chem.*, 2004, **108,** 743–753.
27. F. L. Zhang, N. Trbovic, J. B. Wang and R. Bruschweiler, *J. Magn. Reson.*, 2005, **174,** 219–222.
28. M. Kock, R. Kerssebaum and W. Bermel, *Magn. Reson. Chem.*, 2003, **41,** 65–69.
29. T. N. Pham, K. E. Kover, L. Jin and D. Uhrin, *J. Magn. Reson.*, 2005, **176,** 199–206.
30. B. Luy, K. Kobzar, T. E. Skinner, N. Khaneja and S. J. Glaser, *J. Magn. Reson.*, 2005, **176,** 179–186.
31. L. Jin, K. E. Kover, M. R. Lenoir and D. Uhrin, *J. Magn. Reson.*, 2008, **190,** 171–182.
32. L. Jin and D. Uhrin, *Magn. Reson. Chem.*, 2007, **45,** 628–633.
33. L. B. Krivdin and G. A. Kalabin, 1989, pp 293–448.
34. R. T. Williamson, B. L. Marquez, W. H. Gerwick and F. E. Koehn, *Magn. Reson. Chem.*, 2001, **39,** 544–548.
35. A. Meissner, D. Moskau, N. C. Nielsen and O. W. Sorensen, *J. Magn. Reson.*, 1997, **124,** 245–249.
36. J. Weigelt and G. Otting, *J. Magn. Reson. Ser. A*, 1995, **113,** 128–130.
37. B. Reif, M. Kock, R. Kerssebaum, H. Kang, W. Fenical and C. Griesinger, *J. Magn. Reson. Ser. A*, 1996, **118,** 282–285.
38. T. Parella and F. Sanchez-Ferrando, *J. Magn. Reson.*, 2004, **166,** 123–128.
39. M. Bugaj, P. A. Baran, K. Kamienska-Trela and A. Krowczynski, *Magn. Reson. Chem.*, 2009, **47,** 843–856.
40. K. A. Chernyshev, L. B. Krivdin, L. I. Larina, T. V. Konkova, M. M. Demina and A. S. Medvedeva, *Magn. Reson. Chem.*, 2007, **45,** 661–666.
41. L. B. Krivdin, S. S. Khutsishvili, O. A. Shemyakina, A. G. Mal'kina, B. A. Trofimov and R. H. Contreras, *Magn. Reson. Chem.*, 2007, **45,** 758–765.
42. L. B. Krivdin, L. I. Larina, K. A. Chernyshev and I. B. Rozentsveig, *Magn. Reson. Chem.*, 2005, **43,** 937–942.
43. A. A. Frimer, O. Sharon and H. E. Gottlieb, *Magn. Reson. Chem.*, 2003, **41,** 714–717.
44. M. Witanowski, K. Kamienska-Trela and Z. Biedrzycka, *J. Mol. Struct.*, 2007, **844,** 13–20.
45. N. N. Volkova, E. V. Tarasov, M. I. Kodess, L. Van Meervelt, W. Dehaen and V. A. Bakulev, *Org. Biomol. Chem.*, 2003, **1,** 4030–4038.
46. K. Zangger and H. Sterk, *J. Magn. Reson. Ser. A*, 1996, **121,** 56–59.
47. W. Kozminski and D. Nanz, *J. Magn. Reson. Ser. A*, 1996, **122,** 245–247.
48. W. Kozminski, D. Sperandio and D. Nanz, *Magn. Reson. Chem.*, 1996, **34,** 311–315.
49. B. Reif, M. Kock, R. Kerssebaum, J. Schleucher and C. Griesinger, *J. Magn. Reson. B*, 1996, **112,** 295–301.
50. K. E. Kover and P. Forgo, *J. Magn. Reson.*, 2004, **166,** 47–52.
51. C. M. Thiele and W. Bermel, *Magn. Reson. Chem.*, 2007, **45,** 889–894.
52. B. Bose, S. Zhao, R. Stenutz, F. Cloran, P. B. Bondo, G. Bondo, B. Hertz, I. Carmichael and A. S. Serianni, *J. Am. Chem. Soc.*, 1998, **120,** 11158–11173.
53. F. Commodari, A. Khiat, S. Ibrahimi, A. R. Brizius and N. Kalkstein, *Magn. Reson. Chem.*, 2005, **43,** 567–572.
54. M. Lang, A. Muhlbauer, C. Graf, J. Beyer, S. Lang-Fugmann, K. Polborn and W. Steglich, *Eur. J. Org. Chem.*, 816–825.

55. Y. Fujita, A. Kasuya, Y. Matsushita, M. Suga, M. Kizuka, Y. Iijima and T. Ogita, *Bioorg. Med. Chem. Lett.*, 2005, **15,** 4317–4321.
56. T. S. Bugni, V. S. Bernan, M. Greenstein, J. E. Janso, W. M. Maiese, C. L. Mayne and C. M. Ireland, *J. Org. Chem.*, 2003, **68,** 2014–2017.
57. A. Henckens, P. Adriaensens, J. Gelan, L. Lutsen and D. Vanderzande, *Magn. Reson. Chem.*, 2004, **42,** 931–937.
58. C. Mahieux, M. Laguerre, Y. Landais and I. Pianet, *Magn. Reson. Chem.*, 2004, **42,** 467–473.
59. D. A. Mulholland, C. Koorbanally, N. R. Crouch and P. Sandor, *J. Nat. Prod.*, 2004, **67,** 1726–1728.
60. D. Intelmann, G. Kummerlowe, G. Haseleu, N. Desmer, K. Schulze, R. Frohlich, O. Frank, B. Luy and T. Hofmann, *Chemistry*, 2009, **15,** 13047–13058.
61. M. T. Hancock, R. E. Minto and A. R. Pinhas, *Tetrahedron Lett.*, 2003, **44,** 8357–8360.
62. W. Henze, T. Gartner and R. M. Gschwind, *J. Am. Chem. Soc.*, 2008, **130,** 13718–13726.
63. H. Y. He, J. E. Janso, R. T. Williamson, H. Y. Yang and G. T. Carter, *J. Org. Chem.*, 2003, **68,** 6079–6082.
64. R. T. Williamson, A. Boulanger, A. Vulpanovici, M. A. Roberts and W. H. Gerwick, *J. Org. Chem.*, 2002, **67,** 7927–7936.
65. L. H. Abdeljebbar, M. Humam, P. Christen, D. Jeannerat, B. Vitorge, S. Amzazi, A. Benjouad, K. Hostettmann and K. Bekkouche, *Helv. Chim. Acta*, 2007, **90,** 346–352.
66. H. V. Dang, N. S. Habib, T. Kappe, K. Zangger and W. Stadlbauer, *J. Heterocycl. Chem.*, 2007, **44,** 161–165.
67. N. M. Kogan, R. Rabinowitz, P. Levi, D. Gibson, P. Sandor, M. Schlesinger and R. Mechoulam, *J. Med. Chem.*, 2004, **47,** 3800–3806.
68. G. Bringmann, T. F. Noll, T. Gulder, M. Dreyer, M. Grune and D. Moskau, *J. Org. Chem.*, 2007, **72,** 3247–3252.
69. G. Bringmann, J. Mutanyatta-Comar, M. Greb, S. Rudenauer, T. F. Noll and A. Irmer, *Tetrahedron*, 2007, **63,** 1755–1761.
70. Y. Uruma, K. Sakamoto, K. Takumi, M. Doe, Y. Usuki and H. Iio, *Tetrahedron*, 2007, **63,** 5548–5553.
71. T. Murakami, Y. Takahashi, E. Fukushi, J. Kawabata, M. Hashimoto, T. Okuno and Y. Harada, *J. Am. Chem. Soc.*, 2004, **126,** 9214–9220.
72. M. S. Meier, H. P. Spielmann, R. G. Bergosh and M. C. Tetreau, *J. Org. Chem.*, 2003, **68,** 7867–7870.
73. L. Chaker, G. E. Ball, J. R. Williams, G. A. Burley, B. C. Hawkins, P. A. Keller and S. G. Pyne, *Eur. J. Org. Chem.*, 5158–5162.
74. G. E. Ball, G. A. Burley, L. Chaker, B. C. Hawkins, J. R. Williams, P. A. Keller and S. G. Pyne, *J. Org. Chem.*, 2005, **70,** 8572–8574.
75. T. Tsuchiya, T. Wakahara, Y. Maeda, T. Akasaka, M. Waelchli, T. Kato, H. Okubo, N. Mizorogi, K. Kobayashi and S. Nagase, *Angew. Chem. Int. Edit.*, 2005, **44,** 3282–3285.
76. M. Yamada, T. Wakahara, Y. F. Lian, T. Tsuchiya, T. Akasaka, M. Waelchli, N. Mizorogi, S. Nagase and K. M. Kadish, *J. Am. Chem. Soc.*, 2006, **128,** 1400–1401.
77. T. Asakura, M. Demura and T. Hayashi, *in*: *Annual Reports on NMR Spectroscopy*, (G. A. Webb ed.) Vol. 29. Academic Press, 1994, pp. 325–404.
78. Z. Zhou, R. Kummerle, J. C. Stevens, D. Redwine, Y. Y. He, X. H. Qiu, R. J. Cong, J. Klosin, N. Montanez and G. Roof, *J. Magn. Reson.*, 2009, **200,** 328–333.
79. Z. Zhou, J. C. Stevens, J. Klosin, R. Kummerle, X. H. Qiu, D. Redwine, R. J. Cong, A. Taha, J. Mason, B. Winniford, P. Chauvel and N. Montanez, *Macromolecules*, 2009, **42,** 2291–2294.
80. R. Fischer, J. Baumgartner, G. Kickelbick, K. Hassler and C. Marschner, *Chemistry*, 2004, **10,** 1021–1030.
81. M. Kurfurst and J. Schraml, *Magn. Reson. Chem.*, 2007, **45,** 685–687.
82. A. Bax, R. Freeman and S. P. Kempsell, *J. Magn. Reson.*, 1980, **41,** 349–353.
83. M. Haouas and F. Taulelle, *J. Phys. Chem. B*, 2006, **110,** 3007–3014.
84. S. H. M. Sontjens, M. H. P. van Genderen and R. P. Sijbesma, *J. Org. Chem.*, 2003, **68,** 9070–9075.
85. A. Lycka, S. Frebort and N. Almonasy, *Tetrahedron Lett.*, 2008, **49,** 4213–4215.
86. A. Lycka, I. Frysova and J. Slouka, *Magn. Reson. Chem.*, 2007, **45,** 46–50.
87. K. Ramaswamy, E. G. Tulsky, J. R. Long, J. L. F. Kao and S. E. Hayes, *Inorg. Chem.*, 2007, **46,** 1177–1186.

CHAPTER 2

Phosphorus-31 NMR Spectroscopy of Condensed Matter

Marek J. Potrzebowski, Sławomir Kaźmierski, Hassan Kassassir, and **Beata Miksa**

Contents

Abstract

In this chapter, progress in methodology and new applications of ^{31}P NMR spectroscopy for the study of condensed matter are presented. The review is organised into two sections. First, theoretical background and NMR techniques used to study the solid state are shown. Special attention is paid to progress in ultra-fast (over 60 kHz sample spinning) ^{31}P CP/MAS (cross-polarisation/magic angle spinning) methodology, analysis of ^{31}P spinning sidebands under MAS, homonuclear correlations via direct (dipolar) couplings (D-HOMCOR), homonuclear correlations via indirect *J*-couplings (*J*-HOMCOR) and heteronuclear correlations (HETCORs). The second part presents applications of ^{31}P NMR spectroscopy in structural studies of natural products (phosphorylated amino acids, nucleotides and nucleic acids, phospholipids (PLs) as well bones and teeth) and new materials (i.e. phosphate glasses, aluminophosphates, silicoaluminophosphates and other associated porous materials classified as molecular sieves, catalysts, polyoxometalates (POMs), metal-organic frameworks (MOFs) and inclusion complexes).

Centre of Molecular and Macromolecular Studies, Polish Academy of Sciences, Łódź, Poland

Annual Reports on NMR Spectroscopy, Volume 70
ISSN 0066-4103, DOI: 10.1016/S0066-4103(10)70005-3

Key Words: P-31 solid-state NMR, ^{31}P CP/MAS, Ultra-fast MAS, Phosphorylated amino acids, Nucleotides, Nucleic acids, Phosphate glasses, Aluminophosphates, Molecular sieves, Catalysts, Polyoxometalate (POM), Metal-organic framework (MOF), Inclusion complexes.

1. INTRODUCTION

Phosphorus is a key element in biology, chemistry and material science. In living organisms, phosphorus is found in bones, teeth and nucleic acids (DNA and RNA), as well as in the energy carriers (such as adenosine triphosphate (ATP)), lipids, proteins and enzymes.[1] Most of the given compounds mentioned above contain phosphorus in the form of the phosphoryl group, which is one of the most important functional molecules of biological systems. Phosphoryl group transfer is involved in numerous biochemical processes.[2] Phosphorylation and dephosphorylation involve replacement of the hydroxyl group by a phosphate residue and vice versa in numerous biologically active compounds. In enzymatic reactions, the transfer proceeds via the phosphorylation of the OH function of serine residue; however, the threonine and tyrosine can also be involved. The incorporation of the phosphate group in the polypeptide chain may change its conformation and mode of the intermolecular interactions.

Different phosphorus derivatives are components of products of daily use. They are among the best flame retardants for many flammable materials; many are used as plasticisers and flame retardants as two in one.[3] High-temperature lubricants often contain organophosphates, which, apart from being good lubricants, have thermal stability and fire-resistant properties.[4] Phosphorus compounds can be found in toothpastes (cavity protection or tartar control), shampoos and many more commonly used items. In advanced technologies, organic and/or inorganic phosphorus compounds are components of glasses and ceramic materials as well as ligands for new-generation catalysators (e.g. metathesis) and so on.[5]

It is not surprising that, because of their number of important applications, spectroscopic techniques allowing the investigation of phosphorus derivatives at the molecular level are highly desired. Very early (in the 1950s), NMR spectroscopy became the method of choice in structural studies of the moieties under discussion. Shortly after the publication of the paper by Knight, who first observed shifts in the magnetic resonance of chemically different forms of a given nucleus,[6] Dickenson reported the shifts in the resonances of several phosphorus compounds.[7] Soon, Gutowsky and others discovered and explained the multiplet structure arising from the interaction between non-identical magnetic nuclei in the family of fluorophosphates.[8]

The NMR spectra of phosphorus compounds can be recorded relatively easily. ^{31}P belongs to so-called friendly nuclei with spin ½, characterised by a high gyromagnetic ratio ($\gamma^{31}\mathrm{P} = 0.40$ $\gamma^{1}\mathrm{H} = 1.61$ $\gamma^{13}\mathrm{C}$) and 100% natural isotopic

abundance. The ^{31}P isotropic chemical shifts (δ_{iso}) cover nearly 2000 ppm, allowing a clear distinction between the various local environments of phosphorus atoms.

At the beginning, most of the ^{31}P NMR experiments were carried in the liquid phase and in solutions. Solid-state NMR (SS NMR) was treated as a rather ''exotic'' technique, mostly used by researchers with a ''physics slant''. Early NMR spectra recorded on solid-phase samples were very broad and of quality far from what chemists would normally expect. The main difference between solids and liquids is the mobility of the molecules in a sample. In the liquid state, tumbling of the molecules averages interactions influencing line shape (e.g. dipolar and quadrupolar couplings), so the NMR response is mainly due to chemical shifts and scalar coupling. In the solid state, the dipolar coupling, chemical shift anisotropy (CSA) and quadrupolar effects do not average and therefore cause significant broadening of the resonance lines. In the 1970s, Schaefer and Stejskal introduced the cross-polarisation/magic angle spinning (CP/MAS) methodology, which solved a number of problems.[9] By combining high-power proton decoupling with CP and MAS, they observed enormous increases in the resolution and sensitivity of solid-state spectra.

During last two decades, ^{31}P high-resolution NMR spectroscopy has become a very powerful tool for the investigation of solids. SS NMR spectroscopy has been treated extensively, and several treatises provide detailed information about the technique.[10–12] Four years ago, Iuga et al. in the *Annual Reports on NMR Spectroscopy* published a review showing the state of the art in ^{31}P SS NMR.[13]

In this review, which is a continuation of the cited work, we present the recent achievements of NMR spectroscopy as a tool for the study of condensed matter. The term ''condensed matter'' is actually very broad and covers such sub-fields as solid state, liquid crystals, soft materials, fluids, etc. Historically, condensed matter physics grew out of solid-state physics, which is now considered one of its main sub-fields. One of the reasons for introducing this term is that many of the concepts and techniques developed for studying solids can also be applied to fluid systems. Since in present review we report progress in ^{31}P NMR spectroscopy of solid and soft matter (e.g. PLs), the title of the chapter seems justified.

2. PROGRESS IN METHODOLOGY

2.1. Magic angle spinning technique

In the presence of a strong magnetic field, a nucleus possessing spin $I > 0$ is in one of $2I+1$ equally spaced Zeeman energy levels. Each nucleus is also exposed to the influence of other nuclei, which modify the local magnetic field. Thus, the total Hamiltonian is expressed by the sum of the six individual interactions. The units for the Hamiltonians are given elsewhere.[14]

$$H_{total} = H_z + H_{rf} + H_s + H_D + H_J + H_Q$$

where H_Z is Zeeman interactions given by the equation

$$H_Z = -\mu \cdot \mathbf{B}_0/h = -\gamma_n \mathbf{B}_0 \cdot \mathbf{I}$$

where γ_n is the magnetogyric ratio characteristic for nucleus n, $\mathbf{I}$ is the nuclear spin and $\mathbf{B}_0$ is the magnetic field vector; H_{rf} is the radio frequency (RF) interaction given by

$$H_{\mathrm{rf}} = -\gamma_n \mathbf{B}_{\mathrm{rf}} \cdot \mathbf{I} \quad \text{where } \mathbf{B}_{\mathrm{rf}}(t) = \{[\mathrm{B}_1(t)\cos\omega t], 0, 0\}$$

H_σ is the chemical shielding interaction given by

$$H_\sigma = \gamma_n \mathbf{I} \cdot \sigma \cdot \mathbf{B}_0$$

where σ is the chemical shielding tensor of the observed nucleus; H_{D} is the direct dipolar interactions expressed as

$$H_{\mathrm{D}} = \gamma_{\mathrm{I}}\gamma_{\mathrm{S}} h^2 d^{-3}[\mathbf{I} \cdot \mathbf{S} - 3(\mathbf{I} \cdot \mathbf{r})(\mathbf{S} \cdot \mathbf{r})d^{-2}](\mu_0/4\pi)$$

where $\mathbf{I}$ and $\mathbf{S}$ may be like or unlike spins, $\mathbf{r}$ is $\mathbf{I}$–$\mathbf{S}$ inter-nuclear vector and d is the distance between $\mathbf{I}$ and $\mathbf{S}$ nuclei; H_{Q} is the quadrupolar interaction, important for all nuclei possessing a nuclear quadruple moment (with nuclear spin $\mathbf{I} > ½$) described by

$$H_{\mathrm{Q}} = eQ\mathbf{I} \cdot \mathbf{V} \cdot \mathbf{I}/[6I(2I-1)]$$

where eQ is the quadrupolar moment, $\mathbf{I}$ is the nuclear spin vector and $\mathbf{V}$ is the electric field gradient (EFG) and H_J is the indirect spin–spin interaction which is given by

$$H_J = \mathbf{I} \cdot \mathbf{J} \cdot \mathbf{S}$$

where $\mathbf{J}$ is the indirect spin–spin coupling tensor.

In the solid state, all interactions contribute to the line shape. The resulting spectrum is usually observed as a very broad line, which in many cases is useless in subtle structural analysis of phosphorus compounds.[15] Figure 1A shows a typical ^{31}P NMR spectrum recorded without sample rotation (static spectrum).

When the sample is placed in a gas-driven rotor and spun at the rate of a few kilohertz under θ equal 54.7° (Figure 1B and C), the anisotropic part is zero. In such an experiment, the so-called MAS, narrowing of the resonance lines is observed. However, it is only true when the spin rotation is larger than anisotropy $\Delta\delta$ given in hertz. In cases when the rotor rotation $(\omega_{\mathrm{r}}) \leq \Delta\delta$, the isotropic signal is flanked on both sides by rotational sidebands. In a strong applied field $\mathbf{B}_0$, the only measurable quantity of the shift tensor is the component oriented along z-axis in the laboratory frame:

$$\delta = \delta_{\mathrm{iso}} + 1/3\Delta\delta[(3\cos^2\Theta - 1) + \eta\sin^2\Theta\cos^2\beta)]$$

The anisotropy $\Delta\delta$, asymmetry parameter η and isotropic chemical shift δ_{iso} are expressed by the following equations:

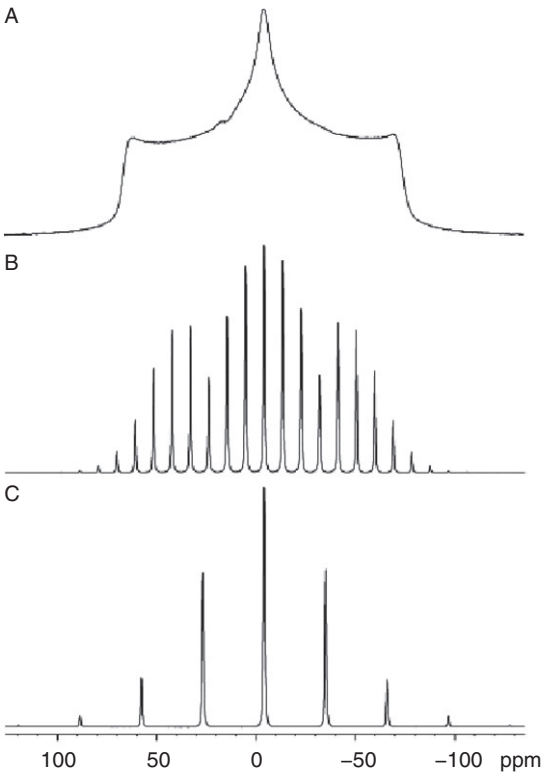

Figure 1 ^{31}P MAS spectra of *O*-phosphothreonine recorded at different MAS rotation speeds: (A) $\omega_r = 0$ Hz (static sample); (B) $\omega_r = 1.5$ kHz and (C) $\omega_r = 5$ kHz.

$$\Delta\delta = \delta_{33} - (\delta_{11} - \delta_{22})/2$$

$$\eta = (\delta_{22} - \delta_{11})(\delta_{33} - \delta_{\text{iso}})$$

$$\delta_{\text{iso}} = (\delta_{11} + \delta_{22} + \delta_{33})/3$$

where δ_{ii} are usually defined as follows: $\delta_{11} > \delta_{22} > \delta_{33}$. Θ and β are the polar angles defining the orientation of $\mathbf{B}_0$ in the principal axis frame of the shielding tensor. In the recent literature, the parameters $\Delta\delta$ and η are replaced by[16]:

$$\Omega = \delta_{11} - \delta_{33}$$

$$\kappa = 3(\delta_{22} - \delta_{\text{iso}})/\Omega$$

For a powdered sample, the δ value can be expressed by the equation

$$\delta = \delta_{\text{iso}} + \left\{\sum \delta_{ii}(3\cos^2\theta_R - 1)\right\}/3$$

where θ_R is the angle between $\mathbf{B}_0$ and the spinning axis (Figure 2)

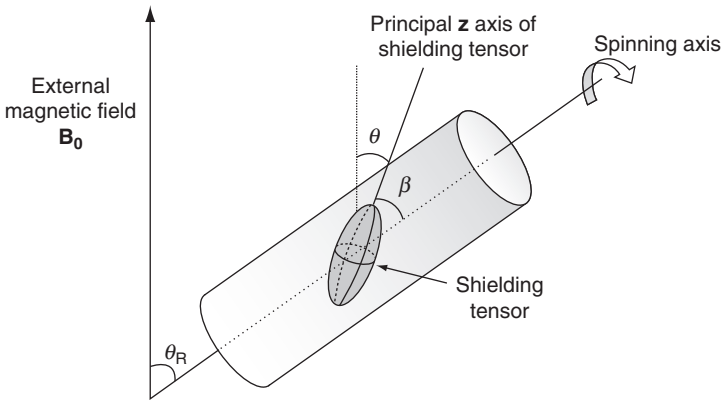

Figure 2 Schematic view of the rotor and shielding tensor placed in a magnetic field. The angle *y* is the angle between $\mathbf{B}_0$ and the principal *z*-axis of the shielding tensor; *b* is the angle between the *z*-axis of the shielding tensor principal axis frame and the spinning axis.

2.1.1. ^{1}H–^{31}P CP under ultra-fast MAS

Despite that ^{31}P NMR spectra can be recorded in a simple one-pulse (Bloch decay) experiment, very often MAS technique is combined with CP. CP under MAS has been extensively studied in the past.[17,18]

In general, the ^{1}H spin serves as the source of polarisation. After the excitation of ^{1}H by a $\pi/2$ pulse, both spins are locked by simultaneous resonance RF during the contact time (see Figure 3).

The precession frequencies of the ^{1}H and ^{31}P in their respective rotating frames are given by:

$$\omega_{1\mathrm{H}} = \gamma_{\mathrm{H}} B_{1\mathrm{H}} \text{ and } \omega_{1\mathrm{P}} = \gamma_{\mathrm{P}} B_{1\mathrm{P}}$$

When the ratio $\mathrm{B}_{1\mathrm{H}}/\mathrm{B}_{1\mathrm{P}}$ of the RF field applied to ^{1}H and ^{31}P is adjusted properly, the matching condition (known as the Hartmann–Hahn condition) is fulfilled:

$$\gamma_{\mathrm{H}} B_{1\mathrm{H}} = \gamma_{\mathrm{P}} B_{1\mathrm{P}}$$

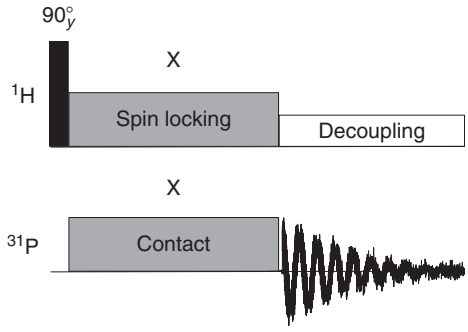

Figure 3 ^{31}P CP/MAS pulse sequence. Spin-locking ^{1}H pulse acts to maintain the ^{1}H magnetisation along *x*-axis.

In principle, two goals are achieved by CP: first is an enhancement of the signal intensity of the rare spin (in the case of CP from ^{1}H to ^{31}P, the maximal enhancement is $\sim$2.5), while the second is related to the reduction of the relaxation delays.

At the beginning of the development of the CP/MAS NMR technique, powdered samples placed in rotors with diameter 7 mm were routinely spun at the rate of few kilohertz. With the progress in the technique, 7-mm rotors, allowing sample rotation with frequency up to 6 kHz, were gradually replaced by rotors with smaller diameters such as 4.0, 3.2 and 2.5 mm. Rotational frequencies have gone correspondingly from the so-called slow (6 kHz), to the medium (15 kHz), fast (25 kHz) and very fast (35 kHz) regimes. Actually, the ''ultra-fast'' regime of more than 60 kHz has been reached using commercially available 1.3-mm rotors. This frequency exceeds the strength of homonuclear proton dipolar coupling and is therefore expected to enter a new regime for spin dynamics. However, it may be more interesting to note that ultra-fast MAS opens new perspectives for CP techniques, which make use of low-power irradiation. Very recently, this problem was discussed in a few papers for the ^{1}H and ^{13}C spin pair.[19,20] Meier studied the effect of fast MAS on CP and has proved the possibility of double-quantum (DQ) Hartmann–Hahn matching.[21] CP under MAS can thus theoretically occur through two kinds of mechanisms: one involves the zero-quantum (ZQ) part of the heteronuclear dipolar coupling whereas the other relies on the DQ part of the same interaction. Zero-quantum cross polarisation (ZQCP) occurs when $\omega_{1H}-\omega_{1P}=n\omega_r$ and gives rise to peaks with positive intensity. Here, ω_r is the sample spinning rate, and $n=0, \pm1, \pm2, \pm3, \ldots$. Double-quantum cross polarisation (DQCP) occurs when $\omega_{1H}+\omega_{1P}=n\omega_r$ and gives rise to peaks with negative intensity. To the best of our knowledge, the problem of $^{1}H \rightarrow {}^{31}P$ CP under ultra-fast MAS has not been discussed so far.

Figure 4 shows the profiles of the ^{31}P signal in *O*-phosphoro-L-threonine after a conventional CP experiment as a function of the proton RF field strength, in which the phosphorus RF field is kept constant at $\omega_{1P}/2\pi=160$ kHz (Figure 4A), $\omega_{1P}/2\pi=100$ kHz (Figure 4B), $\omega_{1P}/2\pi=40$ kHz (Figure 4C) and $\omega_{1P}/2\pi=20$ kHz (Figure 4D). The MAS frequency $\omega_r/2\pi$ was 60 kHz. The orders of the various matching conditions are labelled on the figures, and correspond to both ZQCP and DQCP conditions.

It is worth noting that the efficiency of CP under low-power conditions is high. Figure 5 shows the relative intensities of the signals of *O*-phosphorylated L-threonine recorded under ZQ or DQ conditions for a phosphorus RF field equal to 160, 100, 40 and 20 kHz. In most CP studies to date, with spinning rates up to 30 kHz, the best CP transfers have always been obtained with high-power ^{1}H irradiation. Low-power schemes have performed poorly in this regime, although fields of a few kilohertz should, in principle, be sufficient to lock ^{1}H and ^{31}P magnetisation and drive the polarisation transfer process. On the contrary, at the high-rotation frequencies used in the experiments presented, comparable transfer efficiencies are found for the high-power regime and for the low-power $n=1$ DQCP condition.

The unique feature of ultra-fast MAS NMR spectroscopy is the possibility of using the band-selective CP experiment. This approach was recently reported by

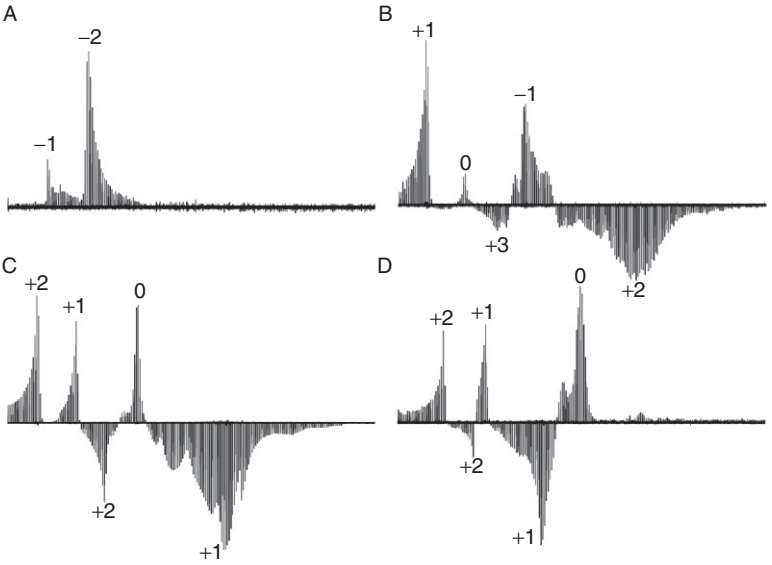

Figure 4 ^{31}P CP profiles of *O*-phosphorylated L-threonine at 60 kHz MAS. The intensity of the phosphorus signal is monitored in a CP experiment (1 ms contact time) where the field strength $\omega_{1P}/2\pi$ on the phosphorus channel is set to: (A) 160 kHz; (B) 100 kHz; (C) 40 kHz and (D) 20 kHz. The proton RF-field strength $\omega_{1H}/2\pi$ is varied from 220 to 20 kHz.

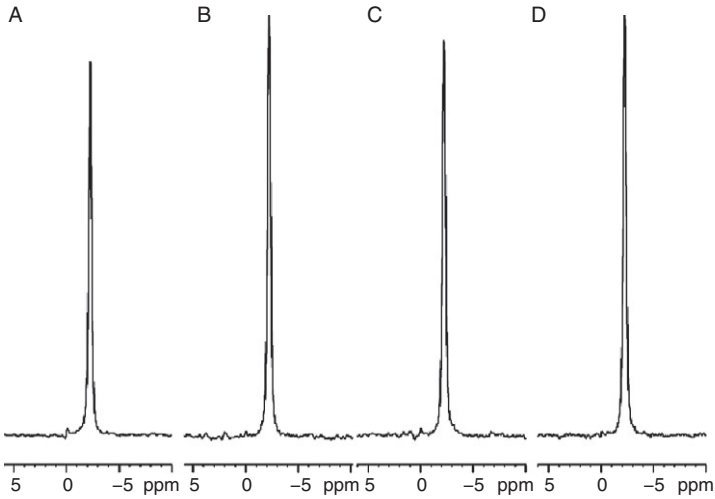

Figure 5 The intensities of ^{31}P CP/MAS signals of *O*-phosphorylated L-threonine recorded under ZQ or DQ conditions for phosphorus. The 31p RF field is equal to (A) 160 kHz, (B) 100 kHz, (C) 40 kHz and (D) 2 kHz.

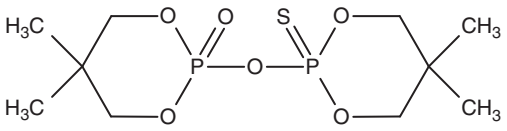

1

Scheme 1

several groups for sequential assignments of proteins.[22,23] As revealed, by employing spectrally induced filtering in combination with CP (SPECIFIC–CP), it is possible to direct dipolar coherence transfer between N and C spins, based on the difference in the chemical shifts of the carbon resonances.

Band-selective SPECIFIC–CP experiment can be also carried out for phosphorus samples with distinct ^{31}P chemical shifts. To the applicability of this approach, we present a model compound **1** (Scheme 1) with P=S and P=O residues separated by 60 ppm.

Band-selective ^{1}H–^{31}P CP transfer can be achieved using either ZQ or DQ matching conditions if careful attention is paid to the choice of the RF field amplitudes and ^{31}P carrier. SPECIFIC transfer is possible whenever one of the following conditions is fulfilled:

$$(\Omega_{\mathrm{I}}^2 + \omega_{1\mathrm{I}}^2)^{1/2} \pm (\Omega_{\mathrm{S}}^2 + \omega_{1\mathrm{S}}^2)^{1/2} = n\omega_{\mathrm{r}} \; for \; n = \pm 1, \pm 2$$

where the + and − signs on the left-hand side of the equation apply to DQ and ZQ transfer, respectively. Ω_{I} and Ω_{S} are chemical shift offsets, $\omega_{1\mathrm{I}}$ and $\omega_{1\mathrm{S}}$ are RF field amplitudes for I and S spins, respectively, and ω_{r} is the spinning frequency. In the absence of chemical-shift offsets, the above equation is the familiar selection rule for DQ and ZQ transfer in normal CP experiments.

Figure 6 shows the spectra when the carrier is placed on the P=S (Figure 6A) or P=O (Figure 6B) regions, and the matching condition is chosen so that the ^{31}P amplitude is smaller (in this case 10 kHz) than the frequency differences. In a perfectly selective experiment, CP with no loss in sensitivity is achieved. Figure 6C presents the spectrum of sample **1** without chemical-shift offsets. It seems that ^{1}H–^{31}P SPECIFIC–CP will find limited applications to study of bioorganic samples. This approach can be useful in material science when different derivatives of phosphorus are the building units of matter.

Finally, we wish to comment on the problem of proton decoupling under MAS.[24] Meier's group as well as Emsley and co-workers have demonstrated the use of low-power decoupling at high-frequency MAS for ^{13}C samples.[19,21] Figure 7 shows ^{31}P spectra for *O*-phosphothreonine spun at 60 kHz and recorded employing different decoupling sequences, cw (Figure 7A), tppm (Figure 7B),[25] spinal (Figure 7C)[26] and xix (Figure 7D).[27] As one can see, for each technique at ultra-fast MAS, the best decoupling over the whole range from 0 to 220 kHz is found when $\omega_{\mathrm{H1}} \approx 28$ kHz, which corresponds roughly to $\omega_{\mathrm{H1}}/\omega_{\mathrm{r}} = ½$, which is the Homonuclear Rotary Resonance (HORROR) condition.

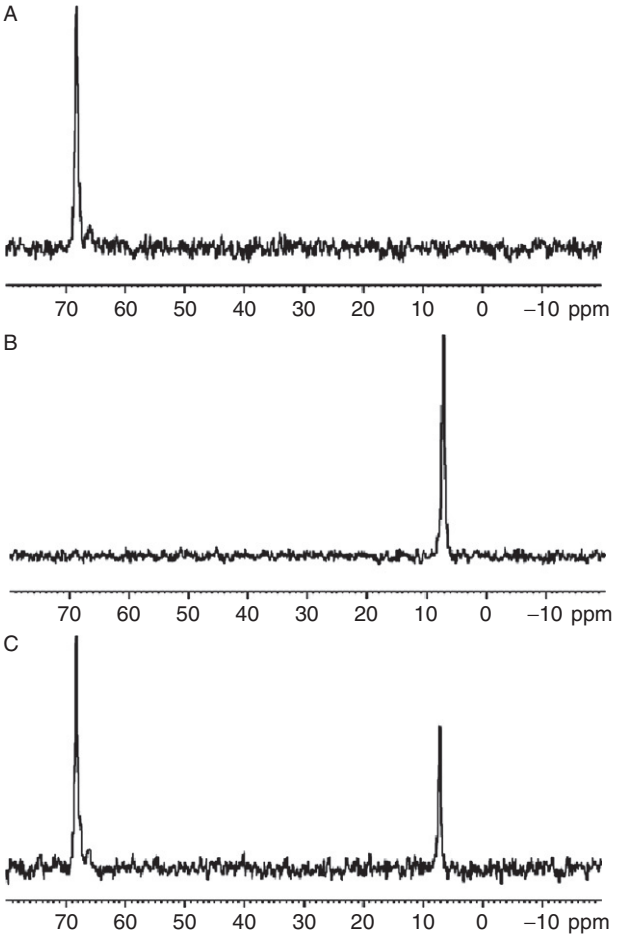

Figure 6 ^{31}P SPECIFIC–CP spectra of compound **1** recorded with ^{31}P RF = 10 kHz and (A) carrier set on P=S phosphorus; (B) carrier set on P=O phosphorus. (C) Spectrum without chemical shift offset.

It is known that, at the HORROR condition, homonuclear dipolar couplings between ^{1}Hs are reintroduced, leading to partial removal of the heteronuclear coupling.[28,29] It is worth noting that at 60 and 120 kHz the proton decoupling is insufficient due to the rotary resonance effect. It has been shown theoretically by Emsley and co-workers,[19] that the first and second rotary resonances are partially quenched by the presence of homonuclear couplings.

2.1.2. Analysis of ^{31}P spinning sidebands under MAS

Fast and ultra-fast spinning are able to remove all spinning sidebands and simplify the analysis of spectra leaving only the isotropic lines. However, in some cases static or slow sample spinning spectra are required since their inspection

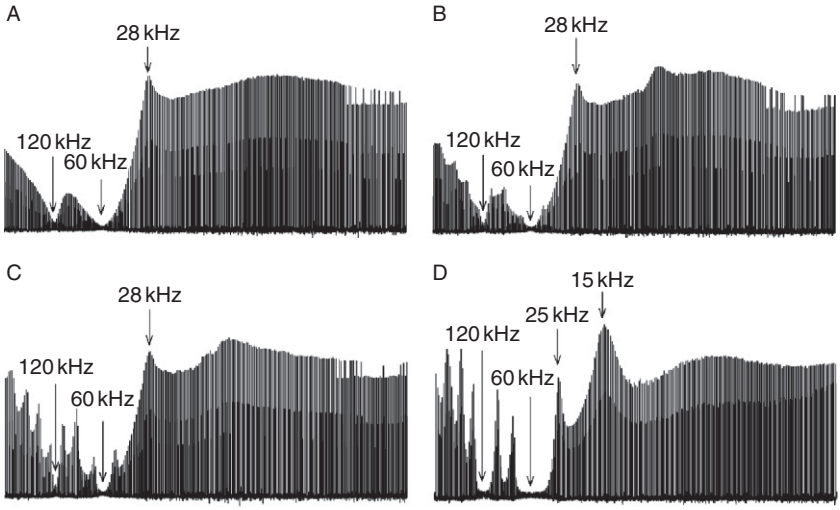

Figure 7 ^{31}P CP spectra for *O*-phospho-L-threonine spun at 60 kHz and recorded employing different decoupling sequences: (A) cw; (B) tppm; (C) spinal and (D) xix.

provides unique structural information. The ^{31}P line shape analysis can be a source of information on the local geometry, electron distribution, inter- and/or intramolecular interactions, molecular dynamics and phase alternation.[30] At a low MAS frequency, the sideband manifold is observed to map out the shape of the static spectra (see Figure 1).

In principle, it is possible to extract the anisotropy and asymmetry of CSA by fitting the observed MAS sideband intensities.[31,32] For accurate results to be achieved, it is necessary that many spinning sidebands are present in the spectrum: about 5 significant spinning sidebands are needed to determine the anisotropy (for asymmetry parameters in the range $0.1 < \eta < 1$), whereas 6–10 sidebands are required to determine the asymmetry ($0.3 < \eta < 1$). By employing the Herzfeld–Berger analysis protocol, the anisotropy, asymmetry and chemical shift tensor (CST) parameters can be obtained.[33] The meaning of CST and how these parameters can be used for the description of the electronic surrounding are discussed in a number of textbooks and reviews.[14,15] The ^{31}P CST parameters are capable of accurately characterising changes of conformation, molecular dynamics and phase transition.[34] Hydrogen-bonding distances have also proved to be correlated to ^{31}P tensor components in phosphorylated peptides and amino acids.[35–37]

It has to be stressed that the Herzfeld–Berger analysis is restricted to relatively simple molecules, since it is necessary to be able to resolve, at a low spinning rate, the sidebands of different resonances. As the number of distinct resonances increases, the 1D spectrum becomes increasingly more crowded (Figure 8).

The separation of isotropic and anisotropic parts of spectra with heavy overlapped systems is still a challenge for SS NMR spectroscopy. There are several approaches that can allow this goal to be achieved. Pines and co-workers introduced variable angle correlated spectroscopy (VACSY), for instance, and

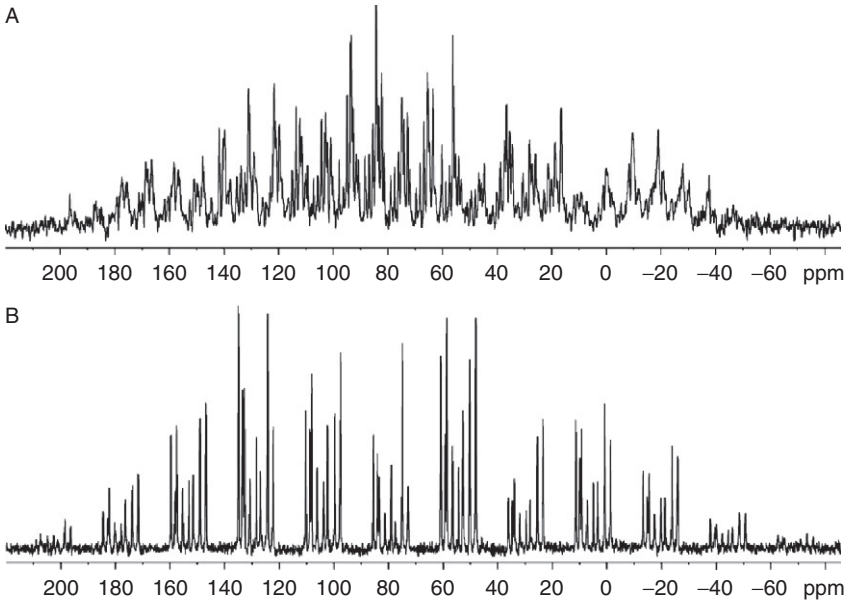

Figure 8 ^{31}P CP/MAS spectra of compound **5** (see Scheme 5) recorded at an MAS rotation speed equal to (A) 1 kHz and (B) 3 kHz.

employed it with great success to the analysis of tyrosine samples.[38] The merits of the TOSS–de-TOSS (TOSS means TOtal Sideband Suppression) experiment were presented by Kolbert and Griffin.[39] Grant's group, modifying Gan's MAT (magic angle turning) approach, has revealed the power of PHORMAT (PHase cORrected Magic Angle Turning) and FIREMAT (FIve π REplicated Magic Angle Turning) pulse sequences in structural studies of complex organic compounds.[40] As shown by Levitt and co-workers, the δ_{ii} parameters can be obtained with the aid of the phase-adjusted spinning sidebands (2D PASS) sequence, which offers good sensitivity and does not require any special hardware.[41] A number of papers showing the power of 2D PASS approach has been published.[42]

In recent years, few modifications of basic 2D PASS pulse sequence have found interesting applications in the structural study of phosphorus compounds. Orr, Duer and Ashbrook have reported a method allowing one to correlate the chemical shift spinning sideband pattern under fast and slow sample spinning employing as model compound sodium phosphate, which is characterised by a small CSA.[43] As was mentioned above, for such a system to get reliable results, a sufficient number of spinning sidebands is required. It can be achieved by very slow sample spinning in range of few hundred hertz. Unfortunately, such approach has at least two drawbacks. First, the slow sample spinning frequency is difficult to be stabilised, in particular for the routinely used 4, 3.2 and 2.5 mm MAS probe heads. Second, the homonuclear dipolar interactions affect the sideband intensities to a greater extent at slow spinning rates. In approach of Orr et al., the two-dimensional (2D) spectra give a fast MAS sideband pattern in the directly

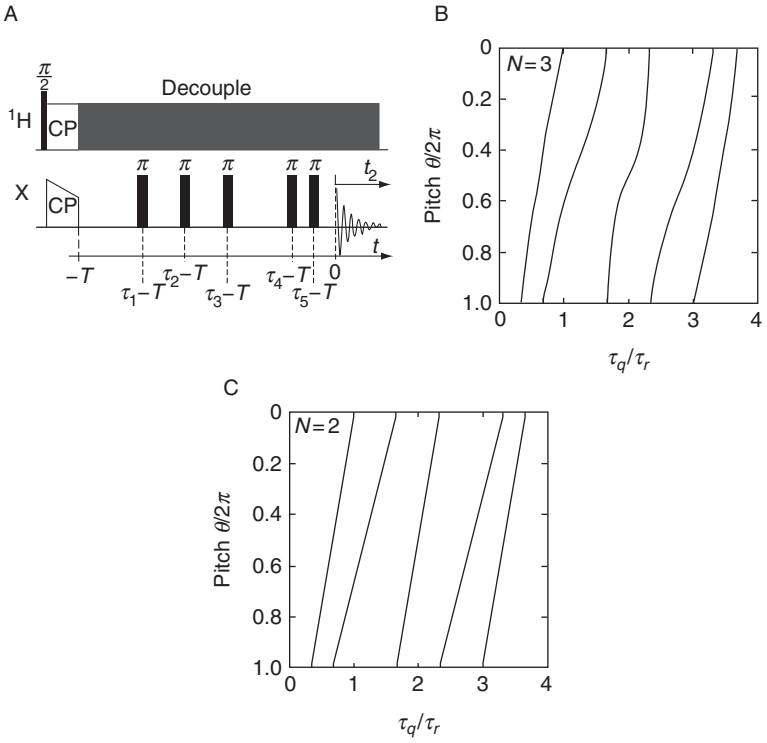

Figure 9 (A) The five-pulse 2D CSA-amplified PASS sequence for scaling factors of $N \leq 3$. The sequence is illustrated with the initial transverse magnetisation generated using ramped cross-polarisation (CP). During the 2D experiment, the pseudo-t_1 variable Θ is incremented between 0 and 2π; the π-pulse timings required for each value of Θ are illustrated in the plots (B) for $N = 3$ and (C) for $N = 2$. Each line plots the timing of one pulse as a function of Θ. Taken from Ref. [43].

observed dimension with the spinning sideband intensities equivalent to the CSA scaled by a factor of N, or equivalently the sample spinning frequency scaled by $1/N$, in the indirectly observed dimension. This experiment (the pulse sequence shown in Figure 9) is in essence a combination of the 2D-PASS[41] and Titman and co-workers' CSA amplification method.[44]

As proved by the authors, the 2D CSA-amplified PASS has a number of favourable features. First, a gain in signal intensity by a factor of 2 is achieved over experiments that require either a storage period or quadrature detection in the indirect dimension. Second, in common with the XCS (chemical-shift modulation) and CSA amplification experiments, isotropic shifts do not occur in the ω_1 dimension, leading to efficient sampling of the indirect dimension. Finally, spinning sideband intensities are the same as in conventional MAS spectra allowing routine analysis.

Another problem, which very often complicates the analysis of ^{31}P spectra, is overlapping of the isotropic lines. Ironside et al.[45] while investigating a mixture of hydroxyapatite, $Ca_{10}(PO_4)_6(OH)_2$ and sodium dihydrogen phosphate,

$NaH_2PO_4 \cdot H_2O$, for which the phosphate sites show very similar ^{31}P isotropic shifts, have shown that the problem of resolving ^{31}P δ_{iso} can be elucidated by employing CSA-amplified PASS. In this method, the isotropic chemical shifts are distinguished according to their CSA and asymmetry. The technique involves correlating sideband spectra at different effective spinning rates using CSA-amplification pulse sequences. The resulting 2D correlation pattern allows very accurate determination of the chemical shift principal values in addition to the recovery of parameters for two overlapping patterns, which allows the resolution of overlapping signals. The other methods of analysis of spinning sidebands and experiments that can be carried out have been reported elsewhere.[46]

2.2. Multi-dimensional SS NMR spectroscopy

In 1971, the idea of 2D NMR spectroscopy was proposed by Jeener and later implemented by Aue, Bartholdi and Ernst, who published their work in 1976.[47] The first experiments, carried out mostly in the liquid phase, have unambiguously proved that 2D NMR spectra provide more information about a molecule than 1D NMR spectroscopy and are especially useful in determining the structure of molecules that are too complicated to work with using 1D NMR. With the progress in the methodology and software improvement, three-dimensional (3D) and four-dimensional (4D) NMR experiments were gradually introduced into the laboratory practice. Such strategy, the so-called multi-dimensional (or ND) NMR spectroscopy, has found a number of spectacular applications in the structure analysis of natural products.

In the early stage of development of NMR spectroscopy, the applicability of multi-dimensional approach was tested for condensed matter. Today, because of the excellent progress on this field, the ''library'' of different ND techniques used in SS NMR is pretty rich. On the basic level, these methods can be assigned to two groups: homo- (HOMCOR) and heteronuclear correlations (HETCORs). Both correlations employ indirect (through-bond) or direct (through-space) coupling to correlate different spins.

Homo- and heteronuclear correlated spectroscopy has found a number of applications in structural studies of phosphorus compounds. Some of the commonly used 2D sequences employing though-space correlations (proton-driven spin diffusion (PDSD), phase-modulated Lee–Goldburg HETCOR (PMLG HETCOR), frequency-switched Lee–Goldburg (FSLG HETCOR) and through-bond correlations (INADEQUATE (incredible natural abundance double quantum transfer), TOBSY)) were reviewed by Iuga et al.[13] In this section, we present other techniques that were used for investigation of phosphorus derivatives or new variants of existing sequences that were published during last 3 years.

2.2.1. Homonuclear Correlations via direct (dipolar) couplings, D-HOMCOR

Many techniques in SS NMR make use of dipolar couplings in order to transfer spin polarisation between adjacent spins. The usefulness of this type of experiments is due to the fact that value of dipolar coupling R_{dip} depends only on the distance between spins and is expressed by the simple equation:

$$R_{\mathrm{dip}} = -(\mu_0/8\pi^2)\gamma^2 h/d^3$$

where d is the internuclear distance and γ is the magnetogyric ratio of the ^{31}P spin.

The simplest technique that enables phosphorus–phosphorus correlations for complex multi-component system and elucidation of structural constraints is the PDSD sequence.[48] This experiment is relatively easy to set up; however, the distances between spins cannot be established with satisfactory precision. One common way of determining distance type information using spin-½ NMR is based on the acquisition of the DQ filtered spectra as a function of the DQ mixing time.[49] The recently introduced DQ homonuclear recoupling sequences based on C and/or R symmetry developed by Levitt and co-workers allows very precise analysis of internuclear distances.[50] The accuracy of distances obtained from these DQ experiments depends on the effective suppression of contributions to the spin Hamiltonian other than the required homonuclear dipolar coupling terms.

One of the most popular DQ sequences commonly used in the study of organic and bioorganic phosphorus compounds is the C7 sequence and the permutationally offset stabilised variant of C7 (POST-C7).[51] Figure 10A shows, in pictorial form, the pulse sequence and DQ coherence pathway. Figure 10B displays the SQ–DQ ^{31}P–^{31}P POST C7 spectrum of the disodium salt of ATP trihydrate recorded at 10 kHz MAS.[52] The correlation peaks between α and β as well between β and γ phosphorus centres confirm the presence of two molecules in the asymmetric units and show the connectivity between them.

From an inspection of the sequence, it is clear that, after CP and first ^{31}P $\pi/2$ pulse, the DQ period is divided into two sections: excitation time (τ_{DQ1}) and reconversion time (τ_{DQ2}). DQ experiments can be carried out by employing different procedures: symmetric, asymmetric and constant time.[53] The ^{31}P build-up curve, which in the final step is used for distances analysis, is taken from a series of 2D spectra recorded as a function of DQ time.

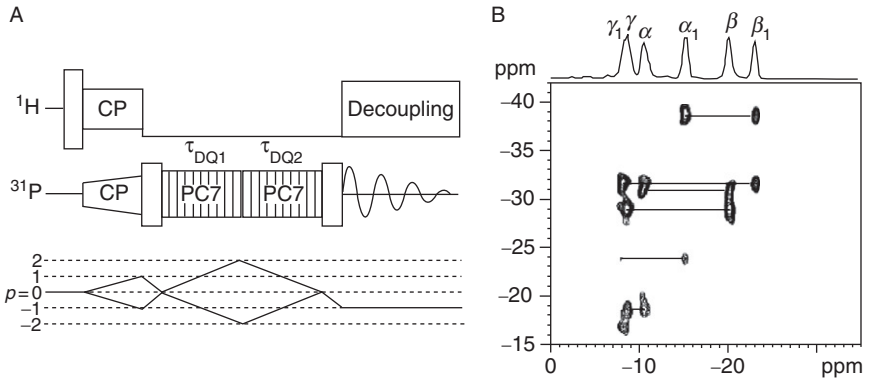

Figure 10 (A) POST C7 pulse sequence and double-quantum coherence transfer pathway. (B) ^{31}P–^{31}P POST-C7 correlation spectrum for disodium ATP trihydrate recorded at 287 K: spinning rate, 10 kHz; RF 70 kHz; and excitation time (τ_{ex}) 1.4 ms.

In the symmetric procedure, excitation and reconversion times are incremented such that $\tau_{DQ1} = \tau_{DQ2}$. In the asymmetric procedure, either τ_{DQ1} or τ_{DQ2} is fixed at a value corresponding to maximum DQ transfer and the other interval is changed. The oscillation frequency in the asymmetric procedure is about one-half of the oscillation frequency in the symmetric procedure while the oscillation amplitude is twice.[54] In the constant-time procedure, the times are varied such that $\tau_{DQ2} = \tau_{total} - \tau_{DQ1}$, where τ_{DQ1} is incremented from zero to total. The total conversion time needs to be long enough to induce a zero-crossing in the build-up curve, which is necessary for reliable data analysis in terms of the dipolar coupling constant. Such procedures are an additional test that allows verification of the quality of measurement.

In case of inorganic samples which do not contain hydrogen, the CP transfer from ^{1}H to ^{31}P cannot be fulfilled. Hence, in many cases the DQ experiments for inorganic materials are carried out by employing only one channel. Application of different pulse sequences based on C-R symmetry theory for inorganic compounds was exhaustively discussed by Günne.[55] Comparing the crystal structure and NMR data, Günne has revealed that the distances derived from ^{31}P DQ NMR carry only small systematic errors caused, for example, by anisotropic *J*-coupling, dipolar contributions from adjacent spins and relaxation.

With the progress in magnet technology, NMR samples can be measured now at very high-static magnetic field (e.g. $\mathbf{B}_0 = 23.49$ T). Higher magnetic field can lead, in principle, to substantial benefits in terms of sensitivity and resolution. However, the magnitude of the CSA, in hertz, is proportional to $\mathbf{B}_0$. For a 1-GHz instrument, ^{31}P nuclei in phosphate groups can experience CSAs as large as 81 kHz. In that case, the magnitude of ^{31}P CSA is comparable with that of the RF fields and is much larger than the ^{31}P–^{31}P dipolar interactions, which do not exceed 1.8 kHz in magnitude.[13] Large ^{31}P CSA can interfere with the homonuclear recoupling sequences and they may decrease the excitation efficiency of DQ coherences. The problem of DQ NMR spectroscopy of ^{31}P species submitted to very large CSAs was recently discussed by Amoureux and co-workers.[56] The authors have tested different recoupling sequences shown in Figure 11: $BR2_2^1$ ($\tau\pi\tau$), SPIP, BABA and fp-RFDR. They revealed that $BR2_2^1$, which is a modified version of the rotor-synchronised $R2_1^2$ sequence, is efficient and robust to both CSA and offset.

2.2.2. Homonuclear Correlations via indirect *J*-couplings, *J*-HOMCOR

J-coupling is one of the most important parameters that can be measured by NMR spectroscopy.[57] Since *J*-coupling is mediated by chemical bonds, its observation greatly aids the assignment of molecular geometry and provides significant structural constraints complementary to dipolar and chemical shift interactions. The spin–spin coupling can be relatively easily determined in the liquid phase. In SS NMR spectra, even under MAS, the observed line broadenings usually mask any underlying *J*-splittings. This is particularly the case for disordered samples in which distributions of isotropic chemical shifts cause the free-induction decays (FIDs) of the NMR signal arising from the direct detection of transverse

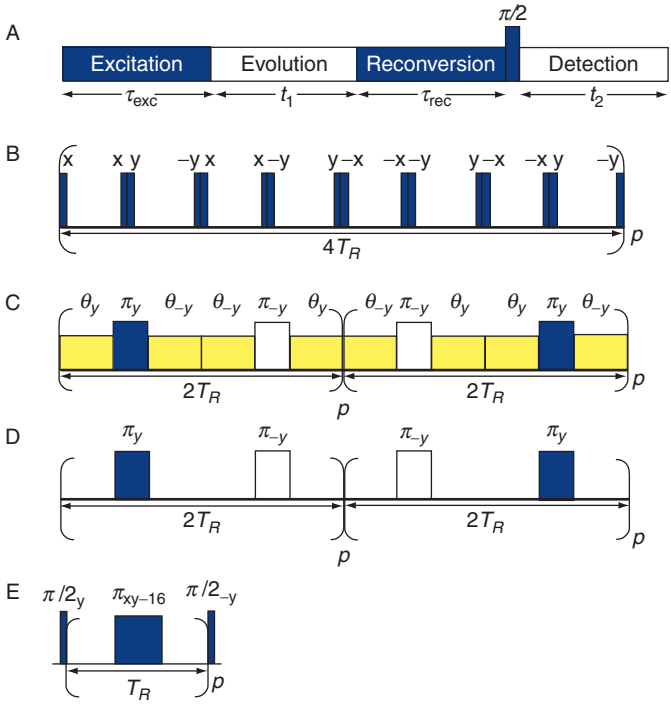

Figure 11 (A) General scheme of 2Q–1Q spectroscopy. Basic cycle of: (B) BABA-4; (C) SPIP; (D) $BR2_2^1$ ($\tau\pi\tau$); (E) [fp-RFDR]. The XY-16 super-cycle consists of (x, y, x, y), (y, x, y, x), ($-x$, $-y$, $-x$, $-y$) and ($-y$, $-x$, $-y$, $-x$). Taken from Ref. [56].

magnetisations to be characterised by dephasing times, T_2^*, which are much shorter than the inverse of typically encountered J-couplings.

In the 1990s, several groups have applied 2D spin-echo experiments to determine ^{31}P–^{31}P indirect spin–spin couplings in organic and organometallic compounds.[58] The spin-echo sequence refocuses evolution under chemical shift offsets, such that for disordered solids the spin-echo dephasing time (T_2') is much longer than the decay time of the FID. Recently, Duma et al.[59] have confirmed the robustness and accuracy of the simple spin-echo pulse sequence for measuring J-coupling constants. They proved that the significantly large CSA and dipolar interactions stabilise rather than perturb the measurement.

Iuliucci and Meier, employing a variant of the 2D TOBSY exchange NMR spectroscopy, have measured the angle between the ^{31}P CSA tensors in the covalently bonded P–O–P cubic unit in the room-temperature structure of SiP_2O_7.[60] The selectivity to covalently bonded pairs was achieved by using the scalar coupling interaction as the driving force for polarisation exchange during the mixing time of a 2D exchange experiment.

This 2D correlation method uses a multiple-pulse sequence to suppress resonance offsets and promote polarisation transfer driven only by the J-coupling while simultaneously avoiding the recoupling of dipolar interactions. A much

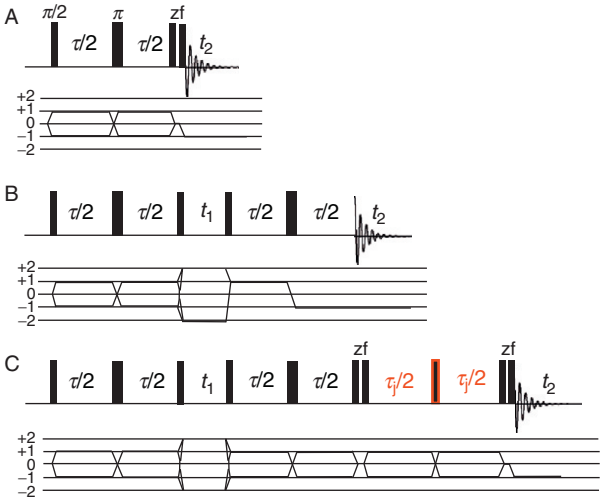

Figure 12 Pulse sequence and corresponding coherence transfer pathway diagram for (A) the *z*-filtered spin-echo; (B) the refocused INADEQUATE; and (C) the refocused INADEQUATE spin-echo (REINE) experiments. Thin and thick rectangles, respectively, represent $\pi/2$ and π pulses. Taken from Ref. [65].

less demanding alternative possibility to determine through-bond connectivities in the solid state is provided by the INADEQUATE[61] and refocused INADEQUATE pulse sequences.[62,63]

Very recently, Cadars et al. have presented a new modification of refocused INADEQUATE pulse sequence with the acronym REINE (*RE*focused *IN*ADEQUATE spin-*E*cho).[64] As shown in Figure 12, the REINE joins two known approaches. The additional spin-echo period in the REINE experiment allows the detection of the *J*-modulation for each 2D peak.

Brown and co-workers tested the applicability of REINE sequence for the cadmium phosphate glass, $0.575CdO–0.425P_2O_5$.[65] It has been shown that this technique could be implemented in SS NMR spectroscopy to accurately measure small $^{31}P–^{31}P$ homonuclear scalar couplings including in cases where no splitting due to the *J*-coupling were observed in the normal CP/MAS spectrum. In conclusion, we note that 2D *J* HOMCOR experiments are particularly useful for the study of non-crystalline systems, providing a new powerful probe for characterising local structural disorder. A number of spectacular SS NMR applications for phosphorus in disordered materials has recently been published.[11]

2.2.3. Heteronuclear correlations

One of the common 2D SS NMR approaches employed for investigation of phosphoro-organic and bio-organic samples is based on high-resolution heteronuclear correlations (HETCOR). In solution-state NMR, this technique is the basic method that allows assignment of proton and phosphorus to the molecular structure. In the solid state, the assignment is more complex because of the very

large linewidth of protons. Even under favourable experimental conditions, proton resonance lines over 1 ppm are typically recorded. The observed residual broadening is assigned to chemical shift distributions, strong homonuclear ^{1}H–^{1}H dipole–dipole coupling and residual anisotropic interactions.

The first successful SS HETCOR measurement was published in 1982 by Caravatti et al.[66] In this pioneering work, homonuclear decoupling in t_1 was achieved by means of multi-pulse sequences at low sample spinning rates (as in the CRAMPS experiment). In the 1990s, several methodological improvements in the technique were reported.[67] The big achievement on this field was the application of FSLG decoupling.[68] A typical FSLG HETCOR sequence is shown in Figure 13.

In FSLG HETCOR experiments, the sample is spun rapidly, at more than 10 kHz, which greatly improves the resolution of carbon and proton projections. After the 90° and magic angle (54.7°) proton pulses (see Figure 13) during the evolution period t_1, the proton–proton dipolar couplings are removed by the homonuclear decoupling sequence (FSLG), whereas the remaining inhomogeneous interactions, that is, the chemical shift and the heteronuclear couplings, are averaged out by MAS to their isotropic part, leaving only the isotropic chemical shifts in both dimensions. After the second 54.7° proton pulse, a CP step transfers the proton magnetisation to the carbon nuclei. By lengthening the

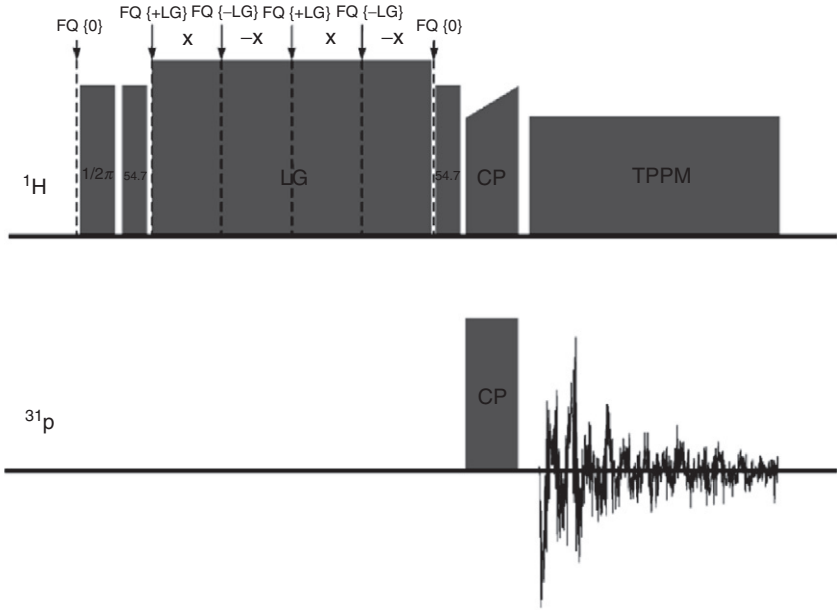

Figure 13 Pulse sequence for the solid-state ^{31}P–^{1}H frequency-switched Lee–Goldburg (FSLG) experiment. Proton–proton homonuclear decoupling was performed by using the FSLG decoupling sequence. Quadrature detection in ω_1 was achieved by using the TPPI method. During the acquisition period, TPPM heteronuclear decoupling was applied.

contact time in the pulse sequences in range from 100 μs to few ms, it is possible to observe short- and long-range inter- and/or intramolecular interactions. During the acquisition period, TPPM heteronuclear decoupling is applied. The strategy for PMLG decoupling experiment is very similar. The applicability of PMLG HETCOR to the structural study of phosphorus derivatives has been reported.[13]

Very recently, an interesting modification of HETCOR correlation was published by Chan and co-workers.[69] In this experiment, a DQ filter is incorporated into the pulse sequence of HETCOR spectroscopy so that a DQ excitation profile can be obtained by measuring a series of 2D spectra (Figure 14). This method offers a simple experimental approach to extract the van Vleck second moment of a multiple-spin system under high-resolution condition. Hydroxyapatite ($Ca_{10}(PO_4)_6(OH)_2$) and brushite ($CaHPO_4 \cdot 2H_2O$) were used as reference samples.

As we highlighted in Section 2.1.1, advances are being made in SS NMR spectroscopy following the development of MAS at rates approaching 70 kHz. Thus, ultra-fast MAS offers new opportunities for through-bond heteronuclear spectroscopy, for example using pulse sequences similar to heteronuclear SQ correlation (HSQC) experiments in solution NMR. The utility of using ^{1}H–^{1}H homonuclear decoupling during INEPT in ^{13}C-detected HETCOR experiments at a lower MAS rate (22 kHz) has been already demonstrated.[70] Indeed, fast MAS by itself enabled the acquisition of directly detected (also referred to as X-detected) and indirectly detected (^{1}H-detected) multi-dimensional HETCOR NMR spectra of organic materials in which ^{1}H spin systems were isotopically diluted, exhibited some degree of motional narrowing or were fully coupled.[71]

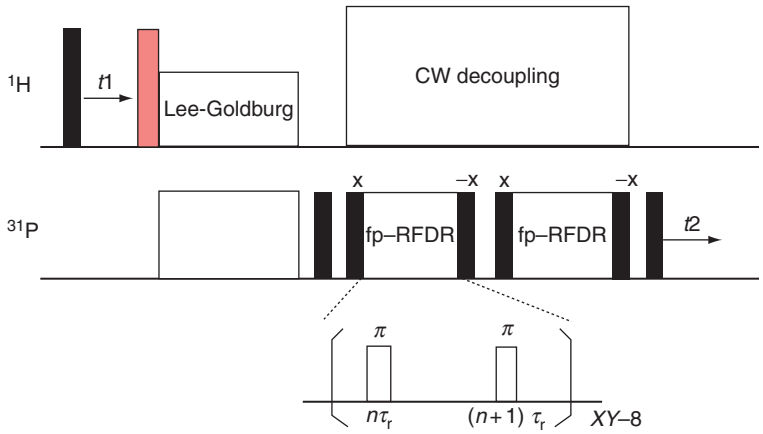

Figure 14 Pulse sequence designed for the measurements of DQF-HETCOR spectra. The rectangle in grey represents the pulse with the flip angle adjusted to bring the ^{1}H magnetisation spin-locked along the effective field. The duration of the π pulses within the fp-RFDR blocks was set equal to 30% of the rotor period and the filled rectangles denote $\pi/2$ pulses of 5 μs. The $\pi/2$ pulse following the ^{31}P spin-locking pulse serves to bring the ^{31}P transverse magnetisation to the *z*-axis. For the measurements of HAp and brushite, the t_1 evolution is removed. Taken from Ref. [69].

Unfortunately, so far, there are no reports showing applications of $^{1}H–^{31}P$ or $^{31}P–^{1}H$ HETCOR correlations under ultra-fast MAS in structural studies of phosphorus compounds but, for sure, this approach traces the future for HETCORs.

3. APPLICATIONS OF ^{31}P SS NMR SPECTROSCOPY

3.1. ^{31}P SS NMR studies of relevant bio-organic compounds

As we stated in Section 1, phosphorus is the key element in a number of very important biological moieties including peptides, proteins, nucleic acids and lipids. Most of these compounds contain phosphorus in form of the phosphoryl group. In some of them, the phosphoryl residue is the central basic unit of structure (nucleic acids) in some of them it is mobile residue, relocated during phosphorylation/dephosphorylation processes (proteins, energy carries). The phosphoryl group transfer, one of the most important vital processes, is related to the change of ionisation state and difference in strength of hydrogen bonding. In this section, we will show that ^{31}P SS NMR is powerful tool that allows precise characterisation of subtle structural restraints.

3.1.1. ^{31}P NMR of phosphorylated amino acids

In enzymatic reactions, the transfer proceeds via phosphorylation of the OH function of the serine residue; however, threonine and tyrosine can be also involved. Hence, much attention has been paid to the fundamental study of the compounds shown in Scheme 2.[36] The attractiveness of these models is due to the fact that X-ray structures both for enantiomeric and racemic forms are known (with exception of *O*-phospho-L-tyrosine). With the local geometry of phosphate groups and hydrogen bonding pattern taken from X-ray studies, it is possible to test the correctness of NMR analysis, the accuracy of measured structural constraints and the applicability of theoretical methods (*ab initio*, density functional

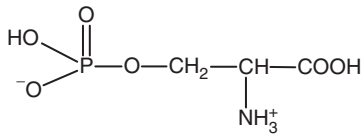

O-phosphoserine

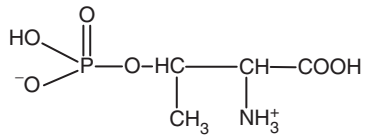

O-phosphothreonine

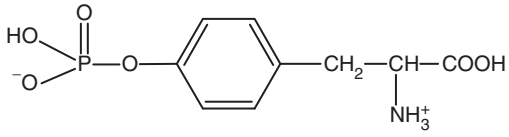

O-phosphotyrosine

Scheme 2

TABLE 1 The values of the principal elements of the chemical shift tensor for selected *O*-phosphorylated amino acids obtained from the analysis of the intensities of the spinning sidebands ^{31}P CP/MAS spectra

O-Phosphorylated amino acid	δ_{iso} (ppm)	δ_{11} (ppm)	δ_{22} (ppm)	δ_{33} (ppm)	$\lvert\Delta\delta\rvert$ (ppm)	Ω (ppm)	η	κ
L-Serine	−0.9	51	4	−57	84.5	108	0.83	0.14
DL-Serine	1.9	54	6	−54	84.0	108	0.86	0.11
L-Threonine	−3.7	56	5	−72	102.5	128	0.75	0.20
DL-Threonine	−0.9	51	5	−58	86.0	109	0.81	0.16
L-Tyrosine	−4.3	66	7	−86	122.5	152	0.72	0.22
	−5.9	61	3	−82	114.0	143	0.76	0.19
DL-Tyrosine	−3.3	60	−7	−63	95.0	123	0.88	−0.09

See text and Ref. [36] for details.

theory (DFT) calculations of NMR shielding parameters). The knowledge gained from basic studies can be further extended to more complex systems for which X-ray data are not available.

In the cited paper, the authors discussed problem of changes of the values of the principal elements of the ^{31}P CSTs in relation to zwitterionic structures and intermolecular contacts. The values of ^{31}P CST parameters obtained by employing the Herzfeld–Berger algorithm are collected in Table 1.

By analysing the X-ray data and the changes of values of principal elements and changes in differences between them (anisotropies), it has been proved that these parameters are more sensitive measures of hydrogen bonding than the isotropic chemical shifts. Upon comparison of the experimental ^{31}P CSA tensor values of *O*-phosphorylated amino acids (Table 1), the biggest differences appear indeed for the δ_{33} element. For two conformers of *O*-phospho-L-tyrosine, this parameter is equal to −82 and −86 ppm, respectively, while for *O*-phospho-L-serine and *O*-phospho-L-threonine it is equal to −57 and −58 ppm, respectively. Un and Klein[72] suggested that the observed differences of this element could reflect the changes in the O–P–O valence angles or in an average length of the shortest P–O bonds. However, a lack of such correlation for the compounds under investigation means that it is not the case for *O*-phosphorylated amino acids and this prompted the authors to look for the dependence of the ^{31}P phosphoryl CST on the type and strength of intermolecular hydrogen bonding.

The correlation of ^{31}P, δ_{ii}, $\Delta\delta$ and Ω parameters versus the intermolecular P–O···H–O–C and P–O···H–O–P hydrogen bond distance in the L and DL forms of *O*-phosphorylated amino acids has been presented (see Figure 15A). Somewhat unexpectedly, these two groups of compounds reveal opposite trends when the hydrogen-bond strength decreases; the δ_{11}, $\Delta\delta$, and Ω values increase and the d_{33} decreases for the L form, with a reverse scenario taking place in the case of the DL form.

The orientation of ^{31}P δ_{ii} in the L-enantiomer of phosphorylated amino acids has been determined on the basis of theoretical calculations. According to

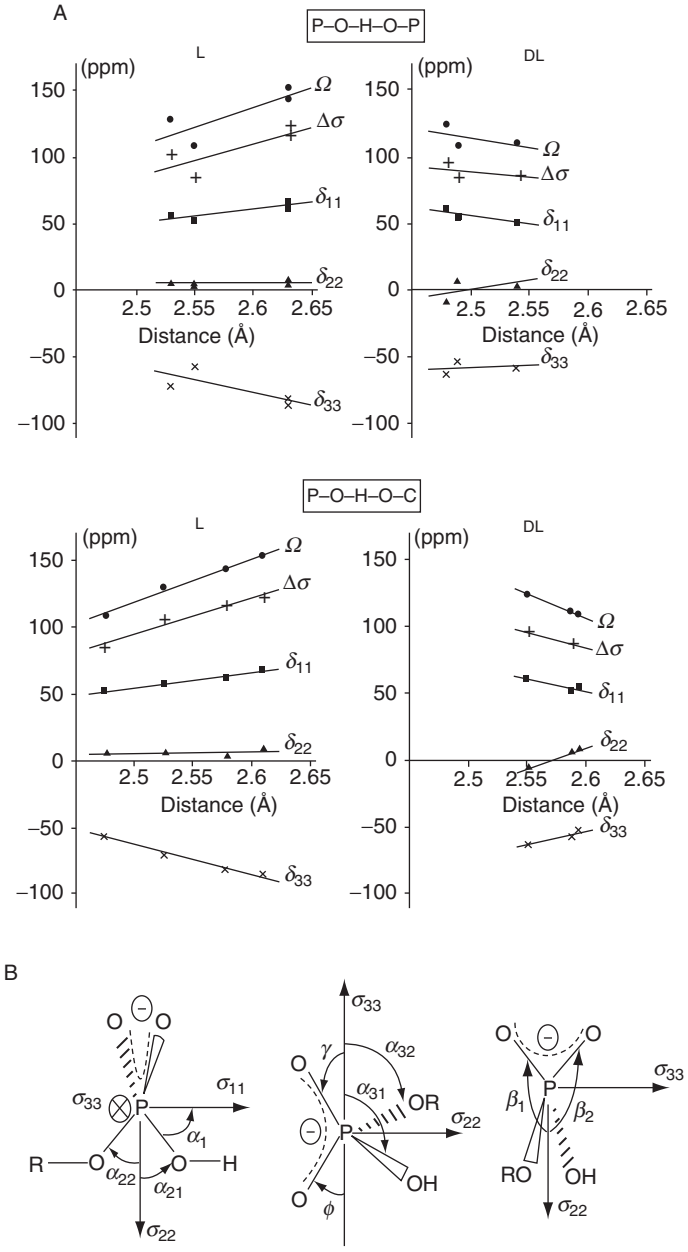

Figure 15 (A) Plots of ^{31}P δ_{ii}, anisotropy $\Delta\delta$ and span Ω parameter versus the intermolecular P–O···H–O–C and P–O···H–O–P hydrogen bond distance in L (left) and DL (right) forms of *O*-phosphorylated amino acids. (B) ^{31}P chemical shielding tensor orientation in *O*-phosphorylated amino acids showing three orthogonal projections of the phosphate group hydrogen bond in tyrosine. Taken from Ref. [36].

Figure 15B, the principal axes of the δ_{11} and δ_{22} elements lie in a plane perpendicular to the O–P–O– plane. The axis corresponding to the δ_{22} element nearly bisects the O(R)–P–O(H) angle (the sum of α_{21} and α_{22} is very close to the O(R)–P–O(H) valence angle). This axis also nearly bisects the O–P–O– angle, since the sum of β_1, β_2, and the O–P–O– angle is very close to 360°. Moreover, the values of α_{31} and α_{32} indicate that the δ_{33} axis is almost perpendicular to the O(R)–P–O(H) plane. The same axis is also in the O–P–O– plane since the sum of γ, ϕ, and the O–P–O– angle is close to 180°. This explains the most pronounced sensitivity of the ^{31}P δ_{33} element as being due to changes in the hydrogen-bond strength.

The change of the local electrostatic potential of the phosphoryl group often induces conformational changes of proteins, influencing their functions, or modulates protein–protein interactions. At physiological pH, phosphate residues usually carry −2 charge. Very recently, Jacobson and co-workers,[73] employing a theoretical approach, revealed that phosphate groups at physiological pH may coexist as −1 and −2 species and that the effect of the phosphate protonation state on the strength of the hydrogen bonds is remarkably subtle.

Tekely and co-workers[74,75] were the first to reveal that SS ^{31}P NMR spectroscopy yields an unambiguous visualisation of the presence and the nature of singly and/or doubly ionised phosphate groups in lyophilisates prepared from parent solutions at different pH values. Employing *O*-phospho-L-serine as a model sample, they showed that both isotropic and anisotropic parameters are very sensitive to the change of the ionisation state (Figure 16).

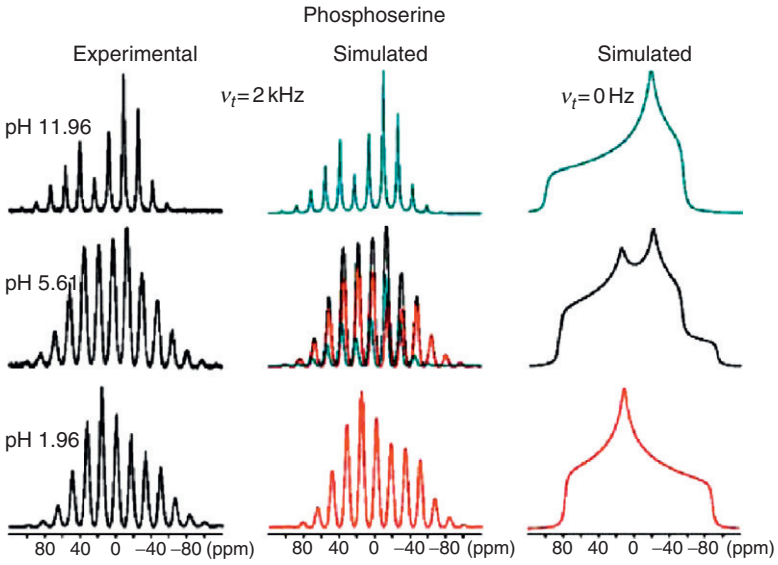

Figure 16 Experimental (left) and simulated (middle) low spinning speed ($\omega_r = 2.0$ kHz) CSA sideband manifolds of phosphate groups in L-*O*-phosphoserine lyophilised from solutions at different pH values. For better visualisation of the changes in the CSA tensor after secondary ionisation, the corresponding simulated static powder spectra are also included (right). Taken from Ref. [74]. Reproduced by permission of *The Royal Society of Chemistry*.

This problem was further discussed by Gajda et al.[76] In cited paper, the authors investigated the ammonium salts of *O*-phospho-L-threonine with well-defined X-ray structures. NH_4PThr exists in crystal lattice as mono-anion and $(NH_4)_2$PThr as dianion. It is worth noting the very unusual molecular packing of NH_4PThr. The unit cell consists of four independent molecules with different hydrogen-bonding patterns (Figure 17). Such models enable very accurate investigation of the influence of the strength of hydrogen bonds on ^{31}P NMR shielding parameters under a given ionisation state of the phosphate group.

Analysing ^{31}P NMR experimental data, the authors show that the skew κ is very sensitive to the change of the ionisation state. Negative values of κ are typical for -2 phosphates. For the -1 species engaged in very strong hydrogen bonds,

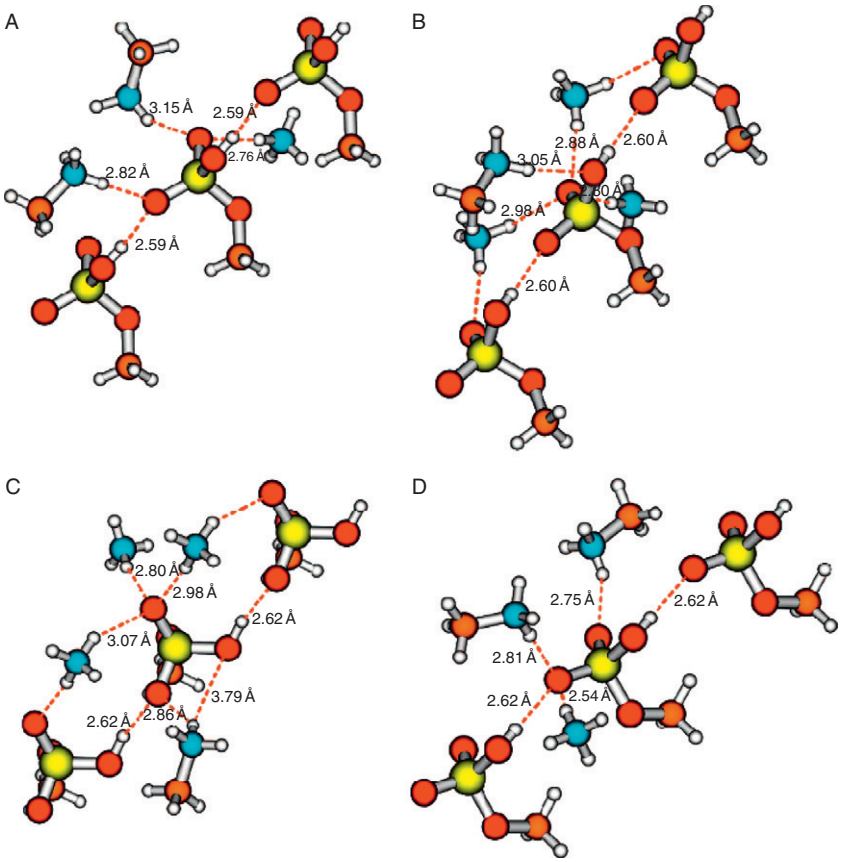

Figure 17 Distances between heavy atoms involved in hydrogen bonds formed by the phosphate group (central molecule) of every independent molecule existing in one asymmetric unit of NH_4PThr given in angstroms. Dotted lines show hydrogen bonds. (A)–(D) correspond to A, B, C and D molecules, respectively, in one NH_4PThr unit. For easier visualisation, the threonine chains are replaced by CH_3 groups in this illustration. Taken from Ref. [75].

the value of span Ω is smaller than that for phosphate groups involved in weak hydrogen bonding.

For phosphates in the −2 state, Ω is significantly smaller compared to the −1 species; however, κ for the −1 sample never reaches negative values. These experimental data are very consistent with the theoretical calculations. DFT calculations were also employed for analysis of the influence of hydrogen in the hydrogen bridge on ^{31}P shielding parameters (Figure 18).

Finally, it has to be stressed that counterions change values of the principal elements of the ^{31}P CST. Comparing the electronic effects of Li^+, Na^+ and K^+ counterions on the principal values of the ^{31}P tensor of the phosphate group of phospho-L-serine and checking to what extent this effect could influence the characteristic fingerprints of deprotonation, Gardiennet-Doucet et al.[75] revealed the opposite shifts of the δ_{22} and δ_{33} principal values (Figure 19).

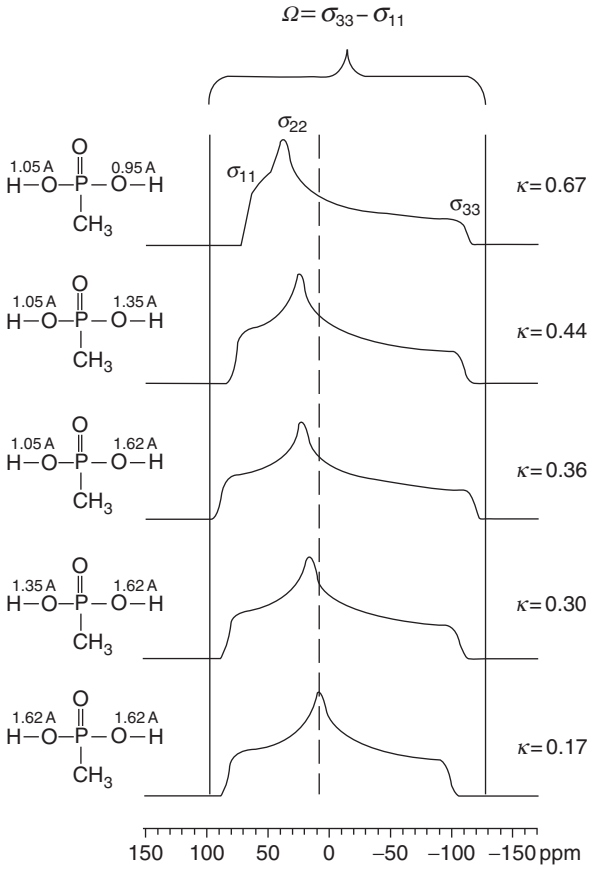

Figure 18 ^{31}P line shape changes versus position of hydrogen in the hydrogen bridge. These simulated static powder spectra were obtained by employing the calculated ^{31}P shielding parameters and converting to chemical shifts. The span is expressed as $\Omega = \sigma_{33} - \sigma_{11}$ and skew is expressed as $\kappa = 3(\sigma_{22} - \sigma_{iso})/\Omega$. Taken from Ref. [35].

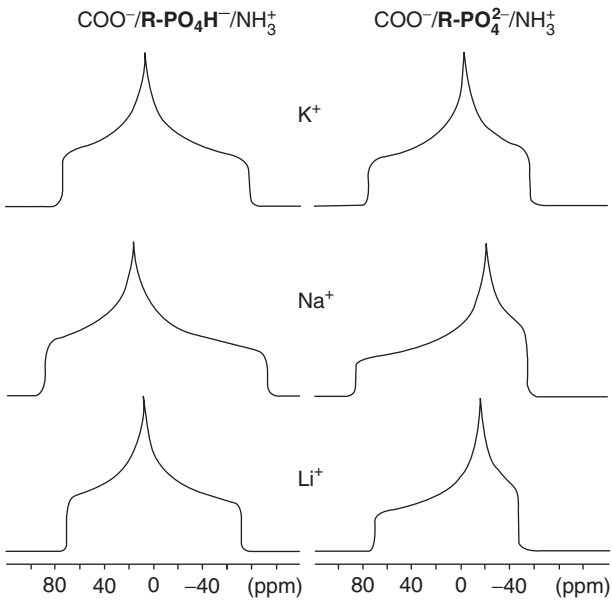

Figure 19 Reconstruction of ^{31}P CSA powder spectra of monoanionic (left) and dianionic (right) phosphate groups in lyophilisates of L-phosphoserine prepared with LiOH, NaOH and KOH. Taken from Ref. [75].

3.1.2. ^{31}P NMR of nucleotides and nucleic acids

Nucleotides play central roles in metabolism. They serve as sources of chemical energy (ATP and guanosine triphosphate (GTP)), participate in cellular signalling (cyclic guanosine monophosphate (cGMP) and cyclic adenosine monophosphate (cAMP)) and are incorporated into important cofactors of enzymatic reactions. Nucleotides are molecules that, when joined together, make up the structural units of RNA and DNA (Scheme 3).

Nucleotides are often used as SS NMR models in structural studies. Adenosine monophosphate was employed by Tekely and co-workers for testing the suitability of high-resolution SS ^{31}P NMR for a straightforward determination of the protonation state of phosphate groups as well as of their pK_2 values.[77]

Adenosine 5′-diphosphate (ADP) potassium salt was used by Olejniczak et al.[53] for examination of the applicability of the DQ recoupling sequence POST-C7 (see Section 2.2.1) to study ^{31}P–^{31}P geometrical constraints. The authors tested the recoupling sequence by employing different procedures (symmetrical, asymmetrical, constant time, see Section 2.2.1 for details). From these studies, it can be concluded that the profile of the theoretical ^{31}P POST-C7 build curve, in particular for asymmetric and constant-time procedures, is very sensitive to change of the Euler angles. Thus, these parameters have to be set very precisely in order to get reliable simulated data. χ^2 error analysis allows making a proper choice of the geometrical parameters (in this case ^{31}P–^{31}P distance), interpreting

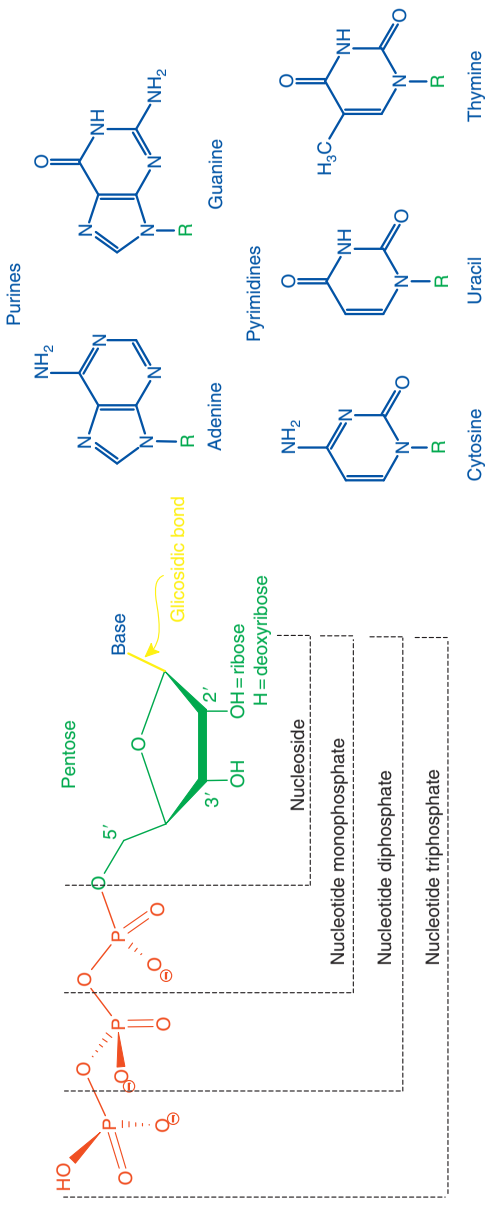
Purines
Pyrimidines
Guanine
Adenine
Thymine
Uracil
Cytosine
Glicosidic bond
Base
Pentose
OH = ribose
H = deoxyribose
Nucleoside
Nucleotide monophosphate
Nucleotide diphosphate
Nucleotide triphosphate

Scheme 3

the trustworthiness of POST-C7 profiles and, further, extending this approach for searching for samples with unknown X-ray structure.

^{31}P NMR studies of disodium adenosine 5′-triphosphate (Na_2ATP) crystals have been reported by several groups.[52,78,79] In the solid state, Na_2ATP exists as monohydrate, dihydrate and trihydrate. Saito and co-workers, employing the ^{31}P CP/MAS technique, have demonstrated that the two steps of conformational changes, from monohydrate to dihydrate and from dihydrate to trihydrate forms of Na_2ATP crystals, can be sensitively detected by using NMR spectroscopy (Figure 20, left).

^{31}P–^{31}P POST-C7 correlation spectra (Figure 20A–C) of Na_2ATP hydrates were employed by Potrzebowski and co-workers for the analysis of the distances between phosphorus centres in crystal lattices.[52] The structural constraints were further used for the prediction of crystal network of the monohydrate for which the X-ray structure is unknown.

Glaubitz and co-workers[80] searching for the ATP-binding cassette (ABC)-transporters, which carry out their specific tasks by utilising energy released during ATP hydrolysis, showed that MAS NMR can be used to probe the kinetics of membrane proteins occurring on a time scale of minutes. It is possible to follow the course of all phosphorylated compounds of an ATP hydrolysis reaction directly and simultaneously with ^{31}P NMR. The ^{31}P SS NMR has also found application as a tool for the study of the complex of Ras (protein product of the human protooncongene H-ras (rat sarcoma)) with the GTP analogue GppCH2p (guanosine-5′-(β,γ-methyleno)triphosphate).[81]

The first reports showing ^{31}P NMR study of nucleic acids were published in the 1970s.[82] Terao et al. determined the size of the principal axis values of the ^{31}P CSA tensor for RNA molecules (polyU, polyG, polyC, polyA and tRNA). Very recently, Rinnenthal et al.[83] have reported the ^{31}P NMR data for RNA cUUCGg tetraloop model hairpin prepared under various salt and hydration conditions. The experimental results were found to be consistent with theoretical DFT calculations published by Sklenar and co-workers.[84]

The application of ^{31}P–^{19}F rotational echo double resonance (REDOR) measurements in structural studies of nucleic acids has been reviewed by Iuga et al.[13] In recent years, this methodology has been further developed.[85]

3.1.3. Phospholipids

Structurally, PLs are diacyl(alkyl) glycerol esterified to a polar head. According to the nature of the headgroup, they are divided into several classes, including phosphatidic acid (PA), phosphatidylcholine (PC), phosphatidylethanoloamine (PE), phosphatidylglycerol (PG), phosphatidylinositol (PI) and phosphatidylserine (PS). The amphiphilic character of PLs allows the formation of self-assembled structures in aqueous environments (the typical arrangement is bilayer). In some cases, PLs also act as intercellular messengers.

Since the headgroup of PLs contains phosphate derivatives, it is apparent that ^{31}P NMR became the method of choice in structural studies of this class of compounds. The NMR measurements provide information about the composition of PLs mixtures, phase of samples, their morphology and molecular dynamics.[86]

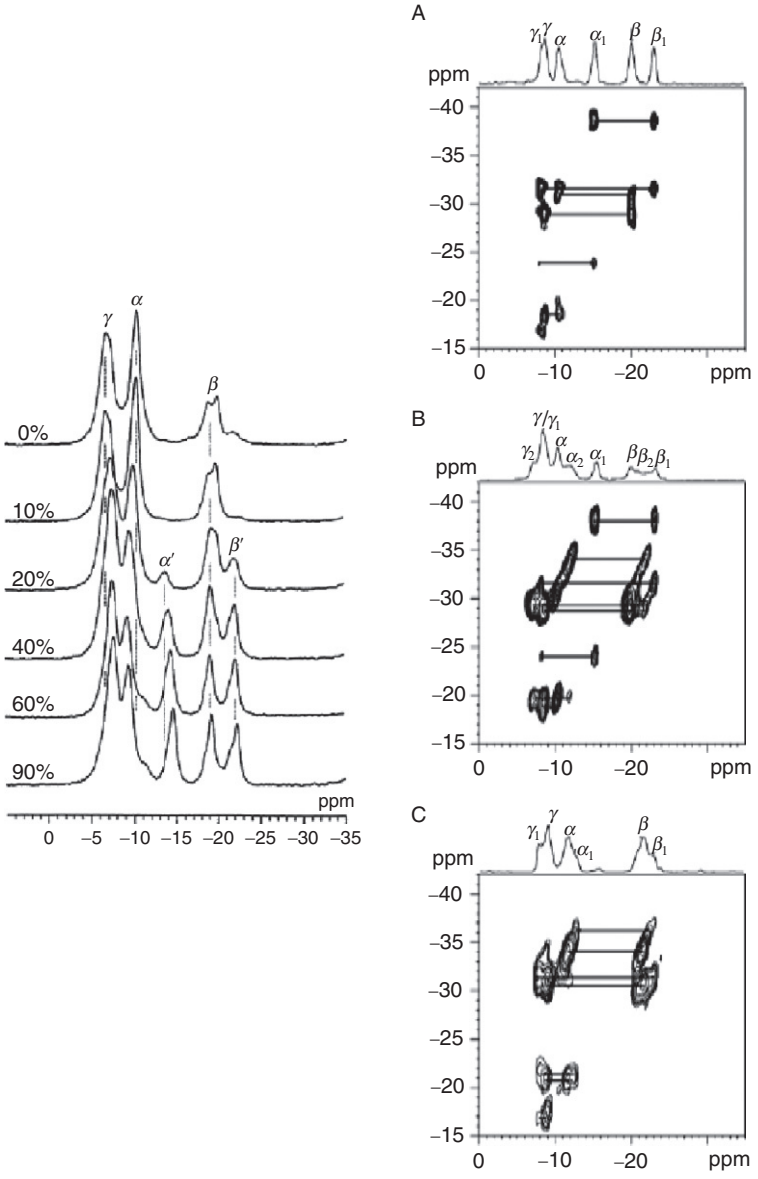

Figure 20 (Left) ^{31}P CP/MAS NMR spectra of Na_2ATP crystals in variety of relative humidities (given in percents) (taken from Ref. [78]). (Right) ^{31}P–^{31}P POST-C7 correlation spectra for disodium ATP hydrates recorded at 287 K (spinning rate 10 kHz, RF 70 kHz and excitation time (t_{ex}) 1.4 ms): (A) trihydrate, (B) dihydrate and (C) monohydrate. Taken from Ref. [52].

Two approaches are commonly used for NMR investigations of biological membranes and membrane-bound peptides: first, the measurement of static spectra of uniformly aligned samples; second measurement of the sample spun under MAS. The former method requires precise preparation and well-oriented samples in order to provide the high-resolution data. In the latter approach, individual species of PLs are randomly oriented in the rotor. The MAS technique is used for averaging the spin interactions (see Section 2.1). A method that combines both the above approaches (MAOSS) will be discussed in Section 3.1.3.2.

3.1.3.1. ^{31}P line shape analysis of static spectra For static measurement, a macroscopically oriented membrane of lipid bilayers is prepared between thin coverglass plates and brought into the magnetic field under a specific angle with respect to $\mathbf{B}_0$. In such preparations, all PL molecules experience the same polar angles with respect to the external magnetic field. Figure 21 shows effect of macroscopic orientation on the ^{31}P NMR spectra of PL membranes. In the multilamellar vesicles, the ^{31}P shielding tensor is axially symmetric (Figure 21A). If the

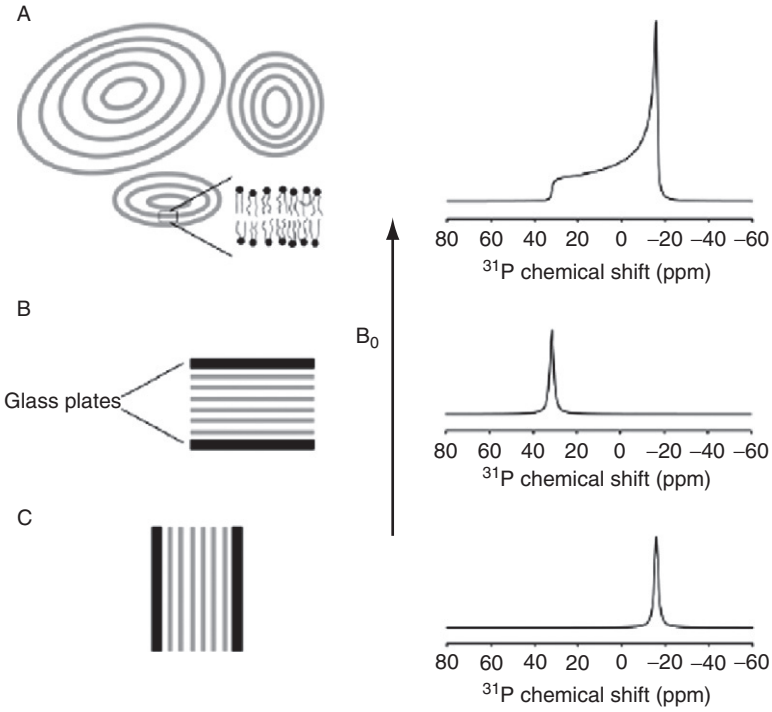

Figure 21 Effect of macroscopic orientation on ^{31}P NMR spectra of PL membranes. (A) Multilamellar PL vesicles yield ^{31}P NMR spectra that are characterised by an axially symmetric shielding tensor. If lamellar lipid membranes are oriented between glass plates, a single ^{31}P NMR signal is obtained for any given orientational angle between the membrane normal and the external magnetic field $\mathbf{B}_0$. ^{31}P NMR spectra for (B) perpendicular and (C) parallel orientations are shown. Taken from Ref. [86].

lamellar membrane is oriented with their normal perpendicular to the $\mathbf{B}_0$ field, a narrow ^{31}P NMR signal is observed at lowest field (Figure 21B). In contrast, if membrane is oriented parallel to the magnetic field, the ^{31}P NMR signal is observed at highest field (−15 ppm) (Figure 21C). Macroscopically oriented membranes are frequently used for structure determination of membrane proteins. SS NMR spectroscopy of mechanically oriented PLs bilayer/protein systems on glass plates can provide pertinent structural information on the protein embedded inside the membrane.[87–89]

The isotropic chemical shift allows distinguishing between different PLs species in a highly resolved ^{31}P NMR spectrum according to their headgroup structure. Anisotropic ^{31}P NMR spectra are indicative of the phase state of the lipid dispersions. The anisotropic part of the chemical shift allows measurement of the molecular orientation and reorientation of the lipid molecule or the headgroup segment. This is particularly applied to determine the morphology of self-assembled lipid phases.[90] As shown in Figure 22, ^{31}P line shape analysis is a simple test that allows distinguishing between a powdered sample, liposome and PLs bilayer.

Line shape analysis of the static ^{31}P NMR spectra and its corresponding CSA values have been successfully used to study the perturbation effect induced by proteins. ^{31}P data for PLs bilayers interacting with antimicrobial peptide (AMP): magainin-2, aurein-3,3, incorporated into structures of supramolecular lipid assemblies such as toroidal pores and thinned bilayers have been reported.[90] Various types of PL systems (1-palmitoyl-d_{31}-2-oleoyl-*sn*-glycero-3-phosphotidylcholine

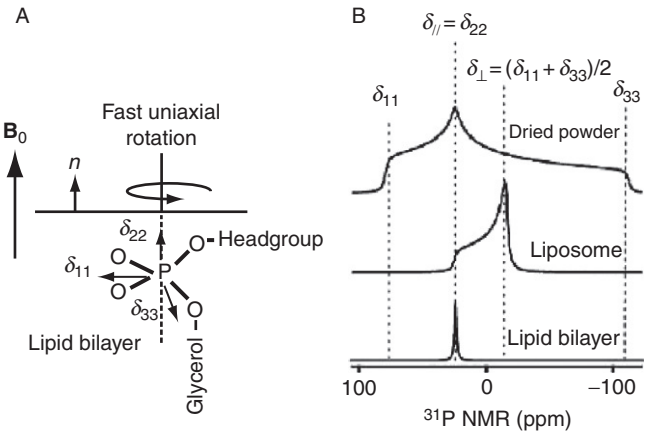

Figure 22 (A) Fast, uniaxial rotation of a phospholipid in a lipid bilayer around its chain axis, which is collinear to the intrinsic δ_{22} component of the ^{31}P CSA of the phosphate group, making motionally averaged, uniaxial ^{31}P CSA tensor components: $\delta_{11} = \delta_{22}$; $\delta = (\delta_n + \delta_{33})/2$. (B) The ^{31}P CSA powder pattern measured on dried powders (top row) decreasing into a motionally averaged, narrower CSA pattern for lipid distributed on a liposome (middle row) due to the fast uniaxial rotations of lipids. When the bilayer normal *n* of a lipid bilayer is collinear to the applied magnetic field, $\mathbf{B}_0$, phospholipids aligned in an oriented lipid bilayer provide a sharp line at the 0° position, which is identical to the δ_{11} direction (bottom row). Taken from Ref. [90].

(POPC-d_{31}), 1-palmitoyl-2-oleoyl-*sn*-glycero-3-phosphotidylglycerol (POPG), POPC-d_{31}/POPG1/POPC-d_{31}/cholesterol) have been investigated to understand the membrane distribution mechanism of peptides at various peptide-to-lipid (P:L) ratios. Interaction of cateslytin (AMP sample) with negatively charged lipids (1,2-dimyristoyl-*sn*-glycero-3-phosphoserine DMPS, DPMC) has been reported.[91]

^{31}P NMR was also used to study of the oriented membranes and pores induced by protegrin-1 (PG-1), which represents AMPs.[92,93] The line shape specifies the toroidal pores and thinned membranes that are formed in membrane bilayers by the binding of AMPs. The lateral diffusion of lipids were analysed from the motionally averaged 2D ^{31}P SS NMR spectra. The mechanism of pore formation due to interaction between the peptide (fallaxidin) with lipids has been investigated.[94]

^{31}P line shape analysis was used to study the interaction of glycoprotein saposin C with negatively charged 1-palmitoyl-2-oleoyl-*sn*-glycero-3-[phospho-L-serine] (POPS) or neutral POPC.[95,96] The destabilisation ability of saposin C to the membrane surface is thought to promote the insertion of the lysosomal enzymes into the bilayer and indicated that saposin C interacts with negatively charged PL membranes under acidic conditions. ^{31}P line shape and CSA width data indicate that the PLs headgroups were perturbed by the insertion of saposin C into only the negatively charged POPS bilayer and not into the neutral POPC lipid. Nomura et al.[97] described the interaction of lipopolysaccharide (which constitutes the outermost layer of Gram-negative bacteria cell) and PLs in mixed membranes studied by means of ^{31}P SS NMR spectroscopy.

Fish antifreeze proteins and glycoproteins (AF(G)Ps) (protecting mammalian cells and tissues from hypothermic damage in sub-zero temperatures) embedded into PL (1,2-dimyristroyl-d_{54}-*sn*-glycero-3-phosphocholine DMPC-d_{54}/DMPC) membranes were investigated by Garner et al.[98] The ^{31}P SS NMR was used for checking the interaction of the 37-residue α-helical type 1 AFP, TTTT and the low molecular weight fraction glycoprotein AFGP8 (Figure 23).

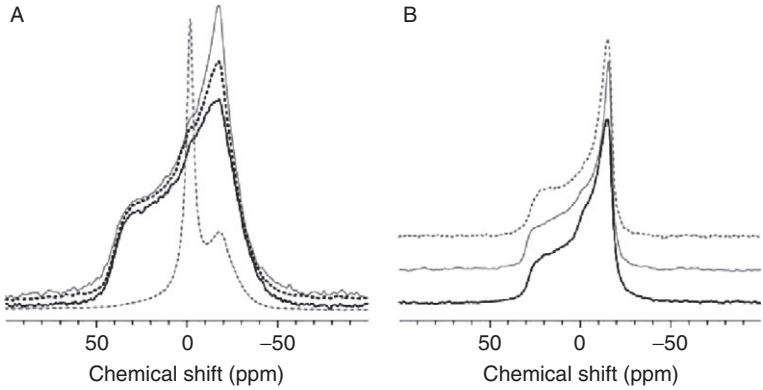

Figure 23 ^{31}P SS NMR spectra of DMPC-d_{54}/DMPC (1:1) bilayers: (A) at 5 °C control (black solid), with AFGP8 (grey solid), TTTT (grey dash) and TTTT after heating to 30 °C and re-cooling to 5 °C (black dash); (B) at 30 °C control (black solid), with AFGP8 (grey solid) and TTTT (grey dash). Taken from Ref. [98].

Tiburu et al.[99] investigated the influence of hCB_1 and hCB_2, G-protein-coupled receptors, on the dynamics of lipid headgroups and lipid acyl chains of the POPC bilayer. The authors described the reduction of the CSA width of ^{31}P spectra in the lipid headgroups, which shows the local motions of this part. These disruptions result from the impact of hCB_1 and hCB_2 peptides which can be either localised on the membrane surface or incorporated in hydrophobic core and leaves this lipid bilayer.

Cloutier and others[100] described the effect of the antibacterial endolysin dp144, on the different membrane lipids. The presence or absence of peptide in DMPC gives typical ^{31}P spectra of lipids in a lamellar phase, with small spectral broadening caused by interactions between the peptide and neutral lipid headgroups. Unlike the appearance of isotropic signals in DMPG and DMPC/DMPG membrane indicates the formation of lipid cubic structures due to interactions with peptide dp144. This confirms the conclusions about the impact of peptides on anionic lipid conformations. The static ^{31}P NMR spectra are shown in the Figure 24.

The processes occurring within lipid membranes are very often pH-dependent and can be measured via ^{31}P SS NMR. Chu et al.[101] investigated the influence of sorbic acid on the DMPC membrane and compared the effects of the longer chain decanoic acid in different acid concentrations (pH). The line shape of the spectra was found to be typical for lipids in the lamellar phase. CSA values were obtained for different pH values and various amounts of peptide. The linewidth broadening after addition of sorbic or decanoic acids suggested a small impact on the dynamics of lipid headgroups (Figure 25).

^{31}P NMR study of the interaction of nucleotide derivatives with membranes was reported by Bunge et al.[102] The authors have used oligonucleotides that are modified by covalent attachment of the cholesterol analogue cholesteryl tri(ethylene glycol) (cholesteryl-TEG) and spontaneously incorporate into lipid membranes. The influence of cholesteryl-TEG on the lipid membrane compared to that of cholesterol within bilayer structure is shown in Figure 26.

Results for membrane-associated cholesteryl-TEG–DNA complexes are similar; however, a different linewidth of the spectrum was noticed (Figure 27). Partly double-stranded DNA is characterised by the dynamics of the free part (narrow line of the isotropic signal) and stability of the chain (broadening on the bottom of isotropic signal) at the same time. However, full double-stranded DNA provides rigidity of whole nucleotide chain, which is reflected in the increase in width of the isotropic signal.

^{31}P SS NMR was found to be useful to demonstrate the relationships between peptides, lipid membranes and metal ions.[103,104] Such methodology is developed with intention to understand the mechanism of Alzheimer's disease. Disruption of the membrane structure by β-amyloid in the presence of metal ions suggests the crucial role of such cations as Zn^{2+} and Cu^{2+}. Metal ions alone have a different impact on the lipid membrane. Zinc induces weak motions on the lipid headgroups, which results in a slight decrease in ^{31}P CSA. Adding the paramagnetic copper ions can cause total disruption of the lipid membrane to form smaller

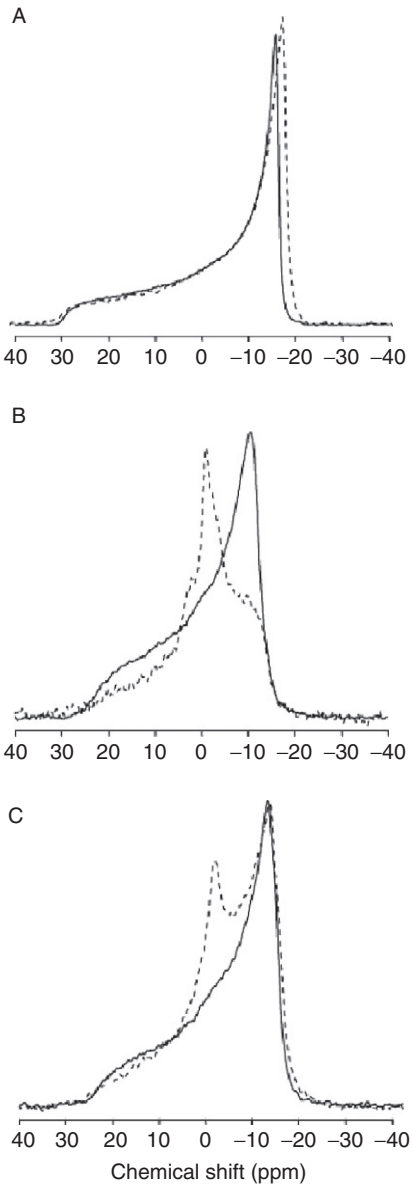

Figure 24 ^{31}P static NMR, spectra of the different lipid system in the absence (solid) and presence (dotted) of gp144 at lipid-to-protein molar ratio of 100:1 at 37 °C: (A) DMPC; (B) DMPG and (C) DMPC:DMPG 1:1at 37 °C. Taken from Ref. [100].

vesicles. These rapidly tumbling structures average the phosphorus anisotropy into an isotropic signal. In case of β-amyloid peptide, the interactions are different for membranes with associated or incorporated peptide. The disturbing role of Cu^{2+} on the bilayer structure was limited in the presence of the membrane-associated peptide, which can be explained by the strong affinity of copper ions

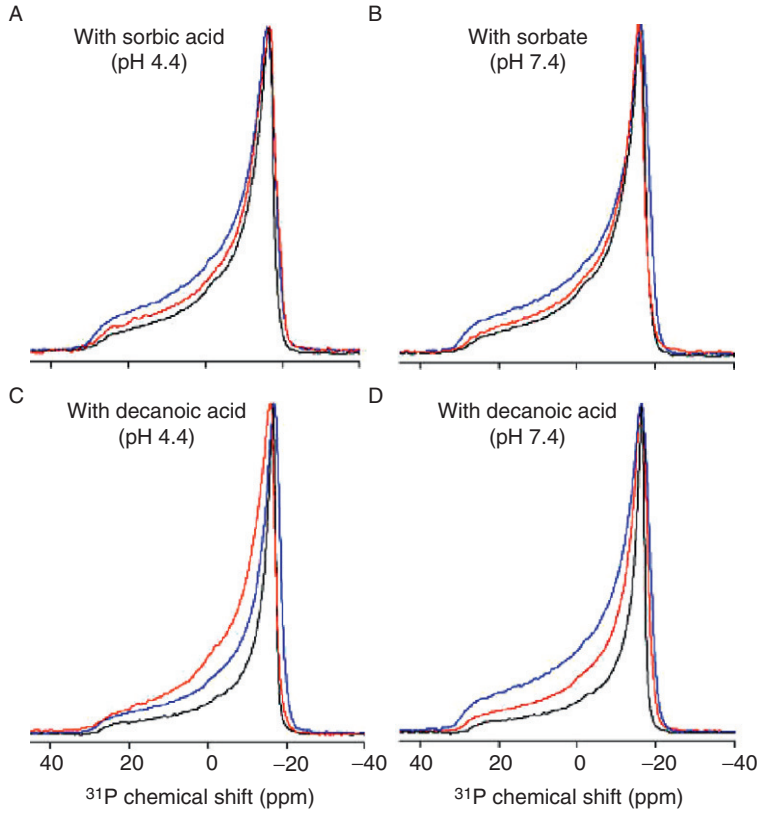

Figure 25 ^{1}H-decoupled ^{31}P NMR powder spectra of DMPC MLV samples as a function of concentration and pH: with sorbic acid at (A) pH 4.4 and (B) 7.4; with decanoic acid at (C) pH 4.4 and (D) 7.4, obtained using a Hahn-echo pulse sequence under static condition at 35 °C. The concentrations of the weak acids are 0 (in black), 5 (in light grey) and 10 (in grey) mol %, respectively. Taken from Ref. [101].

for histidine residues of β-amyloid. However this metal-bound form of the peptide may induce stronger lipid headgroup motions than the peptide alone (the broadening of the ^{31}P spectra). Incorporation of β-amyloid into the lipid bilayer destabilises the membrane structure (formation of isotropic signal) even without the presence of metal ions. Addition of Zn^{2} or Cu^{2+} has no further disrupting effects on the membrane integrity. The impact of β-amyloid peptide on the biological membrane was also considered by Nakazawa et al.[105] and Antharam et al.[106]

Paramagnetic relaxation enhancement (PRE) approach was introduced for identifying the asymmetric insertion depths of membrane proteins in lipid bilayers.[107] By applying Mn^{2+} ions on the outer but not the inner leaflet of lipid bilayers, the sidedness of protein residues in the lipid bilayer was determined. Protein-free lipid membranes with one-side Mn^{2+} bound surfaces exhibit

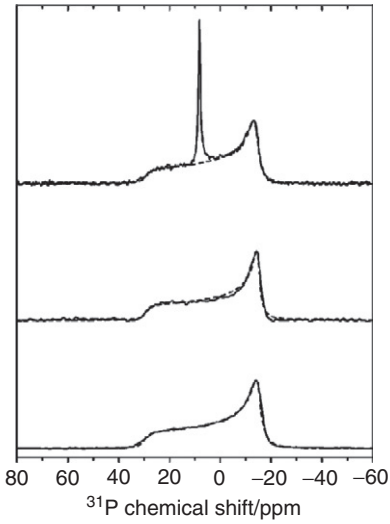

Figure 26 Proton-decoupled 242.9-MHz ^{31}P NMR spectra of POPC bilayers in the absence and in the presence of cholesteryl–TEG or cholesterol, respectively. The spectra shown refer to 4/1 POPC/cholesteryl–TEG (top), 4/1 POPC/Chol (middle), and pure POPC membranes (bottom) recorded at 303 K, at a water content of 40 wt%. The dashed lines indicate the simulated ^{31}P NMR spectra of POPC used to fit the experimental line shape. Taken from Ref. [102].

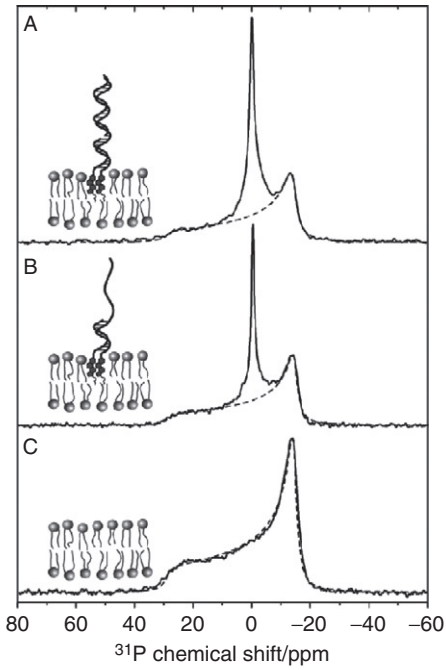

Figure 27 Proton-decoupled 242.9-MHz ^{31}P NMR spectra of POPC bilayers in the presence of (A) O1/O2/O3 and (B) O1/O2 and (C) for pure POPC membranes recorded at 303 K, at a molar ratio of oligonucleotides to phospholipids of 1/130 and 80 wt% buffer solution (100 mM NaCl, 10 mM Tris, pH 7.4). The dashed lines show the simulated ^{31}P NMR spectra of POPC used to fit the experimental line shape. Taken from Ref. [102].

significant residual ^{31}P intensities. In contrast, for two-side Mn^{2+} bound membranes, the ^{31}P signals are mostly suppressed. By applying this method at low peptide concentration, the penetration is distributed in both leaflets of the bilayer. All PRE experiments were carried out above the phase transition temperature of lipids (1,2-dimyristoyl-*sn*-glycero-3-phosphatidylglycerol DMPG, POPC, POPG, DMPC). Static ^{31}P DP experiments on oriented membrane samples were prepared with the glass plate inserted into the magnet with the alignment axis parallel to the magnetic field. Figure 28 shows the ^{31}P spectra of lipid membranes showing the effect of penetration on membrane disorder and of Mn^{2+} on ^{31}P intensity.

Other applications of ^{31}P line shape analysis, including study of cisplatin interaction with the PS headgroup,[109] description coating of polyelectrolyte particles

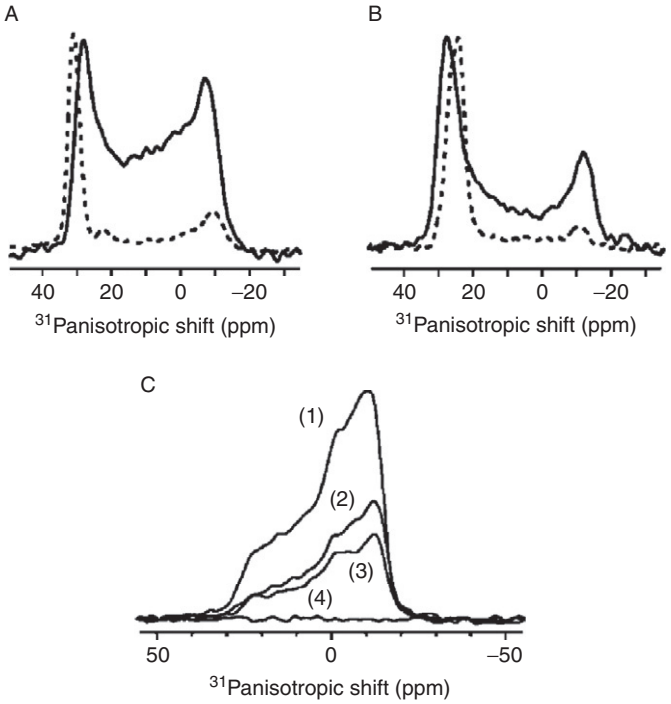

Figure 28 Static ^{31}P spectra of lipid membranes showing the effect of penetration on membrane disorder and of Mn^{2+} on ^{31}P intensity: (A) Oriented ^{31}P spectra POPC/POPG (8:7) bilayer without (dashed line) and with 4 mol% penetration (solid line); (B) oriented ^{31}P spectra of POPC/cholesterol (55:45) bilayer without (dash line) and with 4 mol% penetration (solid line). The lipid membranes are oriented on thin glass plates. Note the absence of any isotropic peak. (C) ^{31}P powder spectra of penetration-containing POPC/POPG (8:7) membrane before and after the addition of Mn^{2+}. Compared to the full control spectrum without Mn^{2+} (1), 15 min after addition of Mn^{2+} a roughly two-fold intensity reduction is seen (2). Three days after Mn^{2+} addition, the ^{31}P intensity is largely retained (3), indicating that radio frequency pulses do not cause Mn^{2+} scrambling. After freeze-thawing, the membrane the ^{31}P intensity was completely suppressed by the strong PRE effect (4). Taken from Ref. [108].

by lipid membranes[108] and interaction between the antibacterial peptide cupiennin (isolated from the spider venom) and the PL bilayer,[110] have been published recently.

3.1.3.2. Application of MAS techniques The theoretical background of MAS techniques, which allow averaging and/or removal of undesired spin interactions and amplify the resonance signals, was briefly discussed in Section 2.1. The power of different MAS experiments was already presented. Glaubitz and Watts introduced a unique technique for the study of PLs that combines the achievements of NMR of oriented samples and MAS.[111] The MAOSS (magic angle oriented sample spinning) methodology has found a number of applications in structural studies of PLs.

In MAOSS, the PLs are uniformly aligned on a thin glass disc which is next settled on the rotor probe (Figure 29). The sample may be used as powder or adsorbed on a polymer sheet (Figure 30).

Two model peptides—alamethicin which is α-helix peptaibol-transmembrane antimicrobial peptide (AMP) and synthetic α-helix alanine-rich peptide ($K_3A_{18}K_3$)—inserted into 1,2-dimyristoyl-*sn*-glycero-3-phosphatidylcholine (DMPC) bilayers[112] were investigated employing the MAOSS strategy. The effect of peptide insertion on the lipid organisation suggests different behaviours between the two transmembrane peptides: strong interactions for alamethicin (disorganised, supported bilayer) and weak interaction for $K_3A_{18}K_3$ peptide not disrupted the hydrophobic part of the DMPC bilayer. The membrane can be parallel to the rotor axis or can be in the perpendicular orientation to the rotor axis (Figure 31). However, the first option is more advantageous because of the better sample filling factor and the mechanical spinning properties achieved. The MAOSS technique provides the maintenance of all static, anisotropic effects (such

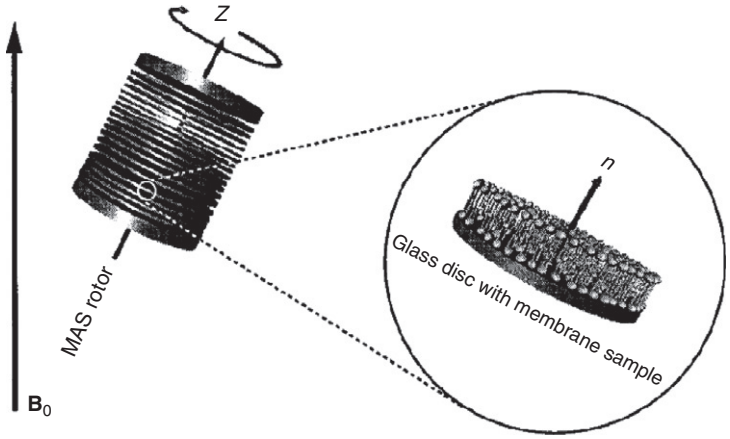

Figure 29 Rotor design for MAOSS: A standard 7-mm Bruker MAS rotor contains a stack of thin glass plates with uniformly aligned phospholipid membranes. The membrane normal *n* is parallel to the rotor axis *z*, which is tilted with respect to $\mathbf{B}_0$ by the magic angle 54.7°. Taken from Ref. [111].

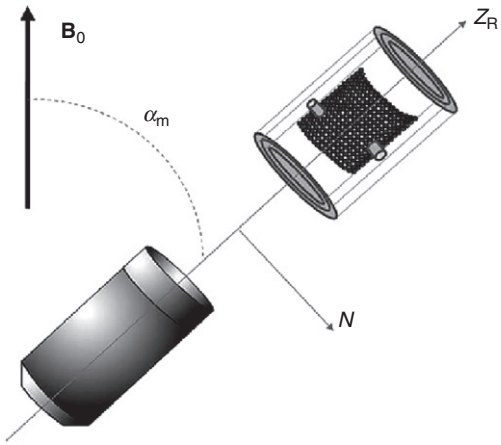

Figure 30 Illustration of the MAOSS strategy with peptide in phospholipid bilayers adsorbed on a polymer sheet (PET). $\mathbf{B}_0$, the magnetic field; α_m is the magic angle (54.74°); *N*, the normal of the bilayer; and Z_R, the rotor axis. Taken from Ref. [112].

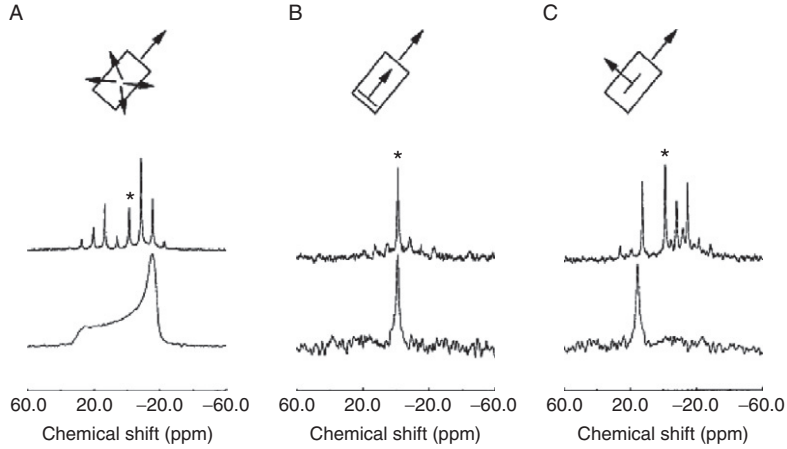

Figure 31 ^{31}P spectra of DMPC at 318 K with different orientational distributions. All MAS spectra were recorded at 1000 Hz MAS rotation. Static and MAS spectra of (A) DMPC with a random orientational distribution ("powder") and (B) static and MAS spectra of DMPC with the membrane normal parallel and (C) perpendicular to the rotor axis. Two thousand forty-eight scans were acquired with a recycle delay of 2 s. The chemical shift is scaled with respect to phosphoric acid. Taken from Ref. [111].

as CSA, dipolar couplings or quadrupolar splitting) in the high-resolution MAS conditions with a low spinning rate, simultaneously. That is why it has been commonly used to investigate the PL orientation and peptides membrane insertion in many studies.[113–116]

Very often, MAOSS and MAS are considered complementary techniques for the study of PL systems. A number of applications of ^{31}P MAS, including the

study of the interaction of the dipeptide β-Ala-Tyr and the amino acid Glu with PL bilayer,[117] antimicrobial peptide (AMPs)[118] and antibacterial peptides, has been published recently [100] (Figure 32).

The crucial matter in the study of biological membranes is the investigation of the interactions between water and PLs. ^{1}H–^{31}P 2D experiment was employed to

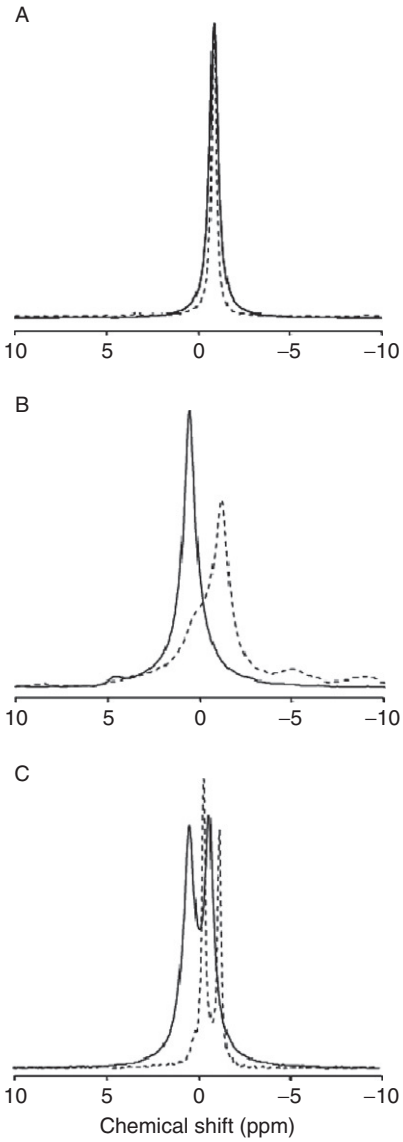

Figure 32 ^{31}P MAS NMR spectra of the different lipid system in the absence (solid) and presence (dotted) of antibacterial peptide gp144 at a lipid-to-protein molar ratio of 100:1 at 37 °C: (A) DMPC, (B) DMPG and (C) DMPC:DMPG 1:1at 37 °C. Taken from Ref. [100].

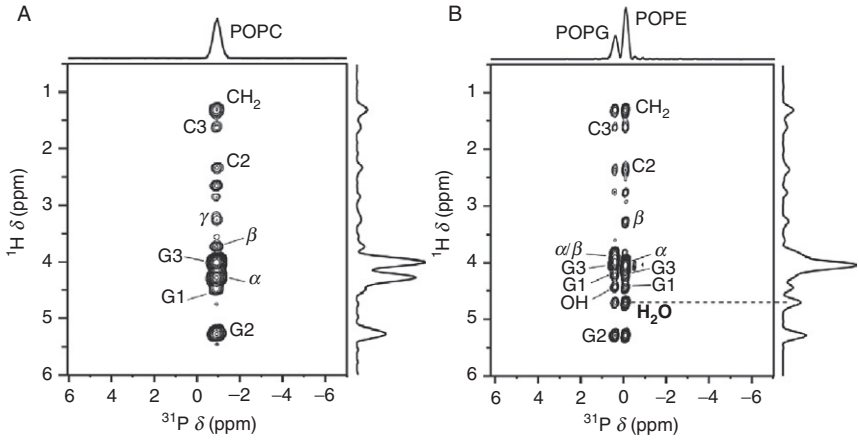

Figure 33 Representative 2D ^{1}H–^{31}P correlation spectra of hydrated lipid membranes with a mixing time of 64 ms. (A) POPC and (B) POPE/POPG (3:2) membrane. ^{1}H peak assignment is indicated. POPC lacks a water–^{31}P cross peak. Extending the mixing time to 225 ms still yields no water cross peak. Spectra were measured under 4.0 kHz MAS. Taken from Ref. [119].

define the dynamics and alignment of water within the structure made by PLs.[119] The intensity of the cross-peaks between ^{1}H and ^{31}P strongly depends on the proton dipolar couplings, which is related to the water dynamics (Figure 33). The lipid–water interactions and the impact of cholesterol on the freezing temperature of water in the bilayers were reported by Ramamoorthy and colleagues.[120]

The application of 2D proton-evolved separated-local-field experiment to measure ^{1}H–^{31}P and ^{13}C–^{31}P dipolar coupling was reported by Dvinskikh et al.[121] These authors used 2D experiments for the analysis of 3.5:1 DMPC: DHPC bicelles with or without the antimicrobial peptide plexiganan. Figure 34 shows the ^{1}H–^{31}P and ^{13}C–^{31}P dipolar interactions. The dipolar splitting for the ^{13}C resonances is displayed in form of tilted doublets. The decrease in splitting after adding the peptide is related to the changes in distances in the headgroup region around phosphorus.

The REDOR experiment, presented in previous sections, has found a number of applications in investigating membrane–peptide interactions. The pore formed by cationic membrane peptides and insertion of phosphate-mediated arginine into lipid membranes were studied using a selective REDOR experiment.[122] The ^{13}C–^{31}P REDOR distance data indicated that residues in prostaglandin (PG) are far from the ^{31}P atoms. The distances are 4.0–6.5 Å in the POPE/POPG membrane and 6.5–8.0 Å in the POPC membrane. The toroidal pore model is strongly supported also by static ^{31}P line shapes of POPC/POPG membrane in the presence of PG-1 (Figure 35).

Arginine (Arg_{10}) and lysine (Lys_{13}) belong to the group of cell-penetrating peptides (CPPs). CPPs are small cationic peptides that cross the cell membrane while carrying macromolecular cargo; therefore they are promising drug-delivery molecules. Low-temperature ^{13}C–^{31}P distances between the peptide and the lipid

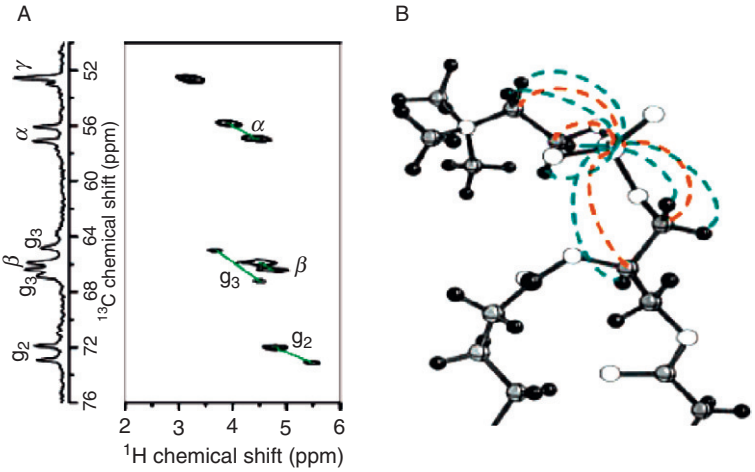

Figure 34 (A) 2D correlation of ^{13}C chemical shift and ^{13}C–^{31}P dipolar coupling (*y*-axis) with the ^{1}H chemical shift and ^{1}H–^{31}P dipolar coupling (*x*-axis) of 3.5:1 DMPC:DHPC bicelles (left). The ^{1}H–^{31}P dipolar split peaks of *R*, α, β and γ are connected by a solid line. (B) The measured ^{1}H–^{31}P (dark dotted line) and ^{13}C–^{31}P (grey dotted line) dipolar couplings in DMPC lipid molecule are highlighted. Taken from Ref. [121].

phosphates indicated that both the $Arg_{10}C\zeta$ and $Lys_{13}C\epsilon$ were close to the lipid headgroup (4.0–4.2 Å), providing the existence of a charge–charge interaction in the gel-phase membrane (the lysine–phosphate interaction is much weaker than arginine).[124] Frequency-selective REDOR experiments were used to measure the distance between peptide ^{13}C and lipid ^{31}P.

^{31}P SS NMR data of 14-mer amphipathic peptide (composed of leucines and phenylalanines modified by crown ethers) embedded into membranes were reported by Ouellet et al.[125] The preliminary study indicated that the 14-mer peptide remains at the surface of bilayers and perturbs the lipid orientation relative to the magnetic field. ^{15}N–^{31}P REDOR experiments have also been used to measure the intermolecular dipole–dipole interaction between the 14-mer peptide and the PL headgroup and polar region of DMPC MLVs. The results strongly suggest that the 14-mer peptide destabilises the lipid bilayer via the induction of a positive curvature strain.

Ramamoorthy and co-workers[126] have recently reported proton-detected local field (PDLF) sequence to define the structure and dynamics of biological membranes. As was shown for this kind of laboratory-frame separated-local-field experiment, simple modification in the 2D PDLF sequence enables the measurement of remote ^{13}C–^{31}P and ^{1}H–^{31}P couplings in magnetically aligned bicelles.

3.1.4. Biominerals (bones and teeth)

Bones and teeth are highly organised structures composed of an organic matrix (mainly collagen type I) and the inorganic mineral phase of nanocrystals (mostly built with calcium hydroxyapatite (HAp) $[Ca_{10}(PO_4)_6(OH)_2]$. Many aspects including bone mineral formation, organisation and distribution of mineral

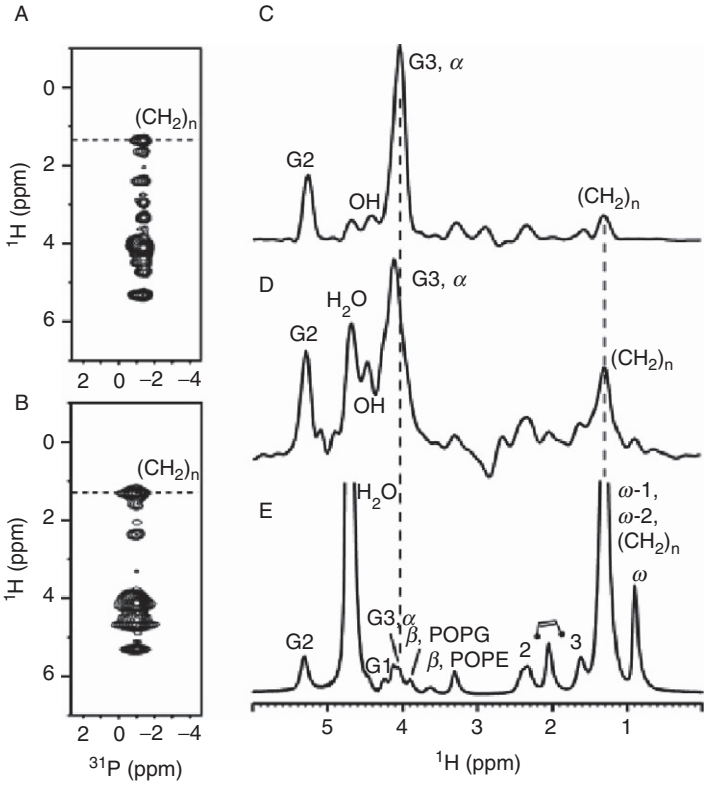

Figure 35 ^{31}P–^{1}H correlation spectra of hydrated POPE/POPG membranes with and without PG after a ^{1}H spin diffusion mixing time of 64 ms. (A, B) 2D spectra of POPE/POPG bilayers without and with PG, respectively.^{1}H cross-sections are shown in (C) for the peptide-free membrane and (D) for the peptide-bound membrane. (E) Direct excitation ^{1}H spectrum of the POPE/POPG membrane for comparison. Assignment is obtained from ^{13}C to ^{1}H 2D correlation. The $(CH_2)_n$ cross-peak in (D) is much higher than that in (C). The low H_2O cross-peak in (C) is attributed to strong hydrogen bonding between the lipid headgroups and water, which immobilises water and prevents their detection by the ^{1}H T_2 filter. PG likely disrupts some of the lipid–water hydrogen bonds, increasing the H_2O peak intensity in (D). Taken from Ref. [122].

crystals within the collagen matrix are still very challenging. Study of calcified tissues such as bones and teeth are important fields of interest for developing biomaterials engineering. It is well known that living organisms produce apatite solids with different crystallite sizes, different degrees of atomic order/disorder and different degrees of hydroxylation. SS NMR spectroscopy as a technique, which is able to follow the above-mentioned very subtle structural nuances, has found a number of applications in the study of titled biominerals.[127] The state of the art of ^{31}P SS NMR upto 2007 in structural studies of bones and teeth was briefly reported by Iuga et al.[13]

During last few years, many papers regarding the improvement of NMR methodology have been published.[128] Recently, Kaflak and Kolodziejski[129]

utilised inverse $^{31}P \rightarrow {}^{1}H$ CP, which eliminated the unwanted signals from water and collagen protons of the organic matrix and facilitated the interpretation of the results. Using this approach, the authors characterised the human bone apatite in comparison with two forms of synthetic hydroxyapatite. Significant differences between the investigated samples were established. It is worth noting that, since the application of the MAS technique may affect the CP kinetics (e.g. $^{31}P \rightarrow {}^{1}H$ magnetisation transfer, proton spin diffusion or proton $T_{1\rho}$), all measurements were made in the static condition. Developing the methodology of SS NMR in searching for the biominerals, Tseng et al.[69] described the influence of the spinning frequency and proton decoupling on the quality of the ^{31}P SS NMR spectra. Moreover, Tseng et al.[130] proposed the use of ^{31}P–^{1}H (FSLG) sequence incorporated into HETCOR. This new scheme was utilised to study the formation of hydroxyapatite in presence of glutaric acid in comparison to aspartic acid.

Few groups have dealt with the problem of ageing of bones and teeth. It is known that with time many physical and chemical properties of bones and teeth mineral components undergo different changes. Kuhn et al.[131] employed ^{31}P SS NMR to study the HPO_4 groups of young and old cancellous and cortical bovine bones. From these data, it was apparent that calcium phosphate in the form of carbonated apatite is the only bone mineral component.

Teeth contain nearly the same components as bones, and hence the same SS ^{31}P NMR methodology can be applied. Tseng et al.[132] have used different NMR techniques to study the changes in the chemical composition of teeth of different ages. ^{31}P SS NMR data were employed to quantify of phosphorus species in different environments and to define changes in rat incisor over its life span. The authors suggested that $HO–H\cdots O–PO_3^{3-}$ interactions are an important factor in the process of dentin growth. This idea was confirmed by Huang et al.[128]

The biomineralisation and its molecular mechanism are the most intriguing processes occurring within the hard tissue of vertebrates. It is found that such arrangement of the crystallites may be related to organic–inorganic interactions in the bone material. Pourpoint et al.[133] applied ^{31}P SS NMR for the investigation of the structure of bone tissue replacement materials, for example calcium phosphates: β- and γ-$Ca(PO_3)_2$, which are used in tissue repair and regenerative applications in the biomedical field.[134,135] Shaw et al.,[136] with the help of dipolar recoupling techniques (both ^{13}C–^{31}P and ^{15}N–^{31}P REDOR), examined the structure and orientation of the C-terminal region of amelogenin, which is thought to be a protein controlling the biomineralisation process of the enamel.

Duer et al.[137] used ^{31}P NMR techniques to define the interactions between the organic matrix, mineral crystals and inorganic species lying on the mineral surface, in the mineralised articular cartilage in comparison with the bone structure. Additionally, ^{13}C–^{31}P REDOR experiment indicated glycosaminoglycans and γ-carboxyglutamic acid as the only organic components interacting with the mineral surface in the calcified articular cartilage. Barheine et al.[138] described in detail the investigation of borate incorporation in apatitic biomaterials. To define the interactions between HAp and BCaP, they utilised different SS NMR techniques including simple $^{1}H \rightarrow {}^{31}P$ CP, triple resonance ^{11}B–^{31}P CP, edited ^{31}P NMR, ^{31}P REDOR together with ^{11}B–^{31}P CP/MAS and ^{11}B–^{31}P HETCOR measurements. The

matter of artificial bone implants and formation of the extracellular bone matrix as well as the possibilities of ^{31}P SS NMR techniques were demonstrated in the work of Schulz et al.[139]

^{31}P SS NMR was found to be a very useful tool to investigate the impact of some drugs on the bones structure. This problem is very important in the treatment of osteoporosis. Mukherjee et al.[123] carried out studies on the binding of bisphosphonate drugs to the human bone. From the double CP experiment (^{1}H → ^{13}C → ^{31}P) of [^{13}C, ^{15}N] pamidronate, it was apparent that the binding of bisphosphonates to bone occurs in a rigid or an irrotational manner (Figure 36).

Roussiere et al.[140] used ^{31}P MAS NMR and ^{31}P–^{1}H CP methods in investigating zoledronate with β-tricalcium phosphate (TCP) for the design of potential drug device combine systems. Andersson et al.[141] investigated a new bifunctional material that can be used as both drug carrier matrix and osteoconductive material. To characterise it, the authors implemented a wide range of SS NMR techniques, including ^{31}P MAS and ^{23}Na–^{31}P TRAPDOR experiments.

Another important problem that has received a great deal of attention is the fixation between the implants, for example made of the apatite, and the surrounding tissues. Haque et al.[142] studied synthetic HAp as a nano-biocomposite by chemical coupling with a polymer matrix. Similar investigations were presented by Jena et al.[143] In the cited work, the problem of different microstructures of HAp depending on the method of synthesis was studied by means of ^{31}P MAS NMR. The dispersion of silicate in tricalcium phosphate, a resorbable biceramic for bone replacement, was investigated by Rawal et al.[144] by employing various SS NMR

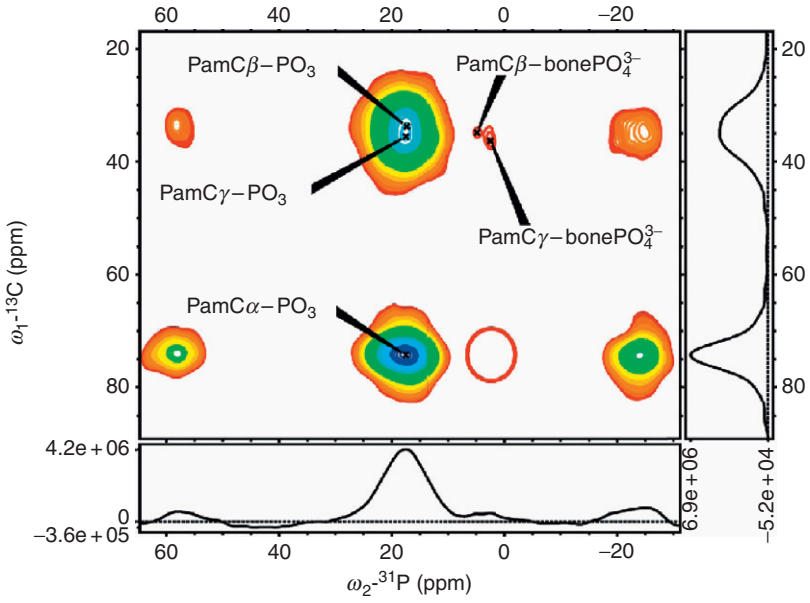

Figure 36 Double cross-polarisation spectrum (^{1}H → ^{13}C → ^{31}P) of [^{13}C, ^{15}N] pamidronate on human bone. Taken form Ref. [123].

methods, mainly ^{29}Si–^{31}P REDOR. Ndao et al.[145] carried out a ^{13}C–^{31}P REDOR SS NMR investigation to establish the distances between the carboxyl C atoms in glutamic acid side chains in statherin and phosphorus atoms located in the HAp crystal surface.

3.2. ^{31}P SS NMR in material science

SS NMR is one of the powerful physical methods widely applied in materials science.[14,146] This method is particularly successful even for highly amorphous molecular systems. The various SS MAS NMR techniques can show important structural details that are often unobtainable by other physical methods.

3.2.1. Phosphate glasses and ceramics

Phosphate-based and phosphate-containing glasses belong to the non-crystalline group of materials that are of increasing interest in basic and applied science. They have a wide range of applications including as optical fibres and waveguide devices,[147] sealing materials and low-melting solders[148] and biomaterials.[149] This great interest is due to their attractive chemical and physical properties, which can be easily modified and diversified, for example by doping with a small amount of rare-earth elements, which gives great possibilities for modifying the properties of the glasses.

3.2.1.1. Notation used for phosphate glasses classification Classification of the phosphate-based glasses depends on both the kind and the number of modifier (s) used. Usually, both types of classifications are mixed. Taking into consideration the number of network modifiers, glasses can be classified as binary (e.g. lithium-, sodium-, cesium-, and boron-phosphate glasses), ternary (e.g. Al_2O–P_2O_5–SiO_2, P_2O_5–B_2O_3–Na_2O) or higher (e.g. (Na_2O)–CaO–SiO_2–P_2O_5) order glass systems.

The structure of phosphate glasses can be sketched as a number of PO_4 groups—named Q units—linked by bridging oxygens (BOs) to form various phosphate anions. Surrounding of the Q units can be described on the basis of Q^n speciation, where n ($0 \leq n \leq 3$) indicates the number of BO atoms per tetrahedron, to distinguish between groups with different degrees of connectivity to other phosphate units. For more complex systems, Q^n speciation is extended to the Q^n_{mX} notation, where m denotes the number of next nearest X atom neighbours. According to this convention, vitreous P_2O_5 composed exclusively of cross-linking tetrahedra is classified as Q^3 group. The incorporation of the network modifier, for example alkali or alkaline-earth oxides, causes the depolymerisation of the glass network and the formation of Q^2, Q^1 and Q^0 units, which is achieved through the inclusion of network-modifying cations (Na^+, Ca^{2+}, Cd^{2+}, etc.).

Each type of Q^n unit displays different NMR properties (e.g. isotropic chemical shift value, CSA) and therefore can be resolved, distinguished and analysed by ^{31}P NMR spectroscopy. ^{31}P NMR spectra of the modified glasses show a decreasing number of Q^3 units with simultaneously increasing number of Q^2 sites. When the amount of modifier increases, Q^1 units appear and are formed in increasing amount.

3.2.1.2. Applications of ^{31}P 1D MAS NMR techniques 1D MAS NMR spectroscopy is the method of choice allowing the understanding of the local structure and site distribution of phosphorus and/or other atoms in the sample. Employing the deconvolution of overlapped ^{31}P signals, different Q^n units can be estimated and unambiguously assigned. The applicability of this approach was demonstrated by Carta et al.[150] in a structural study of a series of ternary glasses in the system $40(P_2O_5)$–$x(B_2O_3)$–$(60-x)(Na_2O)$, where the P_2O_5 content was kept constant at 40 mol% and x was varied between 10 and 30 mol%.

Relatively large differences were observed on the ^{31}P spectra of the investigated compounds (see Figure 37). On the basis of line shape analysis, it was possible to distinguish among the various PO_4 units (P^1_{0B}, P^2_{1B}, P^2_{0B}, P^3_{2B} and P^3_{1B}) represented differently from different types of phosphorus tetrahedra. In

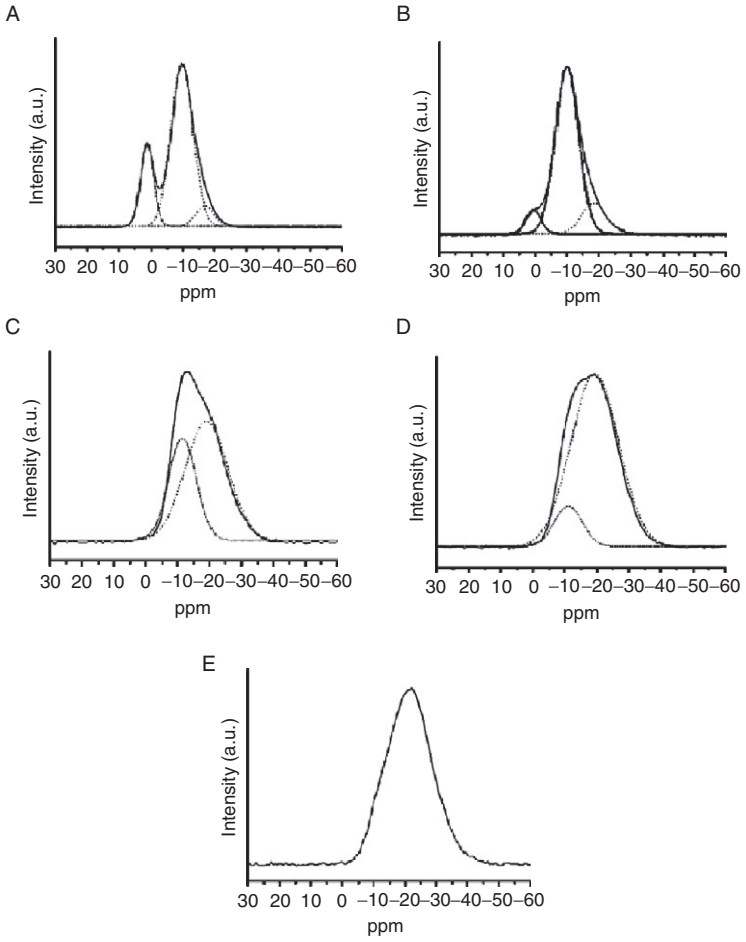

Figure 37 ^{31}P NMR, spectra of (A) P40B10Na50; (B) P40B15Na45; (C) P40B20Na40; (D) P40B25Na35 and (E) P40B30Na30. See Ref. [150] for details. Taken from Ref. [150].

addition, the influence of the boron content on the ^{31}P chemical shift was established. From the analysis of the ^{31}P NMR (and ^{11}B NMR) data, it was concluded that cross linking between phosphate and borate network is present even at the lowest content of B_2O_3 and increases with boron oxide content. It is worthy of note that in the P40B30Na30 glass, Q^3 units alone are present (P^3_{2B} and P^3_{1B} phosphorus atoms). The absence of a resonance at about -30 ppm, typical of BPO_4 units, indicates the absence of $P(OB)_4$ groups.

A similar methodology was employed for the investigation of aged samples of the glasses.[151] During ageing, the peaks become more negative with increasing B_2O_3 content. However, in comparison with fresh samples, the intensities of the peaks with the less negative chemical shift increase. This indicates the breakdown of the structure during storage in air. The degradation of the structure is associated with the attack from moisture. Therefore, the higher the boron oxide content, the more substantial the decrease in the chemical stability with respect to ageing. Moreover, for the aged samples, the presence of the crystalline phase was observed with a higher tendency towards crystallisation with increasing born oxide content upon storage in air.

Newport and co-workers[152] reported the structure of the phosphate network of the P_2O_5–CaO–Na_2O ternary glasses obtained through the sol–gel and melt-quenched route. From ^{31}P SS NMR data, the evolution of the phosphate network with the increase of the $CaO/CaO+Na_2O$ fraction was construed. NMR data suggested that the phosphate network is mainly formed by Q^2 groups (methaphosphate) with only a small amount of terminal Q^1 groups and demonstrated that Ca^{2+} ions increase the stiffness of the network while Na^+ depolymerises the phosphate network.

Bioglass® is a commercially available bioactive glass, also known as 45S5 glass.[1] 1D ^{31}P SS MAS NMR data of melt-quenched silicate glasses containing calcium, phosphorus and alkali metals revealed that phosphorus exists as isolated PO_4^{3-} anions in the glass structure, which will remove Na^{2+} and Ca^{2+} cations from a network-modifying role in the silicate network.[153] The possibility that a small number of pyrophosphate units (Q^1) exist was taken into consideration. No evidences for presence of a significant concentration of Si–O–P were found (Q^2 units). These observations, together with optical data, seem to rule out the 33% presence of Q^1 fraction in this material. This is an important observation in the context of the dissolution of Bioglass® in physiological fluids.

Most of the phosphate glasses are non-crystalline. It means that the signals observed on ^{31}P MAS NMR spectra are rather broad. Therefore, the only way to obtain specific resonances is the deconvolution of the broad signals into Gaussian components. Contrary to non-crystalline samples, crystalline solids give well-resolved spectra with sharp signals, making the analysis straightforward. It is possible to distinguish between the crystalline and non-crystalline phases on the basis of simple 1D MAS NMR measurements.

Newport and co-workers,[154] searching for the series of $40(P_2O_5)$–$x(B_2O_3)$–$(60-x)(Na_2O)$ ternary borophosphates glasses obtained by sol–gel synthesis,

[1]Bioglass® is produced commercially and sold under the brand names of PerioGlas®, NovaBone® and NovaBone-C/M®.

noticed that some samples after the calcination process gave sharp signals on ^{31}P spectra indicating partial crystallisation of the samples. Sharp signals were observed for samples with high Na_2O/B_2O_3 ratios: P40B10Na50 and P40B15Na45 (see Figure 38). The presence of the crystalline phase does not depend on the calcination temperature for sample P40B10Na50. For P40B15Na45, they occur for samples calcinated at 400 and 300 °C. In particular, the P40B10Na50 samples calcinated at 300 and400 °C show two sharp peaks at 1.5 and −7.2 ppm. From XRD data, it was known that this sample contains well-crystallised pentasodium triphosphate ($Na_5P_3O_{10}$). Therefore, the two sharp resonances were assigned to two different phosphorus environments in $Na_5P_3O_{10}$.

For the P40B15Na45 sample calcinated at 200 °C, two peaks are observed at 2.5 and −4.6 ppm (see Figure 38). These peaks are broader than the peaks for samples calcinated at higher temperatures, which indicates a more disordered environment around two phosphorus sites. In addition to the sharp peaks due to the crystalline phases, all P40B10Na50 show more resonances in range −8/−11 ppm

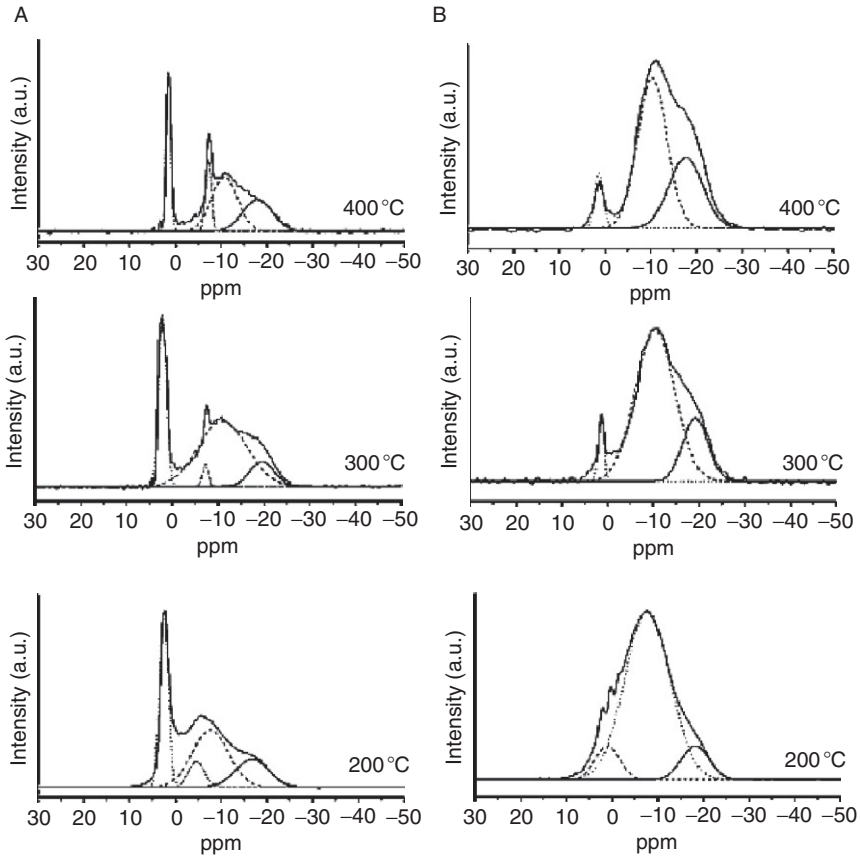

Figure 38 ^{31}P MAS NMR spectra of (A) P40B10Na50 and (B) P40B15Na45. Taken from Ref. [154]. Reproduced by permission of *The Royal Society of Chemistry*.

and −17/−20 ppm, which were assigned to Q^2_{1B} and Q^3_{1B}/Q^3_{2B} phosphorus sites, respectively. For samples with a low Na_2O/B_2O_3 ratio (samples P40B20Na40 and P40B25Na35), crystallisation is suppressed at all calcination temperatures. For all the samples under investigation, from the exact analysis of ^{31}P and ^{11}B spectra, the occurrence of cross linking between the phosphate chains through the formation of P–O–B links was confirmed.

The formation of the P–O–B links was also postulated by Eckert and co-workers[155] for ternary Na/B/P glass system. The authors investigated the structure and properties of sodium borophosphate glasses with the composition $(Na_2O)_{0.4}[(B_2O_3)_x(P_2O_5)_{1-x}]_{0.6}$ $(0.0 < x < 1.0)$ using ^{31}P and ^{11}B MAS NMR spectroscopy. From detailed quantitative spectral analyses, it was confirmed that the addition of the borate component to the binary sodium phosphate glass leads to the appearance of various distinct new resonances on the ^{31}P MAS NMR spectra. These new peaks arising from the formation of P–O–B linkages were assigned to Q^3_{mB} $(m \leq 3)$ and Q^2_{mB} $(m \leq 2)$ phosphorus sites. The formation of P–O–B links has the effect of moving the resonances of a given Q^n phosphorus unit towards higher frequencies. Although no clear discrimination between Q^2_{1B} and Q^2_{2B} units could be done, the observed continuous chemical shift trend reveals that, evidently, the number of P–O–B linkages increases with the increasing x factor. For glasses with high boron content $(x > 0.7)$, the spectra showed the formations of Q^1 and Q^0 units—peaks at 3 and 10 ppm appeared on the spectra.

^{31}P MAS NMR spectroscopy was used for the investigation of the process of formation of aluminophosphate (AlPO) glasses by the sol–gel method.[156] In this route, glasses are obtained from the gel by annealing at 400 °C. Although the composition of the sols and gels strongly depends on the used substrates (polyphosphate or orthophosphate), from this study it was apparent that the structures of the obtained final glasses were virtually the same. Hayashi and co-workers,[157] on the basis of ^{31}P NMR spectroscopy, postulated the transformation of $P_2O_7^{4-}$ anions into a pair of PO_4^{3-} and $P_2O_6^{4-}$ anions during the charge/discharge process occurring in lithium/67SnO·33P_2O_5 glass electrochemical cells.

3.2.1.3. 2D MAS NMR techniques In the previous section, we reported applications of 1D NMR spectroscopy, which enables the determination and quantitative characterisation of different phosphorus groups Q^n via deconvolution of ^{31}P resonances. Unfortunately, such an approach has at least two limitations. First, the ^{31}P MAS NMR spectra suffer from broad and overlapping signals, and these methods fail when more complicated systems are to be analysed. Second, the structural information is significantly limited, for example the connectivities of Q^n group or through-space interactions cannot be established from only 1D spectra. To overcome these limitations, it is necessary to apply more advanced 2D NMR techniques.

3.2.1.4. Correlations via dipole–dipole interactions In Section 2.2.1 we showed that the method for achieving the identification and characterisation of the chemically different phosphorus sites in complex structures is through the exploitation of the dipole–dipole interactions that occur in crystalline as well as glassy materials.

The outstanding method for this purpose is REDOR experiment, originally introduced by Gullion and Schaefer.[158] In a REDOR experiment, the dipolar interaction can be quantified on a spin system of unknown order and geometry and therefore can be applied for structural investigation of amorphous materials. Employing the REDOR technique allows overcoming the low resolution of 1D ^{31}P MAS NMR spectra of glasses. The development of this strategy into an experimental tool for chemical site characterisation in glassy materials was made by Eckert and coworkers.[159] Based on the data that characterised the local environments in the $Na_5B_2P_3O_{13}$,[160] $K_3[BP_3O_9(OH)_3]$, $NH_4[ZnBP_2O_8]$ and $Rb_3[B_2P_3O_{11}(OH)_2]$[161] crystalline borophosphates, it was proved that REDOR experiment is a well-suited tool for the investigations of medium-range order in glasses. In the cited works, ^{11}B and ^{31}P MAS, together with ^{11}B{^{31}P} and ^{31}P{^{11}B} (REDOR) NMR, were applied to obtain the necessary structural information.

Making use of this advanced NMR methodology, the local structure of Na–Al–P–O–F glasses was investigated by Zhang et al.[162] On the basis of a detailed quantitative analysis of the heteronuclear dipole–dipole interactions, a complete structural model for this kind of glasses was presented, together with full structural specification as a function of composition.

Mohr et al.[163] for the first time, applied ^{45}Sc MAS NMR and ^{45}Sc{^{31}P} REDOR experiments for investigation of the glass system $(NaPO_3)_{0.83}$–$(Al_2O_3)_{0.172x}(Sc_2O_3)_x$ $(0<x<0.11)$. From the obtained data, it was concluded that scandium ions are well dispersed in the glass network, ruling out the possibility of rare-earth ion clustering. They form isolated six-coordinated environments dominated by phosphorus atoms in their second coordination spheres.

The combination of ^{31}P{^{23}Na} and ^{23}Na{^{31}P} REDOR experiments, together with ^{23}Na triple-quantum MAS NMR (TQMAS NMR) and ^{125}Te NMR spectroscopy, made it possible to obtain important insights into the mixed-network–former interaction in $NAPO_3$–Te_2O glasses.[164] The obtained data indicated that in this glass the effect of mixed network is minimal and no new structural units are formed. The glass structure can be viewed as a collection of interlinked anionic Q^2 tetrahedra and neutral $TeO_{4/2}$ antiprisms. The connectivity distribution is not random, but homoatomic linkages are favoured. Therefore, some degree of sodium cation clustering occurs. These results indicate the significantly different behaviour of sodium ions from that in other oxide glasses.

For searching the sodium aluminophosphosilicate glasses along the composition line $(Na_2O)_x$–$[(AlPO_4)_{0.5}(SiO_2)_{0.5}]_{1-x}$, Deshpande et al.[165] utilised single- and double-resonance NMR techniques. From the obtained data, it was apparent that the addition of Na_2O to the pseudo-binary $AlPO_4{\cdot}SiO_2$ glass causes the depolymerisation of the AlPO network and the formation of Al–O–Si linkages, instead of Al–O–P. Finally, the structural model for $(Na_2O)_x$–$[(AlPO_4)_{0.5}(SiO_2)_{0.5}]_{1-x}$ glasses, developed on the basis of the conducted experiment, was proposed. Very recently, Aitken et al.[166] made use of multi-nuclear SS NMR experiments in the characterisation of the ternary xAl_2O_3–$(30-x)P_2O_5$–$70SiO_2$ glasses. The extent of P–O–Al connectivities was quantified on the basis of ^{27}Al{^{31}P} REDOR and ^{31}P{^{27}Al} REAPDOR (Rotational Echo Adiabatic Passage DOuble Resonance) measurements. The structure of phosphorus-rich glasses $(Al/P<1)$ is characterised by

four-, five- and six-coordinated Al species, whose second coordination sphere is dominated by phosphorus. ^{31}P static and MAS NMR spectra suggested the presence of at least three distinct phosphorus environments, corresponding to silicon-bonded Q^3 units, anionic methaphosphate Q^2 species interacting with octahedral aluminium and tetrahedral $PO_{4/2}$ groups (Q^4 units) bonded similarly as in $AlPO_4$.

The best SS technique that makes it possible to monitor and establish the degree of proximity of pairs of different nuclei such as ^{27}Al and ^{31}P seems to be TRAPDOR (TRAnsfer of Population via DOuble Resonance).[167] Recently, Marzke et al.,[168] by means of TRAPDOR experiment (and other techniques), established the structure of the newly synthesised lanthanum phosphate calcium aluminate glasses. The obtained results implied that a large number of the phosphorus atoms are in close proximity to aluminium, that is as second-nearest neighbours, less than 4 Å distant. NMR and Raman spectroscopy showed PO_4^{3-} groups as orthophosphate units coordinated to one La and one or two Al second neighbour ions. Moreover, at high content of La in glasses, some samples revealed the presence of the crystalline double phosphate $Ca_3La(PO_4)_3$. It was possible to establish the possible structure of the investigated glasses (see Figure 39).

The ^{27}Al–^{31}P HSQC MAS NMR experiment turned out to be one of the best ways to establish the bond connectivities between ^{31}P and ^{27}Al nuclei. Rakhmatullin and co-workers[169] applied this experiment, together with ^{19}F, ^{23}Na, ^{27}Al, ^{17}O and both ^{31}P 1D and 2D experiments, to elucidate the process of creation the ^{31}P–^{27}Al set of connections in molten and solidified Na_3AlF_6–$AlPO_4$ glass systems.

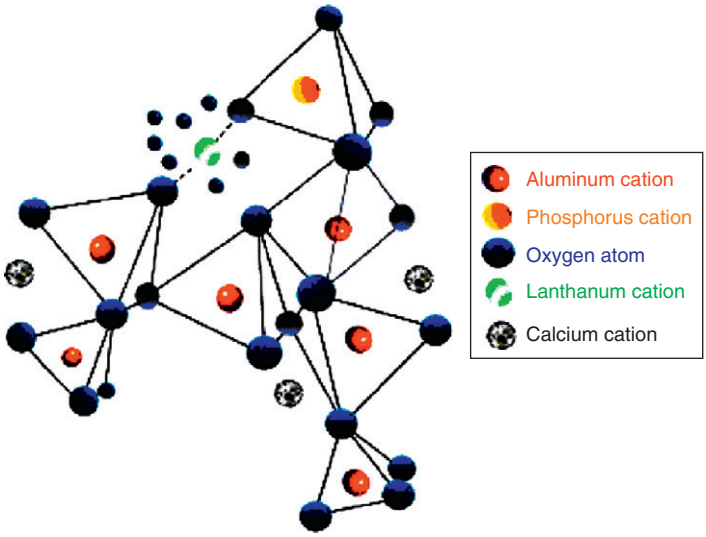

Figure 39 Illustration of a possible lanthanum phosphate–calcium aluminate glass structure for lower $LaPO_4$ content in calcium aluminate, derived from Raman and NMR data. For clarity, only a segment of the network is portrayed, with some oxygen atoms removed from the diagram. Taken from Ref. [168].

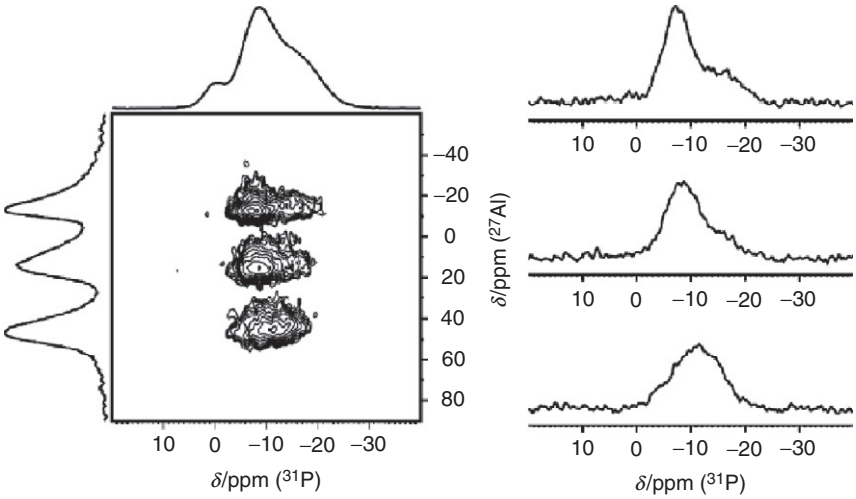

Figure 40 ^{31}P {^{27}Al}-CP-HETCOR NMR spectrum of the studied glass sample together with slices parallel to F_2, taken at the positions of AlO_4, AlO_5 and AlO_6 in F_1. (See Ref. [170] for experimental details). Taken from Ref. [170].

In 2007, van Wüllen et al.[170] proposed an advanced protocol for the structural characterisation of AlPO glasses. In this work, a combination of complementary advanced SS NMR strategies was employed to analyse the network organisation in $50K_2O–10Al_2O_3–40P_2O_5$ AlPO glasses to an unprecedented level of detailed insight. The combined results from MAS, MQMAS and $^{31}P–\{^{27}Al\}–CP–HETCOR$ (Figure 40) NMR experiments allowed a detailed speciation of the different phosphate and aluminate species present in the glass. The interconnection of these local building units to an extended three-dimensional network was explored by employing heteronuclear dipolar and scalar NMR approaches to quantify P–O–Al connectivity by $^{31}P\{^{27}Al\}–HMQC$, REAPDOR and HETCOR NMR as well as $^{27}Al\{^{31}P\}–REDOR$ NMR experiments.

Apart from the two pure phosphate species Q_0^2 (−17.9 ppm) and Q_0^1 (0.5 ppm), five additional phosphate species connected via P–O–Al bridges to AlO_x polyhedra, $Q^n_{m\mathrm{AlO}_x}$,[2] could be identified using this experiment. The authors suggested that the AlPO network is built of two phosphate species connected to AlO_6, two phosphate species connected to AlO_5 and one phosphate unit connected to AlO_4 polyhedra. Moreover, from the $^{31}P\{^{27}Al\}–REAPDOR$ NMR experiment, the number of aluminate species connected to the five identified mixed AlPO species was determined (m value in the $Q^n_{m\mathrm{AlO}_x}$ notation).

[2]Here, the modified Q notation, $Q^n{}_m\mathrm{AlO}_x$ is applied, where n denotes the number of connected tetrahedral phosphate, m gives the number of aluminate species connected to a central phosphate unit and x specifies the nature of the bonded aluminate species (i.e. 4, 5 or 6 coordinate aluminium).

3.2.1.5. Correlations via spin–spin interactions (J-coupling) The 2D *J*-coupling strategy has found a number of applications in structural studies of disordered solids.[11] It is due to the fact that *J*-coupling distribution is more sensitive to the variations of the local environments compared to the individual chemical shift distributions. The measurement of 2D distributions of *J*-couplings requires the recording of an additional chemical shift dimension. 2D correlations are measured both in SQ–SQ and in SQ–DQ modes. Several 2D techniques employing ^{31}P–^{31}P spin–spin couplings have been applied for the investigation of glasses.

^{31}P 2D *J*-resolved MAS NMR experiment to probe P–O–P connectivity utilising the through-bond scalar *J*-coupling was reported by van Wüllen et al.[170] Figure 41 displays 2D ^{31}P–*J*-resolved spectra showing P–O–P connectivity. The slices taken at 0.5, −7.4 and −11.1 ppm all exhibit clearly resolved doublets, indicating that the phosphate species under consideration are connected to one further phosphate tetrahedron. This information first supports the Q^1_0 assignment of the 0.5 ppm signal and then shows that the three other phosphate moieties at −7.4, −8.1 and −11.1 ppm are all Q^1. The combination of obtained results from various NMR experiments enabled the complete assignment of the different phosphate units presented in the glass network: Q^1_0 (0.5 ppm), $Q^1_{1AlO_{5/6}}$ (−7.4/−8.1 ppm), $Q^1_{1AlO_4}$ (−11.1 ppm), $Q^1_{2AlO_{5/6}}$ (−15.7/−15.1 ppm) and Q^2_0 (−17.9 ppm). Moreover, a structural model for the AlPO network was proposed.

A similar approach was applied for studying of the network organisation in the complete $50K_2O$–xAl_2O_3–$(50x)P_2O_5$ ($2.5 < x < 20$) system as a function of the Al_2O_3 content.[171] 2D ^{31}P–*J*-resolved data were supported by other advanced SS NMR strategies including $^{31}P\{^{27}Al\}$–CP–HETCOR NMR, $^{31}P\{^{27}Al\}$–REAPDOR

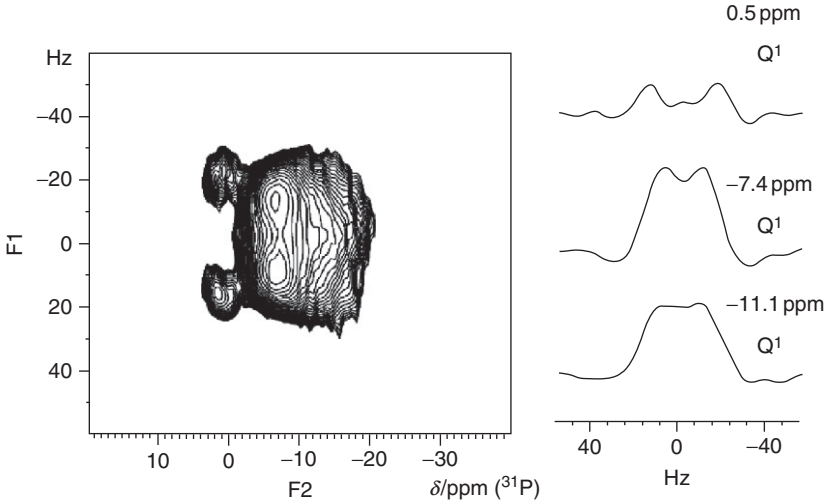

Figure 41 ^{31}P *J*-resolved NMR spectrum. Extracted slices (parallel to F_1) on the right show the individual resolved *J*-couplings for the signals at 0.5, −7.4 and −11.1 ppm with estimated 2*J*(P–P) couplings of 34, 23 and 20 Hz, respectively. Taken from Ref. [170].

NMR and $^{27}Al\{^{31}P\}$–REDOR NMR. Aluminium enters the network as AlO_4, AlO_5 and AlO_6 polyhedra, which proved to be fully connected to phosphate units. From the obtained data, it was apparent that the depolymerisation of the phosphate network is evolving from Q_0^2 units which are successively replaced by a set of different Q_m^1 moieties connected to either one ($m=1$) or two ($m=2$) aluminate units. With increasing alumina content, the fraction of Q_0^2 and the Q^1 units connected to penta- and hexa-coordinated aluminium, $Q^1_{1;AlO_6}$ and $Q^1_{2;AlO_6}$, is gradually decreases and replaced by $Q^1_{1;AlO_4}$ as the dominating phosphate species at intermediate alumina content and finally by $Q^0_{1;AlO_4}$ and $Q^1_{3;AlO_4}$ species at high-alumina content.

Eckert and co-workers[172] investigated the composition and the structure of $(100-x)\%$ $NaPO_3$–$x\%$ MoO_3 ($0<x<70$) glass-forming system. They confirmed that the Mo–O–Mo bond formation took place only in the case of high MoO_3 content ($x>45$). Both ^{31}P MAS and *J*-resolved NMR spectra allowed a clear distinction between species having two, one and zero P–O–P linkages. These sites are denoted as Q^2_{2Mo}, Q^2_{1Mo} and Q^2_{0Mo}, respectively. Finally, on the basis of the $^{23}Na\{^{31}P\}$ REDOR data and the ^{95}Mo MAS NMR spectra, it was deduced that structure of the searched glass with high molybdenum content is characterised by isolated phosphate species (most likely of the $P(OMo)_4$ type) and molybdenum oxide clusters with a large extent of Mo–O–Mo connectivity.

Edén and co-workers[173] complemented the nanometre/micrometre structural picture of highly ordered mesoporous bioactive CaO–SiO_2–P_2O_5 glasses as derived previously from TEM/SEM (transmission/scanning electron microscopy) by combining the atomic-scale information accessible from ^1H, ^{29}Si and ^{31}P 1D MAS NMR (revealing the immediate nuclear environments over ≤ 3 Å) with that obtained over a range ≤ 6 Å from homonuclear ^1H–^1H and ^{31}P–^{31}P DQ NMR and heteronuclear (^1H–^{29}Si and ^1H–^{31}P) CP-based correlation experiments.

A number of spectacular applications in structural studies of glasses were reported employing the INADEQUATE experiment.[174,175] The basic sequence and different modifications were discussed in Section 2.2.2. Smith and co-workers[176] used ^{31}P refocused INADEQUATE MAS NMR experiment for searching the length of phosphate chain and quantification of crystalline phases in ternary sodium calcium phosphate ceramic of composition $(CaO)_{0.4}(Na_2O)_{0.1}(P_2O_5)_{0.5}$.

From the analysis of the ^{31}P MAS and INADEQUATE spectra, it was possible to assign all 13 signals of the ^{31}P MAS spectrum (see Figure 42). Two peaks in the range -10 to -15 ppm are typical for Q^1 (chain-end) phosphorus sites. The remaining peaks in the chemical shift range -24 to -35, are typical for Q^2 sites. On the ^{31}P INADEQUATE spectrum (SQ–DQ correlation), wherever two of the phosphorus sites are directly linked by P–O–P bonding, a pair of cross peaks will occur at the isotropic chemical shifts of the two sites in the SQ dimension and equidistant from the $\nu_{DQ}=2\nu_{SQ}$ diagonal (the dashed line in Figure 42). Each pair of peaks has been connected by a horizontal line, and where two peaks occur at an identical isotropic chemical shift, these have been linked by a vertical line. This allows each phosphate chain to be traced out in the correct sequence.

From these data, it turned out that ceramic under investigation consisted of 48 ± 1 mol% $NaCa(PO_3)_3$ and 40 ± 1 mol% β-$Ca(PO_3)_2$, both forming Q^2-type

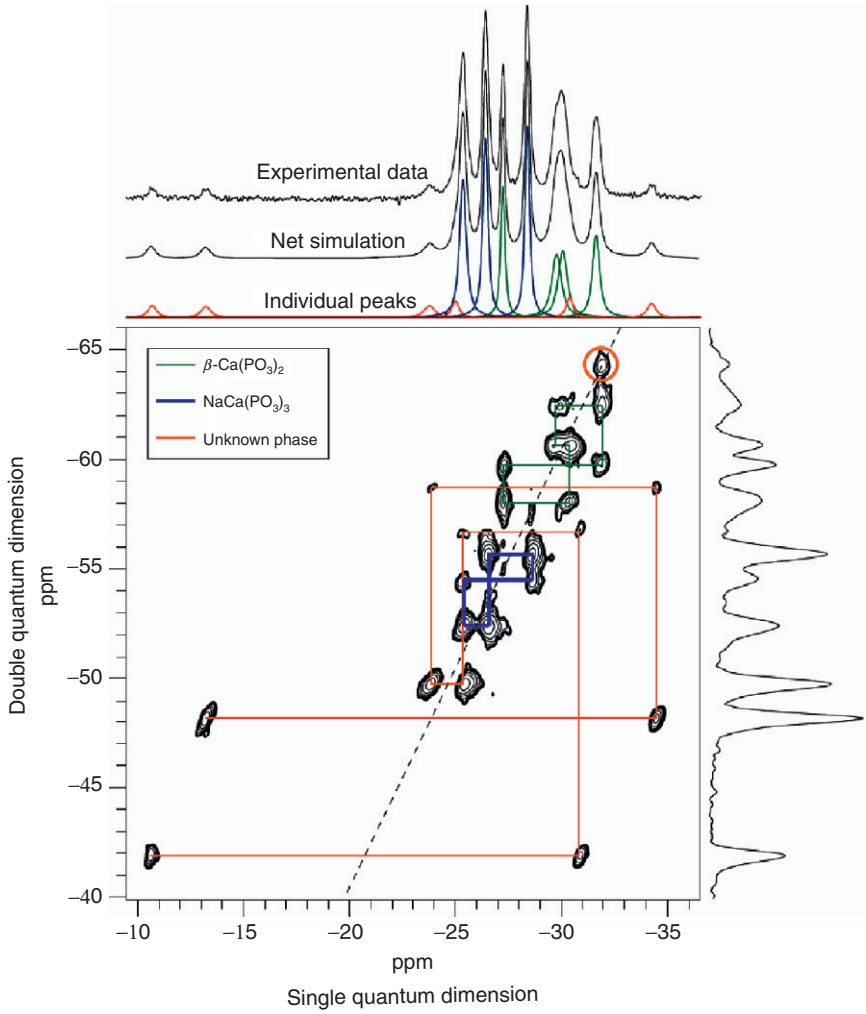

Figure 42 ^{31}P NMR spectra of the $(CaO)_{0.4}(Na_2O)_{0.1}(P_2O_5)_{0.5}$ ceramic. A 1D spectrum is shown at the top along with the deconvoluted peaks. The linking of the different phosphate chains is indicated in the 2D refocused INADEQUATE spectrum. The lowest contour is set at 5% of the maximum peak intensity. A skyline projection of the double quantum dimension is given on the right. (See Ref. [176] for details). Taken from Ref. [176].

units. The remainder exists as an unidentified calcium phosphate phase featuring a chain of six crystallographically distinct PO_4 tetrahedra, the ^{31}P NMR chemical shifts of which have been identified in the correct sequence. No evidences of the α- or γ-$Ca(PO_3)_2$ polymorphs were observed in this sample.

The power of ^{31}P INADEQUATE experiment in the investigations of multiphase phosphate ceramics, especially those composed of a mixture of crystalline and amorphous components, was demonstrated by O'Dell et al.,[177] who investigated Ti-, Sr- and Zn-containing sodium calcium phosphates. From conducted

experiments, it was apparent that each sample consisted of multiple phases—at least seven in the case of the Zn-containing sample—several of which were identified only by NMR but not by XRD.

Very recently, Brown and co-workers[65] published a concise paper in which they presented short review of the possibilities and limitations of the refocused INADEQUATE and refocused INADEQUATE spin-echo (REINE) NMR spectroscopy. The authors discussed how these experiments can be used for obtaining various structural parameters, for example identification phosphate units, phosphate chain length, $^{2}J_{P-P}$ couplings and correlation with chemical shift. It is worthy of note that the approach presented there can be applied not for phosphate glasses alone.

3.2.2. Molecular sieves: Aluminophosphates, silicoaluminophosphates and associated porous materials

AlPO and silicoaluminophosphate (SAPO) porous or zeolitic materials have received a great deal of attention due to their practical applications as molecular sieves and/or catalysts. ^{31}P NMR is a sensitive probe of the local structure of AlPOs and SAPO in the solid state. NMR spectroscopy is able to provide different types of information. Analysis of 1D spectra allows in direct way the specification of the crystallographically non-equivalent sites. 2D homo- and heteronuclear NMR experiments, utilising either the dipolar (direct, through-space) or *J*-coupling (indirect, through-bond) interactions, make available information concerning the neighbourhood of the observed atoms.

In some cases, NMR spectra of AlPO and SAPO are difficult to analyse because of broadening and overlapping effects. It is worth noting that for aluminophosphates, besides the heteronuclear dipolar coupling and molecular disorder, the additional source of line broadening is ^{31}P–^{27}Al *J*-coupling (even though the $J_{^{31}P\ -\ ^{27}Al}$ values are small (10–20 Hz); each phosphorus atom is connected to four different Al atoms having spin $I=5/2$). As was proved recently by Massiot and others,[178] the application of ^{27}Al decoupling during acquisition of ^{31}P gives a significant improvement in the resolution, which is much higher than in the acquisition at ultra-high magnetic field (17.6 T/750 MHz).

3.2.2.1. Characterisation of the newly synthesised materials The synthesis of new microporous materials is one of the most important and challenging areas in material science. Since the discovery of AlPO molecular sieves in 1982,[179] there has been significant interest in designing new AlPO compounds with novel framework. A number of open-framework AlPOs with varied structural architecture have been synthesised, including both neutral and anionic frameworks with 3D, 2D (layer), 1D (chain) and 0D (cluster) structures.[180] Li and co-workers,[181] using various ^{31}P SS NMR techniques (together with $^{19}F \rightarrow {}^{27}Al$ CP/MAS and ^{27}Al MAS), characterised the new layered fluoroaluminephophate $(C_4H_{11}NO\text{-}H)_{3.5}[Al_4(PO_4)5F]\cdot 0.5H_3O$ with extra-large 16-rings.

The simple ^{31}P MAS and $^{1}H \rightarrow {}^{31}P$ CP/MAS experiments were utilised by Ikawa et al.[182] to obtain information concerning the calcium phosphate frameworks in synthesised lamellar mesostructured calcium phosphates. A similar

NMR approach was applied by Lakiss et al.[183] to the characterisation of a new 2D fluorogallophosphate Mu-38 intercalated by a double sheet of morpholine: $Ga_3P_3O_{12}F_3[C_4H_{10}NO]_3$. From the comparison of the signal intensity on ^{31}P MAS and $^{1}H \rightarrow {}^{31}P$ CP/MAS spectra (no significant differences was observed), it was concluded that all atoms have the same proton environment. Liu and others[184] synthesised a series of MgAPSO-34 molecular sieves with different Mg molecular ratios. ^{31}P MAS spectra were recorded and analysed considering the Mg contents. From the analysis of ^{31}P data, it was concluded that Mg is substituted for Al within the SAPO framework. Moreover, a detailed analysis of the chemical environment of phosphorus in MgAPSOs, by the deconvolution of ^{31}P NMR spectra, was applied. These results enabled assigning of all signals to different products of isomorphous substitution of Mg for framework Al, which appears when the content of Mg increases.

Huang and co-workers[185] used more sophisticated NMR experiments to describe the amorphous phases formed during the synthesis of the microporous material $AlPO_4$-5. The structural characterisation was based on the $^{27}Al \rightarrow {}^{31}P$ HETCOR used for selection of P–O–Al bonding connectivities and $^{31}P\{^{27}Al\}$ TRAPDOR for obtaining the information regarding the degree of condensation for phosphorus sites in the amorphous phase. P sites bonding the hydroxyl groups were identified with $^{1}H \rightarrow {}^{31}P$ CP/MAS.

3.2.2.2. Monitoring the crystallisation processes of the microporous materials

Despite of the tremendous progress made in the last decade in the synthesis of AlPOs, the crystallisation process is still not completely understood at the molecular level. Therefore, design of a new framework is still difficult. These difficulties arise from the fact that hydrothermal synthesis of AlPO is an extremely complicated process, involving multiple component reactions and chemical equilibria in a heterogeneous environment with both solid and liquid phases co-existing. By introducing a new approach, named dry-gel, conversion is made possible to study the crystallisation process.

Chen and Huang,[186] on the basis of the quantitative analysis of the ^{31}P MAS NMR spectra, confirmed the amorphous to semicrystalline to AEL phase transition sequence in the process of crystallisation of the $AlPO_4$-11 AlPO. Since the semicrystalline phase is held together by weak intermolecular interactions, washing with water results in the conversion back to the amorphous phase. The weak bonding forces in the semicrystalline phase are important, because they provide flexibility for reorganisation of the local bonding environment to form a 3D covalent AEL framework. Deng and co-workers[187] utilised more sophisticated NMR methods to study the crystallisation of $AlPO_4$-5 AlPO molecular sieves. In combination with powder X-ray diffraction (PXRD) and infrared (IR), multinuclear SS NMR spectroscopy provided insights into the development and evolution of the intermediate gels during crystallisation. The authors used ^{31}P MAS spectra to define the start of the formation of the crystalline framework. More information about the local ordering of the gels was obtained from 2D $^{27}Al \rightarrow {}^{31}P$ HETCOR and $^{31}P/^{27}Al$ double-resonance experiments. In combination with $^{1}H \rightarrow {}^{31}P$ CP/MAS experiments, two microdomains could be identified in the

120 min heated gel. A possible evolution mechanism of the gels consisting of three successive stages was finally proposed for the crystallisation process.

Similar approaches were applied for studying the crystallisation of magnesium-substituted AlPO of type-36 (MgAPO-36).[188] From the obtained data, it was apparent that there exist two types of microstructural region in which five types of P(nAl) (n = 2–4) units could be identified. A three-stage mechanism of crystallisation was proposed.

Very recently, Huang and co-workers[189] examined the formation of the molecular sieve SAPO-34. The local environments of P, Al, F and Si atoms in several solid phases obtained at different stages of crystallisation were characterised by different SS NMR techniques including ^{31}P, ^{27}Al, ^{19}F and ^{29}Si MAS, ^{27}Al TQ MAS, ^{31}P{^{27}Al} TRAPDOR, ^{27}Al{^{31}P} REDOR, ^{27}Al–^{31}P HETCOR, ^{31}P{^{19}F} and ^{27}Al{^{19}F} REDOR as well as ^{1}H–^{31}P CP/MAS techniques. The NMR results provided new insights into the formation of SAPO-34.

Hydrothermal treatment of the initial gel for an extended period leads to the transformation of the prophase to a mixture of triclinic and trigonal phases of SAPO-34. Although the later forms in the presence of the fluoride anion, no F^- was found in the trigonal phase. For Si incorporation, $Si(OAl)_4$ coordination exists in the prephase, but the amount of Si is very small. It appears that there are only two sites, P(1) and P(2), for Si incorporation, which may have implication in the catalytic sites in the framework. The mixture of triclinic and trigonal phases exists at much higher Si content, but most of the Si may locate only in the trigonal phase.

3.2.2.3. Structure elucidation of AlPOs Multi-dimensional SS NMR techniques are essential to developing a detailed understanding of the local and topological structure upon calcination, hydration and subsequent dehydration of the AlPOs and related microporous compounds and materials. Various SS experiments can be implemented to establish the connectivities between the nuclei. As was mentioned previously, the experiments can be divided in two main categories: utilising either homo- or heteronuclear dipolar interactions, that is CP/MAS, HETCOR, REDOR, TEDOR and TRAPDOR. These experiments are able to establish the spatial connectivities. The second category includes *J*-modulation utilising either homo- or heteronuclear *J* (scalar) couplings, like INADEQUATE, HMQC, UC2QF COSY (Uniform-Sign Crosspeak Souble Quantum Filtered Correlation Spectroscopy).

Bonhomme and co-workers[190] demonstrated the efficiency of the original refocused ^{31}P–^{29}Si MAS *J*-INEPT NMR experiment in the characterisation of silicophosphate derivatives (crystalline phases and amorphous gels). They utilised both 1D and 2D experiments for investigating the structure of the crystalline phase $Si_5O(PO_4)_6$ and the complex mixture of SiP_2O_7 polymorphs. The obtained results were in good agreement with crystallographic data.

Kennedy and co-workers[191] studied the structural characterisation of the AlPO and SAPO forms of EMM-8. From ^{31}P MAS NMR, it was apparent that there are at least three distinct environments for P atoms in the as-synthesised AlPO EMM-8 in the ratio 2:1:1 and two in the ratio 1:1 in the calcinated material. MQMAS-selected ^{27}Al–^{31}P HETCOR experiment was used for mapping Al–P connectivities

and indicated multiple P species, which are consistent with the proposed structure of EMM-8. The detailed local structural information obtained by SS NMR helped to guide the ultimate determination of the structure of AlPO EMM-8 using X-ray crystallographic techniques.

Kanehashi et al.[192] attempted to established through-bond and through-space connectivities of amorphous (a-$AlPO_4$) and crystalline (c-$AlPO_4$) AlPO by 2D ^{27}Al–^{31}P *J*-HMQC and CP HETCOR. As a result of the better resolution of 2D HETCOR than conventional ^{31}P MAS spectra, it was possible to establish at least four non-equivalent P sites in a-$AlPO_4$. It was demonstrated that a-$AlPO_4$ has all types of Al–O–P bonds (i.e. P–O–$^{[4]}$Al, P–O–$^{[5]}$Al, P–O–$^{[6]}$Al).

Very recently, Morais et al.[178] presented the use of 1D to 3D SS NMR spectroscopy in the studies of the structure of $AlPO_4$-40 AlPO. From conducted MAS NMR experiments involving ^{31}P and ^{27}Al, it was apparent that the structure of the investigated $AlPO_4$-40 contains at least four times more sites than expected.

From the 3D data, with help of common 2D experiments, the authors were able to determine the NMR parameters of 21 ^{31}P and 20 ^{27}Al resolved sites together with their respective multiplicity (Figure 43). Moreover, the two types of Al_{IV}, segregated by their chemical environment, were attributed to the generic crystallographic sites Al_1 and Al_5, which are the only ones not connected together. It should be pointed out that the set of $^{31}P/^{27}Al$ 1D, 2D experiments along with the new 3D MQMAS-HMQC allowed the direct analysis of binding schemes in the 3D building units. The proposed route opens new possibilities of describing details of 3D bounded networks.

3.2.3. Catalysts, catalysis and surface catalytic activation

Although the majority of catalysts is based on non-phosphorus-containing substances (e.g. silica gels, different types of silicates and zeolites) the phosphoro-organic and inorganic compounds are used for activity treatment of the surface. ^{31}P SS NMR techniques can be used for searching this class of compounds. One of the essential factors characterising catalysts is their surface acidity. Evaluation of the acidic properties is important for developing new catalysts. Moreover, the characterisation of the Brönsted/Lewis nature of solids in addition to the strength and concentration of each active site is helpful in selecting the appropriate catalyst for the desired application. ^{31}P chemical shift of trimethylphosphine oxide (TMPO) is sensitive to acidity, and hence TMPO is frequently used as a probe. In addition, the activity of the catalytic materials often relies on the concurrence of acidic and redox properties. The high diagnostic value of ^{31}P NMR is related to the large difference in δ_{iso} shift between liquid trimethylphosphine (TMP) (−62.2 ppm) and $TMPH^+$ (−3.2 ppm). TMP is also moisture- and oxygen-sensitive. TMPO species with a 36 ppm ^{31}P NMR shift could be used as the oxidation molecular probe. This process can be investigated by the analysis of the gradual transformation of TMP into TMPO.

In 2008, Zheng et al.[193] attempted to predict theoretically the ^{31}P NMR chemical shift of adsorbed TMPO and the configuration of the corresponding $TMPOH^+$

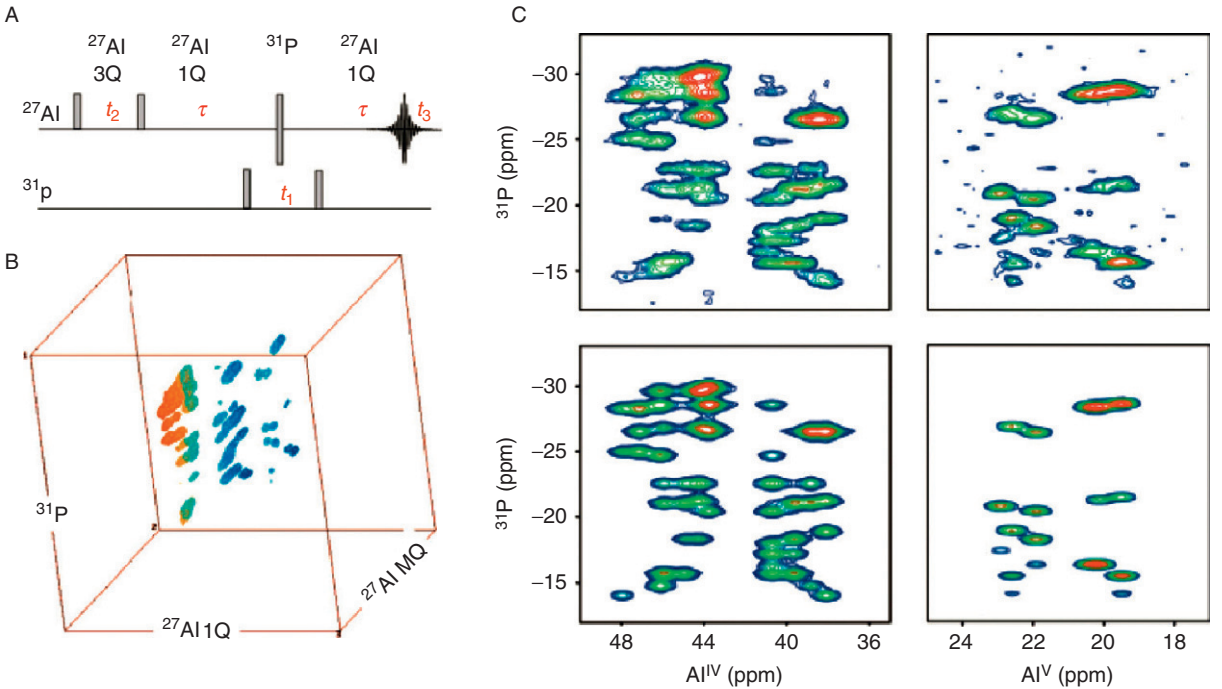

Figure 43 (A) 3D {^{31}P} ^{27}Al MQMAS pulse sequence and (B) spectrum providing isotropic/anisotropic and bonding characterisation of the Al–O–P network. The spectrum was recorded at 17.6 T with a MAS spinning rate of 14 kHz. The shearing of the Al/AlMQ planes in the 3D MQ-HMQC experiment is done for each plane independently, exactly as would be done for a single 2D MQ experiment. (C) Observed and modelled {^{31}P} ^{27}Al (isotropic dimension) 3D MQ-HMQC projections are displayed. See Ref. [178] for experimental details. Taken from Ref. [178].

complexes on Brönsted acid sites in modelled zeolites. These computations were done by means of DFT quantum chemical calculations.

San Gil and co-workers[194] utilised TMP for analysing a series of catalysts: HY, K10 zeolites, KSF and Zr-pillared acid clays. The authors concluded that γ-Al_2O_3 forms only Lewis adducts and does not posses detectable redox properties. ^{31}P MAS NMR spectra of K10 showed three different types of Brönsted sites, but only one seems to be present in the case of KSF and Zr-pillared clay. Hayashi used TMPO in the investigation of the acid properties of H-type mordenite (MOR).[195] Very recently, Guan et al.[196] used ^{31}P MAS NMR combined with the ^{31}P–^{27}Al TRAPDOR experiment for resolving the local structures of various Brönsted and Lewis acid sites in H-beta zeolites employing TMP and TMPO as the molecular probes. In addition, the interacting mechanisms of these acid sites with TMP and TMPO were clarified, which greatly aided the understanding of acid catalysis. The observed strong ^{31}P–^{27}Al TRAPDOR effect suggested the appearance of direct Al–P interactions. The proximity between acidic sites in zeolite HY with n(Si)/n(Al) ratio ranging from 2.6 to 25 was investigated by Peng and Grey[197] by applying ^{31}P MAS NMR. As a probe molecule, they used diphosphine, a molecule with two phosphorus atoms that can bind two nearby acidic sites. By careful analyses of NMR spectra of samples with appropriate loading levels, the fractions of species that are connected to two/one/zero acidic sites were determined. The obtained results suggested that there were no acidic clusters in the high Si/Al-content zeolite HY samples. Kao and others[198] characterised the acidic sites in cubic mesoporous Al-MCM-48 materials, with Si/Al ratios ranging from 10 to 67, using TMPO as a ^{31}P probe. The authors used a combination of multi-nuclear SS ^{1}H, ^{23}Na, ^{27}Al, ^{29}Si and ^{31}P MAS and some double-resonance NMR methods. Variable temperature ^{31}P/^{27}Al TRAPDOR experiments were able to establish the correlation between ^{31}Al and ^{27}Al spins and confirm the presence of Brönsted acid sites. Moreover, from ^{29}Si/^{31}P REDOR data, it was apparent that, in contrast to the pore size constraints of zeolite, the protonated TMPO was highly mobile inside the mesoporous channels of Al-MCM-48, on the NMR time scale.

^{31}P SS NMR experiments were extensively used in searching for the morphology, stability and activity of the catalysts activated with phosphoro-organic compounds. Lan et al.[199] investigated the influence of modification with triphenyl phosphine on the Rh/SBA-15-based catalysts used for hydroformylation of propene. The unusual behaviour of mixed valence cobalt(I)/cobalt(II) complexes stabilised with *p*-triphenylphosphine triphosphonic acid (*p*-TPPTP) in hydroformylation reaction was investigated by Knight and others.[200] Using ^{31}P SS NMR (together with IR and XPS), the $Co_6(CO)_3$(*p*-TPPTP)$_2(H_2O)_{24}\cdot 24H_2O$, $Co_4(CO)_3$(*p*-TPPTP)$_2(H_2O)_{24}\cdot 24H_2O$ transition compounds and final catalyst were characterised.

Multi-nuclear (^{1}H, ^{29}Si and ^{31}P) MAS NMR techniques were employed to study the local structure of catalysators. Pertici and co-workers,[201] using ^{31}P SS NMR, confirmed the higher stability towards the agglomeration of the palladium nanoparticles deposited on polydimethylphosphazene (PDMP). The Pd/PDMP system demonstrated much higher catalytic activity in Heck-type C–C coupling reaction. ^{31}P NMR data highlighted the almost complete structural invariability of

the Pd/PDMP and characterised the strong structural and dynamic modifications induced by palladium nanoparticles on PDMP. Mirkin and co-workers[202] investigated the mechanism of ligand paring and sorting in reversible processes leading to hetroligated palladium(II) complexes.

Cerqueira and co-workers[203] confirmed the appearance of the of the tetrahedral aluminium and phosphorus in AlPO-like crystalline structures both in beta (BEA) and in MOR zeolites treated with phosphoric acid. ^{31}P MAS, ^{27}Al MAS and TQMAS NMR spectra permitted the species present in the samples to be assigned. Possibly, besides the the $Al_{tet\text{-}f}$ species, other Al species are also taking part in the activity and selectivity of the catalysts. The formation of $Al_{oct–O–P}$ can also contribute to the increase in the activity by preventing further dealumination. Dual zeolite additives have no impact on the quality of naphtha when compared to MFI-based additives, which are used in the fluid catalytic cracking processes.

The presence of crystalline phases, influencing the structure and catalytic activity of nickel phosphide-supported catalysts, was investigated by Korányi et al.[204] The author concluded that mesoporous silica (SBA-15) supports treated with $Ni_{12}P_5$ exhibit higher hydrotreating activities than SBA-15 treated with Ni_2P. This different behaviour of the SBA-15-supported catalysts can be due to the inhomogeneous particle size distribution or to the plugging of the mesoporous structure. In addition to that, as was deduced from ^{31}P MAS NMR spectra analysis, different phosphates are present in the Ni_2P phase-containing samples, while the small agglomerates present in the $Ni_{12}P_5$-containing catalysts do not include any phosphate species (NMR). Presumably, the most important effect is the difference in dispersion.

During recent years, an incredible amount of improvement of immobilised homogeneous catalysts has been observed. The catalysis of hydrosilylation by the well-defined surface rhodium siloxide phosphine complexes studied by means of ^{31}P NMR was reported by Marciniec et al.[205] Asymmetric hydrogenation is the most widely used industrial homogeneously catalysed asymmetric reaction. The production of a wide range of pharmaceuticals and fine chemicals relies on asymmetric hydrogenation. Initial attempts at the immobilisation of asymmetric hydrogenation catalysts were expected to improve the enantioselectivity by varying the reaction rates and decreasing metal–metal interactions. Immobilised species are important in such diverse areas as combinatorial chemistry,[206] solid-phase synthesis,[207] chromatography[208] and catalysis.[209]

Mainly the hydrogenations are mediated through a platinum-group-metal-catalysed reaction with chiral ligands bound to the metal. Koten and co-workers[210] proposed the use of Ru- and Rh-containing catalysts immobilised on silica in asymmetric hydrogenation. As a chiral compound, they used BINAP (2,2′-bis(diphenylphosphino)-1,1′-binaphthyl) (Scheme 4).

The novel materials were characterised using ^{31}P and ^{29}Si CP/MAS SS NMR techniques along with IR-DRIFT as well as elemental content measurements. Very recently, Blümel[211] published a concise review describing the classical and modern SS NMR methods that allow gaining insight into catalyst systems where one or two metal complexes are bound to oxide supports via bifunctional phosphine linkers, such as $(EtO)_3Si(CH_2)_3PPh_2$. Many aspects of the immobilised molecular

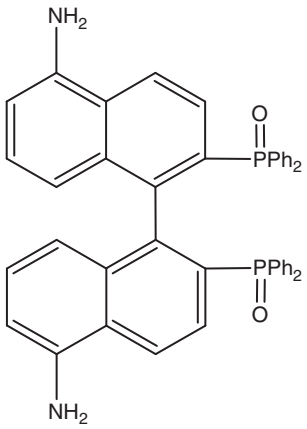

Scheme 4

catalysts can be elucidated with the corresponding NMR technique. The bulk of the support can be studied, as well as the interface of the support with ethoxysilane. With respect to the linkers, their structural integrity and mobility are as easy to investigate by classical ^{31}P CP/MAS and high-resolution magic angle spinning (HR-MAS) NMR techniques as their adsorption behaviour.

Recently, ^{31}P SS NMR was used as a test for probing the catalytic degradation processes of the extremely toxic chemical warfare agents (CWAs). Gershonov et al.[212] proposed a facile solvent-free hydrolysis (chemical destruction) of the CWAs VX (*O*-ethyl-*S*-2-(diisopropylamino)ethylmethylphosphonothioate), GB (*O*-isopropyl methylphosphonofluoridate or sarin), and HD (2,2′-dichloroethyl sulphide or sulphur mustard) upon reaction with various solid-supported fluoride reagents. The mechanisms and the efficiency of these processes were successfully studied by SS ^{31}P, ^{13}C and ^{19}F MAS NMR. ^{31}P SS MAS NMR studies of VX degradation on crushed glass, air-dried sand and oven-dried sand at a variety of temperatures showed that the final product was non-toxic ethyl methylphosphonic acid (EMPA), produced via the toxic diethyl dimethylpyrophosphonate intermediate.[213]

3.2.4. Polyoxometalates/heteropolyacids

Polyoxometalates (POMs), also known as heteropolyacids (HPA),[3] are a class of compounds formed from negatively charged inorganic metal–oxygen building blocks. When charge-balanced with cationic species, POMs self-assemble into unusual 3D structures with specific topological and electronic properties.[214] POMs are commonly formed from polyanions of early transition metals such as W, Mo or V. These anions can be substituted with other transition metals. The diversities in POMs' composition and structure make them attractive for many applications, particularly as Brönsted acid and redox catalysts. For example,

[3]In the literature (and here) the term ''polyoxometalate'' (POM) is used exchangeable with the term ''heteropoly compounds'' or heteropolyacids – abbreviated as HPA.

POMs exhibit catalytic activity in olefin oxidation to epoxides, oxidative dehydrogenation of alkanes or isomerisation due to their redox and acidic properties.[215] Both homogeneous and heterogeneous catalysts have been investigated. The knowledge of the structure is crucial for the understanding and design of solid heteropoly catalysts. As was pointed out by Misone,[216] to understand the HPA catalysators it is necessary to know two important principles. First, the molecular nature of heteropolyanions (metal oxide clusters), which can be preserved in the solid state, enables control of the acid and redox properties over a wide range. Second, the presence of hierarchical structures (primary, secondary and tertiary structures) can lead to three catalysis modes—surface-type, pseudo-liquid (or bulk-type I) and bulk-type II. Precise control of the pore size is possible through the understanding of the microstructure, which results in the unique shape selectivity observed for various reactions. Typical structures of HPA's anions are presented on Figure 44.[216]

POMs/HPA themselves are usually non-porous solids, with surface area less than 10 m^2/g and low decomposition temperatures. Therefore, they have limited surface sites for surface-catalysed reactions. A number of attempts have been made to disperse POMs on inert supports, with the intention of effectively increasing the number of accessible active catalytic sites. A number of materials have been used as solid supports for the dispersion of HPA, for example silica, carbon, zirconia, alumina, and porous silica.

Kumar and Landry[217] used ^{31}P SS NMR for the examination of the physical properties of the material obtained by immobilisation of the $[PV_2Mo_{10}O_{40}]^{5-}$ POM anion on the mesoporous MCM-41. The results obtained showed that the POM structure is intact after impregnation. The texture and structure of the support as a function of POM contents were studied, too.

One of the most attractive compounds used as a molecular tether to form highly stable catalyst materials is the 12-tungstophosphoric heteropolyacid $[H_3PW_{12}O_{40}\cdot xH_2O]$, named HPW. This attraction is due to the fact that HPW is able to form Keggin-type structures (see Figure 44). This kind of HPWs possess

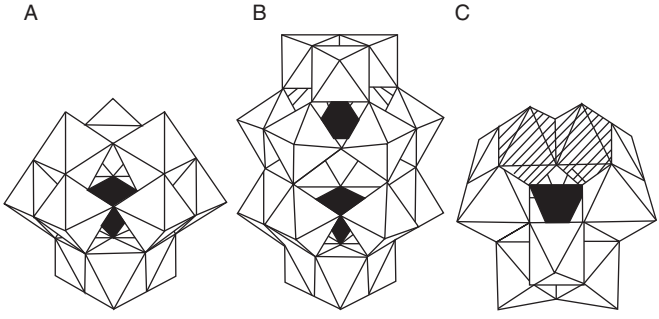

Figure 44 Examples of heteropolyanions: (A) Keggin-type polyanion, for example α-$PW_{12}O_{40}^{3-}$, (B) Dawson-type polyanion, for example $P_2W_{18}O_{62}^{6-}$; (C) disubstituted polyanion, for example γ-$SiW_{10}Fe_2O_{40}^{10-}$. Taken from Ref. [216]. Reproduced by permission of *The Royal Society of Chemistry*.

pure Brönsted acidity, stronger than many conventional solid acids such as SiO_2–Al_2O_3, H_3PO_4/SiO_2 and HY zeolites, making them attractive solid acid catalysts.

The usefulness of ^{31}P SS NMR spectroscopy in the investigation of the properties of HPW-containing catalysts was demonstrated by Hamad et al.[218] The authors investigated the catalyst composed of platinum as well as HPW supported on MSU-type silica. Employing ^{31}P MAS NMR, the authors characterised both the as-synthesised and calcinated HPW/MSU and Pt/HPW/MSU samples. Each as-synthesised sample displays only one ^{31}P resonance line (at −15.4 ppm) assigned to the hexahydrated HPW in which all polyanions are equally hydrogen-bonded by $H_5O_2^+$ cations. The spectra of calcinated HPW/MSU and Pt/HPW/MSU samples exhibit additional resonances coming up from different HPW/SiO_2 species: (i) $[(SiOH_2)^+(H_2PW_{12}O_{40})^-]$ species arising from the interaction of HPW with the support surface; (ii) HPW species differing in hydration levels; and (iii) lacunary and/or dimeric species arising from a partial decomposition of HPW. Moreover, according to the SS ^{31}P NMR analysis, Keggin-type units have been located both in the bulk and on the surface of the support. On the basis of the earlier published ^{31}P NMR data, the presence of Pt/HPW complexes was confirmed, for example $[PW_{11}O_{39}Pt]$ showed a chemical shift at −13.2 and the second $[PW_{11}O_{39}Pt–O–PtPW_{11}O_{39}]$ at 12.8 ppm.

Vinu and others[219] exploited ^{31}P CP/MAS NMR spectroscopy together with other instrumental techniques to describe physicochemical characterisation of a catalyst consisting of tungstophosphoric acid supported on zirconia and mesoporous silica MCM-41 and MCM-48.

Using HPW as a molecular tether to form highly stable crystal materials, Sarkar et al.[220] prepared the palladium complex [Pd(pyca)(PPh_3)(OTs)] (pyca = 2-picolinate) immobilised on zeolite NaY. From the ^{31}P SS NMR data, it was concluded that the Pd complex is attached to the surface of zeolite by the HPW via some ionic interactions. Moreover, neither the support nor the molecular tether (HPW) undergoes any form of degradation during synthesis. This kind of material can be explored as a catalyst for acid-free carbonylation reaction.

Rives and co-workers[221] using ^{31}P MAS NMR spectroscopy were able to distinguish between the different strengths and types of acid sites in silica Aeorosil 380 supported 12-tungstophosphoric heteropolyacid. Using TMP as a molecular probe, the authors demonstrated that silica interacts with TMP by two kinds of acid sites: weak acid support sites through the isolated silanol groups, and strong Brönsted acid, which leads to the formation of $TMPH^+$, through the hydrogen-bonded silanol groups. Silica interacts with HPW only through its isolated silanol groups.

Very recently, Lui and co-workers[215] made an attempt to characterise dispersed HPW on mesoporous zeolites: silicate-1 and meso-silicate-1, by SS ^{31}P NMR spin–lattice relaxations. They concluded that, on the regular silicalite-1 surface, HPA molecules exist as small agglomerates, while on the mesosilicalite-1 surface about 46% of the HPA molecules are successfully dispersed to the mesoporous channel surfaces. The structural integrity of the surface-exchanged HPA molecules is preserved. Coupled with reaction data, it can be concluded unambiguously that the well-dispersed HPA molecules are the active centres for isomerisation of 1-butene.

3.2.5. Metal-organic frameworks

Metal-organic frameworks (MOFs) are crystalline compounds consisting of metal ions or clusters coordinated to often rigid organic molecules to form 1D, 2D or 3D structures that can be porous. The synthesis of phosphorus-containing MOFs has been a subject of intense studies owing to their interesting structural chemistry and potential applications in adsorption and catalysis. Recently, many research efforts have been focused on the synthesis of organic–inorganic hybrid compounds by incorporating organic ligands in the structures of metal phosphates. The organic components can dramatically influence the structures, thus providing a route for the synthesis of new open-framework materials. Moreover, the organic molecule acts as a ligand forming covalent bonds to metal centres and can be considered as a part of the framework. The knowledge on intermolecular interactions among the molecules in the solid state allows understanding of the properties of organometallic compounds. Physical (conductivity, diffusion, magnetic susceptibility, reorientation and second-harmonic generation) and chemical (solid-state reactivity, racemisation, resolution) properties of the compound depend on the ways in which the molecules are organised in the crystal and on the forces that hold them together. The two major types of interactions employed by chemists to engineer supramolecules with predefined dimensions (1D, 2D and 3D) are metal ligand bonding and hydrogen bonding. In addition to strong (O–H$\cdots$O) and weak (C–H$\cdots$O) hydrogen bonds, halogen bonds (C–X$\cdots$O) and weak (C–H$\cdots\pi$) interactions have also been well characterised and exploited to play an important role in crystal engineering and organometallic structures.[222]

In 2007, Lii and co-workers[223] presented the complete multi-nuclear (^{1}H, ^{13}C, ^{31}P and ^{71}Ga) SS NMR spectroscopic characterisation of a new organically templated gallium oxalatophosphate: $(H_2TMPD)_{0.5}[Ga_3(C_2O_4)_{0.5}(PO_4)_3]$ (TMPD = *N*,*N*′,*N*′-tetramethyl-1,3-propanediamine). With the support of single-crystal X-ray diffraction data, it was deduced that the structure contains double 6-ring (D6R) units of the composition $Ga_6(PO_4)_6$ which are connected by oxalate ligands and P–O–Ga bonds to form a 3D framework. The charge-compensating organic ammonium cations, which are disordered over two positions, are located at the intersections of two types of 8-ring channels (see Figure 45).

Single-crystal X-ray diffraction and SS ^{31}P CP/MAS NMR of the zinc phosphate $Zn_2(HPO_4)_3$ family prepared with 1,4-diazabicyclo[2.2.2]octane (DABCO) were conducted by Jensen et al.[224] From obtained results, it was apparent that the structural diversity of amine-templated zinc phosphates is large. A new polymorph of [DABCO]–$[Zn_2(HPO_4)_3]$ with an open framework structure was described. Recently, Humphrey et al.[225] have described the phosphanotriylbenzenecarboxylic acid ($P(C_6H_4$-*p*-$CO_2H)_3$) and its methyl phosphonium iodide ($\{H_3CP(C_6H_4$-*p*-$CO_2H)_3\}I$) as organic building blocks in reaction with Zn(II) salts. The authors obtained five metal-organophosphine and metal-organophosphonium frameworks, which have hexagonal net topologies imposed by the C_3-symetric ligand building block. ^{31}P MAS NMR was used to probe both the composition of obtained materials and resistance of the phosphine ligand to oxidation.

Rocha and co-authors[226] presented a comprehensive study, including ^{31}P, ^{13}C and ^{1}H SS NMR, of the series of layered networks formulated as $[RE(H_2cmp)(H_2O)]$ [$RE^{3+} = Y^{3+}$, La^{3+}, Pr^{3+}, Nd^{3+}, Sm^{3+}, Eu^{3+}, Gd^{3+}, Tb^{3+}, Dy^{3+}, Ho^{3+}

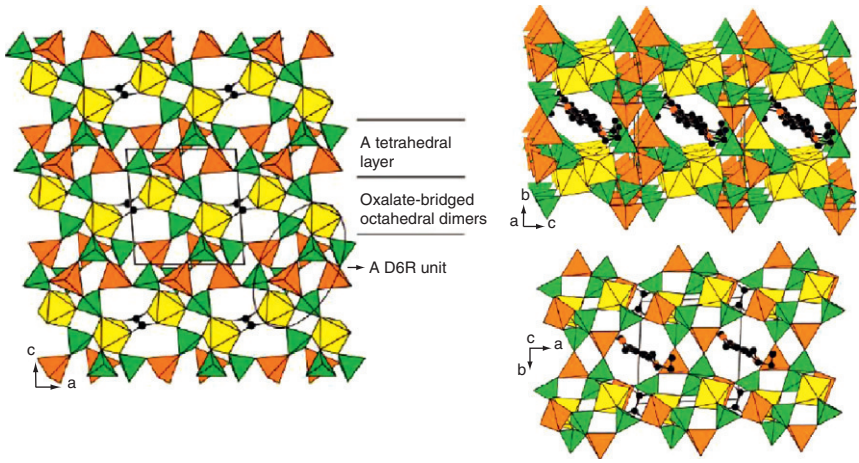

Figure 45 (Left) Structure of $(H_2TMPD)_{0.5}[Ga_3(C_2O_4)_{0.5}(PO_4)_3]$ viewed along the *b*-axis showing the tetrahedral layers, oxalate-bridged octahedral dimers and double 6-ring units. The GaO_6 octahedra, GaO_4 tetrahedra and PO_4 tetrahedra are presented, respectively. Black circles, C atoms. The organic ammonium cations are not shown. (Right) Structure of $(H_2TMPD)_{0.5}[Ga_3(C_2O_4)_{0.5}(PO_4)_3]$ viewed along the *a*-axis (top) and *c*-axis (bottom) showing 8-ring channels. The organic cations are located at the intersections of the channels. Taken from Ref. [223]. Reproduced by permission of *The Royal Society of Chemistry*.

and Er^{3+}]. Those salts were obtained in the reaction of rare-earth chloride with *N*-(carboxymethyl)iminodi(methylphosphonic acid) (H5cmp).

3.2.6. Inclusion compounds formed by phosphoro-organic host molecules

The definition of inclusion compounds, which constitute a sub-field of material science, is very broad. In host–guest chemistry, an inclusion compound is a complex in which one chemical compound (the ''host'') forms a cavity in which molecules of a second ''guest'' compound are located. In the crystal lattice, the host molecules form channels in which the guest molecules can fit. The literature describing practical applications of inclusion complexes is very extensive. Most of the published papers are concerned with applications and structural studies of cyclodextrins and their derivatives.[227] The application of SS NMR spectroscopy for the characterisation of structure, dynamics and host–guest interactions was recently reviewed.[228] The applications of ^{31}P NMR spectroscopy in case of inclusion complexes are limited only to such material when the guest or host or both components contain phosphorus. Bis[6-*O*,6-*O*′-(1,2;3,4-diisopropylidene-α-D-galactopyranosyl) thiophosphoryl] dichalcogenides ($X = S$, Se) (DGTD) shown in Scheme 5[229] represent class of host compounds containing phosphorus in main skeleton and show a strong tendency to form inclusion complexes.[230–232] DGTD belongs to a group of ''wheel and axle host'' molecules.[233] Compared to the classical representative of this group, linear acetylenic spacer coupled with bulky end groups, DGTD can be called a ''four wheeled system'' where the guest molecule can be included in space between the front wheels (and/or rear wheels).

3: X1 = X2 = S; **4:** X1 = X2 = Se; **5:** X1 = Se, X2 = S

Scheme 5

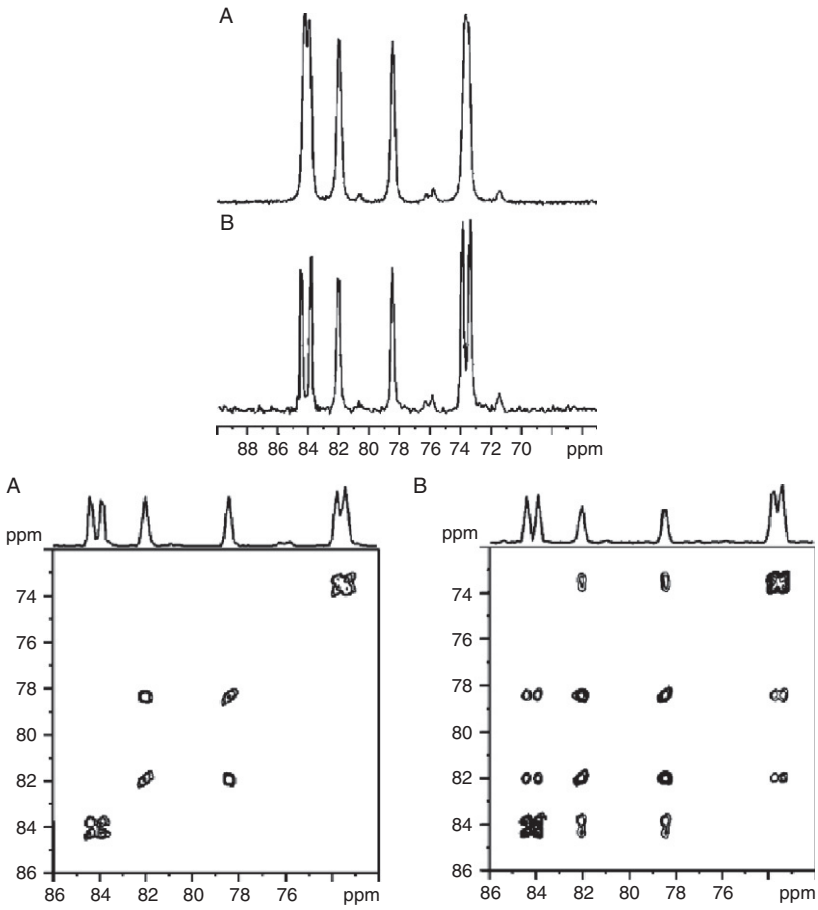

Figure 46 (Top) Experimental ^{31}P NMR spectra of three component sample crystallised from toluene: (A) powdered sample (PS) recorded with CP/MAS sequence and spinning rate 8 kHz; (B) three-component single crystal (TCSC) A held in rotor filled with silica gel recorded with CP/MAS sequence and spinning rate of 8 kHz. Note the much better NMR resolution of resonance lines and small distinction of ^{31}P chemical shifts for the monocrystal compared to powdered sample. (Bottom) ^{31}P–^{31}P proton-driven spin diffusion 2D correlation recorded with mixing times of (A) 0.2 and (B) 10 s. Taken from Ref. [229].

It is interesting to note that samples containing mixtures of disulfide, diselenide and selenosulfide crystallise forming single crystals with solvent molecules occluded in the lattice.[234] ^{31}P CP/MAS measurements (Figure 46) were carried out for a three-component system in order to establish the correlation between powdered sample and single crystal.[229]

^{31}P–^{31}P PDSD 2D correlation was employed to establish the connectivities in the crystal lattice. The 2D NMR measurement was carried out on the single crystal under MAS condition. It was proved by the authors that the guest molecule has influence on crystal form of inclusion complexes. The ^{31}P SS NMR was used to distinguish the space groups. The process of reversible exchange of the solvent molecule in the crystal lattice of DGTD is shown in Figure 47.

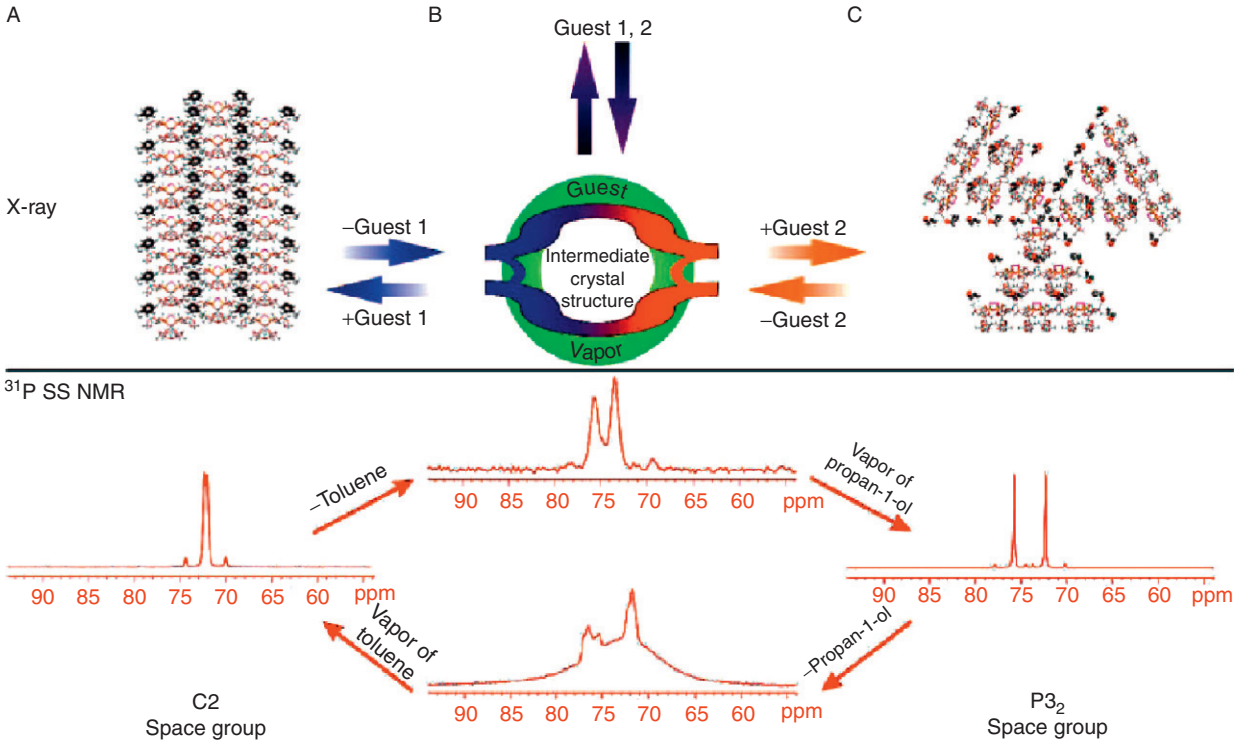

Figure 47 Schematic pathway of reversible space group change: (A) supramolecular array of complex of DGTD diselenide with toluene; (B) crystals surrounded by vapour of guest molecules; (C) supramolecular array of complex diselenide with propan-1-ol. The bottom traces below the solid line show appropriate ^{31}P CP/MAS spectra for crystalline complexes and intermediate crystal structures. Taken from Ref. [229].

Another class of inclusion complexes containing phosphorus in the host structure are cyclophosphazenes. Sozzani and co-workers have reported ^{31}P CP/MAS studies of two organic derivatives: tris(*o*-phenylene-dioxy)cyclotriphosphazene (TPP) and tris(2,3-naphtalene-dioxy)cyclotri-phosphazene (TNP).[235] In the cited works, SS NMR technique was employed to recognise guest-free TNP matrix and of ICs with guests, for example benzene, tetrahydrofuran and *p*-xylene. The ^{31}P NMR spectra were particularly informative regarding the symmetry of the phosphazene ring.

4. CONCLUDING REMARKS

In this review, we have presented the progress in methodology and recent applications of ^{31}P SS NMR in structural studies of natural products and new materials. A similar subject was covered by Iuga et al.[13] in a review published in *Annual Reports on NMR Spectroscopy* in 2007. Although only 3 years have passed from the publication of Iuga et al. report, a number of papers appeared in the mean time. This fact clearly proves how ^{31}P NMR has become a common and important diagnostic tool in structural studies of condensed matter. With the rapid, recent progress in software and hardware technologies, the possibilities of NMR spectroscopy have been greatly extended. Today, multi-dimensional SS NMR spectroscopy, ultra-fast MAS and HR MAS experiments have become routine approaches.

In many cases, the spectra recorded for the condensed phase are similar to those recorded in the liquid phase, but they usually contain a wider range of information than is available in liquid NMR spectroscopy. The solid state represents the best environment for the investigation of intermolecular interactions. Analysis of the tensorial nature of the chemical shifts provides subtle structural information. Strategies based on dipolar recoupling and *J*-coupling indicate a number of ways in which direct and indirect coupling constants can be measured, to yield direct structural constraints. This approach, combined with advanced theoretical calculations, traces new trends in structural studies of the condensed matter.

ACKNOWLEDGEMENT

The authors are grateful to the State Committee for Scientific Research (MNiSW) for financial support, Grant No. N N204 1313 35.

REFERENCES

1. D. E. C. Corbridge, *Phosphorus, An Outline of its Chemistry, Biochemistry and Technology*. 4th edn. Elsevier, Amsterdam/Oxford/New York/Tokyo, 1990 (Chapter 13, pp. 880–956).
2. (a) L. N. Johnson and R. J. Lewis, *Chem. Rev.*, 2001, **101,** 2209–2242. (b) S. M. Jones and A. Kazlauskas, *Chem. Rev.*, 2001, **101,** 2413–2424. (c) A. J. Bridges, *Chem. Rev.*, 2001, **101,** 2541–2572. (d) R. Majeti and A. Weiss, *Chem. Rev.*, 2001, **101,** 2441–2448.

3. F. Laoutid, L. Bonnaud, M. Alexandre, J. M. Lopez-Cuesta and P. Dubois, *Mater. Sci. Eng. Rep.*, 2009, **63,** 100–125.
4. R. I. Taylor, R. Mainwaring and R. M. Mortier, *Part I: Mech. Eng. Part J: J. Eng. Tribol.*, 2005, **219,** 331–346; and references cited therein.
5. G. N. Greaves and S. Sen, *Adv. Phys.*, 2007, **56,** 1–166.
6. W. D. Knight, *Phys. Rev.*, 1949, **76,** 1259.
7. W. C. Dickenson, *Phys. Rev.*, 1951, **81,** 717.
8. (a) H. S. Gutowsky and D. W. Mcall, *Phys. Rev.*, 1951, **84,** 748. (b) H. S. Gutowsky, D. W. Mcall and C. P. Slichter, *Phys. Rev.*, 1951, **84,** 589. (c) H. S. Gutowsky, D. W. Mcall and C. P. Slichter, *J. Chem. Phys.*, 1953, **1953,** 279.
9. J. Schaefer and E. O. Stejskal, *J. Am. Chem. Soc.*, 1976, **98,** 1031–1032.
10. (a) S. P. Brown and H. W. Spiess, *Chem. Rev.*, 2001, **101,** 4125–4155. (b) M. J. Potrzebowski, *Eur. J. Org. Chem.*, 2003, **8,** 1367–1376.
11. A. Lesage, *Phys. Chem. Chem. Phys.*, 2009, **11,** 6876–6891.
12. S. E. Ashbrook, *Phys. Chem. Chem. Phys.*, 2009, **11,** 6892–6905.
13. A. Iuga, C. Ader, C. Groger and E. Brunner, *Ann. Rep. NMR Spectrosc.*, 2007, **60,** 145–189.
14. M. J. Duer, *Solid State NMR Spectroscopy, Principles and Applications*. Blackwell Science Ltd., Oxford, 2002.
15. C. A. Fyfe, *Solid State NMR for Chemists*. CFC Press, Guelph, Ontario, 1983.
16. J. Mason, *Solid State Nucl. Magn. Reson.*, 1993, **2,** 285–288.
17. E. O. Stejskal, J. Schaefer and J. S. Waugh, *J. Magn. Reson.*, 1997, **28,** 105–112.
18. F. Engelke, T. Kind, D. Michel, M. Pruski and B. C. Gerstein, *J. Magn. Reson.*, 1991, **95,** 286–298.
19. S. Laage, J. R. Sachleben, S. Steuernagel, R. Pierattelli, G. Pintacuda and L. Emsley, *J. Magn. Reson.*, 2009, **196,** 133–141.
20. A. Lange, I. Scholz, T. Manolikas, M. Ernst and B. H. Meier, *Chem. Phys. Lett.*, 2009, **468**(1–3), 100–105.
21. B. H. Meier, *Chem. Phys. Lett.*, 1992, **188,** 201–207.
22. S. Laage, A. Marchetti, J. Sein, R. Pierattelli, H. J. Sass, S. Grzesiek, A. Lesage, G. Pintacuda and L. Emsley, *J. Am. Chem. Soc.*, 2008, **130,** 17216–17217.
23. V. Vijayan, J. P. Demers, J. Biernat, E. Mandelkow, S. Becker and A. Lange, *Chem. Phys. Chem.*, 2009, **10,** 2205–2208.
24. M. Kotecha, N. P. Wickramasinghe and Y. Ishii, *Magn. Reson. Chem.*, 2007, **45,** S221–S230.
25. A. E. Bennett, C. M. Rienstra, M. Auger, K. V. Lakshmi and R. G. Griffin, *J. Chem. Phys.*, 1995, **103,** 6951–6958.
26. B. M. Fung, A. K. Khitrin and K. Ermolaev, *J. Magn. Reson.*, 2000, **142,** 97–101.
27. M. Ernst, A. Samoson and B. H. Meier, *J. Magn. Reson.*, 2003, **163,** 332–339.
28. N. C. Nielsen, H. Bildsoe, H. J. Jakobsen and M. H. Levitt, *J. Chem. Phys.*, 1994, **101,** 1805–1812.
29. G. De Paëpe, B. Elena and L. Emsley, *J. Chem. Phys.*, 2004, **121,** 3165–3180.
30. N. F. Ramsey, *Phys. Rev.*, 1950, **78,** 699–703.
31. P. Hodgkinson and L. Emsley, *J. Chem. Phys.*, 1997, **107,** 4808–4816.
32. A. C. Olivieri, *J. Magn. Reson. A*, 1996, **123,** 207–210.
33. J. Herzfeld and A. E. Berger, *J. Chem. Phys.*, 1980, **73,** 6021–6030.
34. M. J. Potrzebowski, G. D. Bujacz, A. Bujacz, S. Olejniczak, P. Napora, J. Helinski, W. Ciesielski and J. Gajda, *J. Phys. Chem. B.*, 2006, **110,** 761–771.
35. M. J. Potrzebowski, K. Ganicz and S. Kaźmierski, *Pol. J. Chem.*, 2001, **75,** 1147–1169.
36. M. J. Potrzebowski, X. Assfeld, K. Ganicz, S. Olejniczak, A. Cartier, C. Gardiennet and P. Tekely, *J. Am. Chem. Soc.*, 2003, **125,** 4223–4232.
37. A. Iuga and E. Brunner, *Magn. Reson. Chem.*, 2004, **42**(4), 369–372.
38. L. Frydman, G. C. Chingas, Y. K. Lee, P. J. Grandinetti, M. A. Eastman, G. A. Barral and A. Pines, *J. Chem. Phys.*, 1992, **97,** 4800–4808.
39. A. C. Kolbert and R. G. Griffin, *Chem. Phys. Lett.*, 1990, **166,** 87–91.
40. (a) J. Hu, W. Wang, F. Liu, M. S. Solum, D. W. Alderman and R. J. Pugmire, *J. Magn. Reson. A*, 1995, **113,** 210–222. (b) D. W. Alderman, G. McGeorge, J. Z. Hu, R. J. Pugmire and D. M. Grant, *Mol. Phys.*, 1998, **95,** 1113–1126.

41. (a) O. N. Antzutkin, S. C. Shekar and M. H. Levitt, *J. Magn. Reson. A*, 1995, **115,** 7–19. (b) O. N. Antzutkin, Y. K. Lee and M. H. Levitt, *J. Magn. Reson.*, 1998, **135,** 144–155.
42. M. J. Potrzebowski, A. Jeziorna and S. Kazmierski, *Magn. Reson. A*, 2008, **32A,** 201–218; and references cited therein.
43. R. M. Orr, M. J. Duer and S. E. Ashbrook, *J. Magn. Reson.*, 2005, **174,** 301–309.
44. (a) C. Crockford, H. Geen and J. J. Titman, *Chem. Phys. Lett.*, 2001, **344,** 367–373. (b) L. Shao, C. Crockford, H. Geen, G. Grasso and J. J. Titman, *J. Magn. Reson.*, 2004, **167,** 75–86.
45. M. S. Ironside, R. S. Stein and M. J. Duer, *J. Magn. Reson.*, 2007, **188,** 49–55.
46. M. S. Ironside, D. G. Reid and M. J. Duer, *Magn. Reson. Chem.*, 2008, **46,** 913–917.
47. P. W. Aue, E. Bartholdi and R. R. Ernst, *J. Chem. Phys.*, 1976, **64,** 2229–2246.
48. N. M. Szeverenyi, M. J. Sullivan and G. E. Maciel, *J. Magn. Reson.*, 1982, **47,** 462–475.
49. I. Schnell, *Prog. Nucl. Magn. Reson. Spectrosc.*, 2004, **45,** 145–207.
50. M. H. Levitt, Symmetry-based pulse sequences in magic-angle spinning solid-state NMR. *in*: *Encyclopedia of Nuclear Magnetic Resonance*, D. M. Grant and R. K. Harris (eds.), Supplementary Volume, Wiley, Chichester, 2002, pp. 165–196.
51. M. Hohwy, H. J. Jakobsen, M. Eden, M. H. Levitt and N. C. Nielsen, *J. Chem. Phys.*, 1998, **108,** 2686–2694.
52. M. J. Potrzebowski, J. Gajda, W. Ciesielski and I. M. Montesinos, *J. Magn. Reson.*, 2006, **179,** 173–181.
53. S. Olejniczak, P. Napora, J. Gajda, W. Ciesielski and M. J. Potrzebowski, *Solid State Nucl. Magn. Reson.*, 2006, **30,** 141–149.
54. M. Carravetta, M. Eden, O. G. Johannessen, H. Luthman, P. J. E. Verdegem, J. Lugtenburg, A. Sebald and M. H. Levitt, *J. Am. Chem. Soc.*, 2001, **123,** 10628–10638.
55. (a) J. Schmedt auf der Günne, *J. Magn. Reson.*, 2003, **165,** 18–32. (b) J. Schmedt auf der Günne, *J. Magn. Reson.*, 2006, **180,** 186–196.
56. B. Hu, L. Delevoye, O. Lafon, J. Trébosc and J. P. Amoureux, *J. Magn. Reson.*, 2009, **200,** 178–188.
57. M. H. Levitt, Spin Dynamics. Basics of Nuclear Magnetic Resonance. Wiley, Chichester, 2001.
58. (a) T. Allman, *J. Magn. Reson.*, 1989, **83,** 637–642. (b) A. Kubo and C. A. McDowell, *J. Chem. Phys.*, 1990, **92,** 7156–7170. (c) G. Wu and R. E. Wasylishen, *Inorg. Chem.*, 1992, **31,** 145–148.
59. L. Duma, W. Lai, M. Carravetta, L. Emsley, S. P. Brown and M. H. Levitt, *Chem. Phys. Chem.*, 2004, **5,** 815–833.
60. R. J. Iuliucci and B. H. Meier, *J. Am. Chem. Soc.*, 1998, **120**(35), 9059–9062.
61. A. Lesage, C. Auger, S. Caldarelli and L. Emsley, *J. Am. Chem. Soc.*, 1997, **119**(33), 7867–7868.
62. F. Fayon, G. Le Saout, L. Emsley and D. Massiot, *Chem. Commun.*, 2002, **16,** 1702–1703.
63. S. Cadars, J. Sein, L. Duma, A. Lesage, T. N. Pham, J. H. Baltisberger, S. P. Brown and L. Emsley, *J. Magn. Reson.*, 2007, **188,** 24–34.
64. S. Cadars, A. Lesage, M. Trierweiler, L. Heux and L. Emsley, *Phys. Chem. Chem. Phys.*, 2007, **9,** 92–103.
65. P. Guerry, M. E. Smith and S. P. Brown, *J. Am. Chem. Soc.*, 2009, **131,** 11861–11874.
66. (a) P. Caravatti, G. Bodenhausen and R. R. Ernst, *Chem. Phys. Lett.*, 1982, **89,** 363–367. (b) P. Caravatti, L. Braunschweiler and R. R. Ernst, *Chem. Phys. Lett.*, 1983, **100,** 305–310.
67. (a) A. Lessage, D. Sakellariou, S. Steuernagel and L. Emsley, *J. Am. Chem. Soc.*, 1998, **120,** 13194–13201. (b) K. Saalwaechter, R. Graf and H. W. Spiess, *J. Magn. Reson.*, 1999, **140,** 471–476.
68. B.-J. Van Rossum, H. Foerster and H. J. M. de Groot, *J. Magn. Reson.*, 1997, **124,** 516–519.
69. Y.-H. Tseng, Y.-L. Tsai, T. W. T. Tsai, C.-P. Lin, S.-H. Huanga, C.-Y. Mou and J. C. C. Chan, *Solid State Nucl. Magn. Reson.*, 2007, **31,** 55–61.
70. B. Elena, A. Lesage, S. Steuernagel, A. Böckmann and L. Emsley, *J. Am. Chem. Soc.*, 2005, **127,** 17296–17302.
71. J. Trebosc, J. W. Wiench, S. Huh, V. S.-Y. Lin and M. Pruski, *J. Am. Chem. Soc.*, 2005, **127,** 7587–7593.
72. S. Un and M. P. Klein, *J. Am. Chem. Soc.*, 1989, **111,** 5119–5124.
73. D. J. Mandell, I. Chorny, E. S. Groban, S. E. Wong, E. Levine, C. S. Rapp and M. P. Jacobson, *J. Am. Chem. Soc.*, 2007, **129,** 820–827.
74. C. Gardiennet, B. Henry, P. Kuad, B. Spiess and P. Tekely, *Chem. Commun.*, 2005, **2,** 180–182.
75. C. Gardiennet-Doucet, X. Assfeld, B. Henry and P. Tekely, *J. Phys. Chem. A*, 2006, **110,** 9137–9144.
76. J. Gajda, S. Olejniczak, I. Bryndal and M. J. Potrzebowski, *J. Phys. Chem. B*, 2008, **112,** 14036–14044.

77. C. Gardiennet-Doucet, B. Henry and P. Tekely, *Prog. Nucl. Magn. Reson. Spectrosc.*, 2006, **49,** 129–149.
78. Y. Shindo, A. Naito, S. Tuzi, Y. Sugawara, H. Urabe and H. Saito, *J. Mol. Struct.*, 2002, **602,** 389–397.
79. C. V. Grant, D. McElheny, V. Frydman and L. Frydman, *Magn. Reson. Chem.*, 2006, **44,** 366–374.
80. U. A. Hellmich, W. Haase, S. Velamakanni, H. W. van Veen and C. Glaubitz, *FEBS Lett.*, 2008, **582,** 3557–3562.
81. A. Iuga, M. Spoerner, C. Ader, E. Brunner and H. R. Kalbitzer, *Biochem. Biophys. Res. Com.*, 2006, **346,** 301–305.
82. T. Terao, S. Matsui and K. Akasaka, *J. Am. Chem. Soc.*, 1977, **99,** 6136–6138.
83. J. Rinnenthal, C. Richter, S. Nozinovic, B. Fuerrtig, J. J. Lopez, C. Glaubitz and H. Schwalbe, *J. Biomol. NMR*, 2009, **45,** 153–155.
84. J. Precechtelova, P. Padrta, M. L. Munzarova and V. Sklenar, *J. Phys. Chem. B*, 2008, **112,** 3470–3478.
85. N. B. Barhate, R. N. Barhate, P. Cekan, G. Drobny and S. Th. Sigurdsson, *Org. Lett.*, 2008, **10,** 2745–2747.
86. J. Schiller, M. Muller, B. Fuchs, K. Arnold and D. Huster, *Curr. Anal. Chem.*, 2007, **3,** 283–301.
87. S. J. Opella, A. Nevzorov, M. F. Mesleh and F. M. Marassi, *Biochem. Cell Biol.*, 2002, **80,** 597–604.
88. A. Ramamoorthy, S. Thennarasu, A. Tan, D. K. Lee, C. Clayberger and A. M. Kreensky, *Biochim. Biophys. Acta.*, 2005, **1758,** 154–163.
89. A. Ramamoorthy, S. Thennarasu, D. K. Lee, A. Tan and L. Maloy, *Biophys. J.*, 2006, **91,** 206–216.
90. C. Kim, J. Spano, E. K. Park and S. Wi, *Biochim. Biophys. Acta.*, 2009, **1788,** 1482–1496.
91. F. J. Franccois, S. Castano, B. Desbat, B. Odaert and M. Roux, *Biochemistry*, 2008, **47,** 6394–6402.
92. S. Wi and C. Kim, *J. Phys. Chem.*, 2008, **112,** 11402–11414.
93. H. Khandelia and Y. N. Kaznessis, *Biochim. Biophys. Acta*, 2007, **1768,** 509–520.
94. P. J. Sherman, R. J. Jackway, J. D. Gehman, S. Praporski, G. A. McCubbin, A. Mechler, L. L. Martin, F. Separovic and J. H. Bowie, *Biochemistry*, 2009, **48,** 11892–11901.
95. S. Abu-Baker, X. Qi and G. A. Lorigan, *Biophys. J.*, 2007, **93,** 3480–3490.
96. S. Abu-Baker, X. Qi, J. Newstadt and G. A. Lorigan, *Biochim. Biophys. Acta*, 2005, **1717,** 58–66.
97. K. Nomura, T. Inaba, K. Morigaki, K. Brandenburg and U. Seydel, *Biophys. J.*, 2008, **95,** 126–1238.
98. J. Garner, S. R. Inglis, J. Hook, F. Separovic and M. M. Harding, *Eur. Biophys. J.*, 2008, **37,** 1031–1038.
99. E. K. Tiburu, E. S. Karp, G. Birrane, J. O. Struppe, S. Chu, G. A. Lorigan, S. Avraham and H. K. Avraham, *Biochemistry*, 2006, **45,** 7356–7365.
100. I. Cloutier, C. Paradis-Bleau, A. M. Giroux, X. Pigeon, M. Arseneault, R. C. Levesque and M. Auger, *Eur. Biophys. J.*, 2010, **39,** 263–276.
101. S. D. Chu, J. W. Hawes and G. A. Lorigan, *Magn. Reson. Chem.*, 2009, **47,** 651–657.
102. A. Bunge, M. Loew, P. Pescador, A. Arbuzova, N. Brodersen, J. Kang, L. Dahne, J. Liebscher, A. Herrmann, G. Stengel and D. Huster, *J. Phys. Chem. B*, 2009, **113,** 16425–16434.
103. J. D. German, C. C. O'Brien, F. Shabanpoor, J. D. Wade and F. Separovic, *Eur. Biophys. J.*, 2008, **37,** 333–344.
104. T. L. Lau, E. E. Ambroggio, D. J. Tew, R. Cappai, C. L. Masters, G. D. Fidelio, K. J. Barnham and F. Separovic, *J. Mol. Biol.*, 2006, **356,** 759–770.
105. Y. Nakazawa, Y. Suzuki, M. P. Williamson, H. Saitô and T. Asakura, *Chem. Phys. Lipids*, 2009, **158,** 54–60.
106. V. C. Antharam, R. S. Farver, A. Kuznetsova, K. H. Sippel, F. D. Mills, D. W. Elliott, E. Sternin and J. R. Long, *Biochim. Biophys. Acta*, 2008, **1778,** 2544–2554.
107. Y. Su, R. Mani and M. Hong, *J. Am. Chem. Soc.*, 2008, **130,** 8856–8864.
108. A. Bunge, M. Fischlechner, M. Loew, A. Arbuzova, A. Herrmann and D. Hustera, *Soft Matter*, 2009, **5,** 3331–3339.
109. M. Jensen and W. Nerdal, *Eur. J. Pharm. Sci.*, 2008, **34,** 140–148.
110. T. L. Pukala, M. P. Boland, J. D. Gehman, L. Kuhn-Nentwig, F. Separovic and J. H. Bowie, *Biochemistry*, 2007, **46,** 3576–3585.
111. C. Glaubitz and A. Watts, *J. Magn. Res.*, 1998, **130,** 5–316.
112. A. Kouzayha, O. Wattraint and C. Sarazin, *Biochimie*, 2009, **91,** 774–778.
113. C. Glaubitz, *Concepts Magn. Reson.*, 2000, **12,** 137–151.
114. C. Sizun and B. Bechinger, *J. Am. Chem. Soc.*, 2002, **124,** 1146–1147.

115. O. Wattraint, A. Arnold, M. Auger, C. Bourdillon and C. Sarazin, *Anal. Biochem.*, 2005, **336,** 253–261.
116. J. J. Lopez, A. J. Mason, C. Kaiser and C. Glaubitz, *J. Biomol. NMR.*, 2007, **37,** 97–111.
117. J. Kyrikou, N. P. Benetis, P. Chatzigeorgiou, M. Zervou, K. Viras, C. Poulos and T. Mavromoustakos, *Biochim. Biophys. Acta*, 2008, **1778,** 113–124.
118. J. D. Gehman, F. Luc, K. Hall, T. H. Lee, M. P. Boland, T. L. Pukala, J. H. Bowie, M. I. Aguilar and F. Separovic, *Biochemistry*, 2008, **47,** 8557–8565.
119. T. Doherty and M. Hong, *J. Magn. Reson*, 2009, **196,** 39–47.
120. D. K. Lee, B. S. Kwon and A. Ramamoorthy, *Langmuir*, 2008, **24,** 13598–13604.
121. S. Dvinskikh, U. Durr, K. Yamamoto and A. Ramamoorthy, *J. Am. Chem. Soc.*, 2006, **128,** 6326–6327.
122. M. Tang, A. J. Waring and M. Hong, *J. Am. Chem. Soc.*, 2007, **129,** 11438–11445.
123. S. Mukherjee, Y. Song and E. Oldfield, *J. Am. Chem. Soc.*, 2008, **130,** 1264–1273.
124. Y. Su, T. Doherty, A. J. Waring, P. Ruchala and M. Hong, *Biochemistry*, 2009, **48,** 4587–4595.
125. M. Ouellet, J. D. Doucet, N. Voyer and M. Auger, *Biochemistry*, 2007, **46,** 6597–6606.
126. S. V. Dvinskikh, U. H. N. Durr, K. Yamamoto and A. Ramamoorthy, *J. Am. Chem. Soc.*, 2007, **129,** 794–802.
127. Kołodziejski, TCC 2004.
128. S.-J. Huang, Y.-L. Tsai, Y.-L. Lee, C.-P. Lin and J. C. C. Chan, *Chem. Mater.*, 2009, **21,** 2583–2585.
129. A. Kaflak and W. Kolodziejski, *Magn. Reson. Chem.*, 2008, **46,** 335–341.
130. Y.-H. Tseng, Y. Mou, P.-H. Chen, T. W. T. Tsai, C.-I. Hsieh, C.-Y. Moua and J. C. C. Chana, *Magn. Reson. Chem.*, 2008, **46,** 330–334.
131. L. T. Kun, M. D. Grynpas, C. C. Rey, Y. Wu, J. L. Ackerman and M. J. Glimcher, *Calif. Tissue Int.*, 2008, **83,** 146–154.
132. Y. H. Tseng, Y.-L. Tsai, T. W. T. Tsai, J. C. H. Chao, C.-P. Lin, S.-H. Huang, C.-Y. Mou and J. C. C. Chan, *Chem. Mater.*, 2007, **19,** 6088–6094.
133. F. Pourpoint, C. Cervais, L. Bonhomme-Coury, T. Azais, C. Coelho, F. Mauri, B. Alonso, F. Babonneau and C. Bonhomme, *Appl. Magn. Reson.*, 2007, **32,** 435–457.
134. F. Pourpoint, A. Kolassiba, C. Gervais, T. Azais, L. Bonhomme-Coury, C. Bonhomme and F. Mauri, *Chem. Mater.*, 2007, **19,** 6367–6369.
135. F. Pourpoint, C. Gervais, L. Bonhomme-Coury, F. Mauri, B. Alonso and C. Bonhomme, *C. R. Chimie*, 2008, **11,** 398–406.
136. W. J. Shaw, K. Ferris, B. Tarasevich and J. L. Larson, *Biophys. J.*, 2008, **94,** 3247–3257.
137. M. J. Duer, T. Friščić, R. C. Murray, D. G. Reid and E. R. Wise, *J. Biophys.*, 2009, **96,** 3372–3378.
138. S. Barheine, S. Hayakawa, A. Osaka and C. Jaeger, *Chem. Mater.*, 2009, **21,** 3102–3109.
139. J. Schulz, M. Pretzsch, I. Khalaf, A. Deiwick, H. A. Scheidt, G. Salis-Soglio, A. Bader and D. Huster, *Calcif. Tissue Int.*, 2007, **80,** 275–285.
140. H. Roussiere, F. Fayon, B. Alonso, T. Rouillon, V. Schnitzler, E. Verron, J. Guicheux, M. Petit, D. Massiot, P. Janvier, J.-M. Bouler and B. Bujoli, *Chem. Mater.*, 2008, **20,** 182–191.
141. J. Andersson, E. Johannessen, S. Areva, N. Baccile, T. Azaïs and M. Lindén, *J. Math. Chem.*, 2007, **17,** 463–468.
142. S. Haque, I. Rehman and J. A. Darr, *Lagmuir*, 2007, **23,** 6671–6676.
143. H. Jena, C. V. Rao, F. P. Eddy, J. Dooley and B. Rambabu, *Phys. Status Solidi A*, 2009, **206,** 2536–2541.
144. A. Rawal, X. Wei, M. Akinc and K. Schmidt-Rohr, *Chem. Mater.*, 2008, **20,** 2583–2591.
145. M. Ndao, J. T. Ash, N. F. Breen, G. Goobes, P. S. Stayton and G. P. Drobny, *Langmuir*, 2009, **25**(20), 12136–12143.
146. C. Bonhomme, C. Coelho, N. Baccile, C. Gervias, T. Avaiz and F. Babonneau, *Acc. Chem. Res.*, 2007, **40,** 738–746.
147. S. G. Kosinski, D. M. Krol, T. M. Duncan, D. C. Douglass, J. B. MacChesney and J. R. Simpson, *J. Non-Cryst. Solids*, 1988, **105,** 45–50.
148. L. Koudelka, P. Mošner, M. Zeyer and C. Jäger, *J. Non-Cryst. Solids*, 2003, **72,** 326–327.
149. A. Saranti, I. Koutselas and M. A. Karakassides, *J. Non-Cryst. Solids*, 2006, **352,** 390.
150. D. Carta, D. Qiu, P. Guerry, I. Ahmed, E. A. Abou Neel, J. C. Knowles, M. E. Smith and R. J. Newport, *J. Non-Cryst. Solids*, 2008, **354,** 3671–3677.

151. D. Qiu, P. Guerry, I. Ahmed, D. M. Pickup, D. Carta, J. C. Knowles, M. E. Smith and R. J. Newport, *Mater. Chem. Phys.*, 2008, **111,** 455–462.
152. D. Carta, D. M. Pickup, J. C. Knowles, I. Ahmed, M. E. Smith and R. J. Newport, *J. Non-Cryst. Solids*, 2007, **353,** 1759–1765.
153. V. FitzGerald, D. M. Pickup, D. Greenspan, G. Sakar, J. J. Fitzgerald, K. M. Wetherall, R. M. Moss, J. R. Jones and R. J. Newport, *Adv. Funct. Mater*, 2007, **17,** 3746–3753.
154. D. Carta, J. C. Knowles, P. Guerry, M. E. Smith and R. J. Newport, *J. Mater. Chem.*, 2009, **19,** 150–158.
155. D. Zieleniok, C. Cramer and H. Eckert, *Chem. Mater.*, 2007, **19,** 3162–3170.
156. L. Zhang and H. Eckert, *J. Non-Cryst. Solids*, 2008, **354,** 1331–1337.
157. T. Konishi, A. Hayashi, K. Tadanaga, T. Minami and M. Tatsumisago, *J. Non-Cryst. Solids*, 2008, **354,** 380–385.
158. T. Gullion and J. Schaefer, *J. Magn. Reson.*, 1989, **81,** 196–200.
159. (a) W. Strojek, M. Kalwei and H. J. Eckert, *J. Phys. Chem. B*, 2004, **108,** 7061–7073. (b) M. Bertmer and H. J. Eckert, *Solid State Nucl. Magn. Reson.*, 1999, **15,** 139–152. (c) J. C. C. Chan and H. J. Eckert, *J. Magn. Reson.*, 2000, **147,** 170–178.
160. W. Strojek, C. M. Fehse, H. Eckert, B. Ewald and R. Kniep, *Solid State Nucl. Magn. Reson.*, 2007, **32,** 89–98.
161. D. B. Raskar, H. Eckert, B. Ewald and R. Kniep, *Solid State Nucl. Magn. Reson.*, 2008, **34,** 20–31.
162. L. Zhang, C. C. de Araujo and H. Eckert, *J. Phys. Chem. B*, 2007, **111,** 10402–10412.
163. D. Mohr, A. S. S. de Camargo, C. C. de Araujo and H. Eckert, *J. Mater. Chem.*, 2007, **17,** 3733–3738.
164. M. T. Rinke, L. Zhang and H. Eckert, *Chem. Phys. Chem.*, 2007, **8,** 1988–1998.
165. R. R. Deshpande, L. Zhang and H. Eckert, *J. Mater. Chem.*, 2009, **19,** 1151–1159.
166. B. G. Aitken, R. E. Youngman, R. R. Deshpande and H. Eckert, *J. Phys. Chem. C*, 2009, **113,** 3322–3331.
167. (a) E. van Eck, R. Janssen, W. Maas and W. Veeman, *Chem. Phys. Lett.*, 1990, **174,** 428–432. (b) D. Lang, T. Alam and D. Bencoe, *Chem. Mater.*, 2001, **13,** 420–428.
168. R. Marzke, S. Boucher, G. Wolf, J. Piwowarczyk and W. Petuskey, *J. Eur. Ceram. Soc.*, 2008, **28,** 2421–2431.
169. M. Keppert, A. Rakhmatullin, F. Simko, M. Deschamps, G. M. Haarberga and C. Bessada, *Magn. Reson. Chem.*, 2008, **46,** 803–810.
170. L. van Wüllen, G. Tricot and S. Wegner, *Solid State Nucl. Magn. Reson.*, 2007, **32,** 44–52.
171. S. Wegner, L. van Wüllen and G. Tricot, *J. Non-Cryst. Solids*, 2008, **354,** 1703–1714.
172. S. H. Santagneli, C. C. de Araujo, W. Strojek, H. Eckert, G. Poirier, S. J. L. Ribeiro and Y. Messaddeq, *J. Phys. Chem. B*, 2007, **111,** 10109–10117.
173. E. Leonova, I. Izquierdo-Barba, D. Arcos, A. López-Noriega, N. Hedin, M. Vallet-Regí and M. Edén, *J. Phys. Chem. C*, 2008, **112,** 5552–5562.
174. A. Bax, R. Freeman and S. P. Kempsell, *J. Am. Chem. Soc.*, 1980, **102,** 4849–4851.
175. F. Fayon, D. Massiot, M. H. Levitt, J. J. Titman, D. H. Gregory, L. Duma, L. Emsley and S. P. Brown, *J. Chem. Phys.*, 2005, **122,** 194313.
176. L. A. O'Dell, P. Guerry, A. Wong, E. A. Abou Neel, T. N. Pham, J. C. Knowles, S. P. Brown and M. E. Smith, *Chem. Phys. Lett.*, 2008, **455,** 178–183.
177. L. A. O'Dell, E. A. Abou Neel, J. C. Knowles and M. E. Smith, *Mat. Chem. Phys.*, 2009, **114,** 1008–1015.
178. C. M. Morais, V. Montouillout, M. Deschamps, D. Iuga, F. Fayon, F. A. A. Paz, J. Rocha, C. Fernandezd and D. Massiot, *Magn. Reson. Chem.*, 2009, **47,** 942–947.
179. S. T. Wilson, B. M. C. Lok, A. Messina, T. R. Cannan and E. M. Flanigen, *J. Am. Chem. Soc.*, 1982, **104,** 1146–1147.
180. J. Yu and R. Xu, *Chem. Soc. Rev.*, 2006, **35,** 593–604; and literature cited therein.
181. M. Zhang, D. Zhou, J. Li, J. Yu, J. Xu, F. Deng, G. Li and R. Xu, *Inorg. Chem.*, 2007, **46,** 136–140.
182. N. Ikawa, Y. Oumi, T. Kimura, T. Ikeda and T. Sano, *J. Mater. Sci.*, 2008, **43,** 4198–4207.
183. L. Lakiss, A. Simon-Masseron, V. Gramlich, G. Chaplais and J. Patarin, *Microporous Mesoporous Mater*, 2008, **114,** 82–92.
184. D. Zhang, Y. Wei, L. Xu, F. Chang, Z. Liu, S. Meng, B.-L. Su and Z. Liu, *Microporous Mesoporous Mater*, 2008, **116,** 684–692.

185. J. G. Longstaffe, B. Chen and Y. Huang, *Microporous Mesoporous Mater*, 2007, **98,** 21–22.
186. B. Chen and Y. Huang, *J. Phys. Chem. C.*, 2007, **111,** 15236–15243.
187. J. Xu, L. Chen, D. Zeng, J. Yang, M. Zhang, C. Ye and F. Deng, *J. Phys. Chem. B*, 2007, **111,** 7105–7113.
188. J. Xu, D. Zhou, X. Song, L. Chen, J. Yu, C. Ye and F. Deng, *Microporous Mesoporous Mater*, 2008, **115,** 576–584.
189. Z. Yan, B. Chen and Y. Huang, *Solid State Nucl. Magn. Reson*., 2009, **35,** 49–60.
190. C. Coelho, T. Azais, L. Bonhomme-Coury, G. Laurent and C. Bonhomme, *Inorg. Chem.*, 2007, **46,** 1379–1387.
191. M. Afeworki, G. Cao, D. L. Dorset, K. G. Strohmaier and G. J. Kennedy, *Microporous Mesoporous Mater*, 2007, **103,** 216–224.
192. K. Kanehashi, T. Nemoto and K. Saito, *J. Non-Cryst. Solids*, 2007, **353,** 4227–4231.
193. A. Zheng, H. Zhang, X. Lu, S.-B. Liu and F. Deng, *J. Phys. Chem. B*, 2008, **112,** 4496–4505.
194. L. M. O. C. Merat, R. A. S. San Gil, S. R. Guerra, L. C. Dieguez, S. Caldarelli, J. G. Eon, F. Ziarelli and H. Pizzala, *J. Mol. Catal. A Chem.*, 2007, **272,** 298–305.
195. S. Hayashi, *Chem. Lett.*, 2009, **38,** 960–961.
196. J. Guan, X. Li, G. Yang, W. Zhang, X. Liu, X. Han and X. Bao, *J. Mol. Catal. A Chem.*, 2009, **310,** 113–120.
197. L. Peng and C. Grey, *Microporous Mesoporous Mater*, 2008, **2008,** 277–283.
198. H.-M. Kao, P.-C. Chang, Y.-W. Liao, L.-P. Lee and C.-H. Chien, *Microporous Mesoporous Mater*, 2008, **114,** 352–364.
199. X. Lan, W. Zhang, L. Yan, Y. Ding, X. Han, L. Lin and X. Bao, *J. Phys. Chem. C*, 2009, **113,** 6589–6595.
200. T. L. Schull, L. Henley, J. R. Deschamps, R. J. Butcher, D. P. Maher, C. A. Klug, K. Swider-Lyons, W. J. Dressick, B. Bujoli, A. E. Greenwood, L. K. Byington Congiardo and D. A. Knight, *Organometal*, 2007, **26,** 2272–2276.
201. N. Panziera, P. Pertici, L. Barazzone, A. M. Caporusso, G. Vitulli, P. Salvadori, S. Borsacchi, M. Geppi, C. A. Veracini, G. Martra and L. Bertinetti, *J. Catal.*, 2007, **246,** 351–361.
202. P. A. Ulmann, C. A. Mirkin, A. G. DiPasquale, L. M. Liable-Sands and A. L. Rheingold, *Organometal*, 2009, **28,** 1068–1074.
203. A. F. Costa, H. S. Cerqueira, J. M. M. Ferreira, N. M. S. Ruiz and S. M. C. Menezes, *Appl. Catal. A Gen.*, 2007, **319,** 137–143.
204. T. I. Korányi, Z. Vít and J. B. Nagy, *Catal. Today*, 2008, **130,** 80–85.
205. B. Marciniec, K. Szubert, M. J. Potrzebowski, I. Kownacki and H. Maciejewski, *ChemCatChem*, 2009, **1,** 304–310.
206. W. Bannworth, and E. Felder((eds.), (2000). *In Combinatorial Chemistry*, Wiley-VCH, Weinheim, 2000.
207. F. Zaragoza Dörwald, Organic Synthesis on Solid Phase. Wiley-VCH, Weinheim, 2000.
208. Z. Lu, E. Lindner and H. A. Mayer, *Chem. Rev.*, 2002, **102,** 3543–3577.
209. J. A. Gladysz, *Chem. Rev.*, 2002, **102,** 3215–3216.
210. A. R. McDonald, C. Müller, D. Vogt, G. P. M. van Klinka and G. van Koten, *Green Chem.*, 2008, **10,** 424–432.
211. J. Blümel, *Coord. Chem. Rev.*, 2008, **252,** 2410–2423.
212. E. Gershonov, I. Columbus and Y. Zafrani, *J. Org. Chem.*, 2009, **74,** 329–338.
213. C. A. S. Brevett, K. B. Sumpter, J. Pence, R. G. Nickol, B. E. King, C. V. Giannaras and H. D. Durst, *J. Phys. Chem. C.*, 2009, **113,** 6622–6633.
214. M. T. Pope and A. Muller, *Angew. Chem. Int. Ed. Engl.*, 1991, **30,** 34–48.
215. K. Zhu, J. Hu, X. She, J. Liu, Z. Nie, Y. Wang, C. H. F. Peden and J. H. Kwak, *J. Amer. Chem. Soc.*, 2009, **131,** 9715–9721.
216. M. Misone, *Chem. Commun.*, 2001, 1141–1152; and references cited therein.
217. D. Kumar and C. C. Landry, *Microporous Mesoporous Mater*, 2007, **98,** 309–316.
218. H. Hamad, M. Soulard, B. Lebeaua, J. Patarin, T. Hamieh, J. Toufaily and H. Mahzoul, *J. Mol. Catal. A Chem.*, 2007, **278,** 53–63.
219. D. P. Sawant, A. Vinu, F. Lefebvre and S. B. Halligudi, *J. Mol. Catal. A Chem.*, 2007, **262,** 98–108.
220. B. R. Sarkar, K. Mukhopadhyay and R. V. Chaudhari, *Catal. Commun.*, 2007, **8,** 1386–1392.

221. J. Deleplanque, R. Hubaut, P. Bodart, M. Fournier and A. Rives, *Appl. Surf. Sci.*, 2009, **255,** 4897–4901.
222. B. Deb and D. K. Dutta, *Polyhedron*, 2009, **28,** 2258–2262; and literature cited therein.
223. M.-F. Tang, Y.-H. Liu, P.-C. Chang, Y.-C. Liao, H.-M. Kao and K.-H. Lii, *Dalton Trans.*, 2007, 4523–4528.
224. T. R. Jensen, A. Goncalves, R. G. Hazell and H. J. Jakobsen, *Microporous Mesoporous Mater*, 2008, **109,** 383–391.
225. S. M. Humphrey, P. K. Allan, S. E. Oungoulian, M. S. Ironsid and E. R. Wise, *Dalton Trans.*, 2009, 2298–2305.
226. L. Cunha-Silva, S. Lima, D. Ananias, P. Silva, L. Mafra, L. D. Carlos, M. Pillinger, A. A. Valente, F. A. A. Paz and J. Rocha, *J. Mater. Chem.*, 2009, **19,** 2618–2632.
227. See for instance thematic issue of Advances in Polymer Science, *Adv. Polym. Sci.*, 2009, **222** and references cited therein.
228. M. J. Potrzebowski and S. Kazmierski, *Top. Curr. Chem.*, 2005, **246,** 91–140.
229. M. J. Potrzebowski, W. M. Potrzebowski, A. Jeziorna, W. Ciesielski, J. Gajda, G. D. Bujacz, M. Chruszcz and W. Minor, *J. Org. Chem.*, 2008, **73,** 4388–4397.
230. M. J. Potrzebowski, G. Grossman, K. Ganicz, S. Olejniczak, W. Ciesielski, A. E. Kozioł, I. Wawrzycka, G. Bujacz, U. Haeberlen and H. Schmitt, *Chem. Eur. J.*, 2002, **8,** 2691–2699.
231. M. J. Potrzebowski, J. Błaszczyk and W. M. Wieczorek, *J. Org. Chem.*, 1995, **60,** 2549–2562.
232. M. J. Potrzebowski, K. Ganicz, A. Skowrońska, M. W. Wieczorek, J. Błaszczyk and W. Majzner, *J. Chem. Soc. Perkin Trans. II*, 1999, **10,** 2163–2170.
233. D. V. Soldatov, *J. Chem. Crystallogr.*, 2006, **36,** 747–768; and references cited therein.
234. M. J. Potrzebowski, J. Helinski and W. Ciesielski, *Chem. Commun.*, 2002, 1582–1583.
235. (a) A. Comotti, M. C. Gallazzi, R. Simonutti and P. Sozzani, *Chem. Mater.*, 1998, **10,** 3589–3596. (b) A. Comotti, R. Simonutti, S. Stramare and P. Sozzani, *Nanotechnology*, 1999, **10,** 70–76.

CHAPTER 3

Recent Applications of Solid-State ^{17}O NMR

K. Yamada

Contents

Abstract

Together with hydrogen, carbon, and nitrogen, oxygen is an abundant element in biological compounds and plays important roles in many biological activities. Although solid-state ^{1}H, ^{13}C and ^{15}N NMR spectroscopy are common tools for investigating molecular structures and dynamics in biological sciences, solid-state ^{17}O NMR is not well developed in spite of its importance. This is because the unfavourable nuclear properties of ^{17}O ($I = 5/2$, natural abundance $= 0.038\%$, $\gamma = 3.62808 \times 10^7$ rad T^{-1} s^{-1}, and $Q = -2.558$ fm^2) have made it difficult to routinely carry out ^{17}O NMR experiments on biological molecules. Thanks to the recent development of solid-state NMR techniques and hardware, however, the last decade has seen a great increase in the number of papers reporting solid-state ^{17}O NMR of biological and related

Department of Chemistry and Materials Science, Graduate School of Science and Engineering, Tokyo Institute of Technology, Ookayama, Meguro-ku, Tokyo, Japan

Annual Reports on NMR Spectroscopy, Volume 70
ISSN 0066-4103, DOI: 10.1016/S0066-4103(10)70001-6

compounds. A number of biological applications are still being developed, and such developments will continue to receive increased attention.

Key Words: Solid-state NMR, ^{17}O, Biological molecules.

1. INTRODUCTION

Solid-state NMR is one of the most powerful spectroscopic techniques for the characterisation of molecular structures and dynamics.[1–4] This is because NMR parameters are highly sensitive to local chemical environments and molecular properties. One advantage of solid-state NMR is that it enables dealing with quadrupolar nuclei, which most of the NMR-accessible nuclei are in the periodic table. Moreover, it provides an opportunity to obtain information regarding the orientation dependence of the fundamental NMR parameters. In principle, such NMR parameters are expressed by second-rank tensors and it is the anisotropy that is capable of yielding more detailed information concerning the molecular properties.

Oxygen is found in almost all biological molecules that are important to bioactivities. Obviously, oxygen is a key element in the research fields of biochemistry and biology. Among the three stable isotopes of oxygen, ^{17}O (nuclear spin quantum number $= 5/2$, natural abundance $= 0.038\%$, $\gamma = 3.62808 \times 10^7$ rad T^{-1} s^{-1}, and quadrupolar moment $Q = -2.558$ fm^2) is accessible to NMR. Nevertheless, solid-state ^{17}O NMR of biological compounds is not well developed compared to ^{1}H, ^{13}C and ^{15}N solid-state NMR, which have already made a tremendous impact on the development of biological sciences. Figure 1 shows the relationship between the signal intensities and the line widths of NMR spectra for typical quadrupole nuclei.[5] The vertical axis in the figure is the square of the nuclear perceptivity relative to that of proton, while the horizontal axis is the line width induced by second-order quadrupolar interaction. In the figure, the magnitudes of the quadrupolar interactions are basically estimated from the quadrupolar moment of the element. This plot suggests that the higher and the more the nucleus is plotted to the left, the easier the NMR experimental conditions are, and vice versa. For example, nuclei such as ^{43}Ca, ^{33}S, and ^{47}Ti are expected to give weaker NMR signals with poor spectral resolutions under common experimental conditions. At a glance, the experimental condition for ^{17}O is not difficult except for poor signal intensity. It is important to point out that the magnitudes of the second-order quadrupolar interactions are also dependent on local electric properties, including molecular symmetry. Hence, for organic and biological molecules in which the molecular symmetry is relatively low, their line widths generally become wider than those of inorganic compounds. Moreover, signal intensities arising from a large size of biological molecules become weaker. Under these circumstances, it might be difficult to routinely carry out solid-state ^{17}O NMR experiments on targeted biological compounds.

There has been significant recent progress in solid-state NMR techniques and hardware. In particular, the advent of ultra-high magnetic fields, which improve

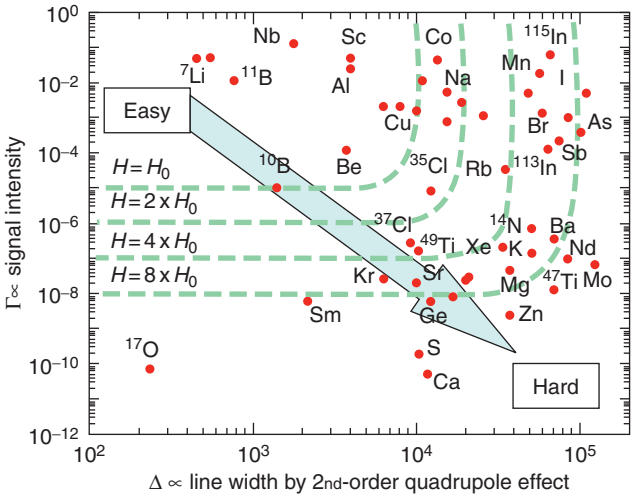

Figure 1 Relationship between signal intensity and line width induced by second-order quadrupolar interaction for typical half-integer quadrupole nuclei. Reproduced from Ref. 5.

NMR sensitivity and resolution, is highly advantageous for solid-state NMR experiments of low-γ quadrupolar nuclei such as ^{17}O. Currently, 1-GHz magnets (23.5 T) are commercially available and there is a research plan to increase the magnetic field more than 1 GHz. Important advances in pulse sequence design, theoretical approaches for NMR calculations, and sample preparation of ^{17}O-enriched compounds have also enabled investigations of higher molecular weight samples and the extraction of accurate ^{17}O NMR parameters or *J*-coupling constants, which could not have been handled so far. Thanks to these recent developments, the last decade has seen a great increase in the number of papers reporting solid-state ^{17}O NMR of biological and related compounds. At the present time, a number of biological applications are still in progress, and such developments will continue to receive increased attention.

Although there are several review articles on various aspects of solid-state ^{17}O NMR,[6–9] those dealing with the fundamentals of solid-state ^{17}O NMR of biological compounds, including the procedure of spectral simulations and discussions of the classifications of ^{17}O NMR parameters, are relatively rare. For those who are not familiar with these research fields, this review aims to provide information specifically relevant to the general trends or understanding of ^{17}O NMR tensors, which will be useful for further investigations of solid-state ^{17}O NMR. Section 2 briefly describes the schemes for ^{17}O isotopic enrichment of amino acids and peptides. Section 3 reviews the theoretical aspects of solid-state ^{17}O NMR, including ^{17}O NMR tensors and spectral simulations. Section 4 concentrates on the fundamentals of solid-state ^{17}O NMR, such as analysis of ^{17}O NMR spectra and the classifications of ^{17}O NMR tensors. Section 5 describes several key examples of solid-state ^{17}O NMR of biological solids, which are particularly notable.

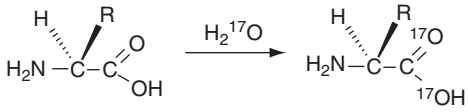

Scheme 1

2. ^{17}O SYNTHESIS

In order to obtain high-resolution solid-state ^{17}O NMR spectra of biological compounds within a practical length of time, isotopic enrichment is needed because the natural abundance of ^{17}O is extremely low (0.038%) with relatively low γ. Unfortunately, not many ^{17}O-enriched compounds are commercially available. So far, a number of chemical labelling methods have been reported on a variety of functional groups, which are well summarised in Ref. 6. One of the most convenient and obtainable precursor compounds for ^{17}O enrichment is $H_2{}^{17}O$, which is commercially available with ^{17}O enrichment levels of 10–90 at.%. The present section focuses mainly on methods for ^{17}O labelling into the carboxylic acids of amino acids, which is a good place to start for the further syntheses of ^{17}O enriched peptides and proteins. From our experience, approximately 10 at.% ^{17}O-enrichment level is enough to obtain high-resolution one-dimensional (1D) ^{17}O MAS spectra of small compounds, but it is insufficient for larger compounds or multi-dimensional NMR experiments. The most common method for the preparation of ^{17}O-enriched amino acids, as shown in Scheme 1, uses a chemical reaction in which isotopic exchange between the carboxylic group of amino acids and $H_2{}^{17}O$ is involved in the presence of a strong acid at high temperatures.[10–12] In a typical experiment, HCl is added to a mixture of an amino acid and $H_2{}^{17}O$, which are sealed in a glass tube, at 100 °C for from several hours to overnight. The advantage of this approach is that the labelling of ^{17}O is equally distributed between the hydroxyl and carbonyl groups, implying that, for the preparation of ^{17}O-enriched peptides, ^{17}O enrichment ratios do not decrease after the peptide-bond formation. On the other hand, the method has the disadvantage that all types of amino acids cannot be applied. This is because such a chemical reaction is allowed to proceed only under severe experimental conditions, such as strongly acidic and/or high-temperature environments where the rate of racemisation generally increases and some amino acids may be decomposed. Another disadvantage is that additional multi-step reactions for the introduction of protecting groups or desalting, which may result in losses in yield, are required for the preparation of ^{17}O-enriched peptides. Recently, the reaction as shown in Scheme 2 has been proposed for the preparation of ^{17}O-enriched amino acids and selectively ^{17}O-labelled peptides[13]. This method is based on the hydrolysis of an active ester of Fmoc/Boc-protected amino acids with ^{17}O-labelled water in organic solvents such as dimethylsulfoxide (DMF) and tetrahydrofuran (THF). This reaction is clean and is allowed to proceed at room temperature and near-neutral pH conditions.

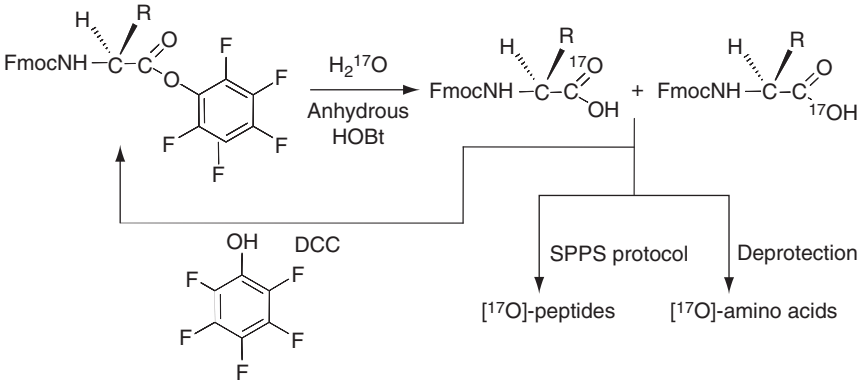

Scheme 2

Free ^{17}O-labelled amino acids can be easily obtained by the removal of the corresponding Fmoc and side-chain protections, while selectively ^{17}O-labelled peptide can be directly synthesised by the standard solid-phase peptide synthesis protocol pioneered by Merrifield[14] without additional reaction steps. The advantage of this approach is that almost all amino acids can be applied, and a small amount of $H_2{}^{17}O$, approximately a few equivalents of ^{17}O-enriched water to an active ester, is enough to allow the reaction to proceed. The method has the disadvantage that only one carbonyl oxygen atom is replaced by one equivalent of ^{17}O-enriched water at one reaction, implying that after peptide-bond formation the ^{17}O enrichment in a peptide theoretically drops by half of that of the parent Fmoc-protected amino acid. In order to minimise such isotope losses, ^{17}O-enriched active esters, for example pentafluorophenyl esters of Fmoc-protected amino acids, are prepared by introducing the corresponding compounds, for example pentafluorophenol, into ^{17}O-enriched Fmoc-protected amino acids. Using labelled active esters as the starting material, the labelling of the oxygen isotope can be performed again, as shown in Scheme 2. Pentafluorophenyl esters of Fmoc-protected amino acids are reported to easily form in good yield[15] so that these procedures can be readily carried out more than once. Figure 2 shows the electrospray ionisation time-of-flight (ESI-TOF) mass spectra of (A) non-labelled and (B) ^{17}O-enriched gramicidin S, *cyclo*-(^{D}Phe-Pro-Val-Orn-Leu)$_2$ using *N*-α-Fmoc-L-leucine doubly labelled with ^{17}O-enriched water (80–85 at. %). The ^{17}O isotope was introduced into one of the leucine molecules in the cyclic peptide. It can be seen that the intensity of the mass peak located at *m/z* 571.8 (one of the $[M+2H]^{2+}$ peaks) increases after ^{17}O is introduced. From the difference, the ^{17}O enrichment could be calculated to be 62%, which is in reasonable agreement with the theoretical value expected for the present case. Although it is not mandatory, it is preferable to perform mass spectrometry analysis, particularly in the case of macromolecules, to know the ^{17}O enrichment level. Once the ^{17}O-labelled amino acids or peptides are obtained, it is possible to extend the synthesis to ^{17}O-labelled proteins or peptide–protein complexes.

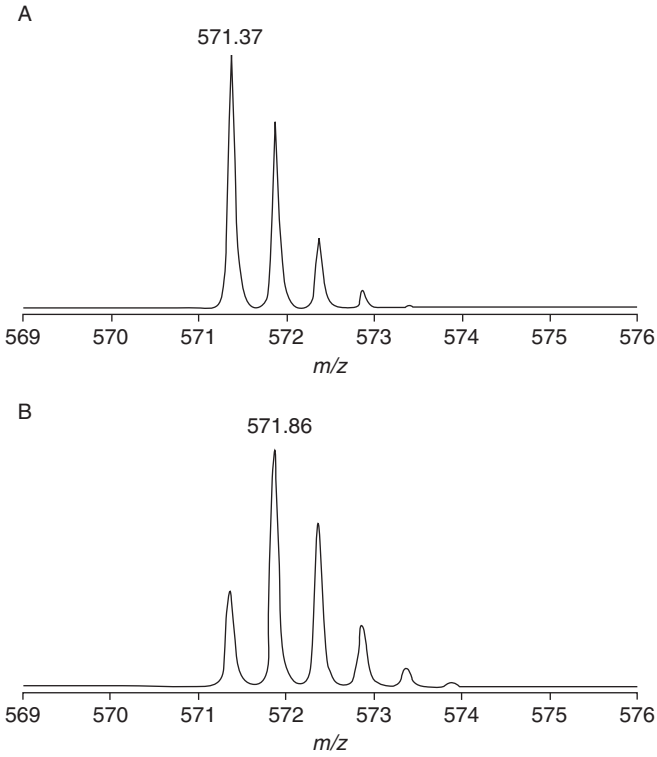

Figure 2 ESI-TOF mass spectra of (A) non-label and (B) ^{17}O-enriched gramicidin S, *cyclo*-(D-Phe-Pro-Val-Orn-[^{17}O]-Leu)$_2$. Reproduced from Ref. 13.

There is an increasing demand for ^{17}O labelling the side chains of amino acids or peptides. Eckert et al. showed the synthetic scheme for ^{17}O enrichment of the phenolic oxygen in tyrosine.[16] For peptides, Theodorou-Kassioumis et al.[17] presented an efficient synthetic route for selective ^{17}O-label the β-carbonyl group of an aspartic acid residue in a peptide. According to the literature, it is advantageous to label the side chain with ^{17}O after the amino acid residue is already incorporated into a peptide. Although the related literature has not yet been reported, the concept may be applied to other side chains of amino acid residues in peptides. There seems little doubt that the development of isotopic enrichment schemes plays a key role in the exploitation of solid-state ^{17}O NMR in biological compounds.

3. BACKGROUND OF SOLID-STATE ^{17}O NMR

Clearly, oxygen plays an important role in many biological activities. The NMR parameters of such a key element are expected to contain valuable information. In general, the solid-state ^{17}O NMR spectra of biological compounds are observed by

magic-angle spinning (MAS) experiments or static solid-state NMR techniques, exhibiting complicated line shapes. Computer simulation is usually required for extraction of the ^{17}O NMR parameters. The following sections review briefly the background of ^{17}O NMR parameters and the theoretical aspects of spectral simulations.

3.1. ^{17}O electric-field-gradient and chemical shielding tensors

In ordinary NMR experiments, the nucleus under observation may experience several different types of spin interactions, the most important of which are homonuclear and/or heteronuclear dipole–dipole, nuclear quadrupolar coupling, chemical shielding (CS), and indirect spin–spin *J*-coupling interactions.[2] For a half-integer quadrupolar nucleus, such as oxygen, in a strong magnetic field, both CS and quadrupolar interactions are dominant. *J*-coupling constants are usually too small (with the magnitude of 1–200 Hz) to be observed in conventional 1D solid-state ^{17}O NMR spectra. Hence, the analysis of solid-state ^{17}O NMR spectra of biological compounds provides ^{17}O electric-field-gradient (EFG) and CS tensors, which are briefly reviewed below.

3.1.1. ^{17}O electric-field-gradient tensor

Nuclear quadrupolar interaction arises from the coupling between the nuclear quadrupole moment Q and the EFG at the nuclear position. The EFG varies in space and is described by a traceless second-rank tensor. The EFG tensor is diagonal and its three principal components are V_{XX}, V_{YY} and V_{ZZ} with the definition of $|V_{ZZ}| \geq |V_{YY}| \geq |V_{XX}|$. Such a principal-axis system for the EFG tensor is defined with the direction of the external magnetic field, as illustrated in Figure 3(A). It is convenient to express such quadrupolar interactions by using the following two parameters:

$$C_Q\,[Hz] = V_{ZZ} \times eQ/h \tag{1}$$

and

$$\eta_Q = (V_{XX} - V_{YY})/V_{ZZ}. \tag{2}$$

Instead of the three principal components, C_Q (quadrupolar coupling constant) and η_Q (asymmetry parameter) are usually obtained from conventional solid-state NMR and NQR experiments. The parameters of C_Q and η_Q describe the magnitudes of the quadrupolar interaction and the asymmetry of the EFG tensors, respectively. η_Q is non-dimensional and its range lies between 0 and 1 because of the property of a traceless tensor. For organic and biological compounds, the magnitudes of C_Q are observed up to 12 MHz. Note that the sign of the three components can be determined with difficulty by a conventional solid-state NMR experiment. As will be explained in a later section, however, the distinction of the sign is of importance in the classifications of ^{17}O EFG tensors in a variety of functional groups. The range of η_Q lies between -1 and $+1$ if the signs of the three principal components are distinguished. A quantum chemical approach, for

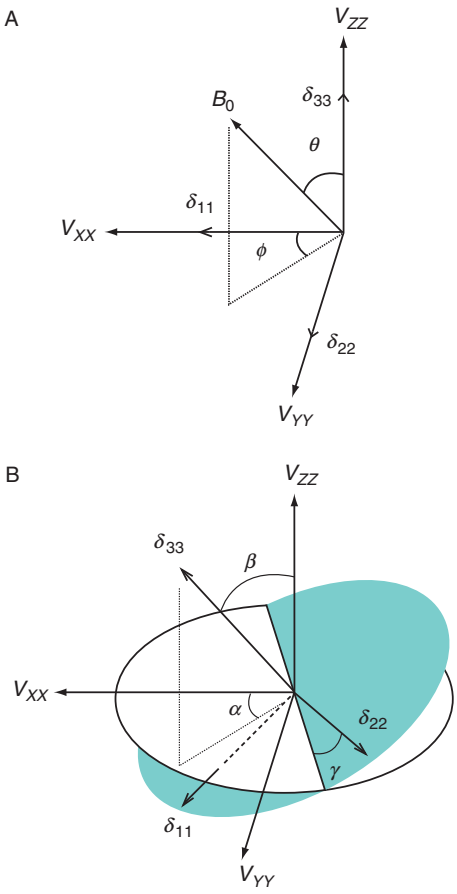

Figure 3 (A) The orientations of the principal axis system for EFG and CS tensors with respect to the external magnetic field, $\mathbf{B}_0$. (B) Relative orientations between EFG and CS tensors, expressed by the Euler angles.

example *ab initio* calculation, which can reproduce experimental data, is very often used for spectral assignment and spectral analysis. The quantum chemical approach yields ^{17}O EFG tensor components in atomic units (a.u.). Therefore, the following relation is useful for converting them to the quadrupolar coupling constant in hertz:

$$C_Q\,[\mathrm{MHz}] = -2.3496 Q\,[\mathrm{fm}^2]\, V_{ZZ}\,[\mathrm{a.u.}], \tag{3}$$

where Q is the nuclear quadrupole moment of the ^{17}O nucleus in fm^2 and the factor of 2.3496 takes care of unit conversion. The literature value for the ^{17}O Q value is -2.558 fm^2.[18] Currently, however, it seems that most quantum chemical approaches with the literature value tend to yield C_Q values larger than the experimental one. Several papers have reported[19–21] that it is advantageous to

use ''calibrated'' Q values in order to yield more accurate ^{17}O EFG parameters. The procedure for obtaining calibrated Q values is as follows. First, the theoretical calculation of C_Q values for small compounds such as O_2, HNCO, CO, H_2O and H_2CO is carried out. These small compounds are chosen because experimental and accurate C_Q values are available in the literature. Then, using Equation (3), the Q value can be calibrated with the corresponding experimental value C_Q, and the calculated EFG components V_{ZZ}. It should be noted that the calibrated Q values depend critically upon the basis sets, molecular structures, and levels of theory.

3.1.2. ^{17}O chemical shielding tensor

For the CS tensor, the following convention for the three principal components is used:

$$\sigma_{11} \leq \sigma_{22} \leq \sigma_{33} \quad \text{and} \quad \sigma_{iso} = (\sigma_{11} + \sigma_{22} + \sigma_{33})/3. \tag{4}$$

The symbol σ means absolute CS while δ is the chemical shift:

$$\delta_{11} \geq \delta_{22} \geq \delta_{33} \quad \text{and} \quad \delta_{iso} = (\delta_{11} + \delta_{22} + \delta_{33})/3. \tag{5}$$

The frequency contribution from a CS tensor also depends on the molecular orientation with respect to the external magnetic field. As illustrated in Figure 3(A), the principal axis system for a CS tensor is defined with the direction of the magnetic field in this text. A liquid sample of H_2O is generally used for chemical shift referencing (set to be 0 ppm). Similar to the case of an ^{17}O EFG tensor, a quantum chemical approach is useful for the spectral analysis. Since quantum chemical calculations yield the CS, σ, the following conversion is required for making a direct comparison between theoretical and experimental values:

$$\delta\,[\text{ppm}] = \text{CS of the reference compound } [\text{ppm}] - \sigma\,[\text{ppm}]. \tag{6}$$

As mentioned, the reference compound for ^{17}O NMR is H_2O. There are several values of the absolute CS for water in the literature.[22–25] For example, Wasylishen et al.[22] reported a value of 307.9 ppm. The theoretical prediction of the ^{17}O CS tensors is one of the challenging topics for theoretical chemists. So far, traditional quantum chemical calculations or solid-state physical approaches with periodic boundary conditions[26] have been applied to the calculations of ^{17}O CS tensors. Very recently, Nakajima[27] has demonstrated the superiority of the ONIOM method[28,29] for ^{17}O NMR calculations, which will be given in a later section.

3.2. Theoretical aspects of spectral simulations

Since nuclear spin interactions are anisotropic, the observed NMR frequency depends on the position of the principal axis systems of ^{17}O EFG and CS tensors with respect to the external magnetic field. In the following, ^{17}O NMR frequencies under quadrupolar and/or CS interactions that will be used for spectral simulations are described in detail. It is convenient to separate the cases into static solid-state NMR techniques and MAS experiments. First, the static conditions are explained.

3.2.1. ^{17}O stationary NMR spectra

For a biological compound, the molecular symmetries are generally low, which results in larger C_Q values compared with those of inorganic compounds. Therefore, second-order quadrupolar interaction needs to be considered for the observed NMR line shapes of the central transition (+1/2,−1/2). Using the orientation of the magnetic field in the principal axis system of the EFG tensor shown in Figure 3(A), the NMR frequency arising from the second-order quadrupolar interaction under static conditions v_Q^{Static} can be written as[30–32]

$$\begin{aligned} v_Q^{Static} &= (v_Q^2/12v_0)\{3/2\,\sin^2\theta[(A+B)\cos^2\theta - B] - \eta_Q\cos 2\phi\,\sin^2\theta[(A+B)\cos^2\theta + B] \\ &\quad +(\eta_Q^2/6)[A-(A+4B)\cos^2\theta-(A+B)\cos 2\phi(\cos^2\theta-1)^2]\,, \end{aligned}$$

$$\begin{aligned} v_Q &= 3C_Q/2I(2I-1), \\ A &= 3-4I(I+1), \\ B &= 1/4\left[\frac{3}{2}-2I(I+1)\right], \end{aligned} \tag{7}$$

where v_0 and I are the Larmor frequency and spin number, respectively. If a sample is a single crystal, the observed NMR frequency can be simply calculated with a single pair of ϕ and θ from the above equation. Apparently, crystalline or polymeric materials are used for most NMR experiments and space-averaging in the above equation yields the powder pattern. Figure 4(A) shows the simulated ^{17}O stationary NMR spectra as a function of η_Q from 0 to 1.[33]

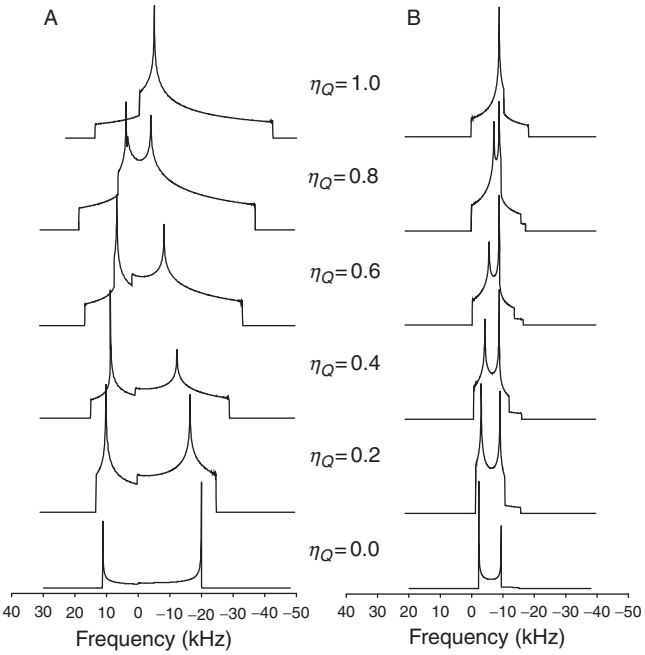

Figure 4 Simulated ^{17}O ($I = 5/2$) (A) stationary and (B) MAS NMR spectra as a function of η_Q from 0 to 1, with C_Q value of 10 MHz and v_0 of 100 MHz. Reproduced from Ref. 33.

These calculations were carried out using a C_Q value of 10 MHz and ν_0 of 100 MHz. As seen, the powder patterns exhibit complicated line shapes and there is a dependence of the line shape on η_Q. In addition, there is a dependence of the spectral width on C_Q and ν_0. For example, larger C_Q values show wider spectral width, while higher ν_0 gives narrower width. Practically, computer simulation is required for extracting C_Q and η_Q from experimental NMR spectra. Substituting the appropriate values of C_Q and η_Q in Equation (7) with powder-averaging yields a simulated NMR line shape, which is compared with the experimental one. These NMR parameters are varied until the simulated NMR line shape coincides with the experimental one. It should be noted that all the relevant nuclear interactions need to be considered for spectral simulations, and, in the case of solid-state ^{17}O NMR of a biological compound, a CS interaction is also required. The CS contribution to the NMR frequency under static conditions, ν_{CS}^{Static}, is given by

$$\begin{aligned} \nu_{CS}^{Static} &= -\nu_0(\sigma_{11}X^2 + \sigma_{22}Y^2 + \sigma_{33}Z^2), \\ X &= \sin\theta\cos\phi, \\ Y &= \sin\theta\sin\phi, \\ Z &= \cos\theta, \end{aligned} \tag{8}$$

where θ and ϕ describe the orientation of the magnetic field in the principal axis system of the CS tensor illustrated in Figure 3(A), and X, Y, and Z are the directional cosines. Very often, the CS and EFG tensors exhibit different orientations in the molecular frame of reference. This simply means that θ and ϕ in the above equation are not identical to those of Equation (7). Thus, it is helpful to use the relative orientation term between the two tensors, employing the three Euler angles (α, β, γ). In this procedure, the new directional cosines (X', Y', Z') of the CS tensor with respect to the EFG system are created so that the orientation of the CS tensor can be described by a combination of θ and ϕ in Equation (7) and the Euler angles. Note that the opposite procedure, that is the transformation of the EFG tensor with reference to the CS tensor, also provides the same results, although the equation gets more complicated. The Euler angles describing the relative orientation of the two tensors depend critically on the choice of the initial frame, the definition of the Euler angles, and the rotational directions. Therefore, it is sometimes difficult or misleading to reproduce the reported tensor orientations in the literature. There are several different definitions in the literature concerning the Euler angles relating the EFG and CS tensors and the initial alignment of the two tensors.[34–40] Here, the approach of Eichele et al.[39,40] is described, since I believe that this procedure is the most straightforward one. The initial alignment of the two tensors is illustrated in Figure 3(A). The transformation matrix of $R(\alpha, \beta, \gamma)$ can be written as

$$R(\alpha,\beta,\gamma) = \begin{pmatrix} \cos\gamma\cos\beta\cos\alpha - \sin\gamma\sin\alpha & \cos\gamma\cos\beta\sin\alpha - \sin\gamma\cos\alpha & -\cos\gamma\sin\beta \\ -\sin\gamma\cos\beta\cos\alpha - \cos\gamma\sin\alpha & -\sin\gamma\cos\beta\sin\alpha - \cos\gamma\cos\alpha & \sin\gamma\sin\beta \\ \sin\beta\cos\alpha & \sin\beta\sin\alpha & \cos\beta \end{pmatrix}. \tag{9}$$

Now, the frequency contribution from the CS tensor after the transformation can be rewritten as

$$\begin{aligned} \nu_{CS}^{Static} &= -\nu_0(\sigma_{11}X_{New}^2 + \sigma_{22}Y_{New}^2 + \sigma_{33}Z_{New}^2), \\ X_{New} &= C\cos\gamma\cos\beta + D\sin\gamma - \cos\gamma\sin\beta\cos\theta, \\ Y_{New} &= C\sin\gamma\cos\beta + D\cos\gamma + \sin\gamma\sin\beta\cos\theta, \\ Z_{New} &= C\sin\beta + \cos\beta\cos\theta, \\ C &= \sin\theta\cos\phi\cos\alpha + \sin\theta\sin\phi\sin\alpha, \\ D &= \sin\theta\sin\phi\cos\alpha - \sin\theta\cos\phi\sin\alpha. \end{aligned} \tag{10}$$

When $(\alpha, \beta, \gamma) = (0, 0, 0)$, the orientations of the CS tensor become coincident with those of the EFG tensor.[41] It is worth pointing out that the relative orientation of the two tensors can be expressed by different Euler-angle sets.[42] This is because, as mentioned already, the sign of the EFG tensors cannot be distinguished by conventional NMR experiments. For example, a 180° rotation around one of the three principal axis directions yields identical NMR line shapes but different Euler angles. In the present case in which both CS and EFG tensors are involved, there are up to 16 combinations of the principal axis systems for the two tensors. The example of the different combinations of the Euler angles is summarised in Table 1. Particular attention should be given to the comparisons of the Euler angles in the literature, in addition to the definitions of the Euler angles and the initial frames.

3.2.2. ^{17}O MAS NMR spectra

It is well known[2,3] that in the presence of second-order quadrupolar interaction, high-resolution NMR spectra are not achievable by a conventional MAS method, even if the sample spinning frequency is sufficiently high compared to the spectral

TABLE 1 Different Euler angle sets for producing the same NMR line shapes

α	β	γ
α	β	$\gamma+180$
α	$\beta+180$	$-\gamma$
α	$\beta+180$	$-\gamma+180$
$\alpha+180$	β	γ
$\alpha+180$	β	$\gamma+180$
$\alpha+180$	$\beta+180$	$-\gamma$
$\alpha+180$	$\beta+180$	$-\gamma+180$
$-\alpha$	$\beta+180$	γ
$-\alpha$	$\beta+180$	$\gamma+180$
$-\alpha$	β	$-\gamma$
$-\alpha$	β	$-\gamma+180$
$-\alpha-180$	$\beta+180$	γ
$-\alpha-180$	$\beta+180$	$\gamma+180$
$-\alpha-180$	β	$-\gamma$
$-\alpha-180$	β	$-\gamma+180$

width. This is because the second-order quadrupolar interactions are not simply proportional to the term of $(3\cos^2\theta - 1)$, which can theoretically remove dipolar–dipolar, CS, and first-order quadrupolar interactions. This implies that only partial narrowing is achieved by the MAS method so that characteristic NMR line shapes appear in the MAS NMR spectra. When the sample spinning frequency is sufficiently high, the frequency contribution from the second-order quadrupolar interaction, v_Q^{MAS}, can be written as[43–45]

$$\begin{aligned} v_Q^{MAS} &= -v_Q^2/6v_0[I(I+1) - 3/4](E\cos^2\theta + F\cos^2\theta + G), \\ E &= 21/16 - 7/8\eta_Q\cos^2\phi + 7/48(\eta_Q\cos 2\phi)^2, \\ F &= -9/8 + 1/12\eta_Q^2 + \eta_Q\cos^2\phi - 7/24(\eta_Q\cos 2\phi)^2, \\ G &= 5/16 - 1/8\eta_Q\cos 2\phi + 7/48(\eta_Q\cos 2\phi)^2. \end{aligned} \tag{11}$$

Figure 4(B) shows the simulated ^{17}O MAS spectra as a function of η_Q from 0 to 1. These calculations were carried out using the same conditions of the ^{17}O stationary NMR spectra. In the similar manner as in the case of the stationary NMR spectra, the MAS spectra exhibit characteristic line shapes from which the information on η_Q as well as C_Q can be extracted. The anisotropy of CS tensors is removed by MAS and only δ_{iso} will be obtained if it exists. When the sample spinning frequency is not high enough, the effect of spinning sidebands spaced at the spinning frequency around the central peak needs to be considered in the spectral simulation. The frequency contribution from the second-order quadrupolar interaction under slow/intermediate MAS conditions is given in the literature.[46,47] A complicated line shape is expected to appear in the MAS NMR spectrum so that a computer simulation is not trivial (see Figure 15).

4. FUNDAMENTALS OF ^{17}O NMR IN BIOLOGICAL SOLIDS

Recent developments in solid-state ^{17}O NMR techniques make it possible to analyse ^{17}O NMR spectra of biological solids, from which ^{17}O EFG and CS tensors can be obtained. Instead of isotropic values such as δ_{iso}, which are mainly obtained from solution ^{17}O NMR, the use of tensor components enables understanding of the ^{17}O NMR parameters in more detail. This section describes a few concrete examples of the analysis of solid-state ^{17}O NMR spectra of amino acids and the current understanding of ^{17}O NMR tensors.

4.1. Analysis of solid-state ^{17}O NMR spectra

For biological solids, the relevant ^{17}O NMR parameters are the EFG and CS tensors. In general, *J*-couplings are not observed in conventional ^{17}O MAS spectra because the line width is much larger than the magnitude of the *J*-couplings. Recently, however, Brown and co-workers[48,49] demonstrated that using 2D correlation spectra with R^3-HMQC and spin-echo experiments, invaluable information on *J*-coupling of ^{13}C–^{17}O, ^{17}O–^{17}O and ^{15}N–^{17}O can be obtained. The details are well explained in Ref. 49 but we are not concerned here with *J*-coupling parameters.

In this section, the focus is on the analysis of solid-state ^{17}O NMR spectra (CS and EFG tensors) by using a few concrete examples of ^{17}O-enriched amino acids. In general, three steps are required in order to obtain information on ^{17}O EFG and CS tensors from the experimental data: (1) MAS type experiments are first carried out, and the experimental parameters of δ_{iso}, C_Q and η_Q are extracted; (2) The stationary NMR spectra are analysed with the aid of the previous MAS results, so that the ^{17}O CS tensor components can be obtained; (3) The results of quantum chemical calculations are used to produce absolute ^{17}O NMR tensor orientations with respect to the molecular frame. In the following, each step is explained.

4.1.1. MAS-type experiments

Figure 5 shows the experimental and simulated ^{17}O MAS spectra for [^{17}O]-L-phenylalanine hydrochloride recorded at 11.7 T with a sample spinning frequency of 20.08 ± 0.04 kHz.[50] The peak at approximately 380 ppm (marked by *) arises from the MAS rotor material, ZrO_2. If not preferable, the use of MAS rotors made of silicon nitride is recommended. From the figure, it can be seen that two distinct resonances are observed and completely resolved. Each resonance can be simulated using a typical MAS line shape arising from the central transitions of second-order quadrupolar interactions for half-integer quadrupolar nuclei, as described in Section 3.2. Analysis of the MAS spectrum yielded the following parameters: site A, $\delta_{iso} = 355 \pm 2$ ppm, $C_Q = 8.55 \pm 0.08$ MHz, $\eta_Q = 0.08 \pm 0.04$; site B, $\delta_{iso} = 180 \pm 2$ ppm, $C_Q = 7.41 \pm 0.08$ MHz, $\eta_Q = 0.26 \pm 0.04$. On the basis of the results from quantum chemical calculations or crystal structure determined by X-ray diffraction, the spectral assignment is straightforward; for site A, the left side of the resonance is assigned to be carbonyl oxygen, and for site B, hydroxyl oxygen.

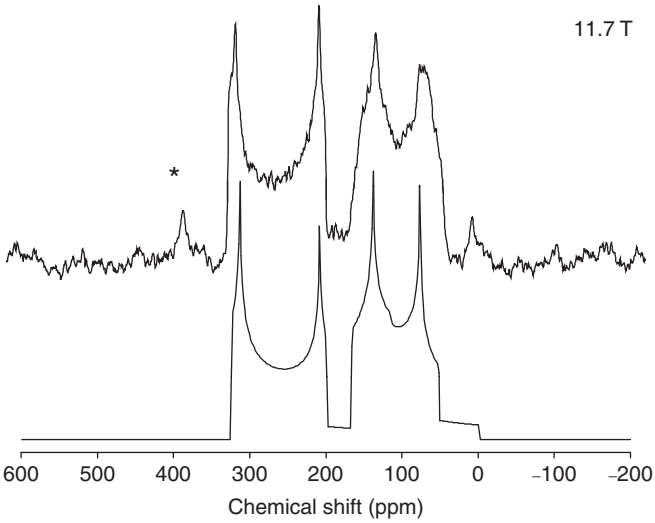

Figure 5 Experimental (upper trace) and calculated (lower trace) ^{17}O MAS NMR spectra for [^{17}O]-L-phenylalanine hydrochloride, recorded at 11.7 T with the MAS rate of 20 kHz. The peak marked by * arises from the MAS rotor material of ZrO_2. Reproduced from Ref. 50.

The spectral assignment will be discussed again in Section 4.2. In another instance, Figure 6 shows the ^{17}O MAS spectrum for [^{17}O]-L-valine, recorded at 16.4 T.[51] According to the crystal structure of L-valine,[52] the molecule exists in the zwitterionic form with two crystallographically independent molecules. Therefore, four carboxylate oxygen sites are expected to be overlapped in the same region, giving a complicated line shape. In such a case, it is useful to use standard experimental approaches, such as dynamic-angle spinning (DAS), double rotation (DOR), multiple-quantum MAS (MQMAS), and satellite-transition MAS (STMAS), which remove second-order quadrupolar interactions. For example, Figure 7 indicates the contour plot of the two-dimensional (2D) ^{17}O triple-quantum MQMAS spectra of [^{17}O]-L-valine obtained with rotor synchronisation for the t_1 increments with the MAS rate of 15.0 ± 0.1 kHz.

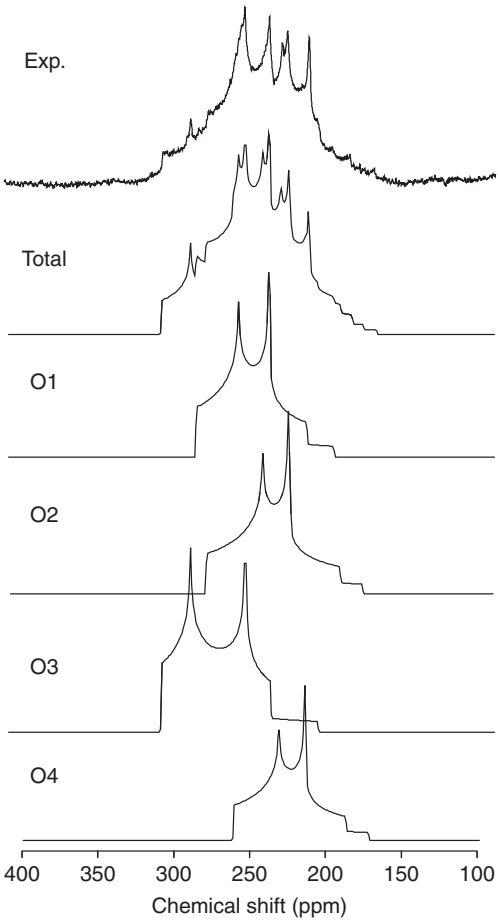

Figure 6 Experimental (top) and calculated 1D ^{17}O MAS NMR spectra for [^{17}O]-L-valine, recorded at 16.4 T. The calculated total spectrum is a sum of O1, O2, O3 and O4 subspectra with a 1:1 intensity ratio. Reproduced with permission from Ref. 51.

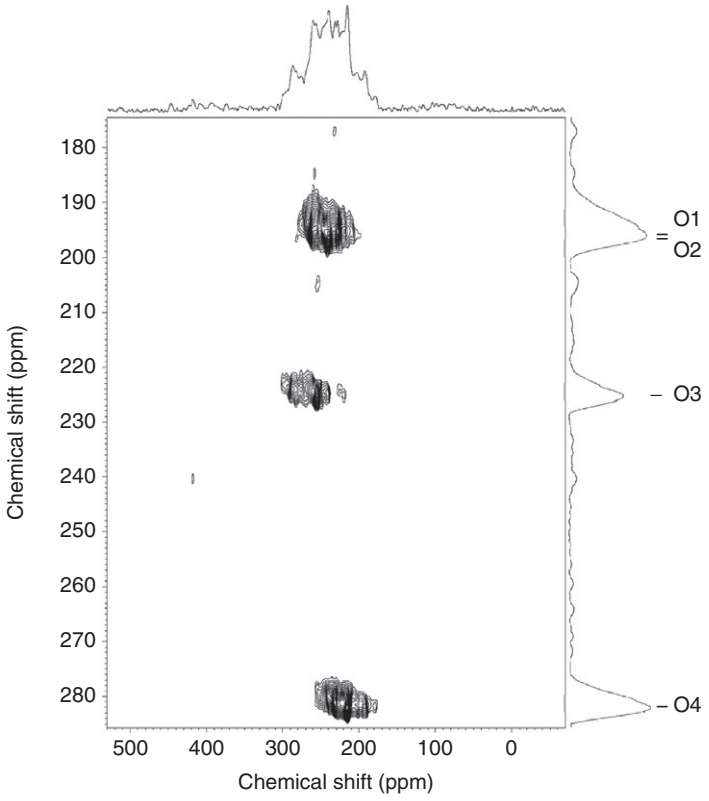

Figure 7 Contour plot of ^{17}O z-filter 3QMQMAS spectrum of [^{17}O]-L-valine, recorded at 16.4 T. Reproduced with permission from Ref. 51.

Both the F1 and F2 projections of the 2D MQMAS spectra are also shown on the side and at the top, respectively. As seen in Figure 7, three isotropic peaks are observed in the 2D MQMAS spectrum. The slice along the t_2 direction of each peak corresponds to the 1D ^{17}O MAS spectrum for each oxygen site, and the spectral analysis can easily be done. It is, however, noted that MQMAS spectra do not generally contain quantitative information concerning peak intensities. Moreover, such cross-sectional spectra are often distorted by multiple-quantum effects. Therefore, spectral simulation of the 1D MAS spectrum is required to confirm the final ^{17}O NMR parameters, and the NMR parameters estimated from the analysis of MQMAS spectra may be used for the initial values of the simulations. Such simulated results are given in Figure 6, where the calculated spectrum is the sum of O1, O2, O3, and O4 sub-spectra with 1:1:1:1 intensity ratio. A source of error arises from the spectral fitting into relatively broad line shapes. Dupree and coworkers[53] report that ^{1}H-decoupled ^{17}O DOR produces high-resolution ^{17}O NMR spectra of amino acids, giving a very small margin of error, for example ± 0.5 ppm and ± 0.05 MHz for δ_{iso} and C_Q, respectively.

4.1.2. Stationary NMR experiments

For extraction of the ^{17}O CS tensor components, analysis of stationary NMR spectra is one of the most straightforward methods. Figure 8 shows the experimental and calculated ^{17}O stationary NMR spectra of [^{17}O]-L-alanine hydrochloride observed and calculated at (A) 9.4, (B) 11.7 and (C) 21.6 T.[54]

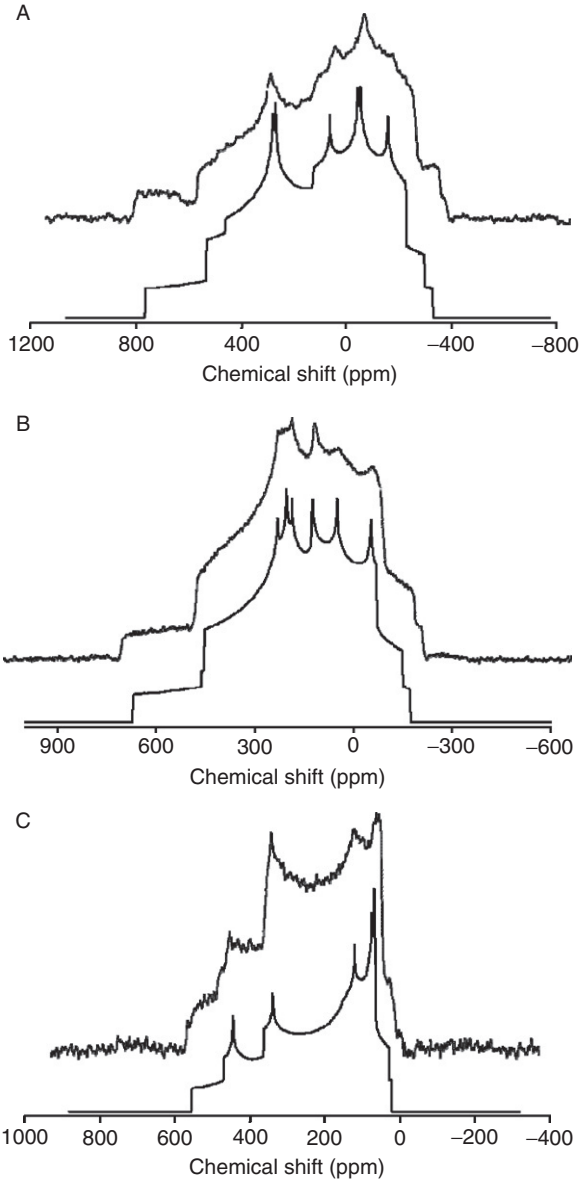

Figure 8 Experimental and calculated ^{17}O stationary NMR spectra for [^{17}O]-L-alanine hydrochloride, recorded at (A) 9.4, (B) 11.7 and (C) 21.6 T. Reproduced from Ref. 54.

Two resonances are expected to arise from the carbonyl and hydroxyl oxygen atoms. In the figure, the simulated total spectrum (C=O and OH) is the sum of C=O and OH sub-spectra with 1:1 intensity ratio, where a stationary NMR line shape, arising from the sum of the CS and the second-order quadrupolar contributions (taking the relative orientations into consideration), as described in Section 3.2, is used for each sub-spectrum. There are 8 independent NMR parameters (δ_{11}, δ_{22}, δ_{33}, C_Q, η_Q, α, β, γ) for each oxygen site, so that many independent NMR parameters (in this case, a total of 16) have to be simultaneously used for spectral simulation. Using the results for the analysis of the ^{17}O MAS experiments that could yield δ_{iso}, C_Q and η_Q for each site, the number of independent NMR parameters can be reduced. Unfortunately, however, it is still not straightforward to analyse a stationary ^{17}O NMR spectrum observed in a single magnetic field because of the fact that a slight change in each NMR parameter is highly sensitive to the theoretical line shape. In particular, the Euler angles are critical. Thus, prior to computer simulation, it is more advantageous to understand or predict the possible set of Euler angles for each functional group. An understanding of ^{17}O NMR parameters, in particular tensor orientations, is very helpful for spectral simulations. From our experience, it is also useful to use multiple magnetic fields, by which ^{17}O stationary NMR line shapes are drastically changed. The simultaneous analysis of stationary NMR spectra observed in various magnetic fields, as shown in Figure 8, is one of the best methods for extracting the ^{17}O CS tensor components unambiguously. As an example, the following ^{17}O NMR parameters were obtained from multiple magnetic field analysis: for C=O, $\delta_{11}=540\pm5$ ppm, $\delta_{22}=425\pm5$ ppm, $\delta_{33}=19\pm5$ ppm, $\delta_{iso}=328\pm2$ ppm, $C_Q=8.3\pm0.1$ MHz, $\eta_Q=0.02\pm0.02$, $\alpha=80\pm8°$, $\beta=90\pm8°$, $\gamma=55\pm8°$; for OH, $\delta_{11}=335\pm5$ ppm, $\delta_{22}=109\pm5$ ppm, $\delta_{33}=87\pm5$ ppm, $\delta_{iso}=177\pm2$ ppm, $C_Q=7.3\pm0.1$ MHz, $\eta_Q=0.21\pm0.04$, $\alpha=56\pm14°$, $\beta=85\pm8°$, $\gamma=105\pm8°$. It is worth pointing out that the error bars of the parameters obtained from the analysis of stationary NMR spectra, that is CS tensor components and the Euler angles, are much larger than those obtained from MAS spectra. Although Dupree and co-workers[55] report that ^{17}O DOR can also produce the same ^{17}O NMR parameters by using information on the intensities and positions of the spinning sidebands, there are still large error bars for those NMR parameters. At the present time, a better solution to the error bar problem has not yet been reported and more work in this direction should be carried out.

4.1.3. Quantum chemical calculations

The last step in the analysis of solid-state ^{17}O NMR spectra is to determine the absolute orientations of the ^{17}O EFG and CS tensors with respect to the molecular frames. For this purpose, one of the best experimental methods is to carry out single-crystal solid-state NMR. There have been several papers in the literature concerning single-crystal ^{17}O NMR of organic/biological solids, reporting the successful determination of ^{17}O NMR tensor orientations in various molecular geometries.[56–59] In general, however, it is quite difficult or nearly impossible to obtain large single crystals suitable for NMR experiments because of the small quantity of ^{17}O-labelled samples. Alternatively, it is convenient to take advantage

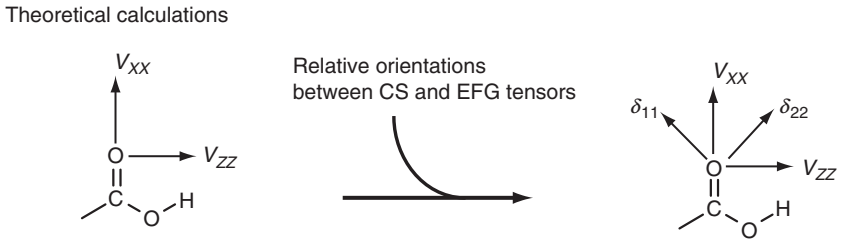

Scheme 3

of the results of quantum chemical calculations. It is assumed that the absolute orientations of ^{17}O EFG tensors obtained from reliable quantum chemical calculations are correct. By combining such ^{17}O EFG orientations with the relative orientations between the CS and EFG tensors, it is possible to determine the absolute orientations of ^{17}O CS tensors with respect to the molecular frame, as depicted in Scheme 3. As examples, the schematic representations for the orientations of ^{17}O NMR tensors in the molecular frame for carboxylate,[60] carboxylic acid[54] and amide[61,62] groups are shown in Figure 9. For the carboxylate groups of amino acids, the V_{YY} and V_{ZZ} components lie in the molecular plane O–C–O, and the direction of the V_{ZZ} component is perpendicular to the C=O bond. Note that because of molecular symmetry, at least one EFG tensor component must be perpendicular to the molecular plane. On the other hand, the δ_{11} and δ_{22} components are roughly found in the molecular plane, and the angles between the δ_{22} components and the C=O bonds are distributed between 20° and 40°, depending on the types of amino acids. For the carbonyl oxygen of the carboxylic group, the V_{XX} and V_{ZZ} components lie in the molecular plane and the direction of the V_{XX} component is parallel to the C=O bond, which is quite different from that of carboxylate oxygen. As can be seen, the tensor orientations are dependent on the local molecular structures, and may become a parameter probing the molecular properties, as well as the magnitudes of the ^{17}O NMR tensor components.

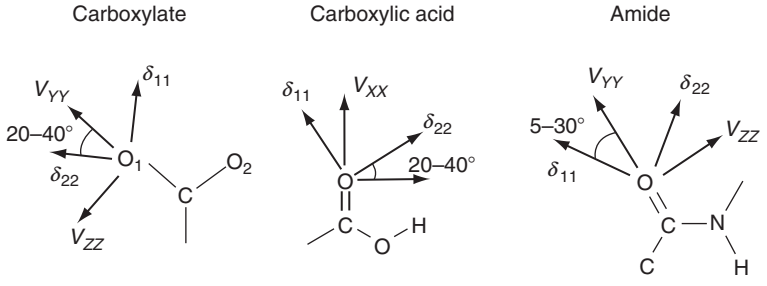

Figure 9 Schematic representations of tensor orientations of typical functional groups.

4.1.4. Experimental confirmation of orientations for ^{17}O NMR tensors

As has been noted, analysis of the ^{17}O MAS and stationary NMR spectra yields not only the magnitudes but also the relative orientations between the ^{17}O CS and EFG tensors. Furthermore, it is possible to establish the absolute orientations of the ^{17}O NMR tensors with the aid of quantum chemical calculations. During this process, theoretical calculations are used for the determination of the ^{17}O EFG tensor orientations. Naturally, it is desirable to obtain experimental confirmation for the calculated results of tensor orientations. Although it is the best experimental method, the single-crystal NMR technique is not always available for biological solids. Alternately, by using polycrystalline samples with double isotropic labels (for example, ^{13}C and ^{17}O), the absolute orientations of the ^{17}O NMR tensors can be determined with the aid of a ^{13}C–^{17}O dipolar vector as an internal reference.[54,63,64] The detailed procedure is explained here. Figure 10 shows the experimental and calculated stationary ^{17}O NMR spectra of polycrystalline [1-^{13}C, ^{17}O]-L-alanine observed at (A) 11.8 T and (B) 16.4 T.[64] In Figure 10(C), the experimental and calculated ^{17}O stationary NMR spectra of [^{17}O]-L-alanine observed at 11.8 T are also shown for reference. Each calculated spectrum is the sum of subspectra for carboxylate oxygen atoms with a 1:1 intensity ratio. The calculated NMR line shapes, including dipolar interactions, will be explained later. On comparison with the experimental ^{17}O NMR spectra of [1-^{13}C, ^{17}O] and [^{17}O]-L-alanine, a dipolar splitting can be clearly observed. It was demonstrated by Chu et al.[35] that, in the presence of dipolar and quadrupolar interactions, stationary NMR line shapes are varied by changes in both the magnitudes and directions of dipolar vectors in the principal axis system of EFG tensors. In other words, information on the direction of ^{13}C–^{17}O dipolar vectors can be obtained by analysing the stationary ^{17}O NMR spectra of [1-^{13}C, ^{17}O]-L-alanine. More importantly, it is possible to determine the absolute orientations of ^{17}O NMR tensors in the molecular frame by combining it with the Euler angles since the dipolar vector is along the C=O bond direction. As shown in Figure 11, the direction of the dipolar vector in the principal axis system of EFG tensors is defined by azimuth and polar angles, denoted as α' and β', respectively.[65] The following three cases are considered when the dipolar vector lies along the (a) V_{XX}, (b) V_{YY} and (c) V_{ZZ} components of the ^{17}O EFG tensors for L-alanine. The azimuth and polar angles for the three cases are (a) $(\alpha', \beta') = (0°, 90°)$, (b) $(\alpha', \beta') = (90°, 90°)$ and (c) $(\alpha', \beta') = (0°, 0°)$. Figure 12 indicates the calculated NMR line shapes of [1-^{13}C, ^{17}O]-L-alanine for the above three cases where the magnetic field is assumed to be at 11.8 T. The magnitudes of the dipolar coupling constants can be estimated from the crystal structure of the L-alanine molecule, determined by the neutron diffraction technique.[66] The dipolar coupling constants are assumed to be -2140 and -2060 Hz for two carboxylate oxygen atoms, whose interactions were included in the above spectral simulations. Clearly, such ^{17}O NMR powder spectra depend upon the orientations of the dipolar vectors. As shown in Figure 10(A) and (B), it is confirmed that the simulated NMR line shapes with a dipolar vector direction of $(\alpha', \beta') = (90°, 90°)$ are in the best agreement with the corresponding two experimental NMR spectra. Thus, the dipolar vector is along the V_{YY} component,

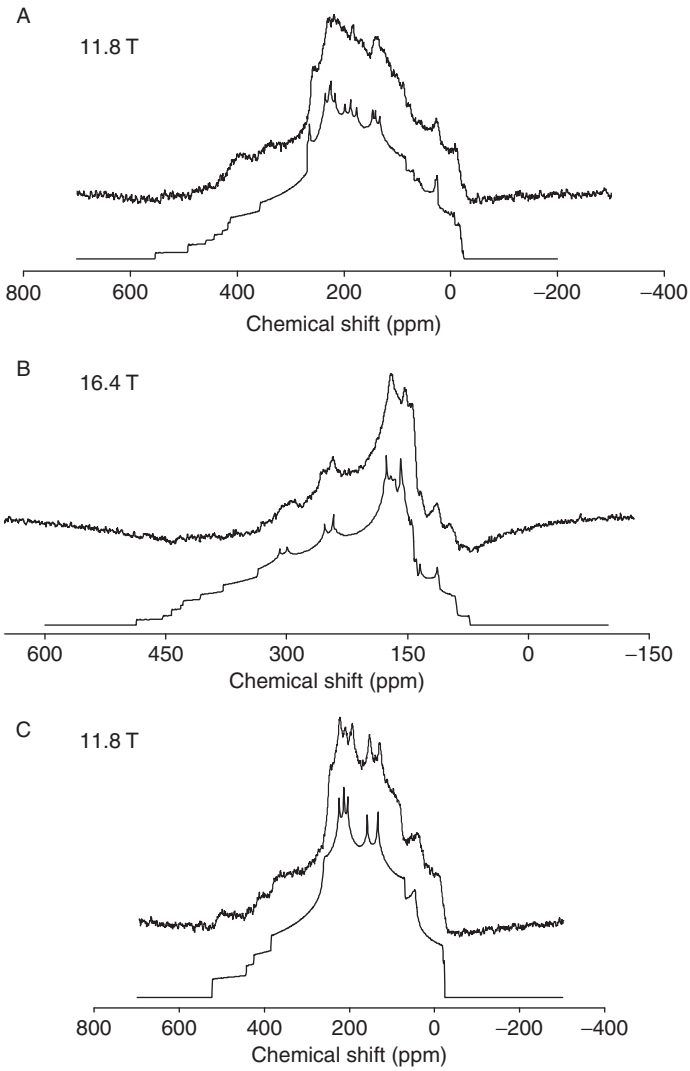

Figure 10 Experimental and calculated ^{17}O stationary NMR spectra for [1-^{13}C, ^{17}O]-L-alanine, recorded at (A) 11.8 and (B) 16.4 T and of [^{17}O]-L-alanine recorded at (C) 11.8 T. Reproduced from Ref. 64.

indicating that the V_{YY} component is parallel to the C=O bond direction. It is important to point out that dipolar interaction is axially symmetric, suggesting that there will be no geometrical information regarding the other EFG tensor components. Due to the molecular symmetry, however, at least one EFG component must be perpendicular to the molecular plane of the carboxylate groups. Moreover, the tensor component associated with the most shielding component, δ_{33}, is expected

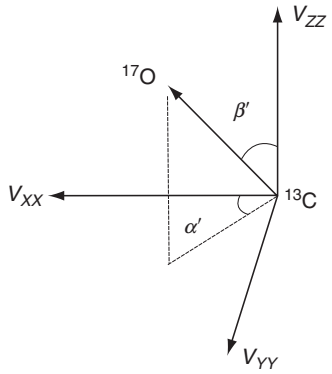

Figure 11 The direction of the dipolar vector, ^{13}C–^{17}O, in the principal axis system of EFG tensors, defined by azimuth and polar angles, denoted as α' and β', respectively.

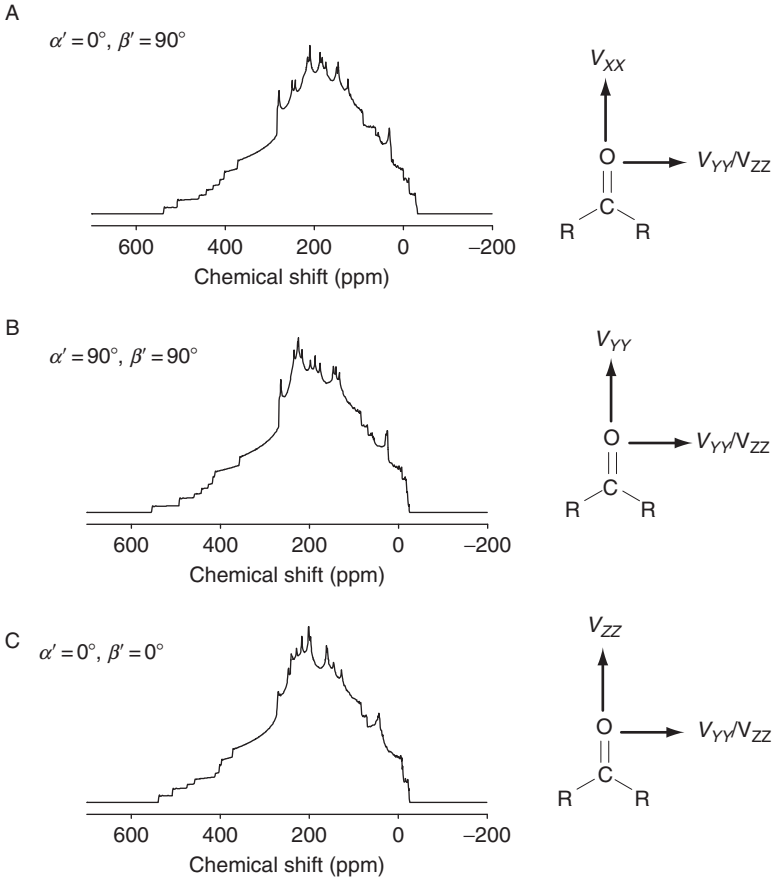

Figure 12 ^{17}O stationary NMR spectra of [1-^{13}C, ^{17}O]-L-alanine calculated at 11.8 T for (α', β') = (0°, 90°), (b) (α', β') = (90°, 90°) and (c) (α', β') = (0°, 0°) together with the schematic representations of the corresponding ^{17}O EFG tensor orientations (right). Reproduced from Ref. 64.

to be approximately perpendicular to the O–C–O plane, in a manner similar to the cases of amide[61,62] and urea,[67] which will be discussed later. Hence, using the Euler angles obtained experimentally, the absolute orientations of the ^{17}O NMR tensors can be unambiguously determined. The schematic orientations of the ^{17}O NMR tensors with respect to the molecular frame in L-alanine are already depicted in Figure 9. Such experimental orientations of ^{17}O NMR tensors become the criteria for evaluating the accuracies of quantum chemical calculations. From our experience, using the standard Gaussian 03/09 program package,[68] high-level *ab initio* calculations, for example B3LYP/cc-pVTZ or 6-311++G(d,p), with a molecular geometry, including hydrogen-bonding partners obtained from neutron or X-ray diffraction experiments, can well reproduce ^{17}O EFG tensor orientations except for cases where η_Q is in the immediate vicinity of 0 or 1. In these areas, it may be difficult to obtain reliable EFG tensor orientations by theoretical calculations.[54]

4.1.5. Dependence of ^{17}O NMR line shapes on experimental conditions

It is worth discussing the relationship between spectral width and experimental conditions, such as the strengths of applied magnetic fields and MAS rates. Figure 13 shows the ^{17}O MAS spectra for [^{17}O]-L-alanine, recorded at (A) 9.4, (B) 14.1, (C) 16.4 and (D) 18.8 T.[33] In principle, the magnitudes of quadrupolar interactions are inversely proportional to the magnetic fields (see Equation (11)). At a glance, the spectral width seemingly decreases as the magnetic fields increase, but such a trend is somewhat different. In order to discuss spectral width, it is necessary to compare the stationary NMR spectra in which the horizontal axes are expressed by the frequency unit, as shown in Figure 14. In the figure, the approximate spectral widths of the ^{17}O NMR line shapes are given in the frequency units. It can be observed that the spectral widths decrease with an increase in the magnetic field from 9.4 to 11.7 T. This is because one primary factor that determines the spectral width is the quadrupolar interaction. On the other hand, the spectral widths increase with an increase in the magnetic field from 11.7 to 16.4 to 21.6 T. Although the broadening effects of quadrupolar interactions decrease, the spectral widths increase because of the fact that the dominant factor is rather CS interactions whose magnitudes are proportional to the strength of the applied magnetic field. As a result, the spectral widths observed at higher magnetic fields become larger than those at lower fields. In addition to the strength of the magnetic field, the sample spinning frequency is an important factor for the determination of line shapes. Figure 15 shows the experimental (left) and calculated (right) ^{17}O MAS NMR spectra of [^{17}O]-*N*,*N*-dicyclohexylurea, observed and calculated at 9.4 T with various sample spinning frequencies.[33] In the range of slow spinning frequencies, the ^{17}O MAS NMR spectra take very complicated shapes. From such complicated line shapes, it is possible to extract information on the CS tensor components and the relative orientations between CS and EFG tensors, that is a slow MAS technique. If the purpose of MAS experiments is simply to extract C_Q and η_Q, and δ_{iso}, however, it is recommended to carry out ^{17}O MAS NMR experiments at MAS rates as high as possible since spectral simulation including spinning sidebands is not trivial. The above two results imply that,

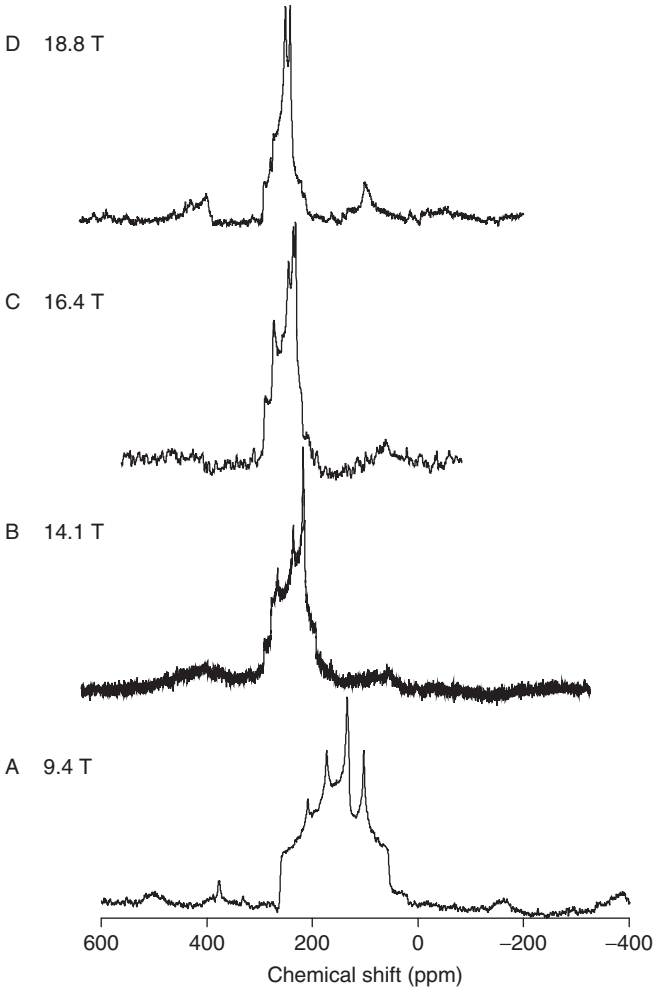

Figure 13 Experimental ^{17}O MAS NMR spectra for [^{17}O]-L-alanine, recorded at (A) 9.4, (B) 14.1, (C) 16.4 and (D) 18.8 T. Reproduced from Ref. 33.

in higher magnetic fields, high MAS frequencies are required for obtaining high-resolution ^{17}O MAS spectra of biological solids.

4.2. Understanding of ^{17}O NMR tensors

The trends in the ^{17}O NMR parameters for carbonyl compounds are reasonably well understood in the comparison between tensor components and molecular properties. In this section, a simple method of spectral assignment using information on hydrogen bond strengths, and the usefulness of current theoretical calculations are given. In addition, the classifications of ^{17}O EFG tensors and the origin of ^{17}O CS tensors are discussed for an understanding of ^{17}O NMR parameters.

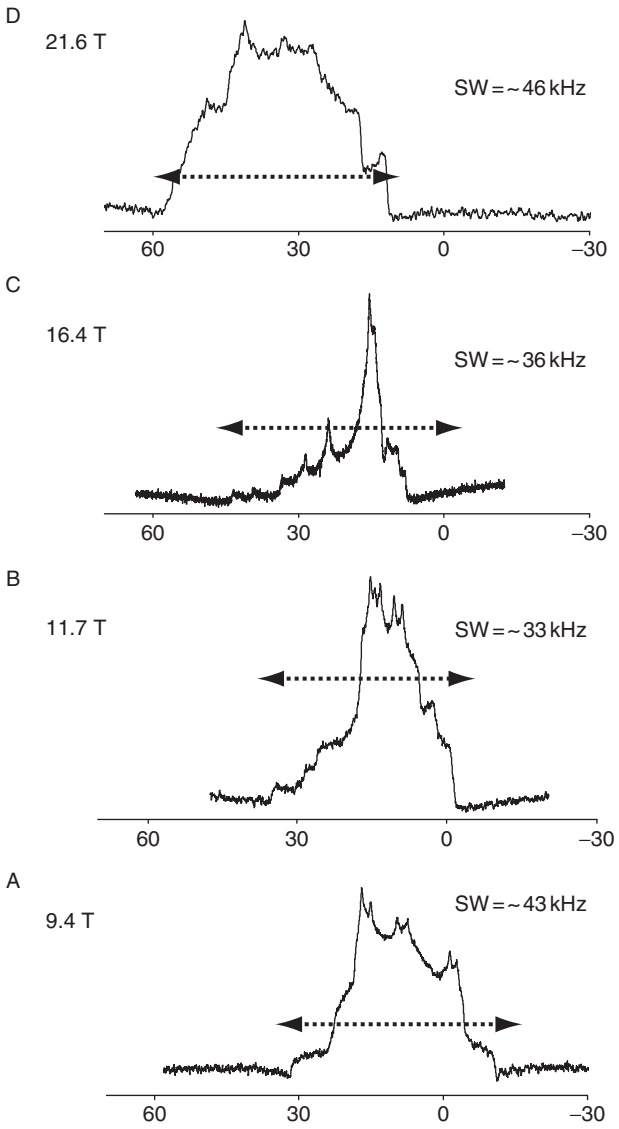

Figure 14 Experimental ^{17}O stationary NMR spectra for [^{17}O]-L-alanine, recorded at (A) 9.4, (B) 11.7, (C) 16.4 and (D) 21.6 T. Each spectral line width in frequency unit, SW, is also given.

4.2.1. Spectral assignment based on hydrogen bonding strength

In comparison with the evaluation of the strength of hydrogen bonds, assignments of ^{17}O NMR spectra may be readily done. The following is the spectral assignment for L-glutamine. In the solid form, L-glutamine molecules exist in the zwitterionic state.[69] Analysis of the MAS spectrum[70] yielded the following parameters: site A, $\delta_{iso} = 301 \pm 1$ppm, $C_Q = 8.10 \pm 0.02$ MHz, $\eta_Q = 0.30 \pm 0.02$; site B,

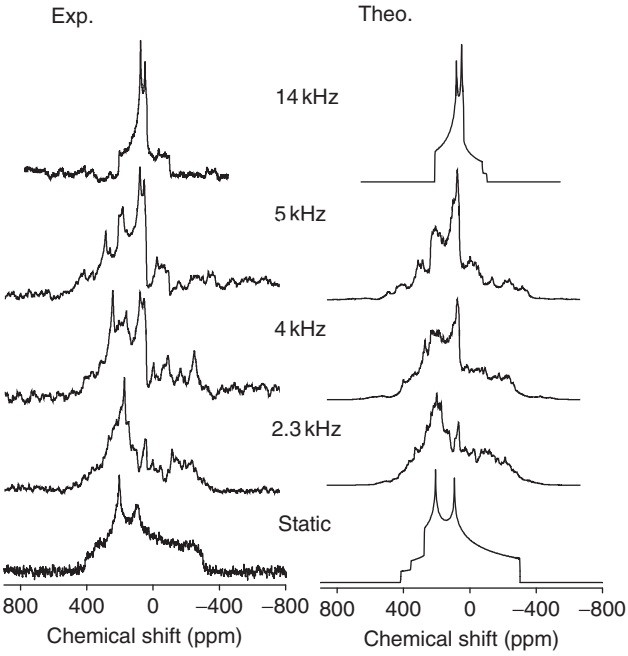

Figure 15 Experimental (left) and calculated (right) ^{17}O MAS spectra of [^{17}O]-*N*,*N*-dicyclohexylurea at various sample spinning rates. Reproduced with permission from Ref. 33.

$\delta_{iso} = 265 \pm 1$ ppm, $C_Q = 7.25 \pm 0.02$ MHz, $\eta_Q = 0.65 \pm 0.02$. Interestingly, the ^{17}O NMR parameters are quite different from each other, and such differences are mainly attributed to different hydrogen-bond environments. Figure 16 displays the schematic representation of the hydrogen-bond geometry for L-glutamine together with C=O bond and hydrogen bond lengths.[69] As seen, O1 is involved in one hydrogen bond, while O2 is involved in two hydrogen bonds. Moreover, the C–O2 bond length (1.260 Å) is larger than the C–O1 bond length (1.238 Å).

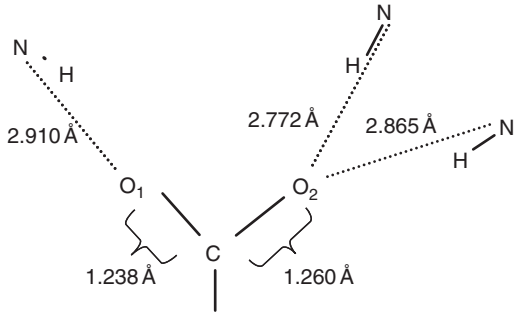

Figure 16 Schematic representation of the hydrogen-bond geometry for L-glutamine together with C=O bond and hydrogen-bond lengths.

Hence, O2 is expected to be involved in a stronger hydrogen-bond environment. Note that the C=O bond length may become a convenient indicator for expressing the strength of hydrogen bonds, for example the stronger the hydrogen bond, the larger the C=O bond length, and vice versa.[25] The relationship between ^{17}O NMR parameters and hydrogen bonding strengths has been well discussed both theoretically and experimentally[25,53,62,71,72] and, for example, the values of ^{17}O δ_{iso} and C_Q tend to decrease with an increase in hydrogen bonding strengths. Thus, it can be deduced that site A (with larger values for δ_{iso} and C_Q) is assigned to O1 (the lower strength of the hydrogen bond).

4.2.2. Examples of quantum chemical calculations

In order to understand the relationship between ^{17}O NMR parameters and molecular properties such as hydrogen bonding strengths and torsion angles, quantum chemical calculations are one of the most powerful tools. Three simple examples are briefly described as follows. As illustrated in Figure 17(A), a theoretical model, in which a single L-alanine hydrochloride molecule forms intermolecular hydrogen bonds with an NH_4^+ molecule[54], can be used for investigating the correlation between C_Q and hydrogen bond lengths. In this model, the hydrogen bond length, $R_{O\ldots N}$, was varied from 1.9 to 3.2 Å in 0.1 Å steps. Figure 18(A) shows the dependence of the carbonyl ^{17}O values on the hydrogen bond lengths, that is the hydrogen bonding strengths. As seen, the C_Q values gradually decrease with a decrease in $R_{O\ldots N}$, which is consistent with the experimental observation.[53,62,71] Although the absolute values are not perfectly predicted by quantum chemical calculations at the present time, the trend, for example the dependence of ^{17}O NMR parameters on the strengths of hydrogen bonds, seems to be true.

Since NMR parameters are highly sensitive to local electric properties, ^{17}O NMR parameters are expected to be affected by not only hydrogen bond lengths but also angles. Figure 17(B) shows another theoretical model in which an Fmoc-L-Ala molecule interacts with a single water molecule.[73] In this model, the hydrogen bond angle, C–O$\cdots$O (water), was varied from 72° to 180° in steps of 12°, and the hydrogen bond distance, R(O$\cdots$O), was kept constant at 2.580 Å. For simplicity, the COOH group and the water (one of the O–H bonds) were placed on the same plane. The calculated results are plotted in Figure 18(B). As expected, the C_Q values depend critically upon the position of the water molecule. Interestingly, a strong influence can be observed at the hydrogen bond angle of approximately 120° (the angle of C–O–H), while a weak effect can be seen at an angle of approximately 180° (the angle of the C_α–C–O bond). This simple model suggests that the three-dimensional position of hydrogen bond donors and the molecular orbitals of hydrogen bond acceptors should be considered to discuss the dependence of ^{17}O NMR parameters on hydrogen bonds. In this sense, the C=O bond lengths may be convenient parameters for simply expressing the strengths of the hydrogen bonds.

The α-helix and β-sheet are common components of the structures of proteins, and such secondary structures are defined by two dihedral angles, ψ and ϕ. Again, it is expected that ^{17}O NMR tensors are related to the changes in the angles. To investigate dihedral angle dependence, a theoretical model of an isolated

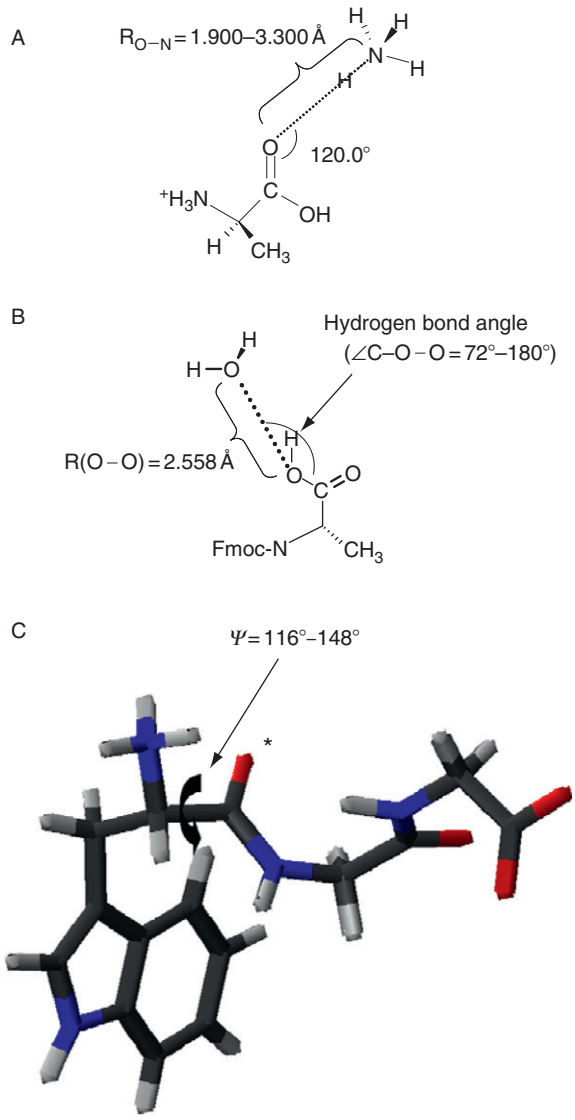

Figure 17 Simple theoretical models for investigations of dependences of C_Q values on (A) hydrogen-bonding lengths, (B) angles and (C) dihedral angles. Reproduced with permission from Refs. [54,70,73].

tripeptide molecule, L-tryptophanyl-glycyl-glycine (WGG), is used, as illustrated in Figure 17(C). In this model, the torsion angle, ψ, was artificially changed from 116° to 148° in steps of 4°.[70] Figure 18(C) indicates the dependence of the carbonyl ^{17}O C_Q values on the torsion angles. From the figure, it can be observed that with an increase in the torsion angles, the values of C_Q gradually decrease.

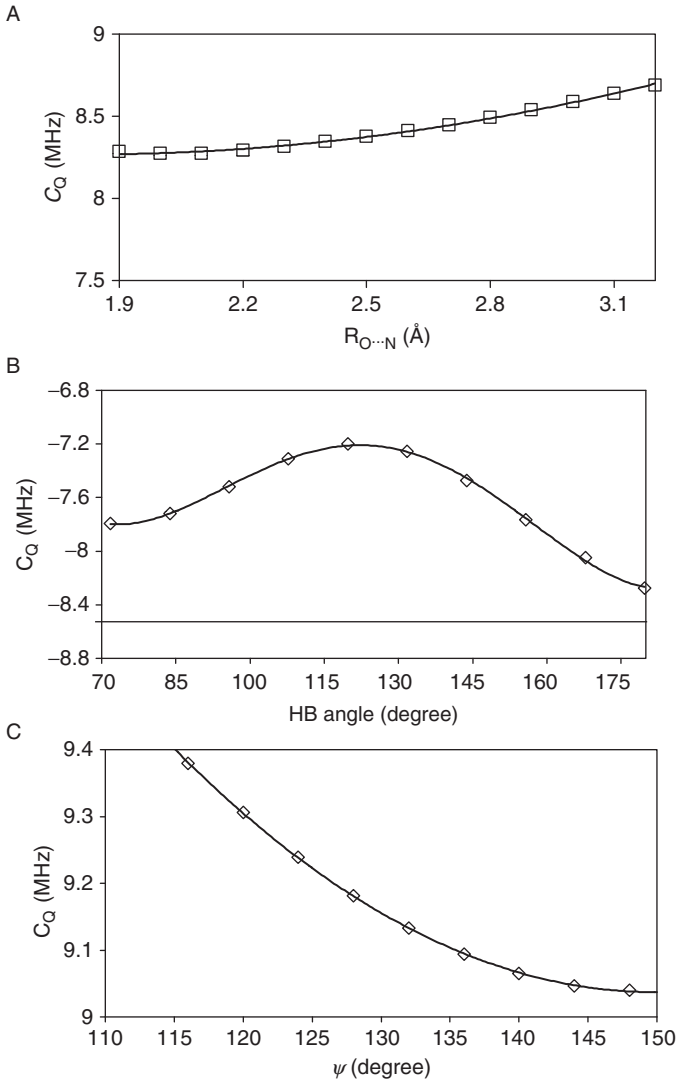

Figure 18 Dependences of calculated C_Q values on (A) hydrogen-bonding lengths, (B) angles and (C) dihedral angles in the models in Figure 17. Reproduced from Refs. 54,70,73.

This indicates that the ^{17}O NMR parameters are potentially sensitive to changes in the conformation of backbone chains in peptides and proteins.[74] The prediction from the above results is that the magnitudes of ^{17}O NMR parameters are the sum of intra- (e.g. secondary structures) and inter- (e.g. hydrogen bonds) molecular interactions. Therefore, in a real biological system, the effects of the two interactions on the NMR parameters should be separated from each other. In the above three examples, only the dependence of the C_Q values are discussed. Of course,

however, any dependence of other NMR parameters such as ^{17}O CS tensors and *J*-coupling, or spectral assignments[75] can be predicted by theoretical calculations for any of the models that experimentalists need. Obviously, the significant potential of theoretical calculations enables more detailed investigations of ^{17}O NMR parameters.

4.2.3. Classifications of ^{17}O electric-field-gradient tensors

As mentioned already, the parameters of the relative orientations between CS and EFG tensors (α, β, γ) are one of the primary factors in determining the line shape of ^{17}O stationary NMR spectra. Thus, it is advantageous to understand and classify the trends of the orientations for ^{17}O NMR tensors. For this purpose, it is helpful to introduce Gready's model,[76,77] by which EFG tensor orientations can be successfully classified into functional groups. It was previously found[78–80], from the literature values obtained by ^{17}O NQR experiments and calculated by quantum chemical approaches, that there are correlations between the C_Q values and η_Q for various carbonyl compounds. It is important to remember that these two parameters are originally independent of each other. As demonstrated by Gready, a linear relationship is observed between the C_Q values and η_Q for carbonyl compounds by a distinction of the signs of three EFG tensor components, V_{XX}, V_{YY} and V_{ZZ}. In this model, the range of η_Q lies between -1 and $+1$, and the signs of the C_Q values are distinguished. The concept of Gready's model is schematically represented in Figure 19.

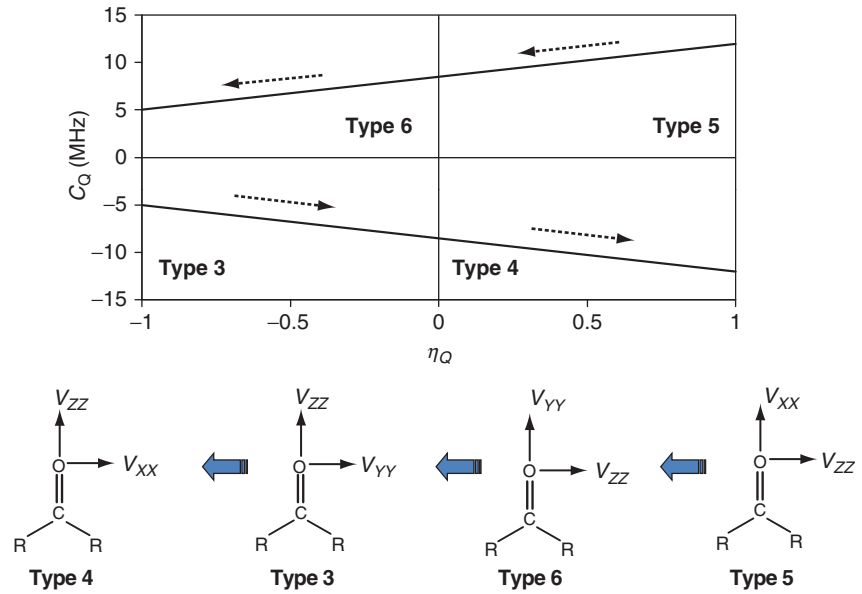

Figure 19 Schematic representation of Gready's model (upper) in which ^{17}O EFG tensor orientations are linked by a linear correlation between C_Q and η_Q. The orientations of ^{17}O EFG tensors (lower) are also shown.

The number of possible orientations of ^{17}O EFG tensors for the carbonyl compound is 12, some of which are illustrated in the figure. For example, the tensor orientation in the fourth quadrant is type 4, where the V_{YY} component is perpendicular to the molecular plane and the V_{ZZ} component is parallel to the direction of the C=O bond. According to Gready's model, all 12 orientations are linked by a linear correlation in a plot where the horizontal and vertical axes correspond to the C_Q values and η_Q, respectively. There are two major rules in this plot: (1) when $\eta_Q = 0$, the V_{XX} and V_{YY} components are interchanged in the tensor orientations; (2) when $\eta_Q = \pm 1$, the V_{YY} and V_{ZZ} components are interchanged by switching the sign of the C_Q values. For example, in the first quadrant in Figure 19, the tensor orientation is type 5, in which the V_{XX} and V_{ZZ} components lie in the C=O plane and the V_{XX} component is along the C=O bond. In the region, the magnitudes of the C_Q values gradually decrease with a decrease in η_Q. When the C_Q values cross over the y-axis, the ^{17}O EFG tensor orientation is switched from type 5 to type 6, according to rule 1, and the linear relationship is still observed in the second quadrant. When the line reaches $\eta_Q = -1$, the orientation is switched from type 6 to type 3, according to rule 2. In this way, the linear correlation between the C_Q values and η_Q continues in all 12 possible orientations. Note that the slope of the line is arbitrary. Using several experimental data for the ^{17}O EFG tensors of aldehyde, ketone, amide and urea, the relationship is plotted in Figure 20.[54] As seen, a linear correlation is clearly observed between the two EFG tensor parameters obtained experimentally. The ^{17}O EFG tensor orientations for aldehydes and ketones are found to be of type 5, while those for amides, amino acids and urea are of type 6. It is expected that, in carbonyl compounds, the C_Q value of approximately 9.5 MHz is a crossover point for ^{17}O EFG tensor orientations. From the literature,[50,53] the carbonyl oxygen in carboxylic acids is reported to have C_Q values of 8.0–9.0 MHz and η_Q in the immediate vicinity of 0. Although recent quantum chemical calculations can provide reliable results, unfortunately, they cannot perfectly reproduce the experimental data. Thus, caution should be

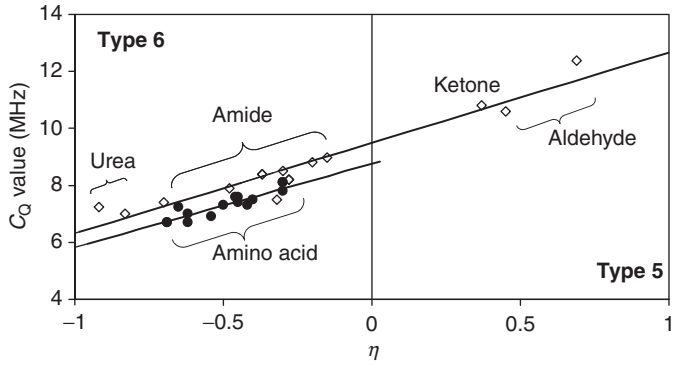

Figure 20 The linear correlation between C_Q and η_Q for various oxygen-containing compounds. Reproduced from Ref. 64.

exercised with theoretical calculations in predicting ^{17}O EFG tensor orientations for the carbonyl oxygen in carboxylic acids. To the best of my knowledge, the EFG tensor orientation of type 3 has not yet been reported, but a compound whose C_Q value is less than approximately 6 MHz may have that orientation. For reference, a C_Q value of 6.65 ± 0.05 MHz and $\eta_Q = 1.00 \pm 0.05$ with the orientation of type 6 was reported for a nucleic acid (thymine) whose oxygen is involved in strong hydrogen bonds.[81] For type 5, larger absolute values for η_Q tend to exhibit larger C_Q values, while for type 6 the opposite trend is observed. One must distinguish cases of amino acids from those of carbonyl compounds since amino acids are classified as compounds having a single bond or conjugation. Nevertheless, a similar trend can be clearly observed for amino acids, as shown in the second quadrant of the figure. It is helpful to take advantage of the above relationship for spectral simulations of ^{17}O NMR spectra. For example, by having information on a functional group, it may be possible to estimate the approximate ranges of the C_Q values or η_Q, which can be useful for setting the initial NMR parameters in the spectral analysis of ^{17}O MAS spectra. From the magnitudes of C_Q, the orientations of ^{17}O EFG tensors can also be deduced. Knowing that for most carbonyl compounds the direction of the δ_{33} components of ^{17}O CS tensors tends to be perpendicular to the molecular plane, one can roughly estimate the Euler angles, which will become good initial NMR parameters for the spectral analysis of ^{17}O stationary NMR spectra.

4.2.4. Origin of ^{17}O chemical shielding tensor components

The range of the ^{17}O CS tensors is widely distributed. For example, the range of δ_{iso} lies approximately between 0 (water) and 400 ppm (carbonyl oxygen). Furthermore, the tensor component with the most paramagnetic contribution, δ_{11}, roughly varies from 300 (ureas) to 1500 ppm (aldehydes). In order to understand the trends of ^{17}O CS tensors, it is meaningful to consider of the origin of ^{17}O CS. According to Ramsey's theory,[82] CS at a nucleus can be divided into diamagnetic and paramagnetic contributions. The diamagnetic contribution shows little orientation dependence, and the effect on CS anisotropy can be safely ignored. On the other hand, the paramagnetic contribution plays a critical role, and the paramagnetic contribution of δ_{11} components is mainly responsible for CS anisotropy. The direction of the δ_{11} component is approximately along the C=O bond in most carbonyl compounds, except for urea. For amides, it is off the C=O bond by approximately 5–30° due to the local molecular symmetry, as illustrated in Figure 9. Assuming that the difference in angular momentum for one electron promotion (L) in Ramsey's equation[82] is ignored among the various carbonyl compounds, the magnitude of the paramagnetic contribution is inversely proportional to the difference in energy gaps between the relevant molecular orbitals. Hence, the variation of δ_{11} mainly arises from a magnetic-field-induced mixing between n and π^* molecular orbitals, as illustrated in Figure 21(A). A formaldehyde molecule was used as a model in the figure. The energy gap between the two molecular orbitals is relatively small because in most carbonyl compounds, the n and π^* molecular orbitals represent the highest occupied molecular orbital (HOMO) and lowest unoccupied molecular orbital (LUMO),

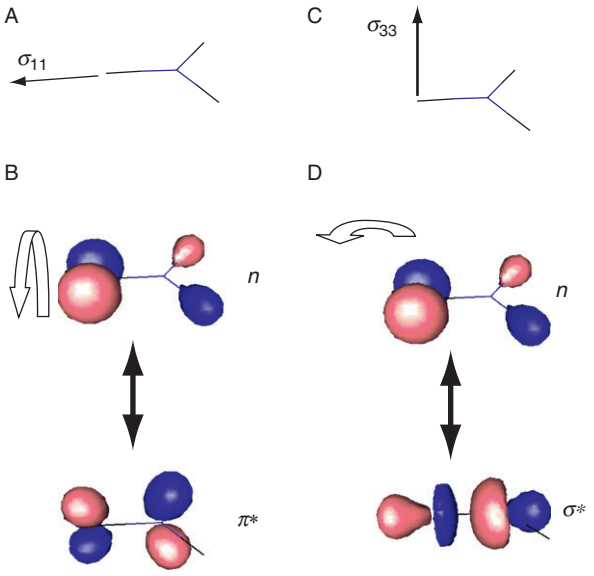

Figure 21 (A) The direction of the δ_{11} component of formaldehyde, (B) the relevant molecular orbital (MO) mixing for the δ_{11} component, (C) the direction of the δ_{33} component and (D) the relevant MO mixing for the δ_{33} components. Reproduced from Ref. 33.

respectively. This is the reason why the magnitudes of the δ_{11} components are large. On the other hand, the tensor component with the most shielding, δ_{33}, exhibits very little change among carbonyl compounds. The direction of δ_{33} is perpendicular to the molecular plane (see Figure 21(C)). Among all the MOs localised at the carbonyl fragment, $n \leftrightarrow \sigma^*$ mixing is the most important for the paramagnetic contribution in δ_{33}, as shown in Figure 21(D). In general, the paramagnetic contribution along this direction is rather small because of the fact that the energy gap of $n \leftrightarrow \sigma^*$ molecular orbitals is large in most cases.

4.2.5. Relationship between electric-field-gradient and chemical shielding

Although they are independent NMR parameters, the ^{17}O CS and EFG tensors show a correlation. Cheng and Brown[79,83] pointed out that there is a linear relationship between the isotropic ^{17}O chemical shifts and C_Q values in carbonyl compounds. Using the Karplus–Pople formula,[84,85] they demonstrated that the calculated ^{17}O paramagnetic components are proportional to the carbonyl π bond population, which is also related to the magnitudes of ^{17}O EFG tensors. Oldfield and co-workers[86] also reported that there are correlations between infrared C=O vibrational frequencies ν(C=O) and ^{17}O δ_{iso}, between ν(C=O) and ^{17}O C_Q, and between δ_{iso} and C_Q, using the experimental data of a variety of C^{17}O-labelled heme proteins. Similar correlations[87,88] have also been reported in ^{59}Co NMR. As a general trend, larger C_Q values tend to give larger δ_{iso} and CS tensor components, except for δ_{33}, which may be useful for spectral simulations.

5. APPLICATIONS OF SOLID-STATE ^{17}O NMR IN BIOCHEMISTRY

There have been many papers reporting the biological applications of solid-state ^{17}O NMR.[89–100] This section briefly describes several notable examples of ^{17}O NMR for biological solids, including ^{13}C–^{17}O Rotational Echo Adiabatic Passage Double Resonance (REAPDOR) experiments,[100] the ONIOM methods for NMR calculations[27] and ^{17}O NMR studies of carbohydrates[98] and a peptide–lipid complex.[92]

5.1. ^{13}C–^{17}O REAPDOR experiments

X-ray diffraction analysis is one of the most common methods for determining the structures of proteins. However, it is not always possible to obtain suitable crystals for diffraction experiments, for example membrane proteins and amyloids. Solid-state NMR is a powerful tool for providing atomic-scale information on structures, which can be applied to non-crystalline samples. For this purpose, one of the most efficient methods is the REDOR-type experiment, by which the quantitative determination of internuclear distances can be successfully made. Recently, Gullion, Asakura and co-workers[100] presented the advantage of ^{13}C–^{17}O REAPDOR techniques for measuring ^{13}C–^{17}O intermolecular distances in peptides. Two types of tripeptide L-alanyl-alanyl-alanine were prepared as a parallel β-sheet or an anti-parallel β-sheet. Using selective labelling procedures, the two short and long intra-sheet distances were arranged for parallel and anti-parallel β-sheets, respectively, as shown in Figure 22. For sample preparations, the ^{13}C isotope was labelled into the carboxylic group in the *C*-terminal residue, Ala-Ala-[1-^{13}C]Ala, and the ^{17}O isotope in the second residue, Ala-[^{17}O]Ala-Ala, which were partially mixed. Figure 23 shows the ^{13}C–^{17}O REAPDOR curves for parallel (●) and anti-parallel (▲) peptides. The solid line is the REAPDOR master curve generated by the ^{13}C–^{17}O internuclear distance of 4.72 Å, taking into account 36% ^{17}O labelling. Although the solid line does not fit well in the longer evolution time, the dashed line (parallel β-sheet), considered as an effective dipolar coupling, which arises from other multiple longer-range C=O distances, is in good agreement with the experimental data. The result clearly demonstrates that ^{13}C–^{17}O REAPDOR experiments can potentially provide accurate internuclear distances in labelled peptides, which will be applied to protein structural analyses in the near future.

5.2. ONIOM method for ^{17}O NMR calculations

Theoretical calculations are valuable tools for analysing solid-state ^{17}O NMR spectra. As mentioned in Section 4.1, for example the absolute orientations of ^{17}O NMR tensors in a molecular frame can be readily determined by *ab initio* calculations. However, a key problem of ''accuracy'' always receives attention. In many papers in the literature,[62,72,75,81,89] the calculated results for the magnitudes of ^{17}O CS tensors are compared with those of experimental data. It seems that the quantum chemical approach is the most frequently used and can yield reasonable

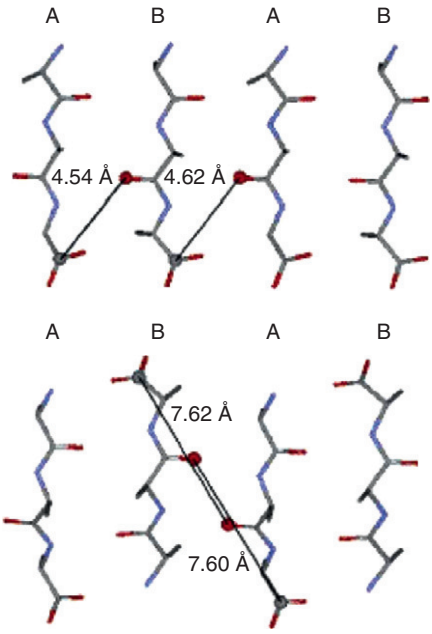

Figure 22 Intrasheet distances between ^{13}C and ^{17}O in the parallel (upper) and anti-parallel (lower) sheets for L-alanyl-alanyl-alanine. Reproduced with permission from Ref. 100.

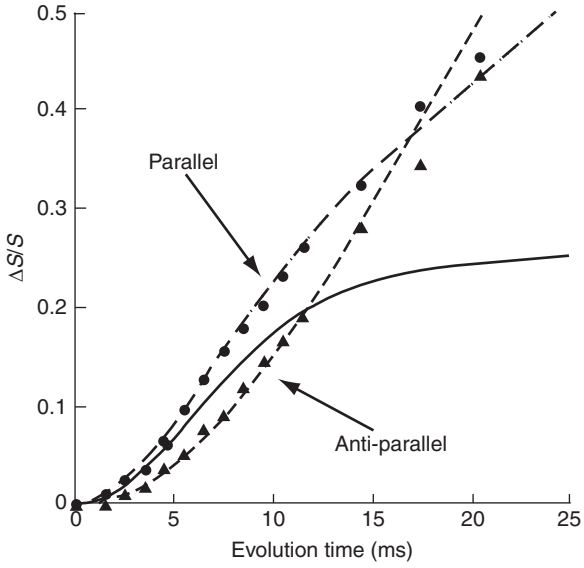

Figure 23 ^{13}C–^{17}O REAPDOR curves for parallel and anti-parallel β-sheets of L-alanyl-alanyl-alanine. Reproduced with permission from Ref. 100.

results for small molecules. Very often, the choice of molecular geometry is of importance for biological solids in the presence of hydrogen bonding networks. It has been established[62,81] that in order to improve the calculated results, intermolecular interactions, that is the effect of hydrogen bonds, have to be considered in the molecular geometry, which is called a molecular cluster model. The molecular cluster model works well for small molecules. Unfortunately, however, high computational cost is involved for larger molecular systems. Moreover, a termination problem cannot be avoided for the cluster model. On the other hand, the solid-state physical approach has recently been applied to calculations of NMR properties with periodic boundary conditions. The advantage of this method is that the limits of cluster size and the termination problem can be neglected. For chemical-shielding calculations, the gauge-including projected augmented wave (GIPAW) method with plane wave pseudopotentials[26] is applied. Solid-state ^{17}O NMR calculations using this approach have been reported.[75] However, there is still a disadvantage with the problem of the exchange-correlation functional since the approach is limited to only DFT calculations. After all, it is safe to say that every method has some drawback and advantage. Recently, Nakajima has proposed a new theoretical scheme for the calculation of solid-state NMR properties, including ^{17}O CS and EFG tensors.[27] This approach is based on the ONIOM method[28,29], which combines quantum chemical and solid-state physical approaches to solid-state NMR calculations. Accordingly, the ONIOM method has the best of both quantum chemical and solid-state physical approaches and successfully reduces the disadvantages. In principle, CS constants are local properties. Thus, a high-level calculation is required only for the close neighbourhood of a nucleus of interest, while a low-level calculation is sufficed in the remaining part. In Nakajima's approach, the high-level calculation is a quantum chemical calculation, such as second-order Møller–Plesset perturbation (MP2), coupled-cluster, complete active-space self-consistent field, and hybrid-type generalised-gradient approximation (GGA) DFT calculations with Gaussian-type orbital (GTO) basis functions, while the low-level calculation is the NMR calculation with local density approximation (LDA) or the pure GGA functional using plane waves and pseudo-potentials. Figure 24 shows the structure of thymine used for ONIOM calculations, which was cut from a crystalline structure determined by X-ray diffraction analysis.[101] Since the positions of the hydrogen bonds were not reported in the literature, partial structural optimisations were carried out by the ONIOM method. The CS constants were converted into chemical shifts using Equation (6) with 310 ppm of the CS for H_2O. The calculated results for ^{17}O CS tensors together with those from the cluster model and the experimental data[81] are summarised in Table 2. As seen, the cluster model gives reasonable values for δ_{iso} in O2 and O4. Unfortunately, however, the δ_{11} and δ_{22} components are largely overestimated. The difference between the theoretical and experimental results of the δ_{11} components for O4 is approximately 150 ppm. Since δ_{iso} is the average value among the three components, the agreement of δ_{iso} may be accidental in the cluster model. On the other hand, the ONIOM method can well reproduce the experimental results, including the tensor components. In particular, the agreement of the δ_{11} components in both oxygen atoms is good.

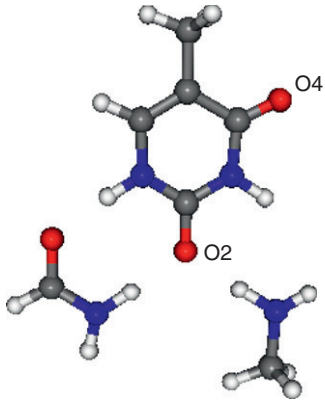

Figure 24 The structure of thymine used for ^{17}O NMR calculations, cut from the experimental structure. Since the positions of hydrogen bonds were not reported in the literature, [ref. 101] the partial structural optimisations were carried out by the ONIOM method. This figure was kindly provided by Prof. Nakajima.[27]

TABLE 2 Calculated results for ^{17}O CS tensors of thymine together with those from the cluster model and the experimental data[81]

Method	Site	δ_{iso}	δ_{11}	δ_{22}	δ_{33}
ONIOM	O2	194	278	260	44
	O4	318	585	408	−39
Cluster	O2	226	327	306	45
	O4	392	720	491	−34
Exp.	O2	200(5)	290(10)	270(10)	20(10)
	O4	325(5)	570(10)	360(10)	20(10)

Values are given in ppm. Uncertainties in the last digits are given in parentheses.

The ONIOM method can also yield ^{17}O EFG tensors accurately (data not shown). At the present time, this approach is one of the best calculation methods for predicting ^{17}O NMR tensors, and is also capable of CS tensor calculations for heavy-element systems, which will be applied to various research fields.

5.3. Solid-state ^{17}O NMR study of carbohydrates

Compared with those of carbonyl oxygen sites, solid-state ^{17}O NMR studies for hydroxyl groups or ether linkages are relatively uncommon in biological compounds. Solid-state ^{17}O NMR investigations of glycosidic and hydroxyl groups in carbohydrates were pioneered by Grandinetti and co-workers.[98] Figure 25 shows the experimental and simulated ^{17}O MAS spectra observed at 19.6 T for a series of ^{17}O-labelled carbohydrates.

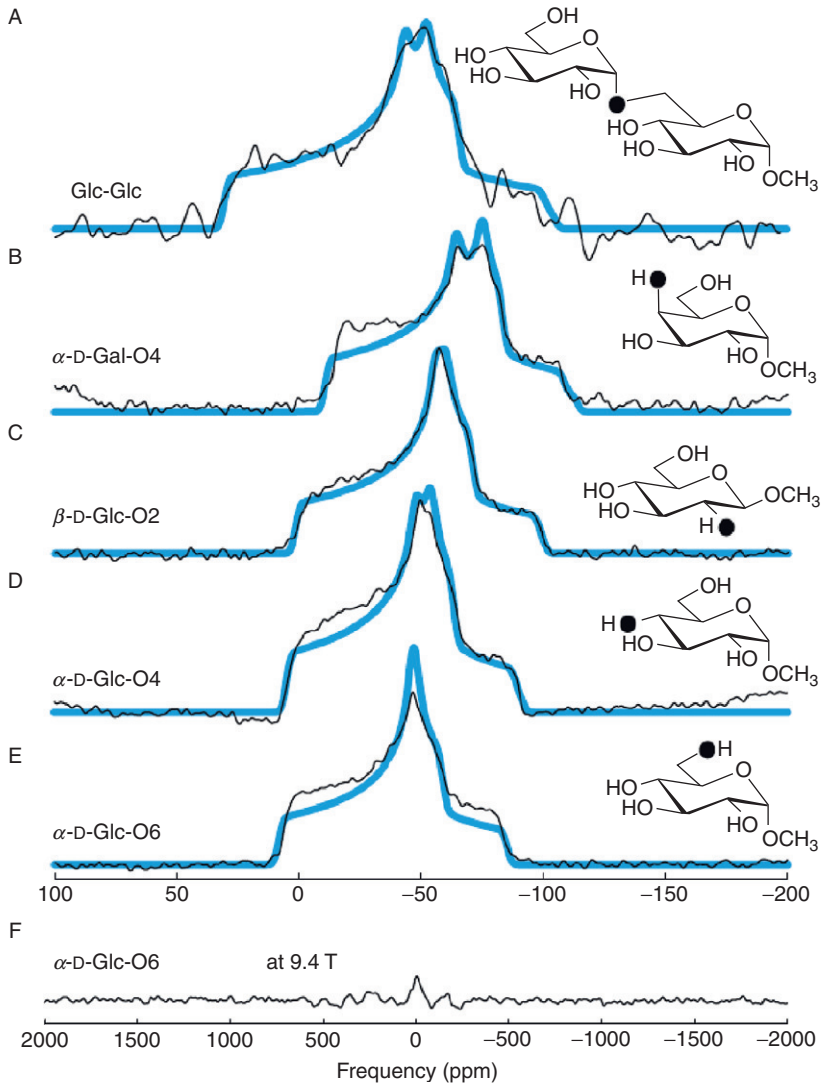

Figure 25 Experimental and calculated ^{17}O MAS spectra of (A) a glycosidic oxygen in disaccharide and (B)–(F) hydroxyl oxygen sites in methyl glycosides, observed at 19.6 T except for (F) at 9.4 T. Reproduced from Ref. 98.

The ^{17}O NMR spectrum of glycosidic oxygen in the disaccharide methyl α-D-glucopyranosyl (1→6) α-D-glucopyranoside (6-^{17}O) is shown in Figure 25(A), and spectral analysis yielded $\delta_{iso} = 32.2$ ppm, $C_Q = 10.75$ MHz, and $\eta_Q = 0.89$. It was previously shown by Clark and Grandinetti[102] that the magnitudes of the ^{17}O EFG tensors at the bridging oxygen atom are dependent on a combination of molecular properties, such as a coordinating atom group number, coordinating atom–oxygen distance, and bridging oxygen angle. In addition, for X–O–X linkage,

the nature of the covalently coordinated atoms plays an important role in determining the magnitude of the C_Q values. Hence, Grandinetti and co-workers proposed the possibility of predicting C–O–C angles and C=O distances from measurements of the C_Q values and η_Q in carbohydrates, which will be valuable information for local structural analyses of glycopeptides, glycoproteins, or saccharide binding proteins. From the spectral analyses of the hydroxyl groups for the methyl glycosides in Figure 25(B)–(D), it was found that the range of C_Q values lies between 8.76 and 9.51 MHz. Interestingly, deviation among the glycosides is very small, approximately less than 10%. In order to evaluate the dependence of the C_Q values of hydroxyl oxygen on local molecular structures, theoretical calculations were carried out for a methanol model in which the C–O–H angles and O–H distances were varied. The results showed that the magnitudes of the ^{17}O EFG tensors of hydroxyl oxygen are hardly affected by changes in the angles and distances, which is consistent with the experimental observations. Grandinetti and co-workers suggested that such structural invariance of the C_Q values of hydroxyl groups will be advantageous for further NMR investigations of oriented samples or correlation experiments.[98] For evaluating the magnetic field dependence, the ^{17}O MAS spectrum of methyl glycoside observed at 9.4 T with an identical number of accumulations is shown in Figure 25(F). Clearly, it is more advantageous to carry out ^{17}O NMR measurements for hydroxyl oxygen at higher magnetic fields. This may be because the primary factor for determining the spectral width of hydroxyl oxygen, whose CS anisotropy is relatively small compared to that of carbonyl oxygen,[50] is second-order quadrupolar interactions. In the end, it is remarkable that current solid-state ^{17}O NMR methods can make it possible to analyse biological compounds whose C_Q values are more than 10 MHz.

5.4. Solid-state ^{17}O NMR study of peptides in lipids

For biological investigations, solid-state NMR has the advantage that, in contrast to solution NMR, molecular size is not limited, in principle. For solid-state ^{17}O NMR, however, weak signal intensities may become serious obstacles to biological applications. Relatively early in time, Watts and co-workers[92] evaluated the signal sensitivity of solid-state ^{17}O NMR using ^{17}O-labelled peptides incorporated in multi-lamellar vesicles. A transmembrane peptide, WALP23, was chosen so that the peptide was expected to form an α-helix in lipids. The peptide was synthesised by an Fmoc solid-phase peptide synthesis protocol, during which ^{17}O-Fmoc-alanine was used for selective labelling. The enriched Fmoc-amino acid was prepared with $H_2{}^{17}O$, whose enrichment level is 70 at.%.[103,104] The selectively ^{17}O-enriched peptide and lipid were mixed in 1:10 molar ratio. Figure 26 shows the experimental and simulated ^{17}O MAS spectra of ^{17}O-[Ala12]-WALP23 in a lipid with a sample spinning frequency of 11 kHz, observed at 14.1 T. The MAS rate was set to be low (~11 kHz) to avoid damage to the sample, and a few spinning side bands appeared in the MAS spectrum. Nevertheless, from the analysis of the ^{17}O MAS spectrum, the following ^{17}O NMR parameters could be successfully obtained: $\delta_{iso} = 315 \pm 1$ ppm, $C_Q = 8.55 \pm 0.15$ MHz and $\eta_Q = 0.24 \pm 0.03$. This experiment obviously demonstrates the feasibility of solid-state ^{17}O NMR for biological

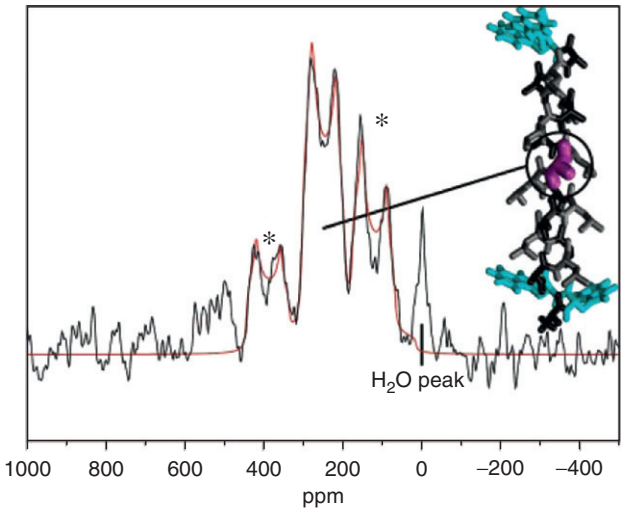

Figure 26 Experimental and calculated ^{17}O MAS spectra of ^{17}O-[Ala12]-WALP23 in lipid, observed at 14.1 T with the MAS rate of 11 kHz. The peaks marked by * are the spinning sidebands. Reproduced from Ref. 92.

applications to membrane proteins. The authors also pointed out the possibility of estimating C=O bond lengths from δ_{iso} determined experimentally because a correlation between δ_{iso} and C=O bond lengths was previously obtained. In this case, the bond length of C=O in the peptide incorporated in the lipid was estimated to be 1.223 Å. Such an application is potentially useful for investigating the local deformation of α-helices induced by a membrane.

As mentioned already, both experimental and theoretical studies of solid-state ^{17}O NMR in amino acids and peptides[25,53,105] demonstrate that there is a linear correlation between δ_{iso} and the corresponding C=O bond lengths. From the paper by Yates et al.,[25] the C=O bond lengths become a convenient indicator for expressing hydrogen-bond strengths, that is the longer the C=O bond length, the stronger the hydrogen-bond character. Figure 27(A) shows the correlation between δ_{iso} and the C=O bond lengths for some amino acids determined by X-ray or neutron diffraction analyses.[105] An approximated straight line is also given with the equation in Figure 27. It should be noted that the data are limited to amino acids, that is carboxylate groups, which result in a narrow range of C=O bond lengths compared to that of carboxylic acids.[25] It is observed that amino acids that have a stronger hydrogen-bond character tend to show smaller δ_{iso}. Such a relationship is more clearly observed in the ^{17}O CS tensor components; with an increase in the C=O bond length, both the δ_{11} and δ_{22} components tend to decrease, while δ_{33} increases. As shown in Figure 27(B), it is found that there is a clear linear correlation between the δ_{22} components and the C=O bond lengths for amino acids. The results simply indicate that the tensor component analysis is more advantageous for investigations of hydrogen bonds than isotropic values.

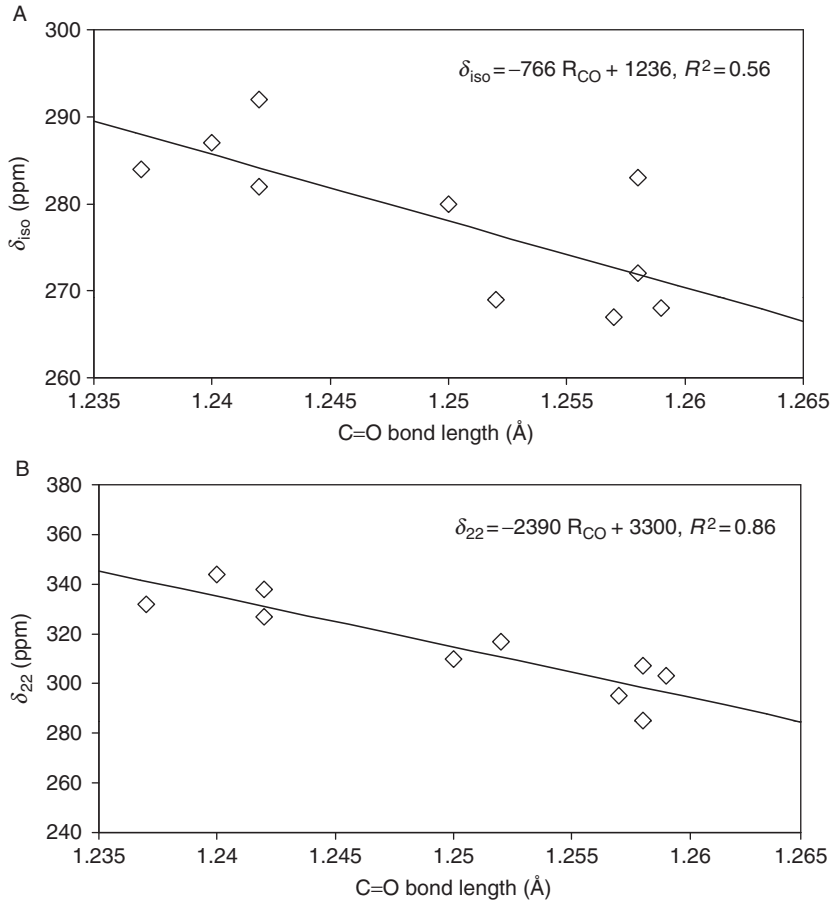

Figure 27 C=O bond dependences of (A) δ_{iso} and (B) δ_{22} components for amino acids. The C=O bond lengths were derived from X-ray or neutron diffraction experiments. Reproduced from Ref. 105.

6. CONCLUSIONS

This review has given an overview of the background and fundamentals of solid-state ^{17}O NMR for biological compounds. Recent developments in solid-state NMR methodology make it possible to obtain and analyse solid-state ^{17}O NMR spectra arising from large-size biological molecules, for example membrane proteins, or ones with large C_Q values of more than 10 MHz. Currently, relevant ^{17}O NMR parameters in biological compounds are EFG and CS tensors. Very recently, *J*-coupling constants have also been available for biological molecules with some advanced pulse sequences. These NMR parameters are highly sensitive to local chemical environments and molecular properties, in particular, hydrogen bonding strengths, and oxygen is the key element, offering advantages in investigations of

secondary structures or molecular recognition in a biological system. Theoretical approaches are also important tools for the interpretation and assignments of solid-state ^{17}O NMR spectra and for an understanding of ^{17}O NMR tensors. Many methodological advances have been made for NMR calculations, which are essential to develop ^{17}O NMR studies of biological solids. In conclusion, solid-state ^{17}O NMR has tremendous potential to become one of the most significant techniques for biological investigations. It is our hope that this review will encourage new NMR researchers to apply solid-state ^{17}O NMR to their biological studies.

REFERENCES

1. A. Abragam, *The Principles of Nuclear Magnetism*. Oxford University Press, Oxford, 1961.
2. M. Mehring, *Principles of High-resolution NMR in Solids*. Springer, New York, 1983.
3. C. A. Fyfe, *Solid State NMR for Chemists*. CFC press, Guelph, Ontario, 1983.
4. C. P. Slichter, *Principles of Magnetic Resonance*. Springer, Berlin, 1990.
5. T. Shimizu, A. Goto, K. Hashi and S. Ohki, *Chem. Lett.*, 2004, **33,** 1502.
6. D. W. Boykin, *^{17}O NMR Spectroscopy in Organic Chemistry*. CRC Press, Boca Raton, FL, 1991.
7. V. Lemaitre, M. E. Smith and A. Watts, *Solid State Nucl. Magn. Reson.*, 2004, **26,** 215.
8. S. E. Ashbrook and M. E. Smith, *Chem. Soc. Rev.*, 2006, **35,** 718.
9. G. Wu, *Prog. Nucl. Magn. Reson. Spectrosc.*, 2008, **52,** 118.
10. I. P. Gerothanassis, R. Hunston and J. Lauterwein, *Helv. Chim. Acta*, 1982, **65,** 1764.
11. I. P. Gerothanassis, R. Hunston and J. Lauterwein, *Helv. Chim. Acta*, 1982, **65,** 1774.
12. E. Ponnusamy and D. Fiat, *J. Labeled Compounds Radiopharmaceuticals*, 1985, **12,** 1135.
13. K. Yamada, T. Yamazaki, M. Asanuma, H. Hirota, N. Yamamoto and Y. Kajihara, *Chem. Lett.*, 2007, **36,** 192.
14. R. B. Merrifield, *J. Am. Chem. Soc.*, 1963, **85,** 2149.
15. L. Kisfaludy and I. Schon, *Synthesis*, 1983, 325.
16. H. Eckert and D. Fiat, *Int. J. Pept. Protein Res.*, 1986, **27,** 613.
17. V. Theodorou-Kassioumis, N. Biris, C. Sakarellos and V. Tsikaris, *Tetrahedron Lett.*, 2001, **42,** 7703.
18. P. Pyykkö, *Z. Naturforsch.*, 1992, **47a,** 189.
19. R. Ludwig, F. Weinhold and T. C. Farrar, *J. Chem. Phys.*, 1995, **103,** 6941.
20. R. Ludwig, F. Weinhold and T. C. Farrar, *J. Chem. Phys.*, 1996, **105,** 8223.
21. G. De Luca, N. Russo, A. M. Koster, P. Calaminici and K. Jug, *Mol. Phys.*, 1999, **97,** 347.
22. R. E. Wasylishen, S. Mooibroek and J. B. Macdonald, *J. Chem. Phys.*, 1984, **81,** 1057.
23. R. E. Wasylishen and R. E. Bryce, *J. Chem. Phys.*, 2002, **117,** 10061.
24. M. Profeta, F. Mauri and C. J. Pickard, *J. Am. Chem. Soc.*, 2003, **125,** 541.
25. J. R. Yates, C. J. Pickard, M. C. Payne, R. Dupree, M. Profeta and F. Mauri, *J. Phys. Chem. A*, 2004, **108,** 6032.
26. C. J. Pickard and F. Mauri, *Phys. Rev. B*, 2001, **63,** 245101.
27. K. Nakajima. In preparation.
28. M. Svensson, S. Humbel, R. D. J. Froese, T. Matsubara, S. Sieber and K. Morokuma, *J. Phys. Chem.*, 1996, **100,** 19357.
29. S. Humbel, S. Sieber and K. Morokuma, *J. Chem. Phys.*, 1996, **105,** 1959.
30. G. H. Stauss, *J. Chem. Phys.*, 1964, **40,** 1988.
31. J. P. Amoureux, C. Fernandez and P. Granger, *in*: *Multinuclear Magnetic Resonance in Liquids and Solids-Chemical Applications*, P. Granger and R. K. Harris (eds.), Kluwer Academic Publishes, Dordrecht, The Netherlands, 1990, p. 409.
32. F. Taulelle, *in*: *Multinuclear Magnetic Resonance in Liquids and Solids-Chemical Applications*, P. Granger and R. K. Harris (eds.), Kluwer Academic Publishes, Dordrecht, The Netherlands, 1990, p. 393.
33. K. Yamada, *J. Spectrosc. Soc. Japan*, 2006, **55,** 99.
34. J. T. Cheng and P. D. Ellis, *J. Phys. Chem.*, 1989, **93,** 2549.

35. P. J. Chu and B. C. Gerstein, *J. Chem. Phys.*, 1989, **91,** 2081.
36. J. T. Cheng, J. C. Edwards and P. D. Ellis, *J. Phys. Chem.*, 1990, **94,** 553.
37. W. P. Power, R. E. Wasylishen, S. Mooibroek, B. A. Pettitt and W. Danchura, *J. Phys. Chem.*, 1990, **94,** 591.
38. P. P. Man, *in*: Encyclopedia of Nuclear Magnetic Resonance, D. M. Grant and R. K. Harris (eds.), *In* 1996, Vol. 6, John Wiley & Sons, Chichester, U.K., 1996, p. 3838.
39. K. Eichele, J. C. C. Chan, R. E. Wasylishen and J. F. Britten, *J. Phys. Chem. A*, 1997, **101,** 5423.
40. K. Eichele, R. E. Wasylishen and J. H. Nelson, *J. Phys. Chem. A*, 1997, **101,** 5463.
41. J. F. Baugher, P. C. Taylor, T. Oja and P. J. Bray, *J. Chem. Phys.*, 1969, **50,** 4914.
42. J. M. Koons, E. Hughes, M. Cho and P. D. Ellis, *J. Magn. Reson.*, 1995, **A114,** 12.
43. D. Müller, W. Gessner, H. J. Behrens and G. Scheler, *Chem. Phys. Lett.*, 1981, **79,** 59.
44. M. D. Meadow, K. A. Smith, R. A. Kinsey, T. M. Rothgeb, R. P. Skarjune and E. Oldfield, *Proc. Natl. Acad. Sci. USA*, 1982, **79,** 1351.
45. A. Samoson and E. Lippmaa, *Phys. Rev.*, 1983, **B28,** 6567.
46. A. Samoson, E. Kundla and E. Lippmaa, *J. Magn. Reson.*, 1982, **49,** 350.
47. J. Skibsted, N. C. Nielsen, H. Bildsoe and H. J. Jakobsen, *J. Magn. Reson.*, 1991, **95,** 88.
48. S. P. Brown, *Macromol. Rapid Commun.*, 2009, **30,** 688.
49. I. Hung, A. C. Uldry, J. Becker-Baldus, A. L. Webber, A. Wong, M. E. Smith, S. A. Joyce, J. R. Yates, C. J. Pickard, R. Dupree and S. P. Brown, *J. Am. Chem. Soc.*, 2009, **131,** 1820.
50. K. Yamada, T. Shimizu, S. Ohki and T. Yamazaki, *Magn. Reson. Chem*, 2008, **46,** 226.
51. K. Yamada, T. Nemoto, M. Asanuma, H. Honda, T. Yamazaki and H. Hirota, *Solid State Nucl. Magn. Reson.*, 2006, **30,** 182.
52. K. Torii and Y. Iitaka, *Acta Crystallogr.*, 1970, **B26,** 1317.
53. K. J. Pike, V. Lemaitre, A. Kukol, T. Anupold, A. Samoson, A. P. Howes, A. Watts, M. E. Smith and R. J. Dupree, *J. Phys. Chem. B*, 2004, **108,** 9256.
54. K. Yamada, T. Shimizu, T. Yamazaki and S. Ohki, *Solid State Nucl. Magn. Reson.*, 2008, **33,** 88.
55. I. Hung, A. Wong, A. P. Howes, T. Anupold, J. Past, A. Samoson, X. Mo, G. Wu, M. E. Smith, S. P. Brown and R. Dupree, *J. Magn. Reson.*, 2007, **188,** 246.
56. W. Scheubel, H. Zimmerman and H. Haeberlen, *J. Magn. Reson.*, 1985, **63,** 544.
57. K. W. Waddell, E. Y. Chekmenev and R. J. Wittebort, *J. Phys. Chem. B*, 2006, **110,** 22935.
58. Q. Zhang, E. Y. Chekmenev and R. J. Wittebort, *J. Am. Chem. Soc.*, 2003, **125,** 9140.
59. Q. W. Zhang, H. M. Zhang, M. G. Usha and R. J. Wittebort, *Solid State Nucl. Magn. Reson.*, 1996, **7,** 147.
60. K. Yamada, H. Honda, T. Yamazaki and M. Yoshida, *Solid State Nucl. Magn. Reson.*, 2006, **30,** 162.
61. G. Wu, K. Yamada, S. Dong and H. Grondey, *J. Am. Chem. Soc.*, 2000, **122,** 4215.
62. K. Yamada, S. Dong and G. Wu, *J. Am. Chem. Soc.*, 2000, **122,** 11602.
63. G. Wu and S. Dong, *Chem. Phys. Lett.*, 2001, **334,** 265.
64. K. Yamada, T. Shimizu, M. Asanuma, T. Yamazaki and S. Yokoyama, *Solid State Nucl. Magn. Reson.*, 2008, **33,** 25.
65. K. Eichele and R. E. Wasylishen, *WSOLIDS NMR Simulation Package*, Ver. 1.17.30, 2001.
66. M. S. Lehmann, T. F. Koetzle and W. C. Hamilton, *J. Am. Chem. Soc.*, 1972, **94,** 2675.
67. S. Dong, R. Ida and G. Wu, *J. Phys. Chem. A*, 2000, **104,** 11194.
68. Gaussian 09, Revision A.1, M. J. Frisch, G. W. Trucks, H. B. Schlegel, G. E. Scuseria, M. A. Robb, J. R. Cheeseman, G. Scalmani, V. Barone, B. Mennucci, G. A. Petersson H. Nakatsuji, *et al.*, *Gaussian*. Gaussian, Inc., Wallingford, CT, 2009.
69. T. F. Koetzle, M. N. Frey, M. S. Lehmann and W. C. Hamilton, *Acta Crystallogr.*, 1973, **B29,** 2571.
70. K. Yamada, T. Shimizu, M. Yoshida, M. Asanuma, M. Tansho, T. Nemoto, T. Yamazaki and H. Hirota, *Z. Naturforsch.*, 2007, **62b,** 1422.
71. S. Kuroki, A. Takahara, I. Ando, A. Shoji and T. Ozaki, *J. Mol. Struct.*, 1994, **323,** 197.
72. A. Wong, K. J. Pike, R. Jenkins, G. J. Clarkson, T. Anupold, A. P. Howes, D. H. G. Crout, A. Samoson, R. Dupree and M. E. Smith, *J. Phys. Chem. A*, 2006, **110,** 1824.
73. K. Yamada, D. Hashizume, T. Shimizu, S. Ohki and S. Yokoyama, *J. Mol. Struct.*, 2008, **888,** 187.
74. M. Torrent, D. Mansour, E. P. Day and K. Morokuma, *J. Phys. Chem. A*, 2001, **105,** 4546.
75. S. E. Ashbrook, A. J. Berry, D. J. Frost, A. Gregorovic, J. E. Readman and S. Wimperis, *J. Am. Chem. Soc.*, 2007, **129,** 13213.

76. J. E. Gready, *J. Am. Chem. Soc.*, 1981, **103,** 3682.
77. J. E. Gready, *J. Phys. Chem.*, 1984, **88,** 3497.
78. I. J. F. Poplett and J. A. S. Smith, *J. Chem. Soc. Faraday Trans. 2*, 1979, **75,** 1703.
79. C. P. Cheng and T. L. Brown, *J. Am. Chem. Soc.*, 1979, **101,** 2327.
80. I. J. F. Poplett and J. A. S. Smith, *J. Chem. Soc. Faraday Trans. 2*, 1981, **77,** 1473.
81. G. Wu, S. Dong, R. Ida and N. Reen, *J. Am. Chem. Soc.*, 2002, **124,** 1768.
82. N. F. Ramsey, *Phys. Rev.*, 1950, **78,** 699.
83. C. P. Cheng, S. C. Lin and G. S. Shaw, *J. Magn. Reson.*, 1986, **69,** 58.
84. J. A. Pople, *J. Chem. Phys.*, 1962, **37,** 53.
85. M. Karplus and J. A. Pople, *J. Chem. Phys.*, 1963, **38,** 2803.
86. K. D. Park, K. Guo, F. Adebodun, M. L. Chiu, S. G. Sligar and E. Oldfield, *Biochemistry*, 1991, **30,** 2333.
87. R. Freeman, G. R. Murray and R. E. Richards, *Proc. Roy. Soc. A*, 1957, **242,** 455.
88. S. C. Chung, J. C. C. Chan, S. C. F. Au-Yeung and X. Xu, *J. Phys. Chem.*, 1993, **97,** 12685.
89. S. Kuroki, K. Yamauchi, I. Ando, A. Shoji and T. Ozaki, *Curr. Org. Chem.*, 2001, **5,** 1001.
90. G. Wu, S. Dong and R. Ida, *Chem. Commun.*, 2001, 891.
91. V. Lemaitre, K. J. Pike, A. Watts, T. Anupold, A. Samoson, M. E. Smith and R. Dupree, *Chem. Phys. Lett.*, 2003, **371,** 91.
92. V. Lemaitre, M. R. R. de Planque, A. P. Howes, M. E. Smith, R. Dupree and A. Watts, *J. Am. Chem. Soc.*, 2004, **126,** 15320.
93. J. Hu, E. Y. Chekmenev, Z. Gan, P. L. Gor'kov, S. Saha, W. W. Brey and T. A. Cross, *J. Am. Chem. Soc.*, 2005, **127,** 11922.
94. C. Gervais, R. Dupree, K. J. Pike, C. Bonhomme, M. Profeta, C. J. Pickard and F. Mauri, *J. Phys. Chem. A*, 2005, **109,** 6960.
95. A. Brinkmann and A. P. M. Kentgens, *J. Am. Chem. Soc.*, 2006, **128,** 14758.
96. E. Y. Chekmenev, P. L. Gor'kov, T. A. Cross, A. M. Alaouie and A. I. Smirnov, *Biophys. J.*, 2006, **91,** 3076.
97. E. Y. Chekmenev, K. W. Waddell, J. Hu, Z. Gan, R. Wittebort and T. A. Cross, *J. Am. Chem. Soc.*, 2006, **128,** 9849.
98. T. H. Sefzik, J. B. Houseknecht, T. M. Clark, S. Prasad, T. L. Lowary, Z. Gan and P. J. Grandinetti, *Chem. Phys. Lett.*, 2007, **434,** 312.
99. I. C. M. Kwan, X. Mo and G. Wu, *J. Am. Chem. Soc.*, 2007, **129,** 2398.
100. T. Gullion, K. Yamauchi, M. Okonogi and T. Asakura, *Marcomolecules*, 2007, **40,** 1363.
101. K. Ozeki, N. Sakabe and J. Tanaka, *Acta Crystallogr. B*, 1969, **25,** 1038.
102. T. M. Clark and P. J. Grandinetti, *Solid State Nucl. Magn. Reson.*, 2000, **16,** 55.
103. A. Steinschneider, M. I. Burger, A. Buka and D. Fiat, *Int. J. Pept. Protein Res.*, 1981, **18,** 324.
104. J. A. Killian, I. Salemink, M. R. de Planque, G. Lindblom, R. E. Koeppe and D. V. Greathouse, *Biochemistry*, 1996, **35,** 1037.
105. K. Yamada, T. Shimizu, M. Tansho, T. Nemoto, M. Asanuma, M. Yoshida, T. Yamazaki and H. Hirota, *Magn. Reson. Chem*, 2007, **45,** 547.

CHAPTER 4

Spatial Inhomogeneity of Cavities in Polymer Network Systems as Characterised by Field-Gradient NMR Using Probe Diffusant Molecules and Polymers with Different Sizes

Kazuhiro Kamiguchi,* **Shigeki Kuroki,†** **Yuji Yamane,‡** **Mitsuru Satoh,**§,¶ and **Isao Ando**¶,‖

Contents

* Magnetic Research Analysis Team, Structure Analysis Group, Research Department, Nissan Arc, Ltd., Natsushima-cho, Yokosuka-shi, Kanagawa, Japan
† Department of Organic and Polymeric Materials, Tokyo Institute of Technology, Ookayama, Meguro-ku, Tokyo, Japan
‡ Silicone-Electronics Materials Research Center, Shin-Etsu Chemical Co., Ltd., Hitomi Matsuida-machi, Annaka-shi, Gunma, Japan
§ Department of Chemistry and Materials Science, Tokyo Institute of Technology, Ookayama, Meguro-ku, Tokyo, Japan
¶ International Research Center of Macromolecular Science, Tokyo Institute of Technology, Ookayama, Meguro-ku, Tokyo, Japan
‖ Department of Materials Science and Engineering, Shonan Institute of Technology, Tsujido Nishikaigan, Fujisawa-shi, Kanagawa, Japan

Annual Reports on NMR Spectroscopy, Volume 70
ISSN 0066-4103, DOI: 10.1016/S0066-4103(10)70002-8

Abstract Most recent studies on the inhomogeneity of a gel network size, characterised through the precise observation of time-dependent diffusion coefficients reflecting sensitive intermolecular interactions between the network and the probe polymers are reviewed. The work uses the field-gradient NMR technique and studies the structural characterisation of a three-dimensional (3D) network for a complicated micrometre-scale cavity produced by dissolving one of two kinds of polymers in a polymer blend, phase-separated by elevating the temperature above room temperature by using a solvent. NMR imaging with irradiated field-gradient pulses from the *x*, *y* and *z* directions is reviewed.

Key Words: Field-gradient NMR, Diffusion coefficient, Polymer network, Spatial inhomogeneity of cavities, 3D NMR imaging.

1. INTRODUCTION

In polymer science and technology, the polymer network materials with nano- and micrometre-scale cavities produced by any specific polymerisation, self-organised polymer assembly, specific polymer aggregation, etc. have been widely developed to gain specifically preferred properties and functions, as seen from a special issue of the *Journal of Molecular Structure in* 2005.[1] Such properties and functions are closely associated with the molecular cavity from the structural standpoint. Therefore, precise structural design, structural control and structural characterisation are needed to prepare such a molecular cavity. For example, in polymer gels and self-organised polymer systems, it is not simple to characterise the cavity because of the inhomogeneous cavity-size distribution of the polymer systems. This is because, in a polymer gel, networks are produced by the concomitant polymerisation and cross-linking, which contain spatial fluctuations of the cross-link density or even phase-separated domains. For example, polyacrylamide networks become more inhomogeneous as the monomer concentration decreases during the process of gel formation, as shown by Dusek and Prins.[2] One of the major problems in these research fields is to characterise precisely the spatial inhomogeneity of polymers with different cavity sizes by using spectroscopic methods.

The spatial inhomogeneity that is inherent in chemically cross-linked polymer gels has so far been detected by light scattering as speckles,[3,4] and then the relationship between the speckles and spatial inhomogeneity has been analyzed.[5–13] On the other hand, it has been well known that pulse field-gradient spin-echo (PFGSE) NMR[14–23] and NMR imaging[24–27] of field-gradient NMR are excellent techniques for determining the diffusion coefficients of low-molecular-weight molecules and high-molecular-weight polymers in the solution state,[28–39] the liquid crystalline state,[40–43] in organic and inorganic matrixes,[44–49] and the gel state[50–77] to elucidate diffusional behaviour and dynamics as well as the stimulus–response process,[78–81] migration of metal ions[82–85] and heterogeneous structure[86] in a gel by NMR imaging. In the polymer network systems considered here, it is demonstrated that PFGSE NMR provides a detailed understanding of the network structure through the observation of the diffusion coefficients of the probe molecules. In addition to this, after a previous work on the diffusional inhomogeneity in polymer gel networks of different sizes by means of time-dependent diffusion NMR by Yamane et al.,[71] the inhomogeneity in the gel network size has been clearly characterised through the precise observation of the time-dependent diffusion coefficients affecting the sensitive intermolecular interactions between the network and the probe molecules.[87–89] It is very important to elucidate the three-dimensional (3D) network structure of the complicated micrometre-scale cavity that is produced by dissolving one of two kinds of polymers in a polymer blend, phase-separated by elevating the temperature to above room temperature by using a solvent. It is shown that the use of NMR imaging as irradiated field-gradient pulses from the x, y and z directions leads to a precise 3D structural characterisation on the micrometre-scale cavity.[90] All of this work is reviewed in this article.

2. NETWORK STRUCTURE OF POLYMER GELS AND DIFFUSIONAL BEHAVIOUR OF PROBE POLYMERS

Self-diffusion coefficient (D) measurements on the solvent and the probe diffusant species in polymer network gels are carried out over a wide range of temperatures by using a standard PFGSE pulse sequence ($\pi/2$ pulse–τ–π pulse), which is the Hahn echo sequence,[91] where τ is the pulse interval, and a field-gradient pulse is added between the $\pi/2$ and π pulses and after the π pulses.[14,15] This is used for probe diffusant species with a relatively long spin–spin relaxation time (T_2). When the T_2 of the probe diffusant is relatively short, a pulsed field-gradient stimulated-echo (PFGStE) pulse sequence ($\pi/2$ pulse–τ_1–$\pi/2$ pulse–τ_2–$\pi/2$ pulse) is used instead of the PFGSE pulse sequence.[18,19,91,92] When the echo signal is predominantly decayed by a still shorter T_2 (^{1}H T_2<2 ms), before decaying by diffusion, the situation can sometimes be avoided by using other nuclear species with relatively small values of the gyromagnetic ratio,[93] by which T_2 is governed besides molecular motion. A pulsed field-gradient generator designed to generate a strong field-gradient pulse is used to measure very small diffusion coefficients [$<10^{-11}$ cm^2 s^{-1}($=10^{-15}$ m^2 s^{-1})] of the probe polymers, or low-molecular-weight

molecules that are extremely restrained in molecular motion at the inside of the cavity but have large intermolecular interactions with the network chains in gels (the gradient-field strength is often over 2000 G cm^{-1}(=20 T m^{-1})). Thus the eddy currents induced are suppressed. In gel work, The use of a field-gradient strength (g) of about 1–15 T m^{-1} in the gels research work introduced here is sufficient for a study of the inhomogeneity of the network size. The diffusion coefficient D of water [2.22×10^{-5} cm^2 s^{-1}(=2.22×10^{-9} m^2 s^{-1}) at 303 K] is often used for the calibration of the field-gradient strength. Only the free induction decay (FID) is recorded after the echo maximum, and then the Fourier transformation (FT) is performed.

The D values have been determined by using the following relationship between the echo signal intensity and field-gradient parameters[94–99]:

$$\ln[A(\delta \text{ or } g)/A(0)] = -\gamma^2 g^2 D \delta^2 [\Delta - \delta/3], \tag{1}$$

where $A(\delta$ or $g)$ and $A(0)$ are the echo signal intensities at $t = 2\tau$ with and without the magnetic field-gradient pulse of strength g, which has the length δ, respectively; γ is the gyromagnetic ratio of any specified nucleus; and Δ, the gradient pulse interval, which is the so-called diffusing time. The echo signal decay depends on T_2 and the diffusion coefficient. For this, the appropriate Δ value must be chosen to determine the diffusion coefficient by considering the T_2 value. For example, if Δ is too long, the echo signal decays by T_2 and disappears within the chosen Δ; on the other hand, if Δ is too short, the echo signal does not decay by diffusion, making it difficult to determine the diffusion coefficient from such a small decay signal. Therefore, the diffusing time Δ is an important parameter associated with the restricted diffusion of the probe diffusant in the cavity and provides information on the inhomogeneity of the cavity-size distribution in gel networks, as described below.[71,87–89,98] The echo signal intensity was measured as a function of Δ or g. The plot of $\ln[A(\delta$ or $g)/A(0)]$ against $\gamma^2 g^2 \delta^2 (\Delta - \delta/3)$, that is a Stejskal–Tanner plot, gives a straight line with a slope $-D$. Therefore, the D value can be determined from its slope. When probe molecules have multi-components in diffusion on the measurement time scale, the total echo attenuation is given by a superposition of contributions from the individual components.

$$\ln[A(\delta \text{ or } g)/A(0)] = -\sum_i f_i \{\gamma^2 g^2 D_i \delta^2 [\Delta - \delta/3]\}, \tag{2}$$

where D_i is the self-diffusion coefficient of the ith component, f_i is the fraction of the ith component and $\sum f_i = 1$. The fraction for the diffusion component can be determined from the intercept of the least-squares-fitted straight line at large Δ. The δ and Δ values employed in the PFGSE experiments are 0.001–1.0 and 10–700 ms, respectively.

In the time scale of t, the self-diffusion coefficient D can be expressed by the mean-square displacement $\langle z^2 \rangle$ in the z direction from its starting point after the diffusing time Δ, followed by the Gaussian distribution as follows:

$$\langle z^2 \rangle = 2Dt = 2D\Delta, \tag{3}$$

where t is approximately Δ. These $\langle z^2 \rangle$ values give us information on the diffusion distance d, which reflects the experimental results expressed as follows:

$$d = \langle z^2 \rangle^{1/2} = (2Dt)^{1/2} = (2D\Delta)^{1/2}. \quad (4)$$

The d values in PFGSE experiments are much larger than the network size considered here but much smaller than the size of a gel.[71,87–89,98]

2.1. Diffusional inhomogeneity of probe amino acid in chemically cross-linked polymer gels

Yamane et al.[71] have studied the diffusional inhomogeneity of networks of polymer gels with different network sizes, such as polystyrene (PS) gel and cross-linked ethoxylate acrylate gel with dimethylformamide (DMF) as solvent by 270-MHz PFGSE ^{1}H NMR with a change of Δ from 10 to 100 ms at a field-gradient strength (g) of about 1400 G cm^{-1}(=14 T m^{-1}). From the experimental results on the diffusion coefficients of the probe amino acid, *tert*-butyloxylcarbonyl-L-phenylalanine (Boc-Phe) [10 wt%], in the Merrifield network polystyrene (MPS) gel (cross-linked by 1 mol% divinylbenzene (DVB)), it was shown that Boc-Phe has a single diffusion component in the Δ range from 40 to 100 ms corresponding to the diffusing time. On the other hand, from the plots at $\Delta = 10$ and 100 ms, it is seen from Figure 1 that the experimental data lie on a straight line at $\Delta = 100$ ms but not at $\Delta = 10$ ms. At short observation time Δ, Boc-Phe in MPS gel has two diffusion components, namely, a slow diffusion component and a fast diffusion component. This means that for the echo attenuation curvature, any diffusant

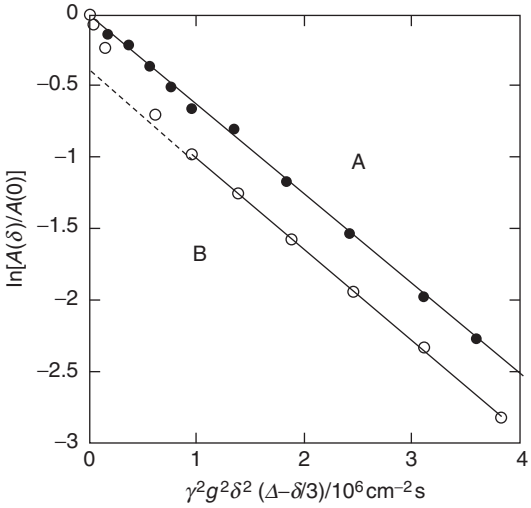

Figure 1 Diffusional spin echo attenuation of Boc-Phe in MPS1 gels with DMF-d_7 as solvent on Δ at 30 °C by varying field-gradient pulse duration (diffusing time) Δ, where the Boc-Phe concentration is 10 wt%. (A) $\Delta = 10$ ms and (B) $\Delta = 100$ ms.

polydispersity, trace solvents, T_2-weighting and host inhomogeneity of gel could produce curvature at shorter Δ, but a single apparent D at longer Δ. Probe molecules used in this work have monodispersity and a single-component T_2. It has been shown that as for Boc-Phe in DMF solution, the experimental data lie on a straight line as a function of Δ and thus Boc-Phe has a single diffusion component.[66,67,69] On the basis of these experimental findings, it is assumed that the echo attenuation curvature is not attributed to diffusant polydispersity, trace solvents, T_2-weighting and artefacts, but to the inhomogeneity of the network size in the host gel. The slow diffusion components are more sensitive to interactions between the gel network and probe molecules than the fast diffusion component, because the slow diffusion component comes from the strong intermolecular interactions between the probe molecule and the smaller network in gels. The slow diffusion component increases with an increase in Δ; that is, the averaged D approaches the slow D. From the slow and averaged diffusion experimental results, it cannot be said exactly that the fast diffusion component is one component or multiple components, but the observed diffusion echo signal is approximately deconvoluted by two of the slow and fast diffusion components. Then, the echo signals are resolved into two of the slow and fast D components. From such plots, the fractions of the slow diffusion component and fast diffusion component can be determined straightaway. The fractions of the slow and fast diffusion components (f_{slow} and f_{fast}, respectively) may depend on Δ. This shows that when Boc-Phe molecules are transported to some network cells with different network sizes during Δ, they have two diffusion components. This also implies that by varying the diffusing time Δ, the diffusion of Boc-Phe molecules with different diffusion coefficients in different network cells can be observed. If probe molecules diffuse over a long Δ time, the observed diffusion coefficient may become an averaged value, diffusion through the network cells with different network sizes contributing to the inhomogeneity of the network size for gels. Therefore, a series of such experiments gives useful information about the diffusion process of Boc-Phe and the inhomogeneities of the network size. In other words, the slow diffusion component gives useful information about the inhomogeneity of the network size for gels through the strong intermolecular interactions between probe molecules and network of the gels.

As for Boc-Phe in MPS gel with DMF-d_7 as solvent, when $\Delta = 5$, 10, 40 and 100 ms, $\langle z^2 \rangle = 0.4$, 0.7, 2.7 and 6.0 μm, respectively.[71] These $\langle z^2 \rangle$ values give us information on the diffusion distance d, which reflects the experimental results. Consequently, the experimental results obtained at $\Delta = 5$, 10, 40 and 100 ms lead to the diffusion distances $d = 0.6$, 0.9, 1.7 and 2.5 μm, respectively, by using Equation (4). The d values in these experiments are much larger than the network size (12–24 nm) considered here but much smaller than the particle size of swollen gel beads (140–304 μm). The network size in the equilibrium swollen state is estimated by using the fraction of DVB cross-linking. This is based on the assumption that PS chains between cross-linking points stretch much longer in the equilibrium swollen state. Therefore, as seen from the obtained S values, it can be said that Boc-Phe molecules go through some network cells during the diffusion time Δ.

As for Boc-Phe in MPS gels with DMF-d_7 as solvent at 30 °C, the f_{slow} value increases with an increase in d and changes from two diffusion components to a single diffusion component at $d = 1.7$ μm.[71] Here, this specified d value is named the 'specific' diffusion distance (S distance). In the short Δ range, in which $d < 1.7$ μm, Boc-Phe molecules cannot diffuse to a large distance through many network cells; so, the diffusion distance is not enough to obtain the single diffusion component, but the two diffusion components are observed. On the other hand, in the long Δ range, in which $d > 1.7$ μm, Boc-Phe molecules can diffuse through many network cells, a single diffusion component is observed. Therefore, it can be said that a series of time-dependent diffusion experiments give useful information about the network structure of polymer gels. If the gel systems are formed by a larger network size as compared with the S distance, the observed diffusion coefficients of Boc-Phe in the individual gel beads reach the same value. However, if the gel systems are formed by a smaller network size as compared with the S distance, the diffusion coefficients of Boc-Phe in the individual gel beads are observed. In other words, all gel beads of sizes larger than S have the same function as molecular separation materials, but gel beads with a smaller size than S have different functions. Therefore, S is a measure for the diffusional inhomogeneity of the probe molecules, the spatial inhomogeneity of the network and the functionalities of the network.

By using the same PFGSE ^{1}H NMR method, inhomogeneities in poly(acrylic acid) (PAA) gels differing in their degree of cross-linking have been detected as a function of the degree of swelling, Q, in the range 2.8–10.0. Q is defined as the mass of the swollen gel divided by the mass of the dry polymer: $Q = M_{swollen}/M_{dry}$.[73] The networks are prepared at 70 °C by simultaneous polymerisation and cross-linking of a mixture of acrylic acid (AA), sodium carbonate, cross-linker (1,4-butanediol diacrylate) and the redox couple sodium persulfate/sodium isoascorbate as the initiator. Two types of network are prepared by using the same monomer concentration (30 wt%) and the same amount of sodium carbonate but different amounts of the cross-linker, 1.1 and 0.5 wt% (GEL1 and GEL2), respectively, in the monomer mixture. Detection of heterogeneities is based on measuring the diffusion coefficients of the probe molecule poly(ethylene glycol) (PEG) as a function of the degree of swelling and diffusing time, Δ, by means of field-gradient ^{1}H NMR spectroscopy. The inhomogeneities emerge as the degree of swelling of the gels is reduced. For highly swollen gels ($Q = 10.0$ and 5.2 for GEL1, and $Q = 10.0$, 5.1 and 4.5 for GEL2), only *one* diffusion coefficient is detected, independent of the diffusing time, Δ, in the range 30–500 ms. For less swollen gels ($Q = 2.9$–4.5 for GEL1 and 2.8–3.9 for GEL2), two diffusion coefficients are detected, D_{fast} and D_{slow}, with values that depend on Δ; for these less swollen gels, the diffusion distances d_{fast} and d_{slow} and the relative fractions of the fast and slow diffusion components, f_{fast} and f_{slow}, are calculated. A specific degree of swelling, Q_s, is defined, above which the diffusion of the probe in the two gel systems changes from one to two components. A larger value of Q_s in GEL1 is taken as an indicator of a more inhomogeneous gel. Analysis of the effect of Δ on the diffusion coefficients, diffusion distances and fractions of slow and fast diffusion components indicate that the gels form a highly cross-linked region in a narrow Q range.

In this Q range, the polymer chains interact and form a highly restricted diffusion region. The extent and distribution of the cross-links form different restricted diffusion regions in the GEL1 and GEL2 systems.

As mentioned above, it can be said that the inhomogeneities of the gels are elucidated from the viewpoint of the diffusion process as a function of temperature, the kind of gel, the degree of the volume swelling and the diameter of gels, and that the diffusion distance provides useful information about the structure and dynamics of the gel as studied by time-dependent diffusion experiments. This method will have potential for applications to the characterisation of smart membranes, aggregation process and lattice-forming process as well as the gels.

2.2. Network structure and its size inhomogeneity of poly(methyl methacrylate) (PMMA) gels through diffusional behaviour of probe PSs with different molecular weights

As described above, Yamane et al. have elucidated the inhomogeneity of network size for a PS gel[71] and PAA gels[73] through the diffusional behaviour of low-molecular-weight molecules such as amino acids as probes in the relevant gel by using time-dependent diffusion NMR and have demonstrated that it is an excellent means for obtaining information about the inhomogeneity of the network size for the polymer gels. For PMMA gels which have different levels of inhomogeneities for the network size, the inhomogeneity has been characterised through observation of the diffusion coefficients of the probe PSs in the polymer gels by the PFGStE ^{1}H NMR method.[18,19,91] The series of inhomogeneities are to be introduced to the gel by preparing the PMMA network in the presence of PSs with a wide range of M_ws (=4000, 19,000, 29,000, 50,000, 170,000 and 400,000) having very narrow distributions of M_w/M_n=1.04–1.09. Thus, the respective incorporated PSs are conveniently employed as probe molecules to investigate the intentionally formed inhomogeneous network.

Before going ahead, preparation of PMMA gels considered here should be described. PMMA gels are prepared by free-radical copolymerisation of MMA (1.4 mol L^{-1}) and ethylene glycol dimethacrylate (EGDM) (47.7 mmol L^{-1}) initiated by 2,2′-azobisisobutylonitrile (AIBN) (4.6 mmol L^{-1}) in dehydrated toluene in the absence of PS (PMAA gel sample 1) and in the presence of PS with M_w=4000, 19,000, 29,000, 50,000, 170,000 or 400,000 (PMMA gel sample 2–7, respectively) at 75 °C for 1 day.[5,100] In these experiments, the PS concentrations were set at 20, 10 or 6 mg/mL for sample 2, samples 3–6, and sample 7, respectively, so as to be retained under the overlap concentration of the PSs in the solution.[101] The seven solution samples are deoxygenated by bubbling nitrogen gas for 10 min, and then gelation is carried out by incubating the sealed solution samples. Rod-like PMMA gels containing PS thus prepared are dried in vacuum for 6 h to remove the remaining monomer and toluene. Dried PMMA gels are immersed in $CDCl_3$ for 24 h again to reach the equilibrium swelling. The swelling degree Q of all of the PMMA gels used is about 12.

2.2.1. Diffusional behaviour of PSs in the PMMA gels

In the PFGStE ^{1}H NMR experiments, the fractions for the first and second diffusion components can be determined from the intercept of the least-squares-fitted straight line at larger g values. The Δ, Δ and g values employed in these experiments are 40–500 ms, 0.04–2.0 ms and 0–11.0 T m^{-1}, respectively. Typical PFGStE ^{1}H NMR spectra of the PMMA gel sample 2 containing probe PS with $M_w = 4000$ and $CHCl_3$ at room temperature are shown as a function of g in Figure 2. The spectral assignments are straightforwardly made by using reference data for PS, PMMA and $CHCl_3$ (which is contained in commercial $CDCl_3$ as an isotope impurity). All the peaks are numbered from high frequency to low frequency. Peak 1 overlaps with two peaks coming from the *o*-phenyl protons of PS and $CHCl_3$. Peak 2 comes from the *m*- and *p*-phenyl protons of PS. Peak 3, the most intense one, is assigned to the methoxy protons of PMMA. Peaks 4–7 are assigned to the main chain protons of PS and PMMA as indicated in Figure 2. From these spectra, it is seen that the intensities of the peaks for PS and $CHCl_3$ decay with an increase in the field-gradient strength. This means that PS and $CHCl_3$ are diffusing in the PMMA network. On the other hand, the intensities of the peaks for the PMMA network chains do not decay. This is natural because the PMMA network chains are only undergoing fast random fluctuations and their displacement is extremely small. From the plots of $\ln[A(g)/A(0)]$ against $\gamma^2 g^2 \delta^2 (\Delta - \delta/3)$ for the

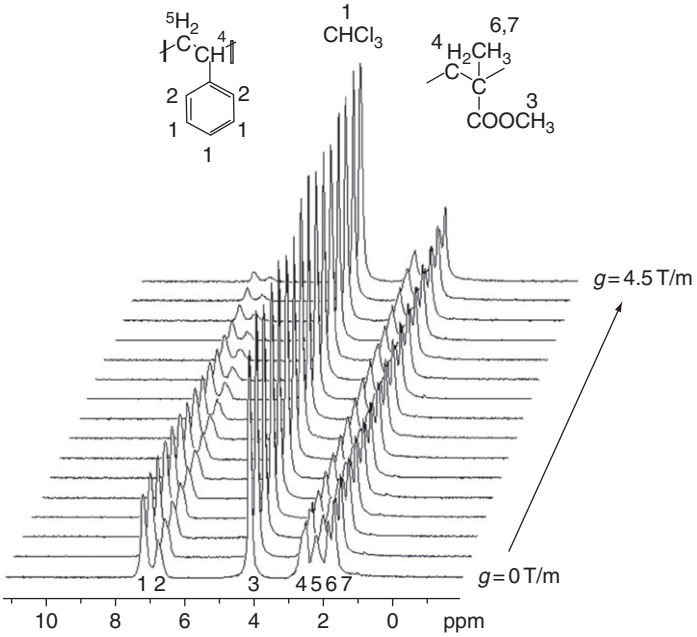

Figure 2 PFGStE ^{1}H NMR spectra of PMMA gel (PMMA gel sample 2) containing PS with $M_w = 4000$ and $CDCl_3$ by varying field-gradient pulse strength (g). The solvent contains a very small amount of $CHCl_3$ as impurity.

PS phenyl peak at 6.6 ppm, the diffusion coefficient can be determined as described below.

PFGStE ^{1}H NMR experiments for PMMA gel samples have been carried out at the diffusing time of $\Delta = 40$ ms and then diffusional behaviour of PSs is observed in the PMMA gels. Figure 3 shows the plots of $\ln[A(g)/A(0)]$ against

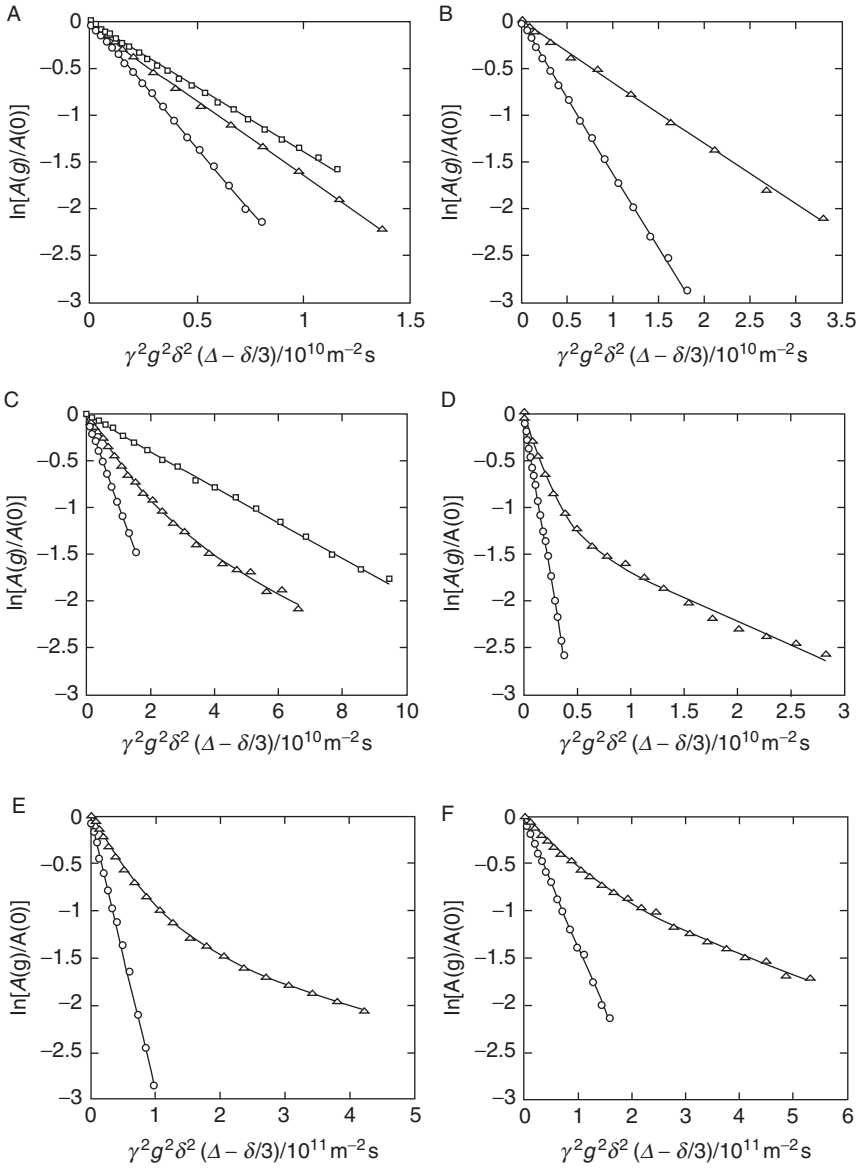

Figure 3 Diffusional stimulated echo attenuations of PSs with different M_ws in PMMA gels (PMMA gel samples 1–7) with $CDCl_3$ as solvent, respectively, and PS in $CDCl_3$ solution by varying field-gradient strength *g*. (○) PS in $CDCl_3$ solution; (□) in PMMA gel prepared without PS (PMMA gel sample 1); (△) in PMMA gels prepared with PS (PMMA gel samples 2–7); The M_ws of PSs are (A) 4000, (B) 19,000, (C) 29,000, (D) 50,000, (E) 170,000 and (F) 400,000.

$\gamma^2 g^2 \delta^2(\Delta - \delta/3)$ for the phenyl peak for PSs in PMMA gels (PMMA gel samples 1–7) and PS in $CDCl_3$ solution by changing g. In Figure 3A and B, the data for PSs in PMMA gel samples 2 and 3 reasonably lie on a straight line in the Stejskal–Tanner plot. It can be said that the network of the PMMA gels is homogeneous in the Δ timescale. However, in Figure 3C–F, the data for PSs in PMMA gel samples 4–7 (open triangle data) appreciably deviate from a straight line. As shown later, these data are successfully analysed in terms of Equation (2). Namely, the diffusion of the PSs within these gel samples consists of two components, a fast component and a slow one. This strongly suggests that PMMA samples 4–7 contain, at least, two kinds of network structures, for example open and dense ones. To confirm that the two-component decay is from such an inhomogeneity introduced by PS that was present during the gel-forming process, we also examined the diffusional behaviours of the PSs in PMMA sample 1. A PMMA sample 1, which was prepared without PS, is placed in a deuterated chloroform solution of PSs with $M_w = 4000$ and 29,000, respectively, for 2 weeks to allow the PSs to penetrate into the PMMA gel. In Figure 3A and C, the open square data for the PS echo decay in the PMMA gel prepared in the absence of PS. As seen from Figure 3A and C, the open square data lie reasonably on a straight line in the Stejskal–Tanner plot. Therefore, it can be said that the network of the PMMA gel prepared without PS is homogeneous on the Δ timescale. Consequently, it is apparent that the addition of PS with $M_w = 29{,}000$ leads to inhomogeneity for the relevant PMMA gel. Actually, it is well known that blends of PS and PMMA are miscible at low molecular weight, but become immiscible at high molecular weight.[102–105] It has been reported[102,103] that PMMA and PS in a benzene solution would become incompatible with increasing both or either of the molecular weights, while no appreciable phase separation is observed at least for a combination of PS with $M_w = 2.07 \times 10^4$ and PMMA with $M_w = 1.6 \times 10^6$. The latter finding seems to be consistent with the present result for the PMMA gel sample 3. Callaghan et al. [104] have reported that when the M_w of PS and PMMA are 2950 and 2400, respectively, the binary blends are completely miscible, while phase separation occurs when either or both of the M_w of PS and PMMA are increased, and the phase boundaries are predicted to be caused by UCST (upper critical solution temperature)-type behaviour. In the present study, since PMMA gels are prepared in the presence of PS, it is expected that micro or macro phase separation occurs in the gelation process; consequently, inhomogeneities are introduced into the gel. The effect of the PS's M_w on the formation of the network in the PMMA gel is explained as follows. Since the M_w of PMMA gradually increases with the progress of polymerisation in the gelation process, the lager the M_w of PS, the earlier the phase separation starts and the more inhomogeneous is the structure of the gel, and vice versa.

2.2.2. Dependence of diffusion coefficient on the diffusing time Δ

PFGStE ^{1}H NMR measurements have been made for PMMA gel samples 1 and 7 containing PS with $M_w = 4000$ and 400,000, respectively, at room temperature by varying the diffusing time Δ in order to investigate the diffusional behaviour of PS in PMMA gels and the PMMA gel network structure. Figure 4 shows the plots of $\ln[A(g)/A(0)]$ against $\gamma^2 g^2 \delta^2(\Delta - \delta/3)$ for the phenyl peak of PS with $M_w = 4000$ in PMMA gel sample 2 by varying Δ. It is seen that the experimental data lie on a

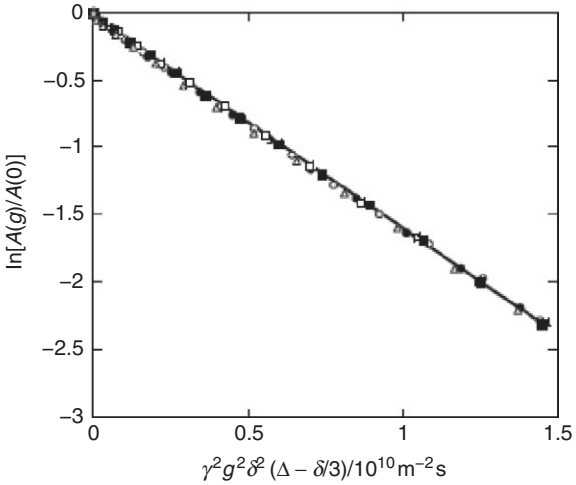

Figure 4 Diffusional stimulated echo attenuation of PS ($M_w = 4000$) in PMMA gel sample 2 with $CDCl_3$ as solvent by varying field-gradient strength g at room temperature, where $\Delta = 40$ ms (○), $\Delta = 60$ ms (●), $\Delta = 100$ ms (□), $\Delta = 300$ ms (■) and $\Delta = 500$ ms (△).

straight line in the Δ range from 40 to 500 ms, and the slope of the plots is independent of the diffusing time Δ. This shows that PS with $M_w = 4000$ in PMMA gel sample 2 has a single diffusion component during the diffusing time Δ in the range from 40 to 500 ms. It can be said that the network size of the PMMA gel sample 2 is homogeneous on the Δ timescale. The diffusion coefficient of PS (D) is determined from the slope of the straight line by using Equation (2) as 1.6×10^{-10} m^2 s^{-1}. Thus, the D/D_0 value, where D_0 is the diffusion coefficient of PS in $CDCl_3$ solution at the same polymer concentration as PMMA gel sample 2, is a constant, 0.6, in the Δ range from 40 to 500 ms. Therefore, it can be said that the translational diffusion of PS in the PMMA gels is significantly restrained as a result of the intermolecular interactions between PS and the PMMA network, and/or the simple obstruction by PS. The diffusion coefficient D can be related with the mean-square displacement $\langle z^2 \rangle$ in the z direction from the starting point after the diffusion time Δ by Equation (3). The $\langle z^2 \rangle$ value gives us information on the diffusion distance d, which reflects the experimental results as expressed by Equation (4). Consequently, by substituting the D values determined at $\Delta = 40$, 60, 100, 300 and 500 ms into this equation, the corresponding diffusion distances d can be obtained as 3.6, 4.7, 5.7, 9.8 and 12.6 μm, respectively. The d values in these experiments are much larger than the network size (4 nm) at equilibrium swelling, which is approximately estimated by using the fraction of EGDM cross-linking. Therefore, as seen from the obtained d values, it can be said that PS chains are going through some network cells within the diffusing time Δ. Figure 5 shows the plots of $\ln[A(g)/A(0)]$ against $\gamma^2 g^2 \delta^2 (\Delta - \delta/3)$ for the phenyl peak of PS ($M_w = 400{,}000$) in PMMA gel sample 7 with $CDCl_3$ as solvent. It is shown that the experimental data do not lie on a straight line at $\Delta = 40$, 60, 100, 300 and

500 ms. These data could be successfully analysed in terms of Equation (2). This means that PS with $M_w = 400{,}000$ in the PMMA gel has two diffusion components: namely, a fast diffusion component and a slow diffusion component in the Δ range from 40 to 500 ms. The diffusion coefficients for the fast and slow diffusion components (as indicated by D_{fast} and D_{slow}, respectively) and the corresponding fractions (f_{fast} and f_{slow}, respectively) that are determined by using Equation (2) are listed in Table 1. As seen from Table 1, the D_{fast}/D_0 changes only slightly from 0.92 to 0.85, while the D_{slow}/D_0 significantly decreases from 0.17 to 0.06 with increasing Δ values. However, the fractions f_{fast} and f_{slow} are independent of Δ. By substituting the D values determined at $\Delta = 40$, 60, 100, 300 and 500 ms into Equation (2), the diffusion distances for the fast diffusion component (d_{fast}) are obtained as 1.0, 1.2, 1.5, 2.6 and 3.3 μm, respectively, and the diffusion distances for the slow diffusion component (d_{slow}) as 0.4, 0.4, 0.5, 0.7 and 0.9 μm, respectively. On the basis of these experimental results, we may obtain information on the network structure of the PMMA gel. First, it is noted that D_{fast}/D_0 is close to unity and significantly larger than that for the PS with $M_w = 4000$ in spite of the much larger radius of gyration for the former than the latter. This means that the diffusion of PS with $M_w = 400{,}000$ is subject to a relatively weak restriction via the intermolecular interactions with the PMMA gel network. On the other hand, the much lower D_{slow}/D_0 values indicate that the PMMA gel sample 7 contains highly dense network structures as probed by the PS with $M_w = 400{,}000$ (Figure 5). As mentioned above, the D_{slow} values significantly decrease with an increase in Δ, whereas the D_{fast} values only slightly decrease. The latter means that the 'open' network structure is so large (probably of the order of 10^{-5} m) that the PS chains 'see' almost the same structure during the diffusion time. However, the former may be realised if the pertinent PS molecules are confined, or trapped, within the dense network structure, the size of which is comparable to the estimated diffusion distance ($\sim 10^{-6}$ m), during the diffusion time Δ; namely,

TABLE 1 Determined diffusion coefficients of probe PS with $M_w = 400{,}000$ in PMMA gel sample 7 as a function of diffusing time Δ by PFGStE ^{1}H NMR method

Diffusing time Δ (ms)		Diffusion coefficient ($m^2 s^{-1}$)	D/D_0	Fraction of diffusion component
40	D_{fast}	1.2×10^{-11}	0.92	0.34
	D_{slow}	2.2×10^{-12}	0.17	0.66
60	D_{fast}	1.2×10^{-11}	0.92	0.34
	D_{slow}	1.7×10^{-12}	0.13	0.66
100	D_{fast}	1.2×10^{-11}	0.92	0.36
	D_{slow}	1.4×10^{-12}	0.11	0.64
300	D_{fast}	1.1×10^{-11}	0.85	0.35
	D_{slow}	0.9×10^{-12}	0.07	0.65
500	D_{fast}	1.1×10^{-11}	0.85	0.35
	D_{slow}	0.7×10^{-12}	0.06	0.65

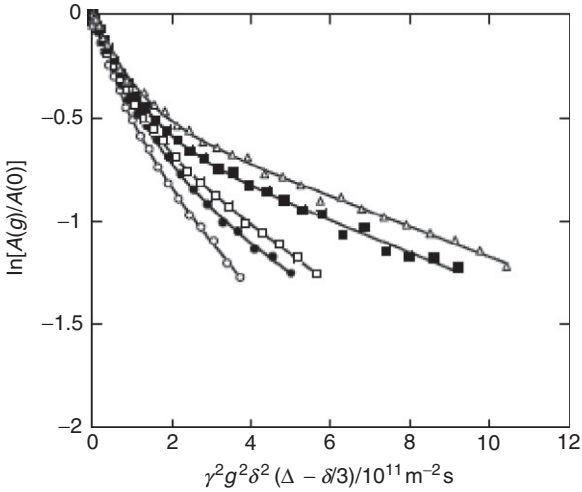

Figure 5 Diffusional stimulated echo attenuation of PS ($M_w = 400{,}000$) in PMMA gel sample 7 with $CDCl_3$ as solvent by varying field-gradient strength g at room temperature, where $\Delta = 40$ ms (○), $\Delta = 60$ ms (●), $\Delta = 100$ ms (□), $\Delta = 300$ ms (■) and $\Delta = 500$ ms (△).

the estimated diffusion coefficients must be only apparent because the diffusion distance is limited up to the local size of the dense structure. Further, from the experimental finding that the f_{fast} and f_{slow} are almost constant irrespective of different diffusing time Δ, it can be said that the PS chains in the open and large-size and the dense and small-size network structures, which correspond to the fast and slow diffusion component, respectively, do not exchange within the Δ range of 40 to 500 ms. This means that PS for the fast diffusion component is also confined in the open structures within the diffusing time. It can be concluded that the network structure of PMMA gels prepared in toluene solutions of PSs with $M_w = 4000$ and 400,000 are homogeneous and inhomogeneous, respectively, within the Δ range from 40 to 500 ms as elucidated by ^1H pulse field-gradient NMR.

2.3. Diffusional behaviour of polystyrenes with different molecular weights in the same PMMA gel network

In Section2.2, the network structure of the resultant gel samples prepared in the presence of larger PSs has been proved to be inhomogeneous, since the probe PS diffusion has been successfully analysed by a dual-mode diffusion consisting of a fast mode and a slow one.[87] The fast and the slow mode diffusions, in turn, must reflect that the PS molecules are moving through an 'open' and a 'dense' network structure, respectively. It has been shown that the inhomogeneity in the PMMA gel network thus detected is enhanced with increasing the probe PS size. This tendency, however, must be complex, since two separate effects may be involved there; namely, the presence of a larger PS would induce a more distinct

inhomogeneity to the surrounding PMMA network during the cross-linking reaction, and/or the diffusion of a larger PS may also be affected even by a larger mesh. In order to distinguish the two PS size effects for probing the gel inhomogeneity through PS diffusion, the following two types of measurements would be appropriate: (1) diffusion of one PS probe in differently prepared PMMA gels and (2) diffusion of different PS probes in one PMMA gel. Here, it is important to clarify how the same gel network is 'seen' by PS probes of different sizes, rather than how they induce different network structures. Thus, in the subsequent work,[88] it is important to perform the second diffusion measurement for clarifying the effect of the probe PS size on the diffusion through an inhomogeneous PMMA network. Further, in order to extend the 'sight' of the probes more than in a study reported previously,[87] the diffusing time(Δ) is widely varied in the range 40–500 ms. With this 'time-dependent diffusion NMR', one may estimate the size of the open and the dense regions, respectively.

The PMMA gel is employed as a common gel matrix for different PS probes with M_w of 4000, 19,000, 29,000 and 400,000 with a very narrow distribution of values of $M_w/M_n = 1.04–1.09$, which are indicated by PS ($M_w = 4000$), PS ($M_w = 19{,}000$), PS ($M_w = 29{,}000$) and PS ($M_w = 400{,}000$), respectively. Preparation of gel samples containing one of the probe PSs is performed as follows. Before evacuating a gel sample containing PS ($M_w = 400{,}000$), the diffusion coefficient of PS ($M_w = 400{,}000$) is measured as a function of the diffusing time Δ, as described below. Then, the PS molecules are all extracted by immersing the gel sample into pure $CDCl_3$, which is refreshed several times over ca. 2 months until the gel showed no PS signals in the NMR spectrum. Next, the evacuated gel sample is immersed in a 1-wt% PS ($M_w = 4000$) solution in order to let the PS get absorbed in the gel. After the NMR measurement on the gel sample thus prepared, another evacuation–immersion (absorption)–NMR measurement cycle is repeated for the other PSs. The evacuation and absorption processes were accomplished in a few days. Although we attempted to immerse PS ($M_w = 50{,}000$) in the gel, even 2 weeks' immersion proved to be futile. Thus, measurements for larger PS probes except for PS (400,000) cannot be performed. Finally, the PMMA gel sample is immersed into pure $CHCl_3$ in order to measure the diffusion coefficient of the solvent $CHCl_3$.

The D measurements on probe PSs in the PMMA gels are carried out at room temperature by the PFGStE ^{1}H NMR method operating at 300.11 MHz for ^{1}H with a pulsed field-gradient generator (the maximum field-gradient strength: 11.6 T m^{-1}). The Δ, δ and g values employed in these experiments are 40–500 ms, 0.04–2.0 ms and 0–10.0 T m^{-1}, respectively. In analysis of the Stejskal–Tanner plot, the SPLMOD approach proposed by Johnson [106] was used to determine D_i and f_i by solving Equation (2) in order to test the validity of the above-mentioned conventional method used here. The SPLMOD approach is a method of carrying out an inverse Laplace transform[107] of Equation (2) to determine D_i and f_i. In this approach, initial guesses are not required, and then the diffusion coefficient(s) and the fraction(s) of polymer gel system with the one, two and three diffusion components are automatically determined. The obtained D_i and f_i values are compared with those obtained by the conventional method.

2.3.1. Diffusional behaviour of PSs in the PMMA gel

Figure 6 shows the experimental results according to Equation (1) at $\Delta = 40$ ms. The linear lines for the solvent and PS ($M_w = 4000$) correspond to a single-mode diffusion, while the curved plots of the other systems [PS ($M_w = 19{,}000$), PS ($M_w = 29{,}000$) and PS ($M_w = 400{,}000$)] mean that the diffusion was multi-mode. Here, the multi-mode diffusion as a two-component (dual-mode) diffusion is analysed. The diffusion coefficients (D, D_{fast} and D_{slow}) and the fractions are estimated respectively by Equations (1) or (2). The obtained D and f values are listed in Table 2 together with diffusion coefficients in the bulk solution (D_0). The molecular weight dependence of the D values of the PS probes is shown in Figure 7. The observed decreasing tendency of the D values with M_w, accompanied by transition from a single-mode to a dual-mode diffusion, demonstrates that the probe diffusion is affected or obstructed by the gel matrix to different extents depending on the probe size, as discussed in the previous work. Namely, the mobility of PS molecules may reflect the difference in the surrounding network density when the probe size is larger than a critical size, which must be comparable to the network mesh of the dense region. This can be seen from the markedly large difference in the fast and slow diffusion coefficients in Table 2, which are ascribed to those in the open and the dense region, respectively.

In Section 2.2,[87] the network size inhomogeneity of PMMA gel was seen to be enhanced by increasing the PS M_w; in other words, the most homogeneous network is obtained by PS-free cross-linking. In the case of the PMMA gel that is

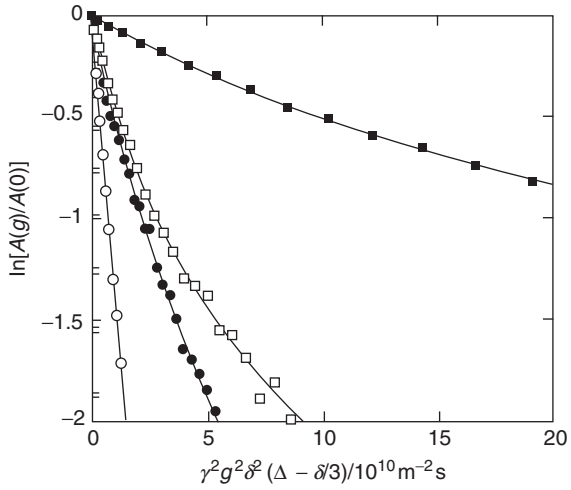

Figure 6 Diffusional stimulated echo attenuations of $CHCl_3$ (×) and PSs [PS ($M_w = 4000$) (○), PS ($M_w = 19{,}000$) (●), PS ($M_w = 29{,}000$) (□) and PS ($M_w = 400{,}000$) (■)] in the PMMA gel with deuterated chloroform as solvent by varying field-gradient strength g at room temperature with the diffusing time $\Delta = 40$ ms.

TABLE 2 Diffusion coefficients of probe polystyrene (PS) molecules in the PMMA gel estimated by the PFGStE ^{1}H NMR method

	$CHCl_3$	PS ($M_w = 4000$)	PS ($M_w = 19{,}000$)	PS ($M_w = 29{,}000$)	PS ($M_w = 400{,}000$)
D_0 ($m^2\ s^{-1}$)	2.4×10^{-9}	$2.7 \times 10^{-10} \pm 0.2 \times 10^{-11}$ ($R_h \sim 1.5$ nm)	$1.6 \times 10^{-10} \pm 0.1 \times 10^{-11}$ ($R_h \sim 2.5$ nm)	$9.4 \times 10^{-11} \pm 0.6 \times 10^{-12}$ ($R_h \sim 4.3$ nm)	$1.3 \times 10^{-11} \pm 0.1 \times 10^{-12}$ ($R_h \sim 31$ nm)
D ($m^2\ s^{-1}$) in PMMA gel synthesised in the presence of PS (400,000)	$1.9 \times 10^{-9} \pm 0.3 \times 10^{-11}$	$1.4 \times 10^{-10} \pm 0.2 \times 10^{-11}$	D_{fast} $1.2 \times 10^{-10} \pm 0.3 \times 10^{-11}$ ($f_{fast} = 0.35 \pm 0.04$) D_{slow} $2.9 \times 10^{-11} \pm 0.1 \times 10^{-11}$ ($f_{slow} = 0.65 \pm 0.04$)	D_{fast} $8.0 \times 10^{-11} \pm 0.2 \times 10^{-11}$ ($f_{fast} = 0.56 \pm 0.03$) D_{slow} $1.3 \times 10^{-11} \pm 0.6 \times 10^{-12}$ ($f_{slow} = 0.44 \pm 0.03$)	D_{fast} $1.3 \times 10^{-11} \pm 0.4 \times 10^{-12}$ ($f_{fast} = 0.34 \pm 0.04$) D_{slow} $2.1 \times 10^{-12} \pm 0.2 \times 10^{-12}$ ($f_{slow} = 0.66 \pm 0.04$)
D^a ($m^2\ s^{-1}$) in PMMA gel synthesised in the presence of the probe PS		$1.6 \times 10^{-10} \pm 0.1 \times 10^{-11}$	$6.4 \times 10^{-11} \pm 0.8 \times 10^{-12}$	D_{fast} $9.5 \times 10^{-11} \pm 0.2 \times 10^{-11}$ ($f_{fast} = 0.51 \pm 0.06$) D_{slow} $2.0 \times 10^{-11} \pm 0.2 \times 10^{-11}$ ($f_{slow} = 0.49 \pm 0.06$)	D_{fast} $1.3 \times 10^{-11} \pm 0.4 \times 10^{-12}$ ($f_{fast} = 0.34 \pm 0.04$) D_{slow} $2.1 \times 10^{-12} \pm 0.2 \times 10^{-12}$ ($f_{slow} = 0.66 \pm 0.04$)

[a]Values obtained from Ref. 87.

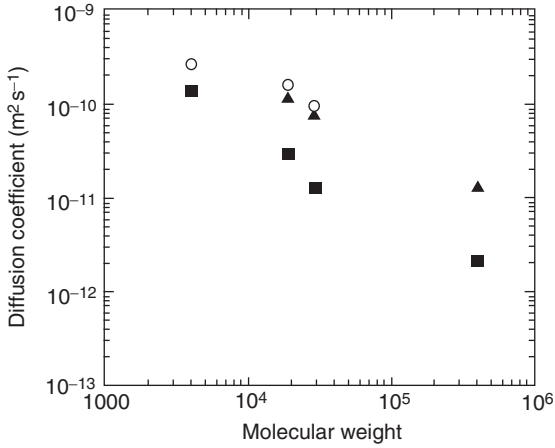

Figure 7 M_w dependence of diffusion coefficients of probe PSs: (○) in deuterated chloroform solution, (▲) fast diffusion component of PS in PMMA gel and (■) slow diffusion component in PMMA gel.

prepared in the presence of PS ($M_w = 400{,}000$), microphase separation is to be induced at the initial stage of the polymerisation cross-linking reaction of MMA by the presence of such large PS chains incompatible with PMMA, which seems to result in a more inhomogeneous network. Thus, it should be interesting to compare the present D values with those obtained in the respective original gel matrix, namely, gels prepared in the presence of the respective probe PSs. Table 2 also contains the data that are estimated with the same analysis. It can be seen that the present D values for PS ($M_w = 4000$) and PS ($M_w = 29{,}000$) are somewhat lower than those for the original gels. This seems to indicate that the network prepared in the presence of PS ($M_w = 400{,}000$) is more inhomogeneous; namely, the dense region is more developed and/or the dense mesh is finer compared with those prepared in the presence of PS probes of lower molecular weights. Further, it is noted that D_{fast}/D_0 values increase with the M_w of the PSs. This curious result means, at least apparently, that obstruction by the PMMA network of the open region becomes less significant for larger PS probes. However, this may be a reflection of averaging the 'sight' of the probe molecules. Namely, a smaller probe PS can also 'see' (or experience) the region of a far away site. Then, a small probe in an open region may also see a denser region, thus resulting in smaller D_{fast} values and vice versa. The smaller probe molecules may diffuse without appreciable obstruction in the polymer matrix, even in the dense region, because of their small size. Thus, the mesh size of the dense region must be larger than the hydrodynamic radius of PS (4000), $R_h \sim 1.5$ nm (Table 2). The largest probe PS ($M_w = 400{,}000$) differently 'sees' the open and the dense region. The much smaller D_{slow} than D_{fast} may be partly ascribed to the large size of the probe PS ($M_w = 400{,}000$). This means that the mesh size of the dense region must be significantly smaller than the R_h, 31 nm (Table 2).

2.3.2. Dependence of diffusion coefficient on the diffusing time Δ

The PFGStE NMR measurements of solvent ($CHCl_3$) and PS ($M_w = 4000$, 19,000, 29,000 and 400,000) in the same PMMA gel matrix have been carried out with varying diffusing time Δ (4–500 ms). In the case of $CHCl_3$ with the diffusing time Δ varying from 4 to 300 ms, all the data obtained with different Δ values are on a straight line. This means that the diffusion coefficient of the solvent and its diffusion behaviour do not change within the diffusing time. Figure 8 shows the corresponding results for the PS probes obtained with Δ values from 40 to 500 ms. All the PS probes except PS ($M_w = 400{,}000$) showed a comparable tendency with the solvent. Although the experimental data in the cases of PS ($M_w = 19{,}000$) and PS ($M_w = 29{,}000$) are slightly scattered, they are not systematic and may be expressed with a single curve, as shown in the figure. Namely, the multi-mode diffusion of the three PS probes may be approximated with the same pair of diffusion coefficients, which are independent of the diffusing time employed. However, the result for PS ($M_w = 400{,}000$) is distinctly different from the others above, and the experimental data for different Δ values are on different curves. As shown in Figure 8D, slopes of the plots of PS ($M_w = 400{,}000$) decrease with an increase in the diffusing time in the range 40–500 ms. That is, restricted diffusion

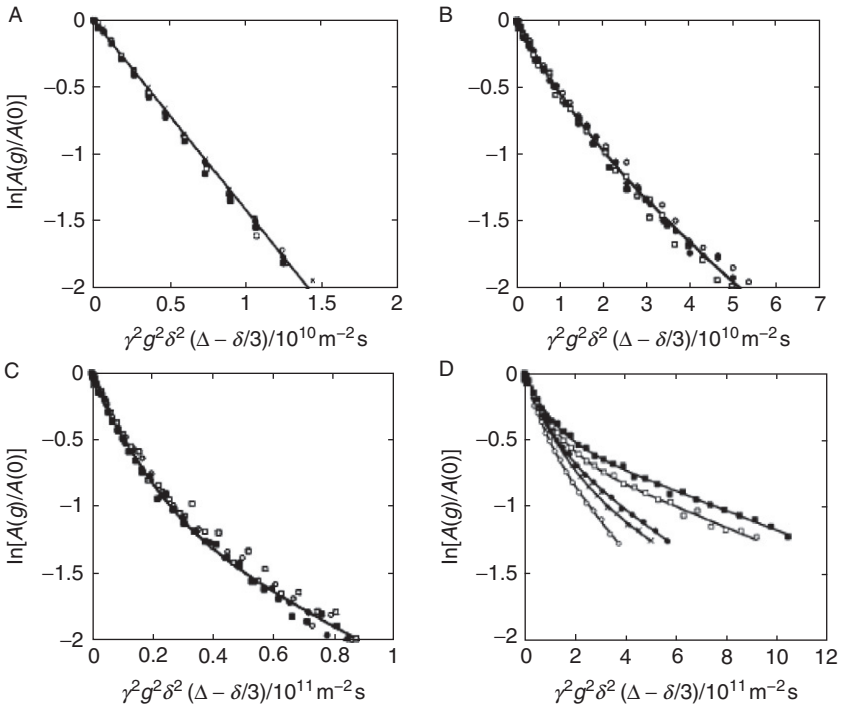

Figure 8 Diffusional stimulated echo attenuations of PSs in the PMMA gel [(A) PS ($M_w = 4{,}000$), (B) PS ($M_w = 19{,}000$), (C) PS ($M_w = 29{,}000$), and (D) PS ($M_w = 400{,}000$)] with deuterated chloroform as solvent by varying field-gradient strength g at room temperature. The diffusing time is varied as $\Delta = 40$ ms (○), $\Delta = 60$ ms (×), $\Delta = 100$ ms (●), $\Delta = 300$ ms (□) and $\Delta = 500$ ms (■).

is observed only for PS ($M_w = 400{,}000$). These results suggest that the diffusion mechanism of PS ($M_w = 400{,}000$) differs from that of the other PSs. The D values obtained by the conventional method with the assumption of two diffusion components judging from the Stejskal–Tanner plot and the SPLMOD method by Johnson[107] are summarised for PS ($M_w = 400{,}000$) in Table 3. It is recognised that the determined D and f results are in good agreement with each other. This means that the two approaches for the present polymer gel systems are reasonable for the determination of the D and f values.

It can be seen from Table 3 that D_{fast} and D_{slow} decrease with increase in Δ, and the former decrement is much smaller than the latter. The decreasing tendency of the diffusion coefficient with diffusing time suggests that so-called restricted

TABLE 3 Diffusion coefficients of probe PS with $M_w = 400{,}000$ in PMMA gel as a function of diffusing time by PFGStE ^{1}H NMR method

Diffusing time Δ (ms)		Diffusion coefficient ($m^2\ s^{-1}$)	Fraction of diffusion component	Diffusion distance (μm)
By SPLMOD method				
40	D_{fast}	1.4×10^{-11} ($\pm 0.1 \times 10^{-11}$)	0.35 ($\pm$0.03)	1.1
	D_{slow}	2.3×10^{-12} ($\pm 0.2 \times 10^{-12}$)	0.66 ($\pm$0.03)	0.4
60	D_{fast}	0.9×10^{-11} ($\pm 0.1 \times 10^{-11}$)	0.46 ($\pm$0.05)	1.0
	D_{slow}	1.7×10^{-12} ($\pm 0.2 \times 10^{-12}$)	0.54 ($\pm$0.05)	0.5
100	D_{fast}	1.2×10^{-11} ($\pm 0.6 \times 10^{-12}$)	0.37 ($\pm$0.01)	1.5
	D_{slow}	1.4×10^{-12} ($\pm 0.5 \times 10^{-13}$)	0.64 ($\pm$0.01)	0.5
300	D_{fast}	1.0×10^{-11} ($\pm 0.5 \times 10^{-12}$)	0.41 ($\pm$0.01)	2.4
	D_{slow}	0.8×10^{-12} ($\pm 0.4 \times 10^{-13}$)	0.59 ($\pm$0.01)	0.7
500	D_{fast}	1.0×10^{-11} ($\pm 0.9 \times 10^{-12}$)	0.35 ($\pm$0.01)	3.2
	D_{slow}	0.7×10^{-12} ($\pm 0.4 \times 10^{-13}$)	0.64 ($\pm$0.01)	0.8
By conventional method (assumed two components)				
40	D_{fast}	1.3×10^{-11} ($\pm 0.4 \times 10^{-12}$)	0.34 ($\pm$0.04)	1.0
	D_{slow}	2.1×10^{-12} ($\pm 0.2 \times 10^{-12}$)	0.66 ($\pm$0.04)	0.4

(*continued*)

TABLE 3 (*continued*)

Diffusing time Δ (ms)		Diffusion coefficient ($m^2\ s^{-1}$)	Fraction of diffusion component	Diffusion distance (μm)
60	D_{fast}	1.2×10^{-11} $(\pm0.5\times10^{-12})$	0.47 ($\pm$0.02)	1.2
	D_{slow}	1.6×10^{-12} $(\pm0.8\times10^{-13})$	0.53 ($\pm$0.02)	0.4
100	D_{fast}	1.2×10^{-11} $(\pm0.1\times10^{-12})$	0.37 ($\pm$0.02)	1.5
	D_{slow}	1.4×10^{-12} $(\pm0.6\times10^{-13})$	0.63 ($\pm$0.02)	0.5
300	D_{fast}	1.2×10^{-11} $(\pm0.3\times10^{-12})$	0.37 ($\pm$0.01)	2.7
	D_{slow}	0.84×10^{-12} $(\pm0.3\times10^{-13})$	0.63 ($\pm$0.01)	0.7
500	D_{fast}	1.1×10^{-11} $(\pm0.4\times10^{-12})$	0.35 ($\pm$0.01)	3.3
	D_{slow}	0.7×10^{-12} $(\pm0.2\times10^{-13})$	0.65 ($\pm$0.01)	0.78

diffusion occurs in this system. In other words, the PS chains are confined in the open or the dense region during the diffusion, and any appreciable transition across the two regions does not occur. That is, if the coming-in and going-out of the probe between the two regions occurs freely, the observed diffusion parameters must be independent of the diffusing time, which is actually observed for the smaller PS probes. The time-dependent decrease in the D values thus observed for PS ($M_w = 400{,}000$) may be safely ascribed to the significantly larger molecular size (31 nm) compared with the approximate mesh size (3.4 nm) of the network at equilibrium swelling, which is roughly estimated by using the fraction of EGDM cross-linking, as shown in Table 3. For this approximate network mesh-size estimation, the effect from chain entanglements is disregarded. The above discussion may be quantitatively reconsidered in terms of diffusion distance, which would give us an estimate of the dimensions of the dense and the open regions. The diffusion coefficient D can be related to the mean-square displacement $\langle z^2 \rangle$ in the z direction from the starting point after the diffusion time Δ by Equation (3). The $\langle z^2 \rangle$ value gives us information on the diffusion distance d, which reflects the experimental results as expressed by Equation (4). Consequently, by substituting the D values of PS ($M_w = 400{,}000$) determined at $\Delta = 40$, 60, 100, 300 and 500 ms into Equation (4), the diffusion distances are obtained as shown in Table 3. The d values in these experiments are much larger than the averaged mesh size (3.4 nm) at equilibrium swelling. Therefore, as seen from the obtained d values, it can be said that PS chains are going through many network mesh cells within the diffusing time Δ. As mentioned above, the D_{slow} values significantly decrease with an increase in Δ, whereas the D_{fast} values decrease only slightly. The latter

means that the 'open' network structure is so large (probably of the order of 10^{-5} m) that PS chains 'see' a matrix with almost the same mesh size during the diffusion time or are actually confined within the open region. On the other hand, the former corresponds to a situation in which the pertinent PS molecules are confined, or trapped, within the dense network structure. Because the estimated diffusion coefficients are only apparent, namely, the nominal diffusion distance is limited up to the local size of the dense region within which the probe is entrapped, then the size of the confinement must be comparable to the estimated diffusion distance ($\sim 10^{-6}$ m), during the diffusion time Δ. Further, the f_{fast} and f_{slow} values are almost constant irrespective of a different diffusing time Δ. This experimental fact means that the PS chains in the open and larger size region and the dense and smaller ones do not exchange within the Δ range from 40 to 500 ms. This is also consistent with the supposed confinement of the PS probe within the open and the dense regions during the diffusing time.

The relation between the determined D values and the diffusing time Δ can be summarised for the respective probe molecules as follows. In the case of the smallest probe molecules, $CHCl_3$ and PS ($M_w = 4000$), which must be smaller than the network mesh size of the dense region, the probe diffusion at $\Delta \approx 0$ is, in principle, divided into two classes. One is fast diffusion in the open region, and the other is slow diffusion in the dense region. There, each of the probe diffusions does not recognise the network mesh but feels the polymer chain only as an obstacle. For $\Delta > 0$, $CHCl_3$ and PS ($M_w = 4000$), which are smaller than the network mesh size, the probes can move through the gel network rather freely. This enables a prompt averaging of the initial two-component diffusion into the single-component one within the shortest diffusing time Δ of the present pulse field-gradient NMR experiment (4 or 40 ms).

In the case of medium-size probes, PS ($M_w = 19{,}000$) and PS ($M_w = 29{,}000$), they are moderately larger than the network mesh. Consequently, probe diffusion in the dense region recognises each network mesh and has a broad distribution of diffusion coefficients corresponding to the distribution of the gel network. Averaging of the two diffusion components (fast diffusion in the open region and slow diffusion that has a broad distribution of diffusion coefficients in the dense region) into the single component needs a considerably long time in comparison with the experimental diffusing time of the pulsed field-gradient NMR experiments. For this reason, its diffusion behaviour apparently does not change within the diffusing time. The largest probe, PS ($M_w = 400{,}000$), which must be much larger than the mesh size of the dense region, also keeps the two diffusion components. In this case, however, the diffusion components are confined in the dense and open regions. They do not exchange within the diffusing time scale. This confinement is, of course, to be ascribed to the mesh fineness, which is much smaller than the probe PS size. Thus, no significant changes in D value, which must be caused by such exchange, are observed within several hundreds of milliseconds. Theoretically, the diffusional behaviours of probe molecules in gels have been interpreted by polymer dynamic model theories: Rouse dynamics, medium region dynamics (for example, entropic trapping model) and reptation dynamics.[108] At this stage, they cannot be compared readily with the experimental results of polymer dynamics model theories.

Therefore, a systematic way has been proposed to estimate mesh sizes and region sizes, each of which has a population in the heterogeneous gel matrix, by utilising a set of probe molecules of different sizes together with time-dependent diffusion NMR spectroscopy. This methodology may be generally developed to examine and establish the gel structure and the diffusion behaviours of small molecules for many complex systems including biological ones.

2.4. Structural characterisation of inhomogeneous PMMA gels by time-dependent diffusion

All PMMA gel samples prepared as described in Section 2.2 and 2.3 are transparent, thus suggesting that any substantial macrophase separation does not occur in the gels. However, it may be expected that pronounced inhomogeneity of the PMMA gels, such as macrophase separation between PMMA and PS, should also be detected by the relevant NMR technique. Thus, PMMA gels which have different levels of phase separation (inhomogeneities for the network size) are proposed by performing PMMA gelation in the presence of PS with $M_w = 400{,}000$ and with various PS concentrations from 6 to 50 mg mL^{-1}. Since the network inhomogeneity is expected to develop with increasing the PS concentration, network structures including micro- to macrophase separation will be introduced to the gel. Inhomogeneities thus introduced into the PMMA gels are characterised through the estimation of the diffusion coefficients of the probe molecules in the PMMA gels by the PFGStE ^{1}H NMR method in order to envisage the phase separation process occurring during the pertinent gel network formation from the viewpoint of the probe polymer diffusional processes.

The radical copolymerisation of MMA and EGDM in addition to PS initiated by AIBN is performed in deuterated toluene solution at 75 °C for 1 day, and then the gelation is carried out.[5,100] PS is added as a diffusional probe polymer during the gelation process. MMA (1.4 mol L^{-1}), EGDM (47.7 mmol L^{-1}) and AIBN (4.6 mmol L^{-1}) are dissolved in deuterated toluene, and this stock solution is divided and transferred into an NMR sample tube of 5 mm diameter. Four different pre-gel solution samples (transparent) are prepared using this stock solution with various PS concentrations $C_{PS} = 6$, 10, 20 or 50 mg mL^{-1} in deuterated toluene (PMMA gel samples A1–A4, respectively). All the pre-gel solution samples in the NMR sample tubes are deoxygenated by bubbling nitrogen gas for 10 min, and then gelation is carried out at 75 °C for 1 day. Four rod-like PMMA gel samples containing PS are obtained. PMMA gel samples A1 and A2 are transparent, while samples A3 and A4 appear to be slightly opaque, showing signs of phase separation. The Q values of all the PMMA gels used are about 6. The concentration of cross-linking is 0.034 units per MMA monomer unit. From the obtained diffusion coefficient $D_0 = 2.0 \times 10^{-11}$ m^2 s^{-1} of PS ($M_w = 400{,}000$) in a dilute solution of toluene (6 mg mL^{-1}), the hydrodynamic radius is obtained as 19.5 nm by using the Stokes–Einstein equation. The approximate average pore size is 2.7 nm, which is roughly estimated by using the fraction of EGDM cross-linking. In the PFGStE ^{1}H NMR experiments, the Δ, δ and g values employed are 40–1000 ms, 0.04–4.0 ms, and 0–10 T m^{-1}, respectively.

2.4.1. ^{1}H NMR spectrum of PMMA gel sample and the assignment

A typical ^{1}H NMR spectrum of a PMMA gel (sample A4) at room temperature is shown in Figure 9. The spectral assignments are straightforwardly made by using the reference data of PS, PMMA and toluene that is contained in commercial deuterated toluene as an isotope impurity.[109–111] All the peaks are numbered from high frequency to low frequency. Peak 1 overlaps with two peaks that come from the *m*- and *p*-phenyl protons of PS and phenyl protons of toluene. Peak 2 comes from the *o*-phenyl protons of PS. Peaks 3 and 4 are assigned to the methylene protons of unreacted MMA, suggesting that MMA of about one-third of the feed remains in each sample. Peak 5, the largest one, is assigned to the methoxy protons of PMMA and unreacted MMA. Area of peak 5 is larger than the area of 3 compared with peak 3. The asymmetric line shape of peak 5 is caused by bad shims. Peaks 6–9 are assigned to the main chain protons of PS and PMMA and methyl protons of unreacted MMA. The diffusion coefficients of PS and the MMA are estimated, as shown below, by use of peak 2 and peak 4, respectively.

2.4.2. Diffusion behaviours of PS in PMMA gels

The PFGStE ^{1}H NMR measurements have been made for PMMA gel samples A1–A4 containing PS with $M_w = 400{,}000$ with the diffusion time $\Delta = 60$ ms at room temperature in order to investigate the diffusion behaviour of PS in PMMA gels and the PMMA gel network structure. Figure 10 shows the plots of $\ln[A(g)/A(0)]$ against $\gamma^2 g^2 \Delta^2(\Delta - \Delta/3)$ for the phenyl peak for PS with $\Delta = 60$ ms in PMMA gel samples A1–A4. First of all, it is noted that the diffusion behaviour of PS is significantly dependent on the PS concentration. The change from the non-linear

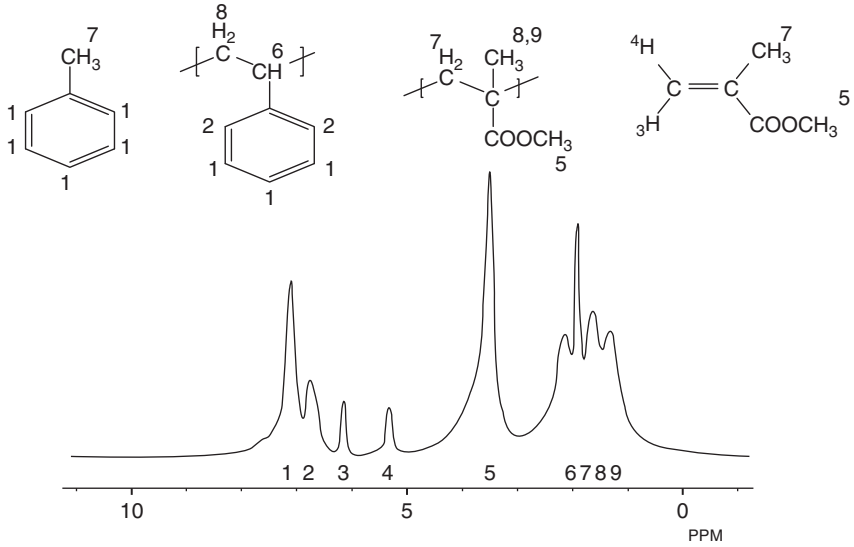

Figure 9 ^{1}H NMR spectrum of PMMA gel (sample A4) containing PS with $M_w = 400{,}000$ and deuterated toluene. The solvent contains a very small amount of toluene as impurity.

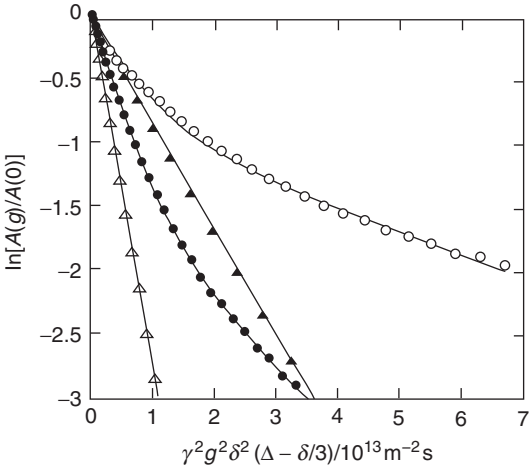

Figure 10 Diffusional stimulated echo attenuations of PSs in PMMA gels [(○) sample A1, (●) sample A2, (△) sample A3, and (▲) sample A4] with deuterated toluene as solvent by varying field-gradient strength g with the diffusion time $\Delta = 60$ ms at room temperature.

plots to the linear ones for samples A1–A4 means that the diffusion mode of the PS varies from a two-component mode to a single-component one with an increase in the PS concentration. The non-linear plots of samples A1 and A2 may be analysed as two diffusion components. The diffusion coefficients of the fast and slow diffusion components and the corresponding fractions that are determined by Equation (2) are plotted in Figure 11. However, the single diffusion coefficients of PS (D) for samples A3 and A4 are determined from the slope of the respective straight lines by Equation (1). Thus, the D and f values obtained are listed in Table 4. The diffusion coefficients are plotted as a function of C_{PS} in Figure 11, where the open circles are the D_0 values, that is diffusion coefficients of the PS ($M_w = 400{,}000$) in pure deuterated toluene solution at the same concentration as used in the gel samples. In order to extract some information on the network structure from the diffusion coefficient data, we plotted D/D_0, instead of D, against C_{PS} (Figure 12). It is noted here that the D/D_0 values significantly increase with C_{PS}. This dependency of D/D_0 on PS concentration suggests that the 'open' structure introduced by the coexistence of PS in the PMMA gel-forming process gradually predominates with an increase in the PS concentration, probably reflecting the phase separation process of the PMMA/PS system. It has been well known that PS is incompatible with PMMA under certain conditions, and the resultant phase separation depends on polymer molecular weight and concentration.[112,113] Thus, in the present system, it is expected that micro- and/or macrophase separation occurs during the gelation process, and there locally exists the 'open network structure' where PMMA chains are considerably dilute. Actually, the appearance of samples A3 and A4 is slightly milky and turbid, which is a sign of phase separation. With increasing C_{PS}, phase separation in the gel sample proceeds so that the 'open' network structure predominates in the PMMA gel samples, and

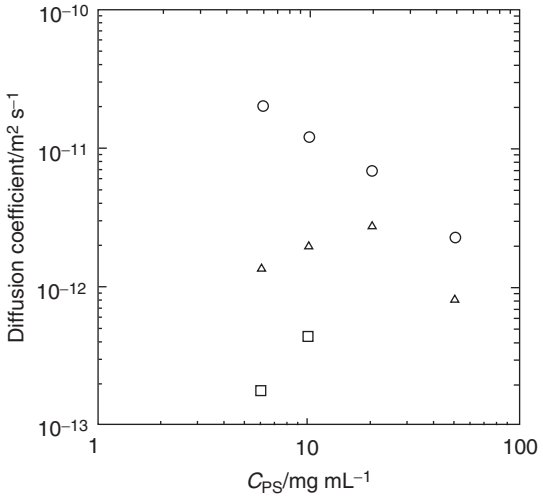

Figure 11 Diffusion coefficients (D_0) of PSs in deuterated toluene solution (○), the diffusion coefficients of fast diffusion component (D_{fast}) of PSs in PMMA gel samples (△) and the diffusion coefficients of slow diffusion component (D_{slow}) of PSs in PMMA gel samples (□) as a function of the PS concentration (C_{PS}).

TABLE 4 Determined diffusion coefficients and fractions for the fast and slow diffusion components of PSs in PMMA gels by PFGSE ^{1}H NMR method

Sample	Diffusion coefficient ($m^2\ s^{-1}$)		Fraction of diffusion component	
	D_{fast}	D_{slow}	f_{fast}	f_{slow}
A1	1.4×10^{-12}	1.8×10^{-13}	0.55	0.45
A2	2.0×10^{-12}	4.4×10^{-13}	0.77	0.23
A3	2.7×10^{-12}	–	1.00	0.00
A4	0.8×10^{-12}	–	1.00	0.00

this process manifests itself with an increase in the D/D_0 values. In order to illustrate this situation, the network structures of samples A1 and A2 and samples A3 and A4 are schematically shown in parts A and B of Figure 13, respectively. From the viewpoint of the diffusion process of PS, three kinds of network regions may be envisaged: one is the 'open' region and exists commonly in Figure 13A and B. In this region, the diffusion of PS must be close to that of a free one in this solvent. In the second and third regions in (A) and (B), respectively, however, PMMA network chains are entangled to different extents; in the second region (equivalent to the 'dense region' in Section 2.3, the diffusion of PS is substantially interfered within the PMMA network. In the third region, the PS chains are not able to enter into the region because of the dense PMMA network structure. Thus, the experimental result suggests that at the later stages of phase separation the PS

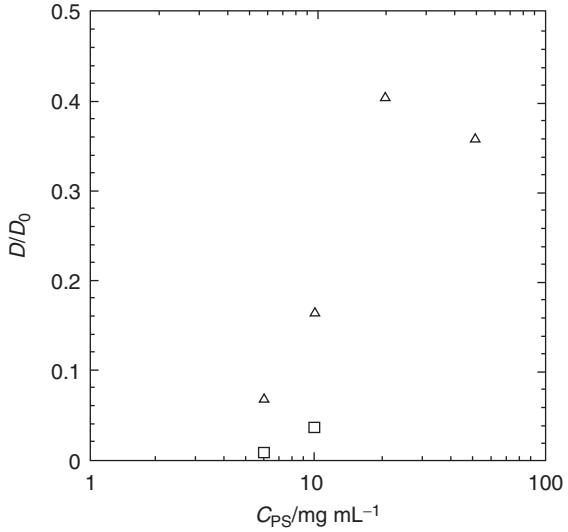

Figure 12 Diffusion coefficients (*D*s) of fast diffusion component (△) and slow diffusion component (□) normalised by diffusion coefficients (D/D_0) of PSs in deuterated toluene solution as a function of the PS concentration (C_{PS}).

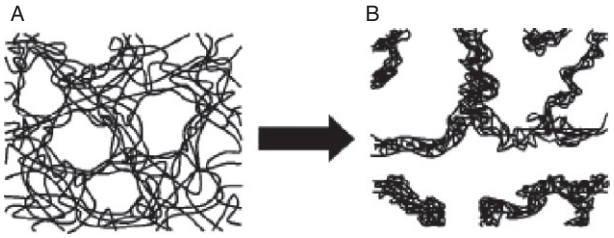

Figure 13 Schematic diagram for the supposed network structures of PMMA gel samples A1, A2 (A) and A3, A4 (B): (A) lower C_{PS} and (B) higher C_{PS}, where the phase separation is developed.

molecules are excluded from such a concentrated PMMA network region because of the inherent incompatibility of the two polymers. On the basis of these supposed network structures, one may understand why the diffusion behaviour of PS changes from a double-component mode to a single-component one with an increase in C_{PS}. This shows that, in the first region, the PMMA chains are considerably dilute, and then the PS molecules diffuse freely to some degree. Here, the fast diffusion component in the samples A1 and A2 and the single components in samples A3 and A4 are both assigned to the PS molecules in the first region. In the second region, the PS molecules are strongly confined or trapped. The PS molecules in the second region correspond to the slow diffusion component in samples A1 and A2. With a further increase in C_{PS}, the second region changes to the third region, to which no PS molecules are accessible. Samples A3 and A4 show only

single-component diffusion. Although the third region is not directly detected by the diffusion experiments of the probe PS ($M_w = 400{,}000$), it should be quite reasonable to suppose its existence on the basis of the alteration of the diffusion mode with C_{PS}. The same thing can be inferred from the component fraction data. The f_{slow} values of samples A1 and A2 are 0.45 and 0.23, respectively. The significant decrease in the slow component, with increasing C_{PS}, seems to be consistent with the supposed trend that the second region diminishes with the phase separation.

2.4.3. Dependence of the diffusion coefficient of PS on the diffusion time Δ

In order to elucidate the PS diffusion behaviour in PMMA gel, the PFGStE ^{1}H NMR measurements have been made with varying values of the diffusion time Δ. For samples A1 and A2, the diffusion coefficients for the fast and slow diffusion components (as indicated by D_{fast} and D_{slow}, respectively) and the corresponding fractions (f_{fast} and f_{slow}, respectively) are determined by using Equation (2), and D_{fast} and D_{slow} are plotted in Figure 14A and B. The single diffusion coefficients of

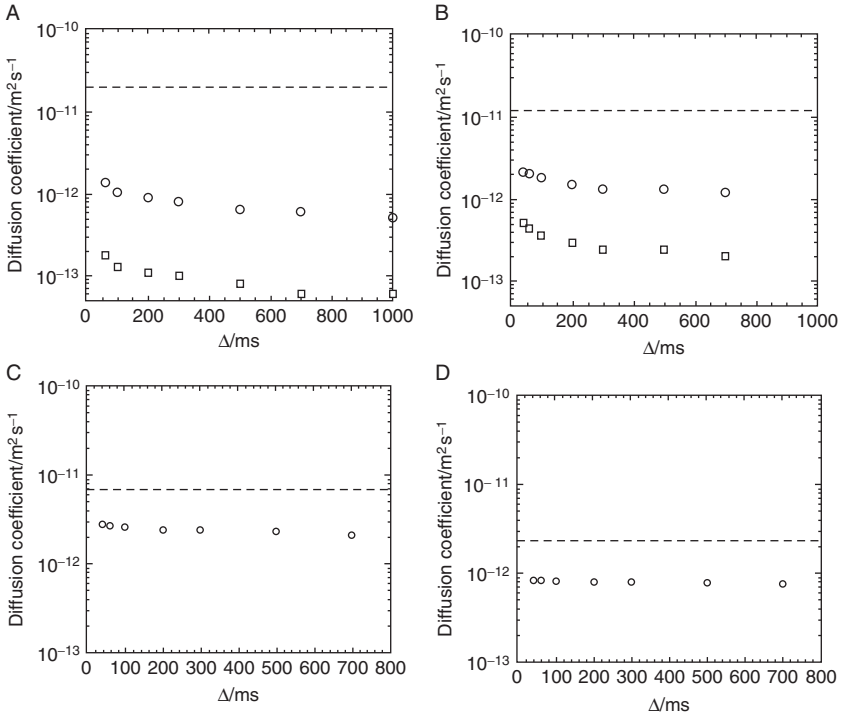

Figure 14 Δ dependence of diffusion coefficients (*D*s) of probe PSs ($M_w = 400{,}000$), where the broken line is the *D* of PS in deuterated toluene solution, the *D* of fast diffusion component of PS: in PMMA gel (○) and the *D* of slow component of PS (□) in PMMA gel [(A) sample A1, (B) sample A2, (C) sample A3, and (D) sample A4].

PS (D) for samples A3 and A4 are determined from the slope of the respective straight lines by Equation (1). The diffusion coefficients are plotted in Figure 14C and D. For samples A1 and A2, the respective fractions f_{fast} and f_{slow} are almost constant irrespective of different diffusion time (Δ) values. This means that PS chains corresponding to the fast and the slow diffusion components do not exchange within Δ. In other words, the PS molecules are confined in the open region and the dense region at least within Δ. It is known that particles confined to any closed space undergo the so-called restricted diffusion.[18] When the size of the closed space is comparable to the diffusion distance of the particles during Δ, the diffusion of some particles is not 'free' but 'restricted'. Thus, the measured diffusion coefficient becomes apparent and decreases as a function of Δ. In the system for samples A1 and A2, D significantly decreases with an increasing Δ value (Figure 14A and B, which is typical for the restricted diffusion. PS chains in PMMA gel samples A1 and A2 are confined within the open region and the dense region within Δ. These experimental results seem to be consistent with the constant f values as well as with the scheme shown in Figure 13A. However, for samples A3 and A4, the diffusion is of a single mode, and the Δ dependence of D values is much less significant compared with those for samples A1 and A2. This suggests that the diffusion of the PS in the former samples is not a typical restricted diffusion. The 'open' structure in gel samples is so much developed that the PS molecules may enjoy an almost free diffusion. These experimental results seem to just correspond to the scheme as shown in Figure 13B.

2.4.4. Diffusion behaviour of unreacted MMA in the PMMA gels

Let us note the diffusion behaviour of small molecules, that is unreacted MMA, in the PMMA gel matrix. Using the vinyl peak of the unreacted MMA, PGSE ^{1}H NMR measurements on the small molecule diffusion are performed for PMMA gel samples A1–A4 with varying Δ. The experimental data lie on a straight line in the Δ range from 60 to 500 ms, and the slope of the plots is independent of the diffusion time Δ. This clearly shows that the diffusion of the small molecule is a single mode and not restricted. The diffusion coefficient of MMA (D) as obtained from the slope of the straight line is also independent of the polymer concentration: for samples A1–A4, D (10^{-9} m^2 s^{-1}) = 1.4, 1.5, 1.5 and 1.4, respectively. The constancy of the diffusion coefficient of the small probe means that the overall density of the PMMA matrix in all the samples is also constant irrespective of the difference in the phase transition level, since the diffusion coefficients of the probe molecules in the gel matrix should depend on the matrix density.[53,73] However, with this small probe, inhomogeneities of PMMA gel samples are not detected from the diffusion behaviour. These experimental results suggest that different levels of inhomogeneities of the gel samples can be detected by employing probe molecules of different sizes.

In Sections 2.2 and 2.3, it is described that the network structures of polymer gels, especially microscopic inhomogeneity, may be detected through the diffusion behaviour of probe molecules of different sizes, which can be obtained by using time-dependent diffusion NMR spectroscopy. In this section, it will be

shown that the same NMR procedure is also available to examine changes in the network inhomogeneity resulting from macroscopic phase separation. The PS probe ($M_w = 400{,}000$), which is much larger than the mesh size, distinctly changes the diffusion behaviour from the dual mode to the single one reflecting the course of the phase separation, while the small probe (MMA) is unable to detect the inhomogeneity change. Thus, these studies so far demonstrate that the time-dependent NMR method, using probe molecules with different sizes, is effective in the structural analysis of gel networks. In order to establish this procedure, however, the diffusion behaviours of the medium-size PS probes, comparable to the gel mesh, are also to be analysed.

2.5. Diffusional behaviour of star polystyrenes with different molecular weights in PMMA gels

In this section, we are concerned with star PS polymers (s-PS) as probes in addition to linear PS (l-PS). Star polymers are typical branched polymers and have a unique three-dimensional shape like a sphere.[114] Some studies on the diffusional behaviour of star polymers in a matrix have been reported by using dynamic light scattering and permeation methods. The diffusivity of star polymers in a gel is typically much lower than that of linear polymers in the same matrix.[6,115] Further, it is predicted that a larger suction flux will be necessary for a star polymer to enter a pore cavity when the radius is smaller than the gyration radius of the polymer, compared with the case of a linear polymer.[116] The diffusion coefficients (Ds) of s-PSs ($M_w = 82{,}000$, 202,000, 282,000 and 375,000), having an octafunctional chlorosilane core and eight PS side chains[117] in PMMA gels swollen with deuterated chloroform ($CDCl_3$), have been measured as a function of the diffusion time by the PFGSE ^{1}H NMR method, and the diffusional behaviour in the gels has been elucidated.

2.5.1. Diffusion coefficients of s-PSs in dilute $CDCl_3$ solution

The diffusion coefficients of the PSs in dilute $CDCl_3$ solution have been measured as a function of the molecular weight by the PFGSE ^{1}H NMR method at 25 °C, where the M_ws of l-PSs and s-PSs are in the range of 4000–650,000 and of 82,000–375,000, respectively. The log–log plots of the Ds against M_ws are shown in Figure 15. It can be seen that the dependence of s-PSs in a $CDCl_3$ dilute solution is similar to that for l-PSs, but the former is somewhat larger than the latter for the same molecular weight. This means that the hydrodynamic diameter of the s-PS is smaller than that of l-PS of a corresponding M_w. This is a common feature of s-PSs as compared with l-PSs.

2.5.2. Diffusional behaviour of s-PSs in the PMMA gels

PFGStE ^{1}H NMR experiments for PMMA gel samples have been carried out with the diffusing time Δ varied from 40 to 500 ms, and the diffusional behaviour of s-PSs in the PMMA gels[117] observed. The D values have been determined from the plots of $\ln[A(g)/A(0)]$ against $\gamma^2 g^2 \delta^2 (\Delta - \delta/3)$ for the phenyl peak of PSs in PMMA gels as shown in Figure 16. Then, the obtained D_{fast} and D_{slow} values are plotted

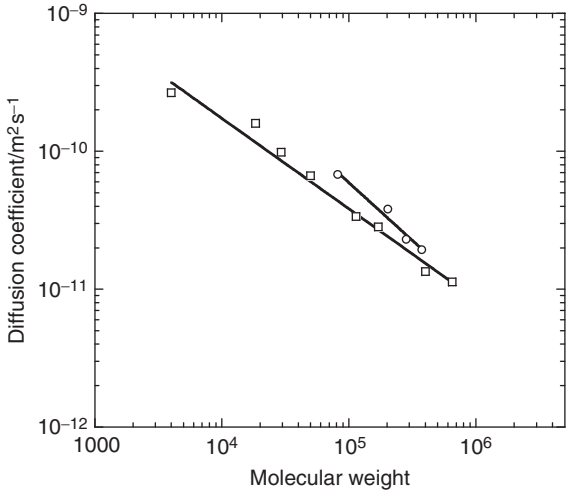

Figure 15 Diffusion coefficients (*D*s) of linear (□) and star (○) PSs in $CDCl_3$ dilute solution against molecular weight M_w.

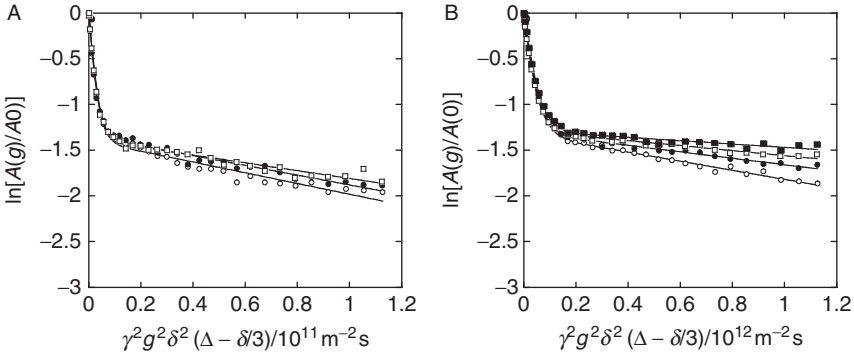

Figure 16 Diffusional stimulated echo attenuations of s-PSs in PMMA gel ((A) $M_w = 82{,}000$ and (B) $M_w = 202{,}000$) with deuterated chloroform as solvent, respectively, by varying field-gradient strength *g* at room temperature, where the diffusing time $\Delta = 40$ ms (○), $\Delta = 100$ ms (●), $\Delta = 300$ ms (□) and $\Delta = 500$ ms (■).

against Δ as shown in Figure 17. The diffusional behaviour may be explained in a similar manner as with the l-PS case, in terms of a inhomogeneous structure consisting of the open and dense regions. Namely, the diffusional mode of the s-PSs ($M_w = 82{,}000$ and 202,000) in the PMMA gel may be expressed as being composed of two components, in the Δ range from 40 to 500 ms. PS molecules of the fast diffusion component exist in the 'open' network structure, and PS molecules of the slow diffusion component exist in the 'dense' network structure region.

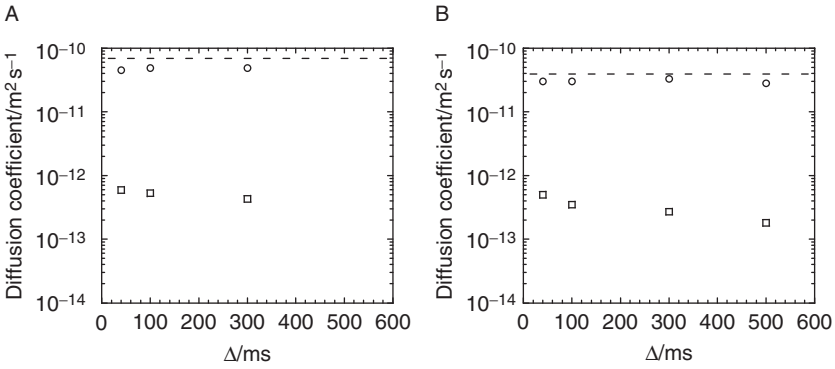

Figure 17 Δ dependence of the *D*s of probe star PSs ((A) 82,000 and (B) 202,000), where the broken line indicates the *D*s of PS in pure deuterated chloroform solution, and (○) and (□) indicate the *D*s of fast and fast diffusion components of PS in PMMA gel, respectively.

Figure 18 shows the M_w dependence of the D values of s-PSs and l-PSs. The estimated D_{slow} values are significantly smaller than those for l-PSs of comparable M_ws, while the D_{fast} values of the s-PSs are slightly larger than those of the l-PSs. The former is ascribed to the enhanced obstruction by the dense network for the diffusion of s-PS molecules due to their failure in adopting the reptation-type diffusion, and the latter may be simply understood as being caused by the smaller hydrodynamic diameter of s-PS molecules than that of a corresponding l-PS with the same M_w.

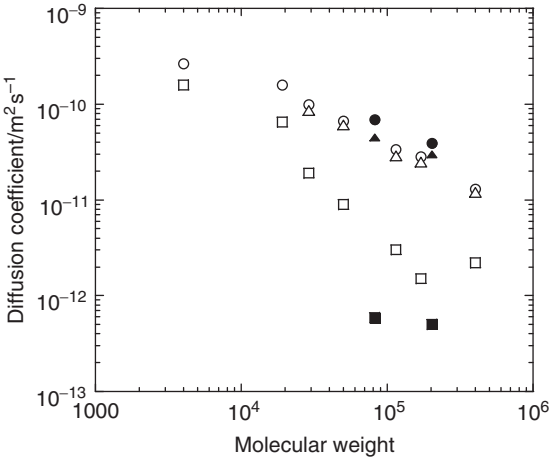

Figure 18 M_w dependence of diffusion coefficients (*D*s) of linear and s-PSs, where the *D*s of l-PS and s-PS in deuterated chloroform solution are indicated by (○) and (●), respectively, and the *D*s of fast diffusion component of l-PS and s-PS in PMMA gel are indicated by (△) and (▲), respectively, and the *D*s of slow component of l-PS and s-PS in PMMA gel by (□) and (■), respectively.

2.6. Schematic diagram of inhomogeneous networks in polymer gels characterised through the observed time-dependent diffusion coefficients

Relations between the determined D values of probe molecules and inhomogeneities of matrix gels are summarised for the respective probe molecules as shown in Figure 19. In Section 2.4, a series of inhomogeneities introduced to PMMA gels by carrying out radical polymerisations containing PS at various concentrations are described. PFGStE ^{1}H NMR measurements were performed for the PMMA gel samples, which enabled us to investigate the PMMA gel network structure on the basis of the diffusional behaviour of large probe PS molecules and small probe molecules (unreacted monomer) in PMMA gels. That is, the diffusional behaviour of large PS probe molecules significantly depends on the amount of PS that is added to the gelation batch. The analysis of the PFGStE ^{1}H NMR measurements has strongly suggested that the PS diffusion consists of two diffusion components, while it changes to a single mode with increasing the PS concentration. These results seem to be correlated with the phase separation, or development, of an 'open' network structure that is induced by the added PS during the gelation of

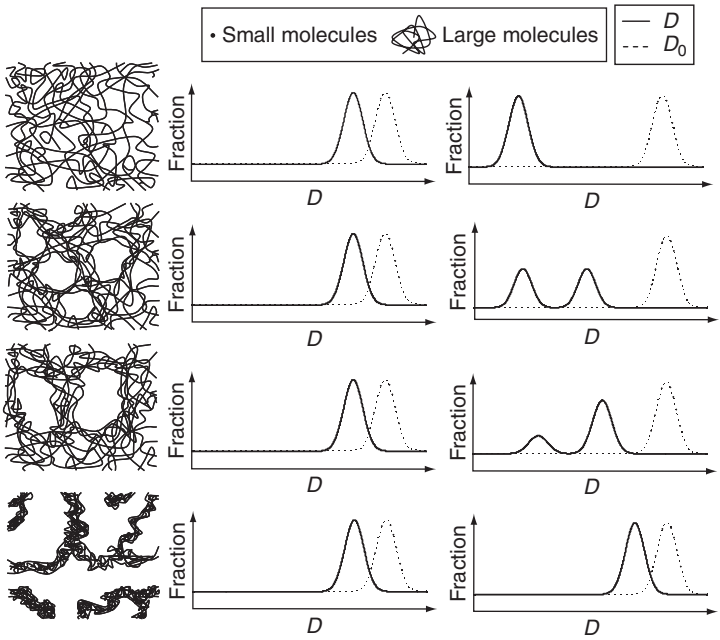

Figure 19 Schematic diagram for the PMMA network structure of PMMA gel samples with different levels of inhomogeneities introduced by performing the PMMA gelation in the presence of PS with various M_w and/or C_{PS} (left figures) and for the distribution curves of the Ds of probe molecules (right ones). The solid line is for the distribution curve of the Ds of probe molecules in PMMA gel sample and the broken line is for the distribution curve of the Ds of probe molecules in solution without PMMA gel matrix.

the PMMA matrix. From these results, the change of PMMA gel network structure introduced during the PMMA gelation in the presence of PS with various C_{PS} values and the diffusional behaviours of small and large probe molecules are reasonably elucidated as shown in Figure 19.

The relation between the determined D values and the observation time t is summarised for the respective probe molecules as shown in Figure 20. At $t \approx 0$, the probe molecule should exist, in principle, either as one that is far from the polymer segments constituting the network and hence has negligible interactions with the chains (assigned to a component with a larger D value, residing in the open region), or as one that significantly interacts with the network because of being close to the chains (assigned as a component with a slower D value in the dense region). For $t > 0$, the observed diffusion behaviour depends on the sizes of probe molecules. In the case of the small probe molecules, which are smaller than the network mesh size of the dense region, they can move through the gel network rather freely. This enables a prompt averaging of the initial two-component diffusion into the single-component one within the observation time of the present PFGSE NMR experiment, as shown in Figure 20A. In the case of medium-size probes that are moderately larger than the network mesh, probe diffusion in the dense region suffers obstruction from each network, depending on the mesh, to lead to a broad distribution of diffusion coefficients corresponding to the distribution of the gel network. Averaging of the two-component diffusion into the single-component one needs a long time in comparison with the experimental diffusing time of the pulse field-gradient NMR experiments as shown in Figure 20B. In the case of large probe molecules, the diffusion components are confined in the dense and the open regions, and they do not exchange within the diffusing time scale as shown in Figure 20C.

3. NETWORK STRUCTURE OF MICROMETRE-SCALE CAVITY OBTAINED FROM PHASE-SEPARATED POLYMER BLENDS AS CHARACTERISED BY USING PROBE MOLECULES

Studies of bicontinuous structures developed via spinodal decomposition (SD) have been a research theme for those dealing with binary mixtures of molecular fluids, binary alloys and polymer blends.[118,119] Scattering techniques such as light, small angle X-ray and small-angle neutron have been extensively used to examine the phase-separated structure of polymer blends.[119–121] As a result of these studies, a great deal of information on the time evolution of the phase-separated structures has been obtained. Most recently, laser scanning confocal microscopy (LSCM) has been shown to be an excellent tool to capture the 3D interface structure of polymer blends.[122–124] By using LSCM, the time evolution of the interface between two coexisting phases developed via SD is quantitatively observed in 3D images. At present, high-resolution X-ray computed tomography (X-ray CT) has been developed and it has provided very useful quantitative information about the micrometre-scale 3D structures of polymer blend systems; thus the mechanism of phase separation for polymer blends has been clarified.[125–127] In the X-ray CT

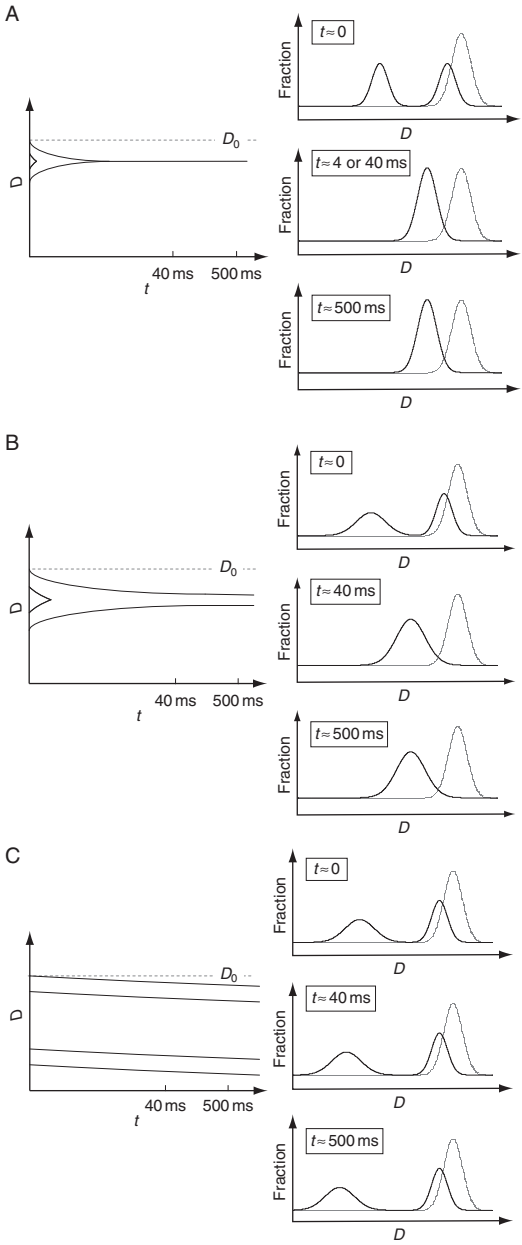

Figure 20 Relations between the observation time *t* and the distribution curve of the *D*s of probe molecules ((A) smaller molecules, (B) similar-size molecules and (C) larger molecules as compared with the network mesh size of the dense region). The solid line is for the distribution curve of the *D*s of probe molecules in PMMA gel sample, and the broken line is for that in solution without gel matrix.

method, the contrast of images comes from the difference of absorption for X-rays, which corresponds to the differences of electron density. Polymers have almost the same absorption for X-rays. Hence if polymer blends are observed by X-ray CT, heavy atom labelling is necessary for contrast enhancement. In the case of LSCM, the labelling by fluorescence species is necessary for contrast enhancement. In ^{1}H NMR microscopy, one can use the contrast of images from the difference of ^{1}H spin density, ^{1}H spin–lattice relaxation time (T_1) and ^{1}H T_2. Here, the difference of T_1 and T_2 values correspond to the difference in molecular motion. Thus, one does not need to label any specified species to obtain contrast enhancement for the observation of polymer blends. Nevertheless, to our best knowledge, there has been no application to investigate phase-separated structures of polymer blends using 3D NMR microscopy. Most recently, several 10-μm-scale 3D structural characterisations of phase-separated poly(styrene-*ran*-4-bromostyrene) (PS-Br)/PMMA blends by 3D NMR microscopy have been carried out, and the potential of 3D NMR microscopy as one of the methodologies for analysing several 10-mm-scale 3D structures of polymer blend systems has been shown by comparing the observation of the same polymer blend samples by means of 3D X-ray CT.[90]

Before going ahead, it is necessary to describe some details of the preparation of the polymer blend in order to understand the formation of the micrometre-scale cavity. The partial bromination (a molar average degree: 0.28) of PS[128] is necessary for contrast enhancement for X-ray CT. The M_w and polydispersity (M_w/M_n) of PS-Br are 1.4×10^5 and 2.36, respectively, and M_w and M_w/M_n for PMMA are 6.0×10^4 and 2.31, respectively. A mixture of PS-Br and PMMA (PS-Br/PMMA. 50/50 wt%) is dissolved in benzene to form a 5% homogeneous solution and then lyophilised. The mixture after lyophilisation is melt-pressed at 180 °C and moulded into a disc of 5 mm diameter and 5 mm thickness. During this moulding process, phase separation between PS-Br and PMMA occurs. Three different phase separation times of the PS-Br/PMMA mixtures are employed: 6, 8 and 10 h. These are termed samples B1, B2 and B3, respectively. In this time range, phase separation is in the advanced stage. The PS-Br/PMMA mixtures, after the heating treatment, are then quenched by placing them on a metal plate that is cooled by liquid N_2. Samples B1, B2 and B3 were observed by optical microscopy (not shown in figure). It is seen that the phase separation is advanced with thermal treatment at 180 °C. However, the optical microscopy observation could provide the 3D structural information only de-constructively.

For the observation of 3D ^{1}H NMR images, the imaging pulse sequence is based on the 3D gradient echo (GE) pulse sequence,[129] as shown in Figure 21. In the 3D GE method, the field gradients in the y and z directions (g_y and g_z) are the phase-encoding gradients, while the field gradient in the x direction (g_x) is the frequency-encoding gradient. The flip angle is 30°, the repetition time is 1 s, and the echo time is 3.771 ms. The data processing of the 3D images is performed by 3D FT using the Para Vision program for the acquisition and processing of NMR data. The 3D observations of the PS-Br/PMMA mixtures are performed with X-ray microtomography instruments. The principles and basic instrumentation are described elsewhere.[130] For the X-ray CT measurements, a high-precision rotating stage with an air bearing is used for rotating the sample. A series of

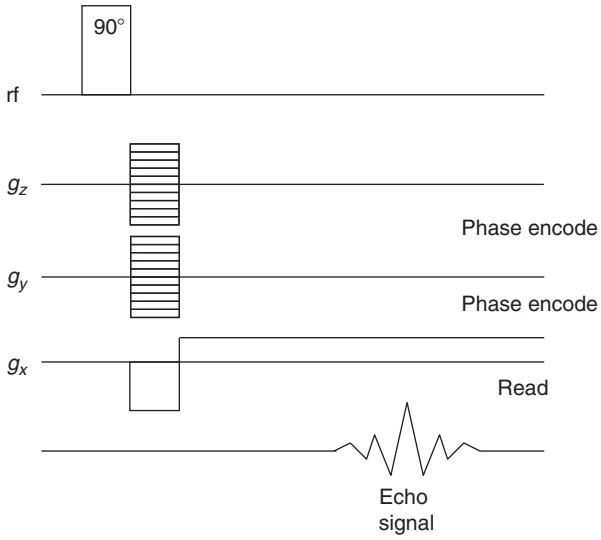

Figure 21 A pulse sequence of the 3D gradient echo method.

X-ray absorption images ('projections') are acquired over 180° in 0.2° increments with a CCD camera (1280 × 1000 pixels) equipped with an image intensifier. The projections obtained are processed by the filtered back-projection method[131] to obtain tomograms of the blend, which are stacked together to generate 3D digital array data, and the speckle noises in the 3D digital array are eliminated by a median filter.[132] The 3D data processing is binarised to find the interface between PS-Br-rich and PMMA-rich domains according to a protocol previously described.[133]

The observed 2D sliced ^{1}H NMR images of PS-Br/PMMA mixture as melt-pressed at 180 °C at three different thermal treatment times 6, 8 and 10 h are observed, where the *xy*-plane sliced images are shown with a thickness of 40 mm in the *z* direction. In this experiment, only the ^{1}H signals from water that exists in spaces that have been PMMA-rich domains are observed. Therefore, the bright regions correspond to spaces that have been PMMA-rich domains. The dark regions in these images correspond to spaces of PS-Br-rich domains. The 2D sliced transmission X-ray CT images were also observed. It is shown that the scale width of both the PMMA-rich and PS-Br-rich domains increases as the treatment times increase in both the NMR and X-ray CT images. In Figure 22A–C, the 3D NMR images are shown of a PS-Br/PMMA mixture reconstructed by the *xy*-plane sliced images, where the bright and dark regions indicate PMMA-rich and PS-Br-rich domains, respectively. The number of data points is 128 × 128 × 128, and the voxel size is 40 × 40 × 40 μm. Figure 22D–F shows the 3D images reconstructed by the 2D transmission X-ray CT image datasets. The features of the 3D NMR images and 3D X-ray CT images are very close to each other. Also, they are very close to the optical microscope photographs. It is well known that polymer blends of PMMA and PS take a bicontinuous structure in the phase separation process.

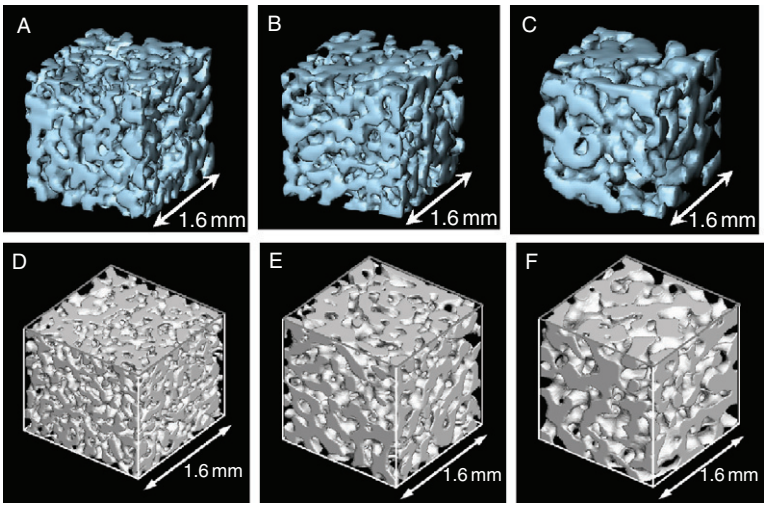

Figure 22 The observed 3D images reconstructed by the 2D NMR images (A–C) and X-ray CT (D–F) datasets. (A–C): 300 MHz 3D ^{1}H NMR images of the PS-Br/PMMA mixtures washed with acetonitrile to solute only PMMA-rich domains and water poured into the flask to replace the space that has been PMMA-rich domains with water, with an imaging system with a maximal gradient strength of 100 mT m^{-1} with a high resolution of several 10 μm at room temperature. (D–F): The 3D X-ray CT observations of the PS-Br/PMMA mixtures performed with X-ray microtomography instruments. The X-ray source is operated at 40 kV. A high-precision rotating stage with an air bearing is used for rotating the sample. A series of X-ray absorption images ('projections') are acquired over 180° in 0.2° increments with a CCD camera (1280 × 1000 pixels) equipped with an image intensifier. The thermal treatment times for polymer blend samples are 6 h for (A) and (D), 8 h for (B) and (E) and 10 h for (C) and (F), respectively, at 180 °C.

The bicontinuous structure of the PMMA-rich and PS-Br-rich domains can be non-destructively observed in both the 3D NMR and X-ray CT images as shown in Figure 16.

The animation video clip for the surface of the phase-separated blend samples and another of the inner cavity of the blend sample can analyse the branch structure for all of the inner cavities. The scale width increases as the thermal treatment time increases. The micrometre-scale phase-separated structure of the PS-Br/PMMA blends is shown in Figure 23. It is seen that phase separation advances with the thermal treatment time. The distribution of the branch structure for a bicontinuous structure obtained from 3D NMR images is shown in Figure 23, where the thermal treatment times for the samples are 6 h for A, 8 h for B and 10 h for C at 180 °C. As seen from this figure, the fraction that the bicontinuous structure takes of the three branches, at each junction point, is more than 50%. The average distribution of the branching number at the junction points is almost independent of the thermal treatment time in the present experiments.

The log–log plots of the integrated intensity ($s(q)$) versus q-space calculated by FT of both the 3D NMR and X-ray CT images of PS-Br/PMMA blend samples are shown in Figure 24A–C, where the thermal treatment times for the samples are 6 h

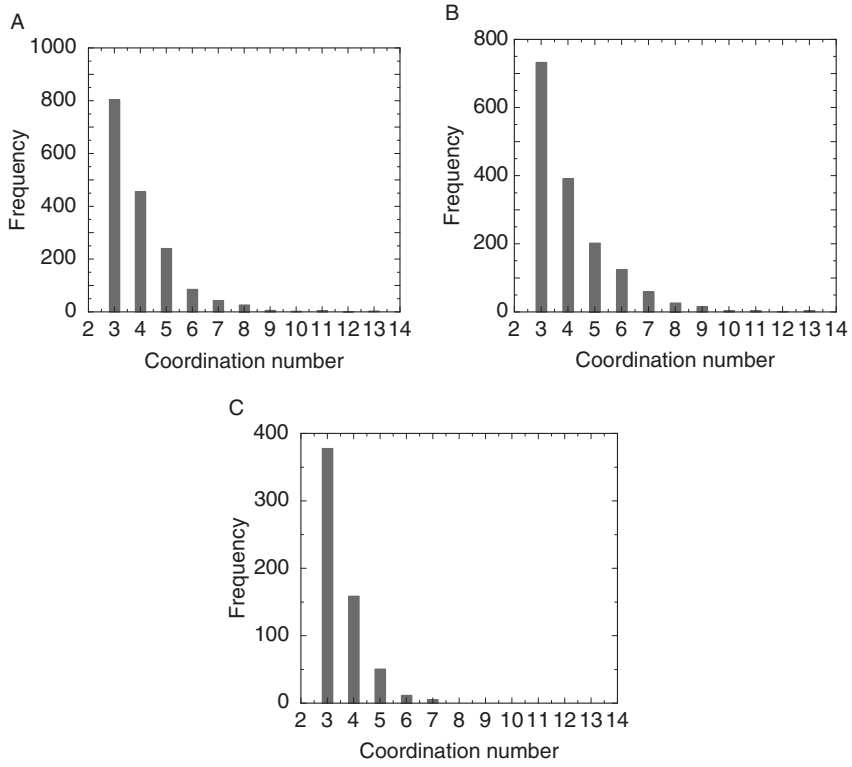

Figure 23 The distribution of the branch structure for a bicontinuous structure obtained by 3D NMR images. The thermal treatment time is 6 h for (A), 8 h for (B) and 10 h for (C) at 180 °C.

for A, 8 h for B and 10 h for C at 180 °C. The overall shapes of $s(q)$ for the 3D NMR imaging and X-ray CT results are very close to each other. The peak positions of these plots are connected with the characteristic wavelength of the PS-Br/PMMA phase-separated structure, which corresponds to the sizes of phase separation domains (Λ_m). Table 5 indicates the sizes of phase-separated domains (Λ_m) calculated by the peak positions in Figure 18A–C, the volume fraction of PS-Br (FPS-Br), the surface area per unit volume (S/V) and the volume (V) used in the calculation by 3D NMR imaging and X-ray CT. The Λ_m values of the PS-Br/PMMA blend samples at three different thermal treatment times, 6, 8 and 10 h, are 225, 278 and 400 μm, respectively, as determined by 3D NMR imaging. The corresponding Λ_m values, as determined by X-ray CT, are 222, 280 and 376 μm, respectively. The Λ_m values determined by 3D NMR imaging and 3D X-ray CT are very close to each other. The Λ_m increases as the thermal treatment time increases. Further, the $\Phi_{PS\text{-}Br}$ and S/V values obtained from the 3D NMR and X-ray CT images are very close to each other. These results show that it is possible to quantitatively evaluate the phase-separated structure of polymer blends by using 3D NMR images as well as 3D X-ray CT images. It is demonstrated that 3D NMR imaging is a very useful means for characterising the micrometre-scale cavity of a polymer network.

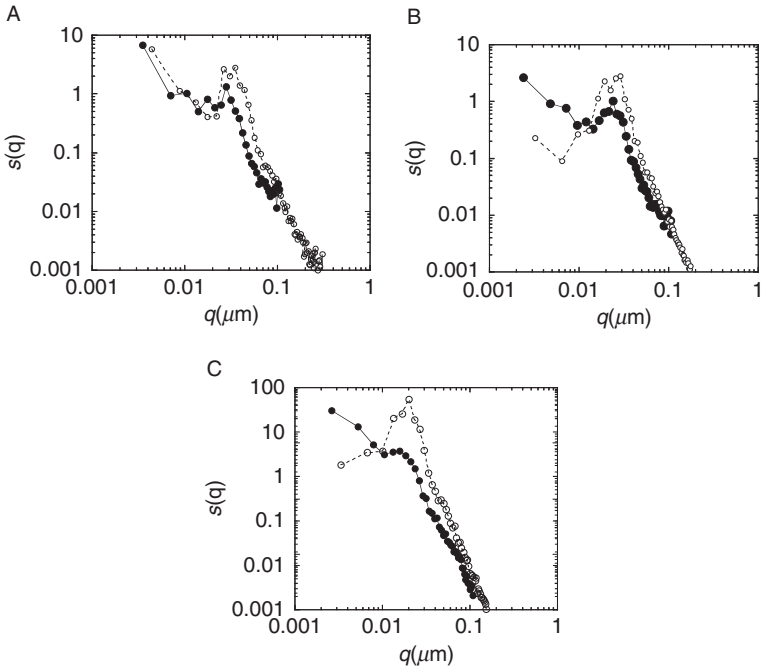

Figure 24 The plots of the integrated intensity versus *q*-space calculated by the FT of the observed 3D datasets. The thermal treatment time is 6 h for (A), 8 h for (B) and 10 h for (C) at 180 ° C. The filled black circles correspond to the 3D NMR imaging results, and the open white circles to the X-ray CT results.

TABLE 5 Structural parameters of the size of phase separation domain (Λ_m), the volume fraction of PS-Br ($\Phi_{PS\text{-}Br}$) and the surface area per unit volume (S/V) and the volume (V) used as calculated by the observed 3D datasets of 3D NMR imaging and X-ray CT

Samples	Λ_m (μm)	$\Phi_{PS\text{-}Br}$	S/V (μm^{-1})	V (μm^3)
3D NMR imaging				
Sample 1[a]	225	0.47	1.1×10^{-2}	9.3
Sample 2[b]	278	0.46	1.0×10^{-2}	22.6
Sample 3[c]	400	0.40	6.3×10^{-3}	14.1
3D X-ray CT				
Sample 1[a]	222	0.50	1.5×10^{-2}	2.3
Sample 2[b]	280	0.51	1.2×10^{-2}	7.1
Sample 3[c]	376	0.51	9.3×10^{-3}	8.1

[a]Thermal treatment time of 6 h at 180 °C.
[b]Thermal treatment time of 8 h at 180 °C.
[c]Thermal treatment time of 10 h at 180 °C.

4. CONCLUSIONS

The inhomogeneity of a gel network size, characterised through the precise observation of time-dependent diffusion coefficients reflecting sensitive intermolecular interactions between the network and the probe polymers, are reported. The methods employed include field-gradient ^{1}H NMR techniques such as PFGSE and PFGStE. Further, structural characterisation for a 3D network of a complicated micrometre-scale cavity, produced by dissolving one of two kinds of polymer in a polymer blend phase-separated by elevating the temperature above room temperature, has been made using a solvent and 3D NMR imaging with irradiated filed-gradient pulses from the x, y and z directions. Therefore, it can be said that the former NMR methodology will give us more significant nanometre-scale structural information on inhomogeneous networks in polymer gels of the nanometre-scale, and the latter NMR technique will provide more significant structural information on the micrometre-scale cavity of polymer systems.

REFERENCES

1. Y. Tsujita, I. Ando and A. J. Barnes, *J. Mol. Struct.*, 2005, **739,** 1–212(Special issue).
2. K. Dusek and W. Prins, *Adv. Polym. Sci.*, 1969, **6,** 1.
3. P. N. Pusey and W. van Megen, *Physica A*, 1989, **157,** 705.
4. S. Mallam, F. Horkay, A. M. Hecht and E. Geissler, *Macromolecules*, 1989, **22,** 3356.
5. R. Bansil, S. Pajević and Č. Koňák, *Macromolecules*, 1990, **23,** 3380.
6. J. Won and T. P. Lodge, *J. Polym. Sci. Polym. Phys. Ed.*, 1993, **31,** 1897.
7. F. Schosseler, R. Skouri, J. P. Munch and S. J. Candau, *J. Phys. II*, 1994, **4,** 1221.
8. F. Ikkai and M. Shibayama, *Phys. Rev. E*, 1997, **56,** R51.
9. M. Shibayama, *Macromol. Chem. Phys.*, 1998, **199,** 1.
10. M. Shibayama, M. Tsujimoto and F. Ikkai, *Macromolecules*, 2000, **33,** 7868.
11. H. Furukawa and K. Horie, *Phys. Rev. E*, 2003, **68,** 31406.
12. Y. Cohen, O. Ramon, I. J. Kopelman and S. Mizrahi, *J. Polym. Sci. Polym. Phys. Ed.*, 1992, **39,** 1055.
13. O. Okay, *Prog. Polym. Sci.*, 2000, **25,** 711.
14. E. O. Stejskal and E. J. Tanner, *J. Chem. Phys.*, 1965, **42,** 288.
15. J. E. Tanner and E. O. Stejskal, *J. Chem. Phys.*, 1968, **49,** 1765.
16. E. D. von Meerwall and R. D. J. Ferguson, *J. Chem. Phys.*, 1981, **74,** 6956.
17. T. Nose, *Ann. Rep. NMR Spectrosc.*, 1993, **27,** 217.
18. W. S. Price, *Ann. Rep. NMR Spectrosc.*, 1996, **32,** 51.
19. R. Kimmich, *NMR: Tomography, Diffusiometry, Relaxometry*. Springer, Berlin, 1997.
20. H. Yasunaga, M. Kobayashi, S. Matsukawa, H. Kurosu and I. Ando, *Ann. Rep. NMR Spectrosc.*, 1997, **34,** 39.
21. A. K. Whittaker, *Ann. Rep. NMR Spectrosc.*, 1997, **34,** 105.
22. S. Matsukawa, H. Yasunaga, C. Zhao, H. Kurosu and I. Ando, *Prog. Polym. Sci.*, 1999, **24,** 995.
23. L. Masaro and X. X. Zhu, *Prog. Polym. Sci.*, 1999, **24,** 731.
24. P. C. Lauterbur, *Nature*, 1973, **242,** 190.
25. (a) P. Mansfield and P. K. Grannell, *J. Phys.*, 1973, **C6,** L422. (b) A. N. Garroway, P. K. Grannell and P. Mansfield, *J. Phys.*, 1974, **C6,** L457.
26. P. T. Callaghan, *Principles of Nuclear Magnetic Resonance Microscopy*. Claredon Press, Oxford, 1991.
27. B. Blümich, *NMR Imaging of Materials*. Clarendon Press, New York, 2000.
28. P. T. Challaghan, K. W. Jolley and J. Levierve, *Biophysics*, 1979, **28,** 133.
29. P. T. Callaghan, K. W. Jolly, J. Levierve and R. B. K. King, *J. Colloid Interface Sci.*, 1983, **92,** 332.
30. P. T. Callaghan and D. N. Pinder, *Macromolecules*, 1983, **16,** 968.

31. P. T. Callaghan and O. Sonderman, *J. Phys. Chem.*, 1983, **87,** 1737.
32. P. T. Callaghan and A. Coy, *Phys. Rev. Lett.*, 1992, **68,** 3176.
33. L. Masaro, X. X. Zhu and P. M. Macdonald, *Macromolecules*, 1998, **31,** 3880.
34. M. Nydén, S. Olle and K. Gunnar, *Macromolecules*, 1999, **32,** 127.
35. K. Nagashima, V. Strashko, P. M. Macdonald, R. D. Jenkins and D. R. Bassett, *Macromolecules*, 2000, **33,** 9329.
36. M. A. Winnik, S. M. Bystryak, C. Chassenieux, V. Strashko, P. M. Macdonald and J. Siddiqui, *Langmuir*, 2000, **16,** 4495.
37. A. Larsson, D. Kuckling and M. Schoenhoff, *Coll. Surf. A*, 2001, **190,** 185.
38. H.-J. Sass, G. Musco, S. J. Stahl, P. T. Wingfield and S. Gresiek, *J. Biomol. NMR*, 2004, **18,** 303.
39. S. Kanesaka, K. Kamiguchi, M. Kanekiyo, S. Kuroki and I. Ando, *Biomacromolecules*, 2006, **7,** 1318.
40. (a) H. Yamakawa, S. Matsukawa, H. Kurosu, S. Kuroki and I. Ando, *Chem. Phys. Letts.*, 1998, **283,** 333. (b) H. Yamakawa, S. Matsukawa, H. Kurosu and I. Ando, *J. Chem. Phys.*, 1999, **111,** 129.
41. Y. Yin, C. Zhao, S. Kuroki and I. Ando, *J. Chem. Phys.*, 2000, **113,** 7635.
42. Y. Yin, C. Zhao, S. Kuroki and I. Ando, *Macromolecules*, 2002, **35,** 2335.
43. Y. Yin, C. Zhao, A. Sasaki, H. Kimura, S. Kuroki and I. Ando, *Macromolecules*, 2002, **35,** 5910.
44. E. Fisher, R. Kimmich, U. Beginn, M. Möller and N. Fatkullin, *Phys. Rev. E*, 1999, **59,** 4079.
45. K. Hayamizu, Y. Aihara, S. Arai and C. G. Martinez, *J. Phys. Chem. B*, 1999, **103,** 519.
46. R. Trampel, J. Schiller, L. Naji, F. Stallmach, J. Kärger and K. Arnold, *Biophys. Chem.*, 2002, **97,** 251.
47. (a) S. Kim, H. Kimura, S. Kuroki and I. Ando, *Chem. Phys. Lett.*, 2003, **367,** 581–585. (b) S. Kim, S. Kuroki and I. Ando, *Chem. Phys.*, 2006, **323,** 545–552.
48. M. Matsui, Y. Yamane, S. Kuroki, I. Ando, K. Fu and J. Watanabe, *J. Mol. Struct.*, 2005, **739**(1–3), 131 (Special issue).
49. M. Matsui, Y. Yamane, S. Kuroki, I. Ando, K. Fu and J. Watanabe, *Ind. Eng. Chem. Res.*, 2005, **44,** 8694.
50. H. Yasunaga and I. Ando, *Polym. Gels Netw.*, 1993, **1,** 267–274.
51. A. Ohtsuka, T. Watanabe and T. Suzuki, *Carbohydr. Polym.*, 1994, **25,** 95.
52. T. Watanabe, A. Ohtsuka, N. Murase, P. Barth and K. Gersonde, *Magn. Reson. Med.*, 1996, **35,** 697.
53. S. Matuskawa and I. Ando, *Macromolecules*, 1996, **29,** 7136.
54. S. Matsukawa and I. Ando, *Macromolecules*, 1997, **30,** 8310.
55. S. Schlick, Z. Gao, S. Matsukawa, I. Ando, E. Fead and G. Rossi, *Macromolecules*, 1998, **31,** 8124–8133.
56. N. Tanaka, S. Matsukawa, H. Kurosu and I. Ando, *Polymer*, 1998, **39,** 4703.
57. C. Zhao, S. Matsukawa, H. Kurosu and I. Ando, *Macromolecules*, 1998, **31,** 3139.
58. K. Hayamizu, Y. Aihara and W. S. Price, *Solid State Ionics*, 1998, **107,** 1.
59. S. Matsukawa and I. Ando, *Macromolecules*, 1999, **32,** 1865.
60. C. Zhao, H. Zhang, T. Yamanobe, S. Kuroki and I. Ando, *Macromolecules*, 1999, **32,** 3389.
61. L. Masaro, M. Ousalem, W. E. Baille, D. Lessard and X. X. Zhu, *Macromolecules*, 1999, **32,** 4375.
62. Z. Gao, S. Schlick, S. Matsukawa, I. Ando and G. Rossi, *Macromolecules*, 1999, **32,** 8124.
63. C. Zhao, S. Kuroki and I. Ando, *Macromolecules*, 2000, **33,** 4486.
64. K. Hayamizu, Y. Aihara, S. Arai and W. S. Price, *Electrochim. Acta*, 2000, **45,** 1313.
65. Y. Aihara, S. Arai and K. Hayamizu, *Electrochim. Acta*, 2000, **45,** 1321.
66. Y. Yamane, M. Matsui, S. Kuroki and I. Ando, *Macromolecules*, 2001, **34,** 5961.
67. Y. Yamane, M. Kobayashi, S. Kuroki and I. Ando, *Macromolecules*, 2001, **34,** 5961.
68. Y. Saito, H. Kataoka and A. M. Stephan, *Macromolecules*, 2001, **34,** 6955.
69. Y. Yamane, M. Kobayashi, H. Kimura, S. Kuroki and I. Ando, *Polymer*, 2002, **43,** 1767.
70. P. Y. Ghi, D. J. T. Hill and A. K. Whittaker, *Biomacromolecules*, 2002, **3,** 554.
71. Y. Yamane, M. Matsui, H. Kimura, S. Kuroki and I. Ando, *Macromolecules*, 2003, **36,** 5655.
72. Y. Yamane, M. Kanekiyo, S. Koizumi, C. Zhao, S. Kuroki and I. Ando, *J. Appl. Polym. Sci.*, 2004, **92,** 1053.
73. Y. Yamane, I. Ando, F. L. Buchholz, A. R. Reinhardt and S. Schlick, *Macromolecules*, 2004, **37,** 9841.
74. E. Wentrup-Byrne, D. J. Hill and A. K. Whittaker, *Biomacromolecules*, 2004, **5,** 1194.
75. Y. Yamane, S. Koizumi, S. Kuroki and I. Ando, *J. Mol. Struct.*, 2005, **739**(1–3), 137(Special issue).
76. J. Gutenwik, B. Nilsson and A. Axelsson, *Biochem. Eng. J.*, 2004, **19,** 1.
77. T. Brand, S. Richter and S. Berger, *J. Phys. Chem. B*, 2006, **110,** 15853.

78. H. Yasunaga, H. Kurosu and I. Ando, *Macromolecules*, 1992, **25,** 6505.
79. T. Shibuya, H. Yasunaga, H. Kurosu and I. Ando, *Macromolecules*, 1995, **28,** 4377.
80. H. Kurosu, T. Shibuya, H. Yasunaga and I. Ando, *Polymer J.*, 1996, **28,** 80.
81. Y. Hotta and I. Ando, *J. Mol. Struct.*, 2002, **602/603,** 165.
82. S. Yokota, A. Sasaki, Y. Hotta, Y. Yamane, H. Kimura, S. Kuroki and I. Ando, *Macromol. Symp.*, 2004, **207,** 105.
83. A. Yamazaki, Y. Hotta, H. Kurosu and I. Ando, *Polymer*, 1997, **28,** 2082.
84. A. Yamazaki, Y. Hotta, H. Kurosu and I. Ando, *Polymer*, 1998, **39,** 1511.
85. Y. Hotta, T. Shibuya, H. Yasunaga, H. Kurosu and I. Ando, *Polym. Gels Netw.*, 1998, **6,** 1.
86. A. Yamazaki, Y. Hotta, H. Kurosu and I. Ando, *J. Mol. Struct.*, 2000, **554,** 47.
87. K. Kamiguchi, S. Kuroki, M. Satoh and I. Ando, *Polymer*, 2005, **46,** 11470.
88. K. Kamiguchi, S. Kuroki, M. Satoh and I. Ando, *Macromolecules*, 2008, **41,** 1318.
89. K. Kamiguchi, S. Kuroki, M. Satoh and I. Ando, *Macromolecules*, 2009, **42,** 231.
90. S. Koizumi, Y. Yamane, S. Kuroki, I. Ando, Y. Nishikawa and H. Jinnai, *J. Appl. Polym. Sci.*, 2007, **103,** 470.
91. L. E. Hahn, *Phys. Rev.*, 1950, **80,** 580.
92. J. E. Tanner, *J. Chem. Phys.*, 1970, **52,** 2523.
93. S. Kanesaka, H. Kimura, S. Kuroki, I. Ando and S. Fujishige, *Macromolecules*, 2004, **37,** 453.
94. W. S. Price, *in*: *Modern Magnetic Resonance*, (G. A. Webb ed.), Kluwer Academic Publisher, London, 2006, p. 105.
95. I. Furó and S. Dvinskikh, *in*: *Modern Magnetic Resonance*, (G. A. Webb ed.), Kluwer Academic Publisher, London, 2006, p. 113.
96. Y. Yamane and S. Kim, *in*: *Modern Magnetic Resonance*, (G. A. Webb ed.), Kluwer Academic Publisher, London, 2006, p. 119.
97. S. Matsukawa, *in*: *Modern Magnetic Resonance*, (G. A. Webb ed.), Kluwer Academic Publisher, London, 2006, p. 125.
98. Y. Yamane, S. Kanesaka, S. Kim, K. Kamiguchi, M. Matsui, S. Kuroki and I. Ando, *Ann. Rep. NMR Spectrosc.*, 2006, **58,** 51.
99. T. Brand, E. J. Cabrita and S. Berger, *in*: *Modern Magnetic Resonance*, (G. A. Webb ed.), Kluwer Academic Publisher, London, 2006, p. 131.
100. Ő. Pekcan and Y. Yilmaz, *J. Appl. Polym. Sci.*, 1997, **63,** 1777.
101. Y. Miyaki, Y. Eninaga and H. Fujita, *Macromolecules*, 1978, **11,** 1180.
102. S. Krause, *J. Macromol. Sci. Rev. Macromol. Chem.*, 1972, **7,** 251.
103. R. Kuhn, H. J. Cantow and W. Burchard, *Angew. Makromol. Chem.*, 1968, **2,** 157.
104. P. T. Callaghan and D. R. Paul, *Macromolecules*, 1993, **26,** 2439.
105. T. P. Russell, *Macromolecules*, 1990, **23,** 890.
106. C. S. Johnson, Jr., *Prog. NMR Spectrosc.*, 1999, **34,** 203.
107. S. W. Provencher and R. H. Vogel, *in*: *Numerical Treatment of Inverse Problems in Differential and Integral Equations*, P. Deuflhard and E. Hairer (eds.), Birkhauser, Boston, MA, 1983, p. 304.
108. G. W. Slater and S. Y. Wu, *Phys. Rev. Lett.*, 1995, **75,** 164.
109. F. Heatley, *in*: *NMR Spectroscopy of Polymers*, (R. N. Ibbett ed.), Blackie Academic & Professional, Glasgow, 1993.
110. K. Matsuzaki, T. Uryu and T. Asakura, *MR Spectroscopy and Stereoregularity of Polymers*. Japan Scientific Societies Press, Tokyo, 1996.
111. C. J. Pouchert and J. Behnke, *The Aldrich Library of 13C and 1H FT NMR Spectra*. Aldrich Chemical Co., Aldrich, 1993.
112. W. W. Y. Lau, C. M. Burns and R. Y. Huang, *J. Appl. Polym. Sci.*, 1984, **29,** 1531.
113. S. Krause, *J. Macromol. Sci. Rev. Macromol. Chem.*, 1972, **C7,** 251.
114. M. Daoud and J. P. Cotton, *J. Phys.*, 1982, **43,** 531.
115. T. P. Lodge and N. A. Rotstein, *J. Non-Cryst. Solids*, 1991, **131,** 671.
116. F. Brochard and P. G. de Gennes, *C. R. Acad. Sci. Paris*, 1996, **323,** 473.
117. K. Kamiguchi, S. Kuroki, M. Satoh and I. Ando. In preparation for publication.
118. J. D. Gunton, M. S. Miguel and P. S. Sahni, *in*: *Phase Transition and Critical Phenomena*, C. Domb and J. L. Lebowitz (eds.), Academic Press, New York, 1983, p. 269.
119. T. Hashimoto, *Phase Transit.*, 1988, **12,** 47.

120. T. Hashimoto, T. Takenaka and H. Jinnai, *J. Appl. Crystallogr.*, 1991, **24,** 457.
121. H. Jinnai, H. Hasegawa, T. Hashimoto and C. C. Han, *J. Chem. Phys.*, 1994, **99,** 8154.
122. H. Jinnai, Y. Nishikawa, T. Koga and T. Hashimoto, *Macromolecules*, 1995, **28,** 4782.
123. H. Jinnai, T. Koga, Y. Nishikawa, T. Hashimoto and S. T. Hyde, *Phys. Rev. Lett.*, 2000, **84,** 518.
124. H. Jinnai, Y. Nishikawa, H. Morimoto, T. Koga and T. Hashimoto, *Langmuir*, 2000, **16,** 4380.
125. K. Yamauchi, K. Takahashi, H. Hasegawa, H. Iatrou, N. Hadjichristidi, T. Kaneko, Y. Nishikawa, H. Jinnai, T. Matsui, H. Nishioka, M. Shimizu and H. Furukawa, *Macromolecules*, 2003, **36,** 6962.
126. H. Jinnai, Y. Nishikawa, T. Ikehara and T. Nishi, *Adv. Polym. Sci.*, 2004, **170,** 115.
127. H. Jinnai, K. Sawa and T. Nishikawa, *Macromolecules*, 2006, **39,** 5815.
128. R. P. Kambour and J. T. Bendler, *Macromolecules*, 1986, **19,** 2679.
129. G. Adam, C. Nolte-Ernsting, A. Prescher, M. Buhne, K. Bruchmuller, W. Kupper and R. W. Gunther, *J. Magn. Reson. Imaging*, 1991, **1,** 665.
130. A. Sasov and D. J. Van Dyck, *J. Microsc.*, 1998, **191,** 151.
131. T. G. Herman, *Image Reconstruction from Projections, the Fundamentals of Computerized Tomography*. Academic Press, San Francisco, 1980.
132. N. Wayne, *An Introduction to Digital Image Processing*. Prentice-Hall International, London, 1986.
133. C. L. Morgan, *In Basic Principles of Computer Tomography*. University Park Press, Baltimore, 1983 (Chapter 5).

CHAPTER 5

Practical NMR Analysis of Morphology and Structure of Polymers

Takeshi Yamanobe,* **Hiroki Uehara,*** and **Masaki Kakiage†**

Contents

Abstract

Practical analytical methods to investigate the relationship between polymer morphology and properties by a combination of ^{1}H pulse NMR and/or high-resolution NMR in the solid state with other techniques, such as electron microscopy, X-ray diffraction and so on, are reviewed. The complete free induction decay (FID) fitting method by exponential, Weibullian and

* Department of Chemistry and Chemical Biology, Gunma University, Tenjin-cho, Kiryu, Gunma, Japan
† Department of Applied Chemistry, Graduate School of Science and Engineering, Saitama University, Shimo-Ookubo, Sakura-ku, Saitama, Japan

Annual Reports on NMR Spectroscopy, Volume 70
ISSN 0066-4103, DOI: 10.1016/S0066-4103(10)70003-X

Weibullian/sine function is introduced. Applications of this method to polyethylenes prepared by various conditions successfully explain the morphology and physical properties. Crystallisation mechanism of nylon 46 by high-resolution NMR in the solid state is also introduced.

Key Words: Polymer, Polyethylene, Nascent power, Nylon 46, Morphology, ^{1}H pulse NMR, *In situ* measurement, Cross-polarisation magic angle spinning.

1. INTRODUCTION

Investigation of the relationship between the structure and physical properties of polymers is one of the most important themes for polymer chemists and engineers. Polymer structures have been determined through many types of spectroscopy. NMR is now an indispensable tool for analysing polymer structures.[1] Polymer structures are divided into primary, secondary and higher order structures. For the primary structure determination, solution NMR is now the standard method and used widely for analysing the fine structure. The degree of tacticity, branching, regioregurality, sequence distribution, terminal group etc. can be estimated by solution NMR as routine work.

The secondary structure, such as a conformation, is studied mainly by solid-state NMR.[2] In the solid state, NMR chemical shift is characteristic of specific conformations because the internal rotation around the chemical bonds is restricted. This shows that the NMR chemical shift can be used for elucidating the conformation of polymers in the solid state. In the amorphous phase, the conformation of the polymer chain is not fixed above T_g. Even in such a case, NMR chemical shift and the relaxation parameters can give us useful information such as the averaged conformation or the dynamics of the exchange. Solid-state NMR can also provide information about the crystalline structures, which are classified under the higher order structures through NMR chemical shift, since for most polymers, different crystalline structures accompany conformational changes which affect their NMR chemical shift.

Although the above-mentioned polymer structures are important for designing a polymer chain, they are related to local structure, which contains only a few polymer chains. When polymers are designed as materials, polymer morphology, which can be defined as the structure and the phase separation of polymer chains on a large scale, also plays an important role in the properties of polymer in addition to the primary and secondary structures. The polymer morphology involves the crystallinity, crystallite, polymer macro-conformation such as fringed micelle and their formation kinetics, etc. The morphology–property relationship of polymers has been discussed for decades, but not fully interpreted. Problems lie in the analytical difficulty caused by the complicated combination of crystalline and amorphous phases, including their contents, arrangements, difference in physical properties (electron density, mechanical and thermal properties, and so on) and the usual existence of an interface region between them. For example,

each method for the determination of crystallinity, such as thermal analysis, density and X-ray measurements, focuses on its own view scale, namely, ''where is the borderline between crystalline and amorphous'' in terms of physical properties. This is one of the reasons why the crystallinity evaluations by different methods often disagree with each other. Further, mechanical or viscoelastic measurements also suffer difficulty in the resolution of each contribution among these combined phases, which always requires several assumptions: ''how much depends on each phase''. The advantage of NMR measurements is attributed to the ability of NMR for simultaneous estimation of both phase contents and properties (relaxation times) on the same scale, which is quite different from the usual combination of results obtained by a few analytical methods. Special measurements and detailed analysis of the obtained NMR parameters, including NMR chemical shift, relaxation times, spin diffusion and so on, allow us to evaluate the true crystallinity. A number of studies have been reported on the structure of polymers by solid-state NMR.[2] Especially, high-resolution methods have been applied to the investigations of conformation, crystalline structure, phase separation and dynamics of various polymers. For example, crystalline and amorphous phases are independently detectable as separated peaks by ^{13}C NMR spectra. Recent development of multi-dimensional techniques allows different spin states or interactions to be correlated.[3] However, the relative ^{13}C peak intensities of these phases significantly depend on experimental conditions such as recycling time, contact time and so on. Further, high-resolution or multi-dimensional NMR measurements are time consuming because of their low sensitivities.

Recently, NMR imaging has been developed and widely used for obtaining information on the spatial distribution of the spin density, the relaxation times and the diffusion coefficient for soft materials such as gels or liquid crystals.[1] However, the spatial resolution is the order of micrometres and insufficient for the analysis of macro-conformation of polymers. As mentioned above, NMR chemical shift and the relaxation times reflect the averaged chemical environments at atomic or nanometre levels. Although, by using spin diffusion, the phase size and structure can be discussed on a larger scale, the obtained data is still averaged about bulk polymer. Thus, the disadvantage of NMR technique exists in the difficulty of obtaining spatial information of the order between the nano- and micrometre.

The above disadvantage of the lack of spatial information can be overcome by a combination of NMR data and other techniques. From the ^{1}H pulse NMR, the fraction and the molecular mobility of different molecular environment can be obtained as free induction decays (FIDs) within a short time, which is suitable for a practical, better understanding of the morphology–property relationship. Wide angle X-ray diffraction (WAXD) and small angle X-ray diffraction (SAXD) as well as electron microscopy provide direct information between the nano- and micrometre scale. A combination of NMR data with those from X-ray diffraction and electron microscopy should be able to analyse the structure from the atomic level to the macro scale. In this review, the morphology–property relationship, the dynamics of morphological transition, the kinetics of crystallisation, etc. analysed by a combination of NMR and other tools are introduced.

2. ANALYSIS METHOD OF FREE INDUCTION DECAY OF ^{1}H PULSE NMR FOR POLYMERS

FID contains information about the chemical environment of each nucleus. The curve-fitting for the observed FIDs gives the individual spin–spin relaxation characteristics in different phases: crystalline, amorphous and interfacial.[4–9] Such a resolution into several components has been long attempted on a broad-line spectrum of solid PE.[10–13] These results will reflect the sample morphologies.

Generally, to fit the observed FID, a series of exponential functions (Equation (1)) are used because the distribution of dipole interaction is expressed by Lorentzian function. This is true for the solution, melt and amorphous phases of the polymers. Actually, a PE melt with low MW exhibits a single exponential curve.[14–17] The shape of the relaxation curve of amorphous molecular motion still retains the combined exponential types on cooling. On the other hand, Weibullian functions (Equation (2))[6,18] are also applicable for the phase with partially restricted motion such as the interfacial phase.[19] Therefore, it is reasonable to introduce the exponential and Weibullian functions as the amorphous relaxation:

$$I_1(t) = A_1 \exp\left\{-\frac{k_1 t}{2}\right\} \tag{1}$$

$$I_2(t) = A_2 \exp\left\{-\frac{(k_2 t)^{d_2}}{2}\right\} \tag{2}$$

where t is the decay time and A the fraction of the component.

As crystallinity increases, the curve contains a beat on the FID.[4–9,20,21] Figure 1 shows typical ^{1}H NMR FIDs for UHMW-PE samples. Each FID has a beat (a drop and subsequent recovery) at about 20–30 μs. The beat arises from the distribution of dipole interaction with the shape of a bell or a trapezoid, which deviates from Lorentzian function when the molecular motion is extremely restricted. This is well known for inorganic molecules. When the proton pair is isolated from each other in a powdered sample, a Pake doublet is observed as a result of dipole interaction. The increase in the number of interacting proton pairs gives rise to the distribution of dipole interaction with the shape of bell or trapezoid as a superposition of Pake doublets. Kristiansen et al. applied a theoretical Fourier transformation of this doublet function to the phase analysis of PE and polypropylele (PP).[8,9] However, the analytical Fourier transformation of a Pake doublet produces an extremely complicated FID function. It has already been recognised that this kind of FID can be characterised by multiplication of Gaussian and sine functions expressed as follows[22]:

$$I_3(t) = A_3 \exp\left\{-\frac{(k_3 t)^2}{2}\right\} \frac{\sin b_3 t}{b_3 t} \tag{3}$$

In this function, there are only three parameters to be fitted. In discussing the morphology–property relationship, this function is suitable practically.

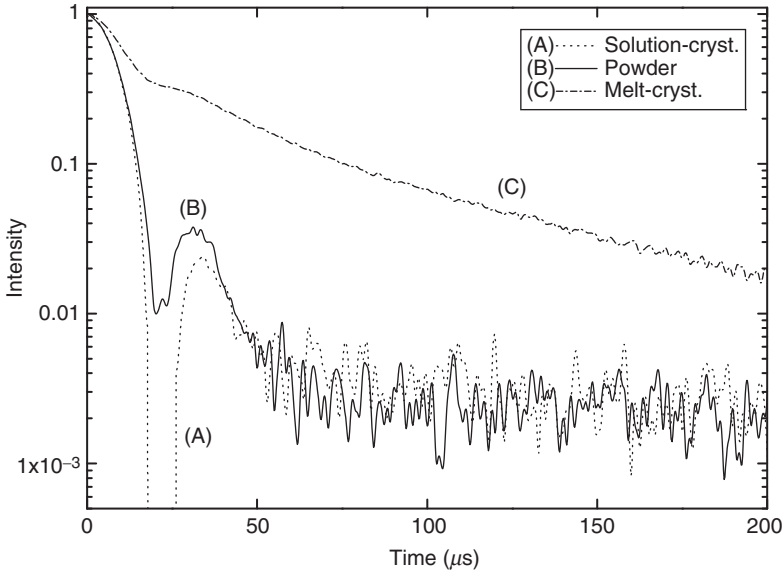

Figure 1 ^{1}H FIDs observed at room temperature for solution-crystallized (A), melt-crystallized (B) and nascent powder (C) samples.

The introduction of Gaussian function in Equation (3) is based on the prediction by Pake[23] for crystals of small molecules, such as 1,2-dichloroethane, where the dipole pairs are isolated from each other. However, in the polymeric materials, not only the dipole interactions between the nearest neighbours but also those between the proton pairs at a longer distance contribute to the FID profile shape. Therefore, the distribution of the dipole interaction may be distorted. This is expressed by the introduction of Weibullian form,[24] as follows:

$$I_4(t) = A_4 \exp\left\{-\frac{(k_4 t)^{d_4}}{2}\right\} \frac{\sin b_4 t}{b_4 t} \tag{4}$$

where d_4 is the power coefficient introduced for the Weibullian part. Here, d_4 of 2 can give the conventional Gaussian/sine function. The actual FID is represented by the sum of these functions ascribed to different relaxation systems.

Figure 2 illustrates the step-by-step FID resolution procedures into two amorphous and one crystalline relaxation curves for a melt-crystallised sample. First, the longest relaxation was fitted in the time region of 200–400 μs (Figure 2A). After subtraction of the first component from the FID, the residual plots were further fitted by another amorphous component (Figure 2B). The resultant crystalline relaxation is well represented by Equation (3) (Figure 2C). Because of a negative drop corresponding to this function, the plots in the beat region sometimes did not appear in the log scale in Figure 1A (see the profile of the solution-crystallised sample). The sum of these curves is in perfect agreement with the observed FID, as shown in Figure 2D.

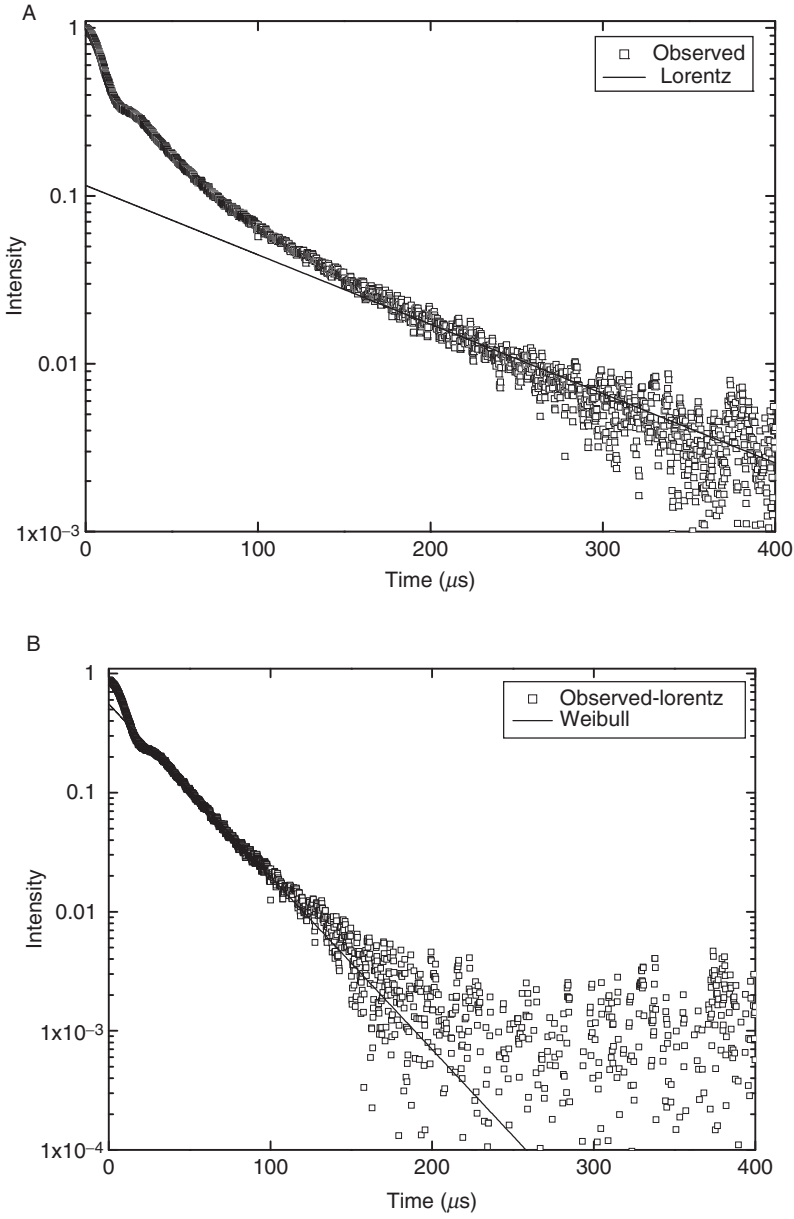

Figure 2 A series of FID resolution procedures into several component decays. The longest relaxation decay, showing a simple exponential function at the longer timescale, was subtracted from the observed FID (A). The other exponential component at the middle timescale was also fitted as amorphous relaxation (B).

continued

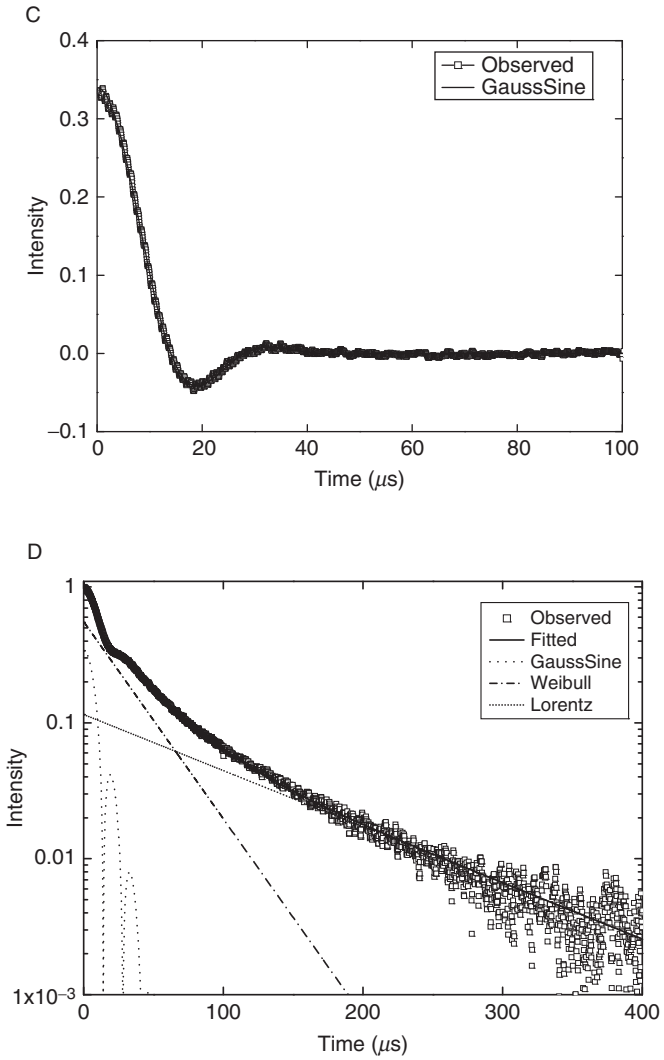

Figure 2—cont'd The final residual curve coincided well with the crystalline Gaussian/sine function (C). The sum of these resolved profiles was compared with observed plots (D).

The molecular mobility is usually discussed by T_2 on the basis of BPP theory.[25] However, parameters k_1–k_4 cannot be directly compared any longer. The mobility should be discussed by using the width of the broad-line spectrum. The obtained crystalline components are Fourier-transformed into broad-line spectra for simultaneous evaluation of changes in the component ratio and molecular motion. The integral peak width on a frequency scale was calculated from these broad-line spectra. Each component ratio of crystalline (Weibull/sine), intermediate

(Weibullian) and relaxed (Lorentzian) amorphous regions can be also evaluated as their integral intensities.

By using these functions and the procedure, the FID can be perfectly fitted without ambiguity. The obtained fraction and integral width or T_2 can be used to discuss the morphology–property relationship directly.

3. MORPHOLOGY AND RELAXATION BEHAVIOUR

3.1. Morphology and molecular mobility of polyethylene

It is well known that the solid morphologies of semi-crystalline polymers are composed of several structural levels of typical modifications: a parallel arrangement of folded molecular chains leading to lamellar crystals and the actual sample filled with a sandwiched structure of amorphous layers and such lamellae. Melt-crystallisation produces a spherulite structure having a distortion of these combined crystalline/amorphous phases, but precipitation of the separated lamellae is obtained for solution-crystallisation. Figure 3 shows the sets of TEM images for solution-crystallised, melt-crystallised and nascent powder samples. For solution-crystallised samples (see Figure 3A), the regular stacking of lamellar crystals of $\sim$10 nm thickness is clearly observed. These crystalline lamellae are located between dark layers indicating the amorphous region and lie laterally within several micrometres length. For the melt-crystallised sample (see Figure 3B), the random arrangement of curved lamellae consists of a spherulite structure. The lamellar thickness of 30 nm for the melt-crystallised sample is much larger than that for the solution-crystallised samples.

The nascent powder sample has quite a different morphology compared to the solution-crystallised or melt-crystallised samples. The nascent powder morphology mainly consists of particles connected by fibrils, which is called the ''cobweb'' structure.[26,27] The nascent powder does not have any typical lamellar morphology but has a domain structure where crystalline domains distribute within the whole powder globule (Figure 3C). The domain size has a wide range of several tens of nanometres radius.

These sample structures cause the corresponding characteristics in the relaxation behaviour. FID profiles of these samples at ambient temperature are shown in

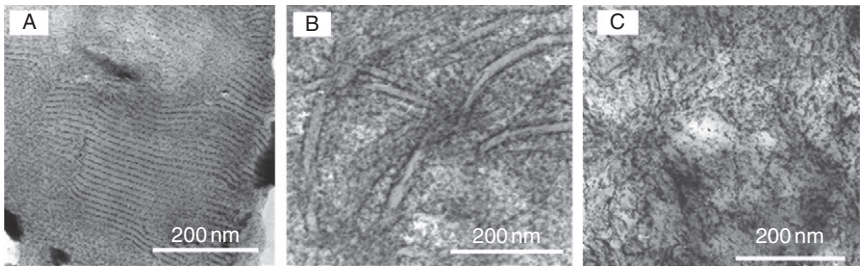

Figure 3 Electron microscopic images of UHMW-PE samples prepared under different conditions; solution-crystallized (A), melt-crystallized (B) and nascent powder (C) samples.

TABLE 1 Spin–spin relaxation characteristics of components resolved from FID observed at room temperature for UHMW-PE samples[a]

Morphologies	Crystalline integral width	Amorphous integral width
Solution-crystallised	66.2 kHz (91%)	41.2 kHz (9%)
Melt-crystallised	70.4 kHz (61%)	17.4 kHz (28%) + 5.8 kHz (11%)
Nascent powder	65.8 kHz (85%)	38.3 kHz (15%)

[a]Value in parentheses represents component ratio for corresponding relaxation.

Figure 1.[28] The beats, showing a combination of intensity drop and subsequent recovery, are clearly observed in the 20–30 μs region on these FIDs for the higher crystalline solution-crystallised materials and the nascent powder. These two samples undergo a rapid decay, indicating that the solution-crystallised and nascent powder samples are more rigid than the melt-crystallised ones.

The relaxation characteristics are summarised in Table 1.[28] For highly crystalline samples of solution-crystallised materials and the nascent powder, two components exist and the melt-crystallised sample requires three components. The crystalline component ratio was the highest for the solution-crystallised sample. The melt-crystallised sample has the lowest value of $\sim$50%. The crystalline integral width for the melt-crystallised sample was the largest of these samples, suggesting constrained crystalline chain motions for the melt-crystallised sample, which may be caused by the thick lamellar size. Concerning amorphous relaxation, larger integral widths were obtained for highly crystalline samples, compared to the usual value of 5–10 kHz, which is common for the PE amorphous phase. This means that the amorphous chains in solution-crystallised and nascent powder samples were restricted. Such a poor molecular mobility of the amorphous phases for the nascent powder sample has also been observed by ^{13}C NMR measurement.[29] For the amorphous phase of the melt-crystallised sample, the usual relaxation of $\sim$6 kHz and hindered motion similar to that of the other highly crystalline samples exist. The latter amorphous relaxation could be ascribed to the interfacial molecular motion.

3.2. Lamellae thickening mechanism of polyethylene with various morphologies

Morphological differences affect the temperature dependence of FID. Figure 4 shows the temperature dependence of the FIDs for the solution-crystallised sample.[28] The sample heating gradually suppresses the crystalline beat on the FIDs, and it almost disappears around 110 °C. The decay in the longer time region also becomes gentler with increasing temperature, which indicates the acceleration of molecular motion in the amorphous phase during heating.

The integral width except for the longest component of the melt-crystallised sample is plotted in Figure 5 for the solution-crystallised, melt-crystallised and

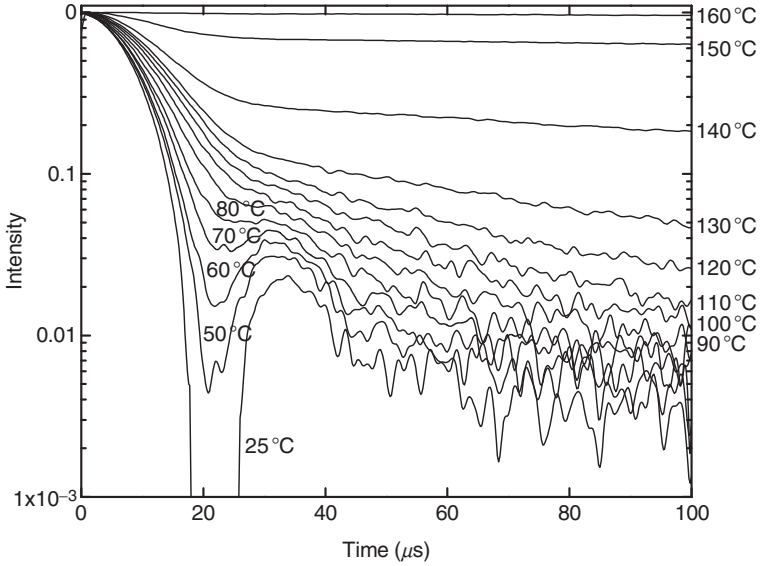

Figure 4 Changes in the FIDs during heating for solution-crystallized UHMW-PE sample.

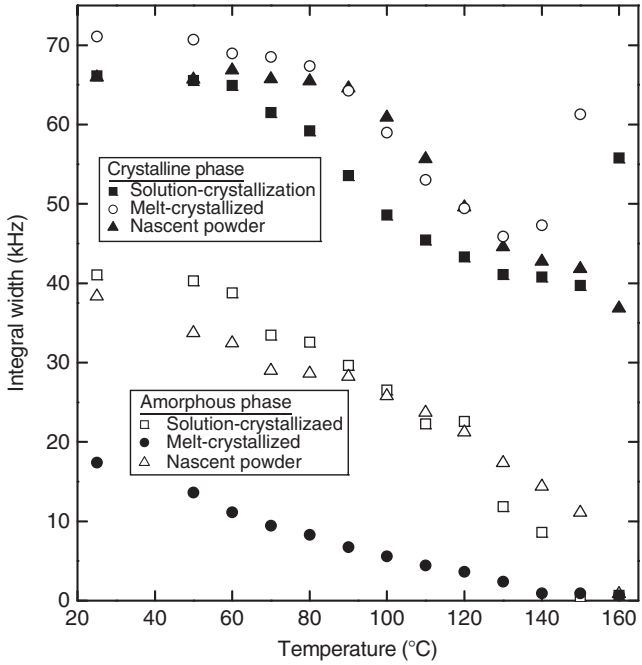

Figure 5 Temperature dependencies of integral widths during heating for solution-crystallized, melt-crystallized and nascent powder samples of UHMW-PE. Changes in both values for crystalline and amorphous relaxations were plotted for each sample.

nascent powder samples.[28] In Figure 5, the larger integral width corresponds to the slower chain motion. For the solution-crystallised sample, the crystalline integral width is held at the same level below 60 °C, followed by a gradual decrease with increasing temperature. This shows that crystalline chain motion starts at a low temperature, reflecting its less entangled lamellar morphology. In contrast, the crystalline chain mobility is accelerated above a higher temperature of 90 °C for the nascent powder sample, due to a sudden release of chain motion restricted below this critical temperature. This higher releasing temperature may be related to the crystalline domain network structure in its nascent morphology. For poorly crystalline melt-crystallised sample, relatively larger integral widths are obtained below 90 °C, compared to the other morphologies.

Concerning the amorphous relaxation, all samples exhibited a successive reduction of integral width and amorphous molecular motion was gradually accelerated during heating irrespective of the sample morphology. The amorphous integral width of highly crystalline, solution-crystallised and nascent powder samples are twice as large as that of the melt-crystallised one.

The component ratios of both crystalline and amorphous phases are plotted in Figure 6.[28] For the melt-crystallised sample, the crystallinity gradually decreases and abruptly drops around 120 °C, before reaching around 0% crystallinity at

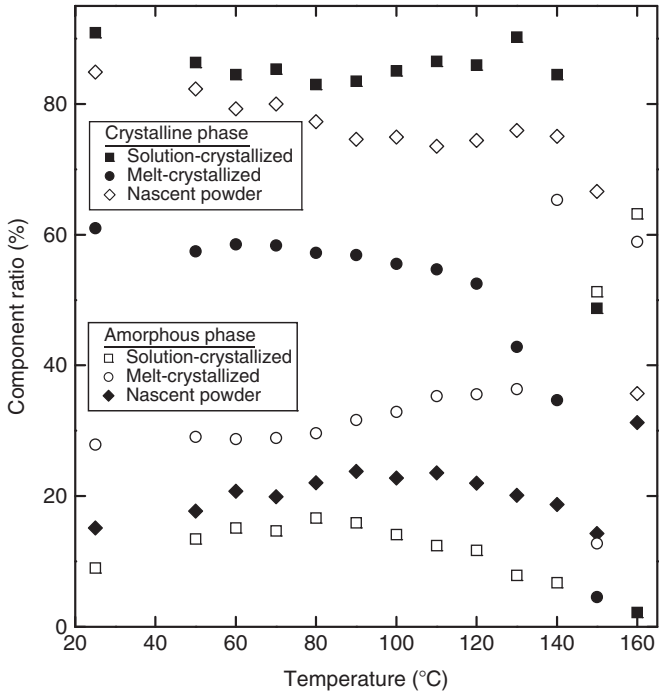

Figure 6 Temperature dependencies of component ratios during heating for solution-, melt-crystallized and nascent powder samples for UHMW-PE.

150 °C because of complete sample melting. This simple crystallinity decrease of melt-crystallised PE has been detected by Kristiansen et al.,[9] based on their theoretical ^{1}H NMR profile analysis. A similar gradual crystallinity decrease at the early stage of heating was also detected for solution-crystallised and nascent powder samples. However, the crystallinity increases between 90 and 130 °C for the solution-crystallised sample. The recovery of crystallinity for the solution-crystallised sample can be attributed to the lamellar rearrangement during the heating process. During this rearrangement, the thickness of lamellae increases. In differential scanning calorimetry (DSC) measurements, any exotherm caused by lamellar rearrangement has never been observed, a long-standing question on the interpretation of the annealing process for semi-crystalline polymers. Combination of synchronised evaluations of both chain mobility and component ratio on the same molecular scale, characterised by ^{1}H NMR relaxation, shows the first and clear evidence of lamellar rearrangement.

Changes in the amorphous relaxation behaviour with rising temperature exhibited a monotonous reduction of the integral width, independent of sample morphology, while a crystalline relaxation change is unique for each sample. Thus, the complete analysis of ^{1}H FID allows us to discuss chain mobility of amorphous and crystalline phase independently.

Which factor dominates the crystalline relaxation? The crystalline decay function composed of the Gaussian/sine function has two individual coefficients, k_1 and b. The k_1 coefficient gradually increases with temperature, independent of sample morphology. The trend of the b factor is quite similar to that of the crystalline integral width in Figure 5. Namely, the complicated behaviour in crystalline relaxation is predominantly defined by the b factor. The decrease in the b coefficient leads to a parallel reduction of the integral width. At elevated temperatures, the b coefficient asymptotically approaches 0, which leads to the term $\sin bt/bt$ equalling 1. Therefore, introduction of the Gaussian/sine function was effective in the evaluation of crystalline relaxation characteristics, such as the existence of a beat and its gradual disappearance with increasing temperature.

The relaxation process of the solution-crystallised sample can be divided into three regimes in terms of the effect of temperature on crystalline relaxation. Figure 7 shows the broad-line spectra converted from the crystalline decays of solution-crystallised UHMW-PE, which exhibits the most typical characteristics of the annealing process.[28] The change in the crystalline spectrum during heating for this sample corresponds well with that of the b coefficient. At the early stage of heating below 60 °C (Process 1), the spectrum integral intensity decreases, but the width and the factor b exhibit no change. From 60 to 130 °C, the spectrum is pushed up as its width and the factor b decrease (Process 2). The final step is that the integral intensity dramatically decreases with almost constant width and the factor b up to complete sample melting (Process 3). These broad-line spectral changes during heating are schematically shown in Figure 7.

Here, the origins of these relaxation processes can be predicted based on a comparison of the spectrum and sample morphology. The regular stacking of

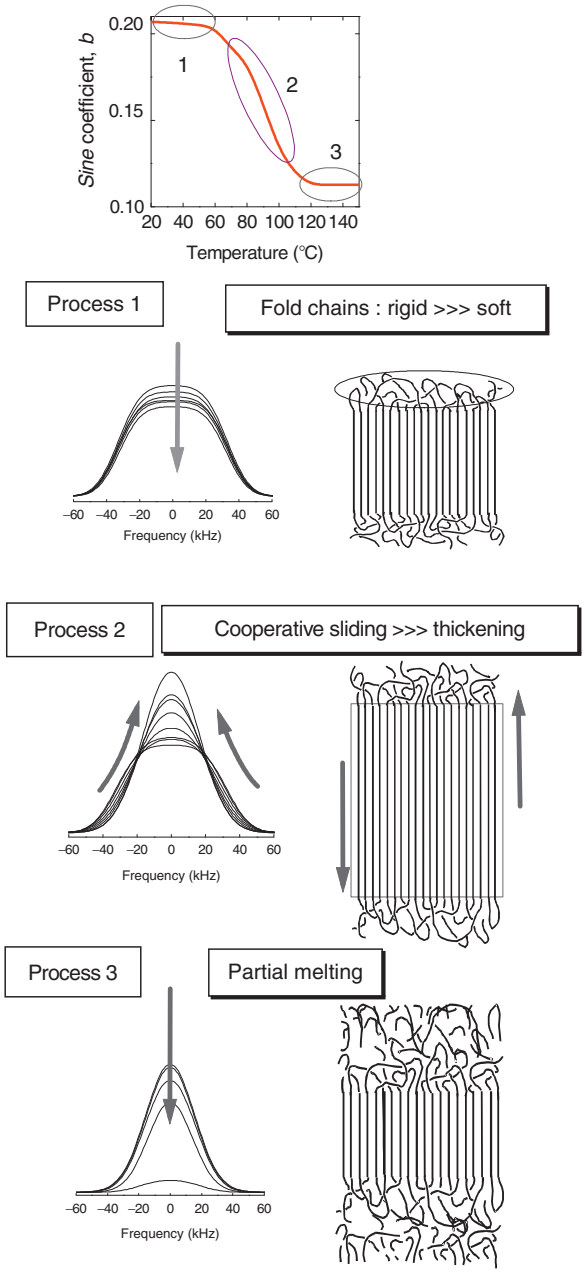

Figure 7 Schematic broad-line spectrum changes through three relaxation processes, divided into different temperature regions.

lamellae for the solution-crystallised samples likely accompanies folding chains on the lamellar surfaces. These chains are trapped by solid crystals. These chains on crystal/amorphous boundaries are considered to be those of the rigid component. The origin of the lower integral width values for highly crystalline samples is attributed to this participation of trapped surface amorphous chains in the crystalline relaxation for these samples. The characteristics of spectral changes during heating could be interpreted for solution-crystallised sample as follows.

Process 1: The early stage of heating causes the relaxation shift of the interfacial chains into amorphous, which leads to the decrease in integral intensity (crystallinity). However, the residual crystalline molecules inside the lamellae still maintain their hindered molecular motion; thus, the integral width of the spectrum exhibits a constant level.

Process 2: Beyond a critical temperature of around 60 °C, a remarkable crystallinity development occurs, which has not been detected by any other crystallinity determination methods. Lamellar growth, causing taking-in of the surrounding amorphous chains, is required for the crystallinity increase. Considering the regular stacking of single lamella of several micrometres wide, this erosion into sandwiched amorphous layer chains progresses parallel to the lamellar normal. Therefore, cooperative molecular motion within the entire crystalline lamella from the surface to the interior takes place and leads to remarkable lamellar thickening.

Process 3: Above 130 °C, rapid progress of partial melting causes a decrease in the crystalline component. The residual crystalline region still retains its saturated molecular motion until the complete melting.

The melt-crystallised sample skipped Process 1 due to the limited relaxation of its entangled molecules on the lamellar surfaces, rather than the adjacent re-entry folding for the solution-crystallised sample.

Annealing of the nascent powder sample passed through Process 1, and above 90 °C, dynamic molecular motion started, as defined by Process 2. This critical temperature is slightly higher than that of the solution-crystallised sample. This difference indicates the restricted crystalline chain motion for the domain network structure crystallised during polymerisation. In Process 2, the crystallinity remained at a constant level for the nascent powder sample. This shows that the lamellar thickening is limited for the nascent powder morphology.

3.3. Chain mobility and entanglement in the amorphous phase

Polymer entanglement has been an important concept governing the physical properties of polymers. For example, UHMW-PE single-crystalline materials can be super-drawn up to a draw ratio of 300.[30] This high drawability is assumed to be due to the existence of entanglement.[31] The first evaluation of entanglement was offered by Porter and Johnson for the MW dependence of melt viscosity and the polymer concentration dependence for the solution viscosity.[32,33]

For amorphous polymers, neutron scattering measurements have been applied to evaluate entanglements.[34,35] These measurements indicate that the molecular weight between entanglements in the amorphous region is identical

to that in the solid and theta states and the molecular draw ratio coincides with the macroscopic draw ratio. For semi-crystalline polymers, entanglements are segregated into the amorphous region during crystallisation. The entanglement characteristics are expected to depend on the prior concentration of polymers. However, a systematic study of entanglement formation has not been reported except drawability.

Many ^{1}H NMR analyses have been carried out for molten- or solution-state of polyethylene to characterise the random-coil molecular chain.[14,17,21,36–39] The relaxation evaluation for solid-state, amorphous polyethylene chains remain ambiguous because of the strong crystalline component that obscures the entanglement component in the amorphous phase. Perfect FID fitting in combination with TEM and SAXS was applied to evaluate the effects of prior concentration on amorphous chain characteristics.

The solution-grown crystal (SGC) from dilute solution forms diamond-like crystals of lateral dimension up to several micrometres, but their thickness is about 10 nm in which polymer chains are folded. The chain axes are parallel to the thickness direction of these lamellar crystals. In SGC materials precipitated from dilute solutions (Figure 3A), the lamellae are stacked and oriented parallel to the material surface.

One of the benefits of direct TEM observation is its possible accounting of the thickness of the crystalline and amorphous layers separately. The distributions of thickness for amorphous and crystalline layers are plotted in Figure 8.[40] Both crystalline and amorphous thickness distribution curves have their individual maxima, whose positions are independent of prior polymer concentration. The peak top is always located at 9 nm for crystalline layer and 1.5 nm for the amorphous one. Their SAXS profiles are compared in Figure 9.[40] The long periods lie in the constant position at around 0.75°, which corresponds to 11.5 nm thickness, independent of prior polymer concentration. As the lamellar thickness obtained by SAXS is the sum of thicknesses of the crystalline and amorphous phases, the average thickness of lamellae measured by TEM coincides with that by SAXS. Therefore, the morphologies seem to be independent of polymer concentration.

However, the scattering peak intensity gradually grows sharper with increasing prior polymer concentration. Recent SAXS analysis[41] shows that sample crystallinity or the difference between the electron densities in the crystalline/amorphous phases significantly affect the obtained scattering. As the crystallinity is independent of the prior polymer concentration and the ratio of crystalline layer thickness to the total long period estimated by TEM layer thickness distribution measurements, the origin of the intensity differences among SAXS profiles could be ascribed to the differences in electron density between the crystalline and amorphous phases. As the electron density of crystalline phase should be unchanged, the reason for the trend of SAXS profile intensity is an increase of electron density in the amorphous layers with decreasing prior polymer concentration.

Such a difference of the amorphous characteristic was accountable by NMR relaxation analysis. Figure 10 compares the FIDs for a series of solution-crystallised materials prepared from different prior polymer concentrations.[40]

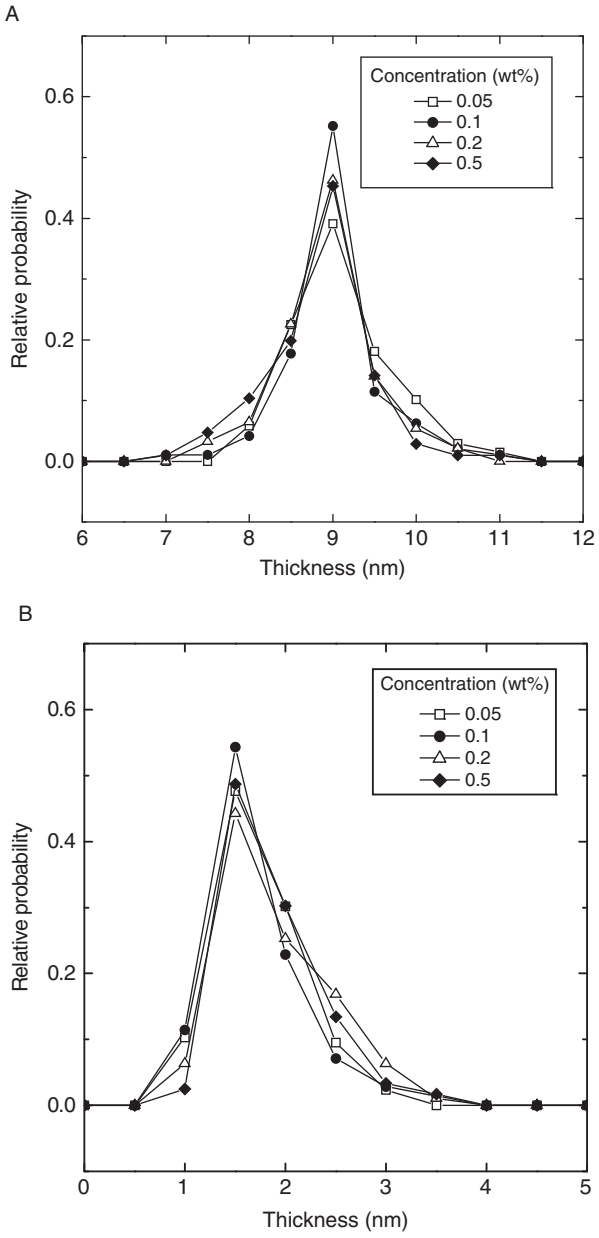

Figure 8 Distribution of thickness for crystalline (A) and amorphous layers (B), estimated from TEM images.

The negative beating drop observed was folded back to the positive side at around 21 μs between two troughs. The back-folding gradually drops downwards with increasing prior polymer concentration. Also, the position of one of the troughs at around 25 μs shifts to the longer time side with increasing prior polymer

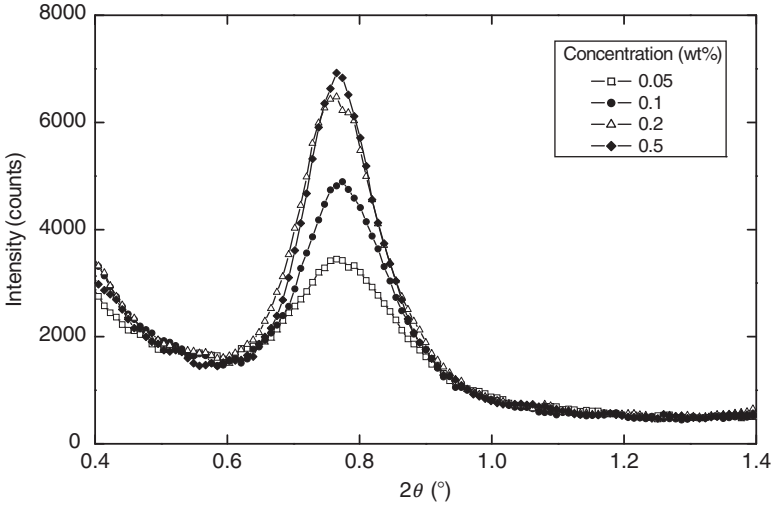

Figure 9 SAXS intensity profile for the series of samples solution-crystallized from 0.05 to 0.5 wt % tetralin solution. The background was subtracted from original data plots.

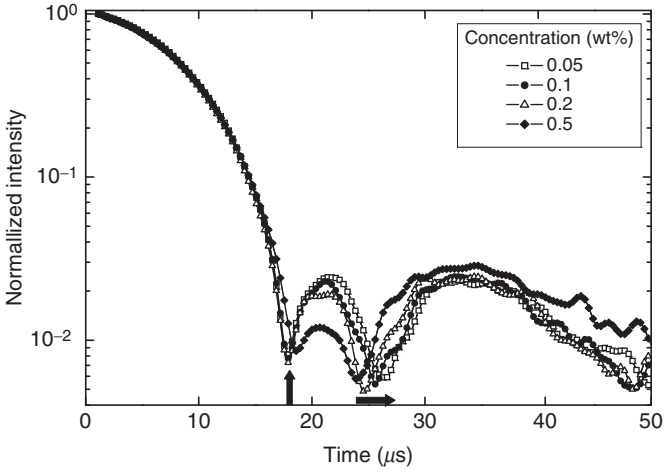

Figure 10 A comparison of ^{1}H NMR FID profiles between different prior polymer concentrations.

concentration. In contrast, the position of another trough at around 19 μs is located always at the same point.

From decomposition of these FID profiles into crystalline and amorphous phases, the integral width and component ratios for relaxation in crystalline and amorphous phases were plotted, as shown in Figure 11.[40] The crystallinity lies around 86%, independent of prior polymer concentration, which agrees well with

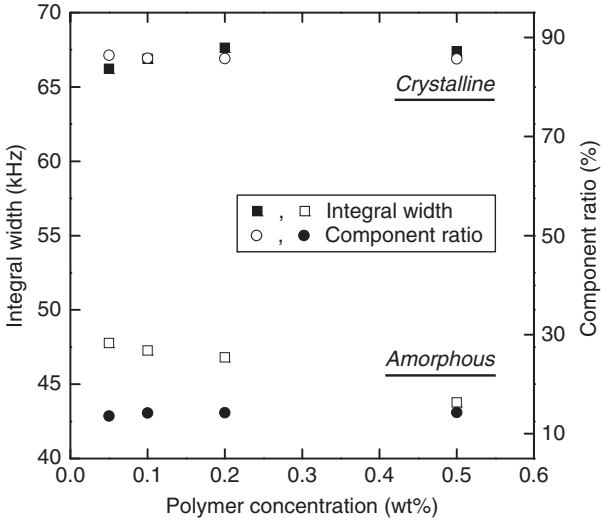

Figure 11 Separated ^{1}H NMR characteristics for crystalline and amorphous relaxations as a function of prior polymer concentration.

the WAXD result. As for the integral width, the crystalline component has a constant value of around 67 kHz; in contrast, the amorphous one exhibits a gradual decrease with increasing prior polymer concentration. This trend of amorphous relaxation exhibits the restricted molecular motion in amorphous phase for a lower prior polymer concentration system.

The positions of the trough are a good measure for the state of the crystalline and amorphous phases. The unchanged position of the first trough at around 19 μs in Figure 10, which is independent of prior polymer concentration, means the constant level of crystalline relaxation. The position of the second trough near 25 μs is significantly influenced by slope of amorphous relaxation decay. A shorter relaxation time in the amorphous phase brings rapidly decreasing FID, which rather emphasises crystalline beating at the lower prior polymer concentration. The trend of FID indicates that the series of the samples has the same level of crystalline relaxation time and crystallinity, and therefore the lower integral width of amorphous region gives deeper drop near beat, leading to the shift of the reversing point at the second trough to the longer time side.

A combination of TEM, X-ray and ^{1}H NMR clarifies that the amorphous molecular characteristics are quite different among the samples prepared from a variety of prior polymer concentrations. The less entangled state is kept for the sample that was solution-crystallised from prior lower polymer concentration, which induces the restricted molecular motion in the amorphous phase, due to the formation of tie chains connecting crystalline layers through the amorphous ones. A prior higher entangled state gives relaxed amorphous chains, compared to that of the former. Such difference of amorphous state could be attributed to an origin of difference in SAXS long period intensity among these samples.

3.4. The morphology and molecular mobility of polyethylene nascent powder

The nascent powder sample has quite a different morphology from the solution-crystallised or melt-crystallised samples. For the nascent powder morphology, the major structure consists of particles having a radius of $\sim 3\ \mu$m, and several fibrils between these particles. The origin of these ''cobweb'' structures, composed of particles and fibrils, is ascribed to the internal expansion stress during polymerisation.[26,27] Much of the polymer product synthesised inside the earlier powder globule causes extensive force, which stretches the outer polymer membrane in the polymerisation process.[42] Fuming nitric acid etching of the nascent powder can eliminate the various structures that exist.

Usually, fuming nitric acid etching does not destroy the crystalline region. In such a case, etching at elevated temperatures is preferred for the rapid etching progress. The molecular weight drops to the crystalline stem length within a shorter treatment time.[43,44] In contrast, the gradual elimination of the amorphous chains is able to classify the multiple amorphous phases with respect to their individual acid resistance. This is achieved by a lower temperature treatment at room temperature. Room temperature etching requires a longer time to get a fully etched state,[45] and NMR analysis of a series of the etched samples can reveal the various states of the amorphous phases.

The values of M_w, M_n and molecular weight distribution (M_w/M_n) calculated from GPC profiles are summarised in Table 2.[24] The initial M_w of 2.6×10^6 and M_n of 5.6×10^5 gradually decrease with increasing etching period, reaching 1.0×10^4 and 2.4×10^4 for a powder etched for 18 months. Crystalline stem length of ~ 30 nm for the nascent powder, which is evaluated from TEM observation, corresponds to a molecular weight $\sim 3 \times 10^3$. Full removal of the amorphous phase should give this minimum molecular weight after etching. Namely, even for the nascent powder etched for 18 month, certain amorphous components still survived under the mild treatment examined.

Nascent powder morphologies of both the nascent and etched samples observed by SEM are shown in Figure 12 for the nascent and 4- and 12-month-etched UHMW-PE powders.[24] Unique ''cobweb'' structures, composed of globules and fibrils, are often observed on the surfaces of nascent PE powders.[2,26,27,43,44] In Figure 12A, very few fibrils are observed for the nascent powder. The paste-like morphologies cover the surface of this nascent powder. The major powder structure

TABLE 2 Molecular weight characteristics of the series of nascent and etched UHMW-PE reactor powders

Sample	$10^{-4}M_n$	$10^{-4}M_w$	M_w/M_n
Initial	56	260	4.7
1-Month-etched	13	38	3.0
4-Month-etched	2.8	16	5.5
7-Month-etched	3.1	6.4	2.1
18-Month-etched	1.0	2.4	2.5

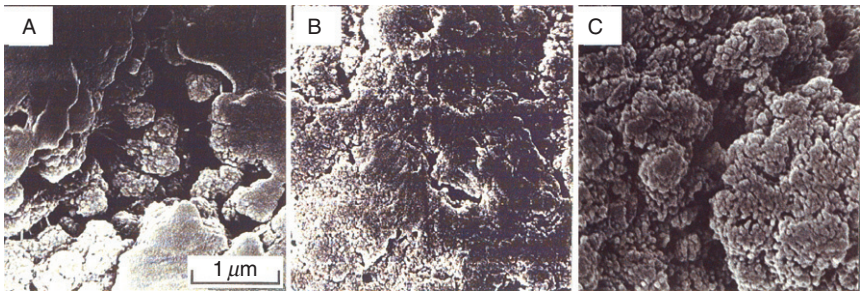

Figure 12 Scanning electron microscopic images of a series of UHMW-PE samples: nascent powder (A), powder treated for 4 months (B) and powder treated for 12 months (C).

consists of globules with radii of a few micrometres, independent of the etching time. After etching for more than 4 months, the paste-like structure on the powder surface almost disappeared (Figure 12B), and the grain structures are slightly recognisable within each globule. Further treatment for 12 months enables clear separation of such grains with radii of ~30 nm, as shown in Figure 12C. This means that the regions located between these grains were gradually sculpted with increasing etching time. From the TEM image of the nascent powder, the crystalline components exhibit distributed domain morphologies, rather than the usual lamellar structure observed for the solution- or melt-crystallised PE.[28,40] These crystalline domains have a size of ~30 nm, which corresponds well with the radii of grains recognised in the SEM images of the 12-month-etched powder (Figure 12C).

Figure 13 shows the ^{1}H NMR FIDs for the series of nascent and etched UHMW-PE powders.[24] The beat profile becomes more prominent with increasing

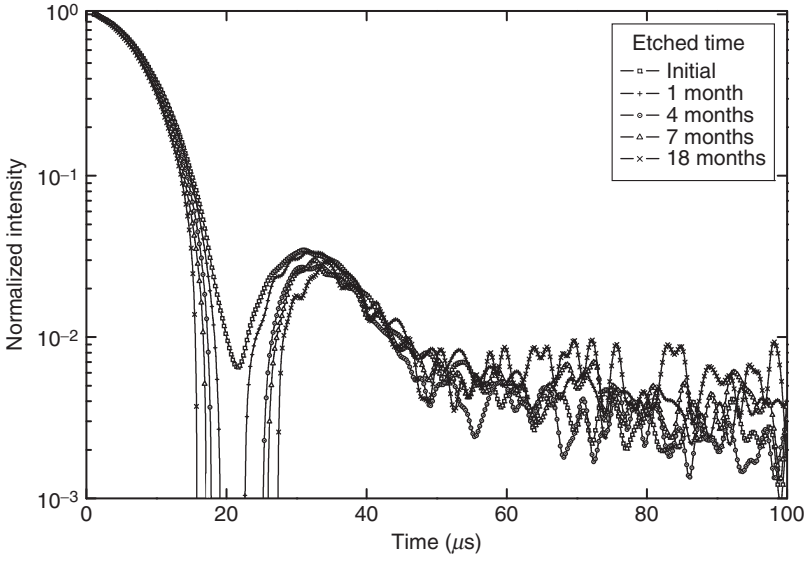

Figure 13 Comparison of FIDs observed at room temperature for nascent UHMW-PE powder and series of samples etched for various periods of time from 1 to 18 months.

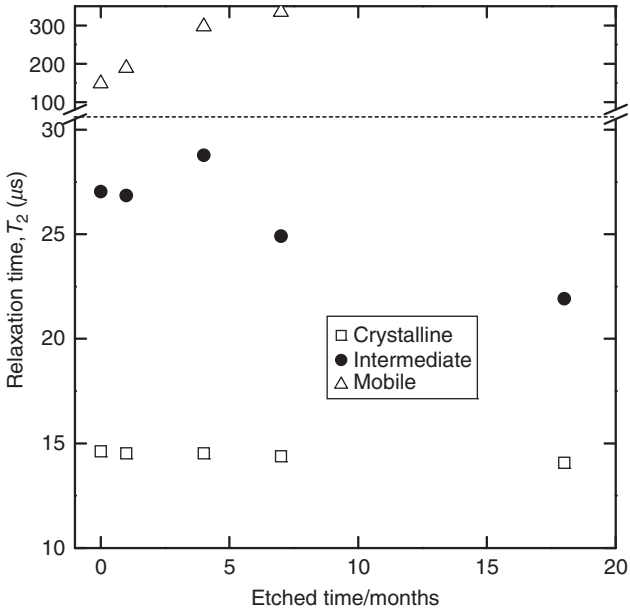

Figure 14 Etching time dependencies of T_2 for a series of nascent and etched powders. Both values for crystalline and two amorphous (intermediate and mobile) relaxations were plotted for each sample.

etching time, which means that the sample crystallinity increases with increasing treatment time. T_2 for each decay function is plotted in Figure 14 as a function of etching time.[24] For the highly crystalline powder etched for 18 months, only a single amorphous decay represented by the Weibullian function was required for sufficient fitting. The T_2 of this component lies around $\sim$22 μs, which implies very limited molecular motion, compared to that of usual amorphous PE chains ($\sim$200 μs). Thus, this relaxation component was attributed to the ''intermediate'' amorphous chains. In contrast, a satisfactory FID fitting for the nascent powder having lower crystallinity requires the additional ''mobile'' amorphous component. In other words, longer etching completely removes this mobile amorphous component. Concurrently, the paste-like morphology on the powder surface disappeared in Figure 12. The T_2 of the mobile amorphous component changes between 100 and 300 μs, which is comparable to the values of amorphous relaxation times in the case of conventional melt-crystallised morphology of UHMW-PE[28]; this phase was below 1%. Thus, the quantitative interpretation of T_2 for this component is difficult. However, it should be noted that such a small amount of this phase is in agreement with the fact that the paste-like morphologies, as seen in SEM images for the nascent powder, seemed to spread on the powder surface, rather than in the globular interior, and almost disappeared in the earlier stage of etching.

In Figure 14, it can be also seen that crystalline T_2 has a constant value of around 14.5 μs, independent of the etching time. The reason for the constant

crystalline T_2 is that the mobility of the crystalline component is not affected by the etching or that the correlation time for the crystalline component lies in the extremely slow region where T_2 is insensitive to the chain mobility. In both cases, the mobility of the crystalline component is slow enough to maintain the crystalline structure. This means that the crystalline region remains undamaged during mild etching. In contrast, the intermediate amorphous T_2 shows a rapid decrease with etching time. Etching for 18 months finally gives the shortest intermediate amorphous T_2 near 22 μs. This phase simultaneously decreased from 17% for the nascent powder to 7% for the 18-month-etched sample, which was estimated from the areas in the Fourier-transformed broad-line spectra. These unique characteristics of the intermediate amorphous region with etching time can be reasonably compared to the results obtained from SEM and TEM observations. With increasing etching time, the regions located between the crystalline grains were gradually removed, as shown in Figure 12. This means that such regions correspond to the intermediate amorphous components. The decreasing T_2 value for this component suggests that the molecular motion of the surviving intermediate amorphous phase is restricted. Among the intermediate amorphous chains, the region far away from the crystalline domains can be destroyed earlier, but more restricted chains that are connected with crystalline domains just at phase boundaries may survive even after prolonged etching.

Figure 15 compares the crystallinity changes estimated from ^{1}H NMR analysis and DSC measurements for a series of the etched powders.[24] The crystallinity values for ^{1}H NMR analysis were calculated from the areas in the Fourier-transformed broad-line spectra, simulated for the crystalline, intermediate

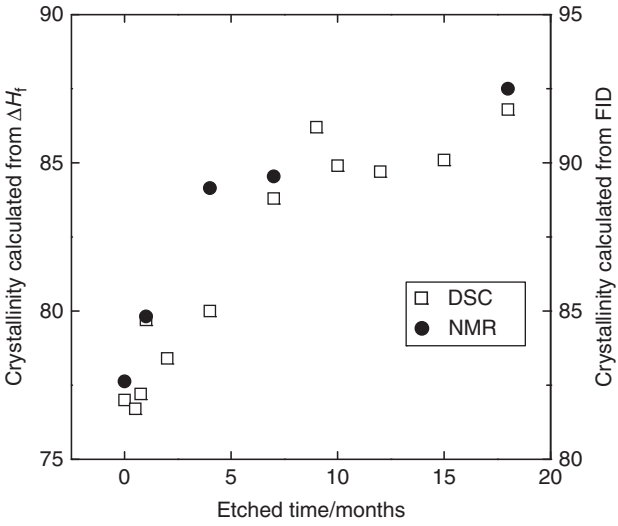

Figure 15 Comparison of etching time dependencies of crystallinity, estimated from DSC and ^{1}H NMR FID analyses for a series of nascent and etched powders. For the latter case, the percentage of the crystalline component is plotted.

amorphous and mobile amorphous relaxation decays. Those for DSC measurements were calculated from the heat of fusion. Both estimation methods show parallel increases in the crystallinity with increasing etching time. The crystallinity change estimated from ^{1}H NMR FID analysis was a gradual increase in crystallinity from initial ~83% to final ~93%. This 10% increase in crystallinity also agrees well with that estimated from DSC. The coincidence between ^{1}H NMR and DSC data confirms that the perfect fitting of the decay functions are desirable for the phase analysis of the UHMW-PE nascent powder samples.

3.5. The structural change of polyethylene nascent powder upon annealing

One of the characteristic of the nascent powder structure is the presence of an intermediate phase included with conventional crystalline and amorphous phases. The higher ductility of polyethylene nascent powders suggested the coexistence of less entangled amorphous phases located between crystalline and amorphous phases.[24,45,46] This arises from the non-equilibrium crystallisation during polymerisation. Therefore, the polymerisation temperature affects the structure and the morphology of the nascent powder.

Figure 16 presents the TEM images for the series of $T_{poly} = 70\,^{\circ}C$ powders (polymerisation temperature is 70 °C) annealed at a T_a of 80, 100 and 120 °C, which are higher than T_{poly}.[46] At $T_a = 80\,^{\circ}C$ (Figure 16A), the typical lamellar morphology of a melt- or solution-crystallised sample is not observed. Rather, crystalline domains of 15 nm size are distributed throughout the powder. Even the increase of T_a to 90 °C does not generate any significant change. At $T_a > 100\,^{\circ}C$, a morphological change occurs. The image contrast in Figure 16B increases owing to increases of the brightness in the crystalline regions and darkness in the amorphous region, which means that the crystalline and amorphous phases are aggregated and the crystalline domain size increases. Above 120 °C, the lamellar structure appears (Figure 16C).

For powder samples with $T_{poly} = 20\,^{\circ}C$, the lamellar formation begins at T_as exceeding 110 °C, which is a little lower than the corresponding T_a of 120 °C for the powder of $T_{poly} = 70\,^{\circ}C$. The WAXD data recorded while these nascent

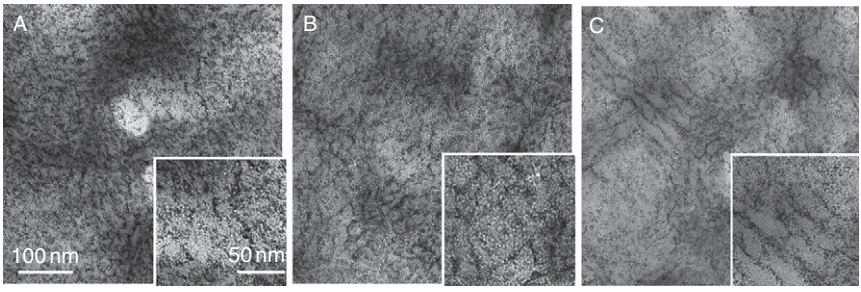

Figure 16 TEM images of $T_{poly} = 70\,^{\circ}C$ powder annealed at T_as (A) 80 °C, (B) 100 °C and (C) 120 °C. Enlarged images are attached at bottom right.

powders were heated suggest a lower melting point for the $T_{poly}=20\,^{\circ}C$ powder than for the $T_{poly}=70\,^{\circ}C$ powder. This difference in the lamellar-forming T_a is attributed to the smaller size of the initial crystalline domains within the un-annealed $T_{poly}=20\,^{\circ}C$ powders. However, the phase arrangements were quite similar for both powder morphologies, exhibiting a homogeneous distribution of the crystalline domains. This morphology is one of the universal characteristics of the PE nascent powders, independent of T_{poly}. The boundaries between the crystalline and amorphous phases become clear as T_a increases, especially when T_a exceeds 40 °C, and the crystalline domains begin to aggregate into larger sizes. These morphological transformations are quite similar to those observed for the corresponding T_a of 90 °C for the former $T_{poly}=70\,^{\circ}C$ powder. No structural change is detectable below these critical T_as, so they are ascribed to the maximum temperatures to which each nascent powder was exposed during the polymerisation process. Since both of these critical T_as are 20 °C higher than that of the preparation T_{poly}s, the domain-aggregating T_as correspond to the temperature near the active sites on the catalyst surface where the chain growth is progressive.

Figure 17 compares the FID profiles recorded at room temperature for powders with $T_{poly}=20\,^{\circ}C$ and $T_{poly}=70\,^{\circ}C$.[46] The plots in the intermediate time region ranging from 30 to 50 μs are the same in both FID profiles, but the regions in the shorter and longer timescales exhibit a higher intensity for the $T_{poly}=20\,^{\circ}C$ powder than for the $T_{poly}=70\,^{\circ}C$ one. T_2 values for these three phases are summarised in Table 3.[46] T_2 values are similar between powders of $T_{poly}=20$ and 70 °C for the intermediate phase, while those of the crystalline and amorphous phases exhibit large differences. Namely, the lower value of the crystalline T_2 was

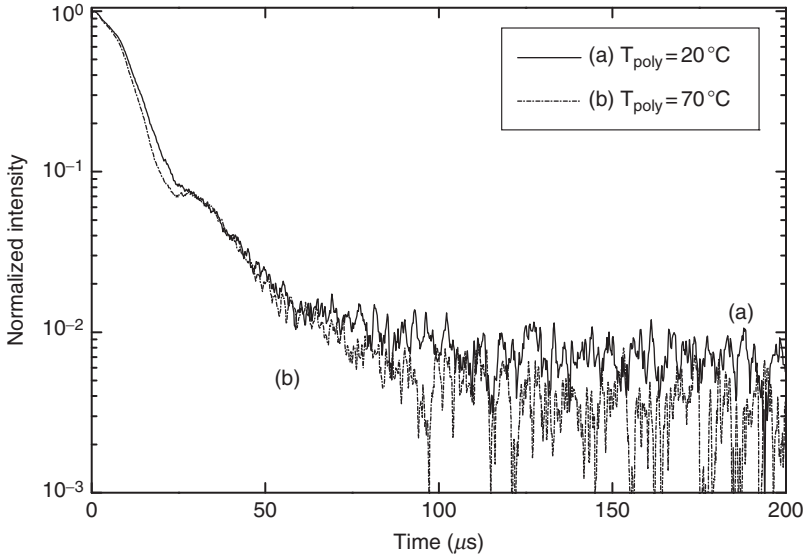

Figure 17 Comparison of ^{1}H NMR FIDs observed at room temperature for the nascent powders prepared at $T_{poly}=20\,^{\circ}C$ (A) and 70 °C (B).

TABLE 3 Spin–spin relaxation times T_2 calculated as the inverse of the integral width for the nascent powders prepared at 20 and 70 °C

T_{poly}(°C)	$T_2(\mu s)$		
	Crystalline	Intermediate	Amorphous
20	17.2	30.8	45.3
70	15.5	31.2	125

obtained for the $T_{poly}=70$ °C powder, but the lower value of the amorphous T_2 was evaluated for the $T_{poly}=20$ °C powder. These results suggest that the crystalline phase is more rigid for the $T_{poly}=70$ °C powder, but the amorphous phase is more rigid for the $T_{poly}=20$ °C powder.

^{1}H NMR relaxation behaviours change gradually with heating. During the early stage of heating, crystallinity decreases and exhibits a minimum value at around 60 °C; then, it increases again for both powders. These decreases and subsequent increases in crystallinity coincide with those of the reflection intensities observed for the WAXD profiles. Heating produces maximum crystallinity at 120 °C for the $T_{poly}=20$ °C powder and at 110 °C for the $T_{poly}=70$ °C powder, followed by the abrupt drops in crystallinities beyond these temperatures attributed to the sample melting. These temperatures exhibiting the maximum crystallinities agree well with the temperatures at which the lamellae appear in the series of TEM observations. These results indicate that the lamellar formation originates from melt-recrystallisation during annealing.

In Figure 18, the temperature dependences of the integral width for crystalline, intermediate and amorphous phases are shown.[46] The integral widths of the three different phases change with increasing temperature for both powders. The trend of the intermediate phases is similar to each other, independent of the preparation

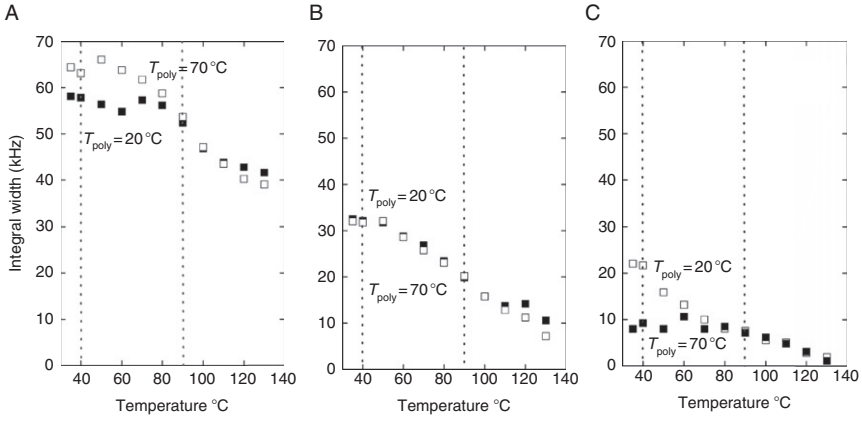

Figure 18 Summarized changes in the integral width during heating of $T_{poly}=20$ °C and 70 °C powders. (A) crystalline, (B) intermediate and (C) amorphous components.

T_{poly}. In contrast, the integral widths of crystalline and amorphous phases show remarkable differences, depending on T_{poly}. There are only negligible difference between the $T_{poly}=20$ °C powder and the $T_{poly}=70$ °C powder above 90 °C in the crystalline phase. However, the value is always lower in the $T_{poly}=20$ °C powder below this temperature. The larger crystallite size gives the higher integral width for the UHMW-PE samples prepared under different crystallisation conditions.[24] Nascent powder contains the monoclinic form at polymerisation temperature below 60 °C.[45] X-ray analysis indicates that the crystalline size for the orthorhombic form is twice as large as that for the monoclinic form. Therefore, the crystalline size for the nascent powder of $T_{poly}=20$ °C has a smaller crystalline size. The smaller crystallite size of the monoclinic crystals within the $T_{poly}=20$ °C powder is attributed to the lower integral width value. This difference in the integral width of the crystalline phase continues from room temperature to 90 °C. However, both powders exhibit similar crystalline widths above 90 °C because the aggregation of the crystalline domains into the larger size is completed at the higher temperature.

In contrast, the integral width of the amorphous phase is always larger for the $T_{poly}=20$ °C powder than for the $T_{poly}=70$ °C powder below 90 °C. This means that the molecular mobility of the $T_{poly}=20$ °C powder is lower due to the more restricted progress of the structural formation at the lower T_{poly}. The integral width of the $T_{poly}=70$ °C powder coincides with that of the conventional melt-recrystallised PE,[28] indicating the so-called random-coiled state of the amorphous chains. Additionally, the amorphous width in the $T_{poly}=70$ °C powder is constant below 90 °C. However, the integral width in the amorphous phase of the $T_{poly}=20$ °C powder begins to decrease at 40 °C, and finally duplicates those of the $T_{poly}=70$ °C powder above 90 °C. The critical temperature at which the aggregation of the crystalline domains is evident in the TEM observations is 40 °C for the $T_{poly}=20$ °C powder. This synchronisation of the morphological and molecular mobility changes suggests that the spatial motion of the amorphous chains induces an increase in the size of the crystalline domains during annealing. In contrast, the corresponding change for the $T_{poly}=70$ °C powder occurs at 90 °C. Similar coincidence of the critical temperatures for the morphological and molecular mobility changes for both nascent powders supports the above assignment of the phase development mechanism during annealing. The constrained molecular motion of the as-polymerised amorphous chains surrounding the crystalline domains is released when the annealing reaches the critical temperature, which always exceeds the maximum temperature experienced during polymerisation. This molecular motion of the amorphous phases unlocks the crystalline domains, so they can be aggregated into the larger spatial area.

The structural development model in Figure 19 is a combination of all the information obtained from TEM observation, WAXD and NMR measurements.[46] The results of the morphological changes during annealing demonstrate that the actual polymerisation commenced when the temperature was 20 °C higher than the preparation T_{poly} for each of the nascent powders. This low temperature difference corresponds to an exothermic reaction near the active sites on the catalyst, where continuous chain growth occurs. Rapid crystallisation occurs for

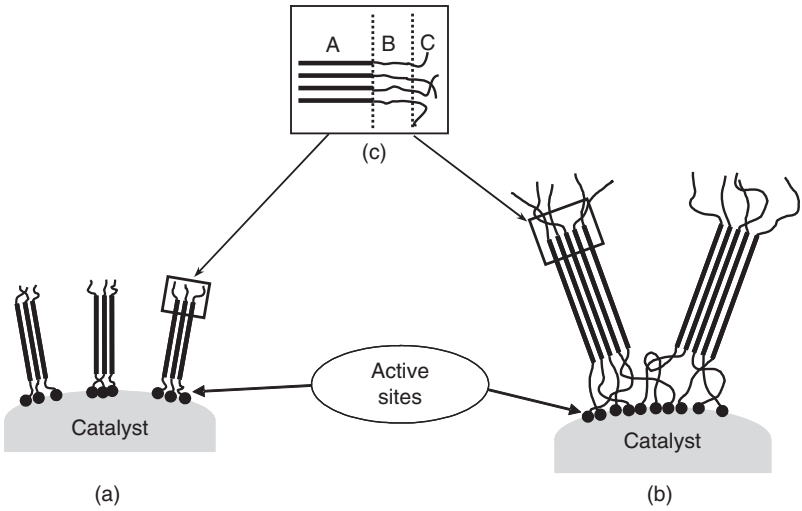

Figure 19 Structural development model during polymerization including chain growth and crystallization at $T_{poly} = 20\ ^{\circ}C$ (A) and 70 °C (B). Panel (C) indicates the intermediate region B sandwiched between crystalline A and amorphous C phases.

the lower T_{poly} as soon as the shorter chains are produced at the active sites, and the resultant crystalline domains retain the constraints of the molecular chains. Therefore, the crystalline phase of the lower T_{poly} powder contains a larger amount of the monoclinic form within a smaller domain. The molecular mobility of the amorphous phase is also restricted in the nascent powder prepared at the lower T_{poly}. In contrast, the higher T_{poly} generates the step-wise processes of the initial chain growth and subsequent crystallisation of the grown chains. Therefore, larger crystalline domains with the usual orthorhombic form are produced with a less constrained amorphous phase. After these nascent powders are annealed beyond the temperature experienced during polymerisation near the active site, the amorphous chains surrounding the crystalline domains become mobile. This characteristic amorphous chain motion unlocks and induces the aggregation of the crystalline domains by releasing the lattice constraint. These phase changes in the crystalline and amorphous phases are synchronised through the intermediate phase that connects them. Thus, the molecular motion of the intermediate phase exhibits a gradual change during heating for both nascent powders.

4. KINETICS OF DYNAMIC PROCESS OF POLYMERS

4.1. Molecular mobility during drawing from highly entangled polyethylene melts

UHMW-PE can be drawn even from the molten state because of its high melt viscosity.[47–51] Transient crystallisation into a hexagonal form occurs during oriented crystallisation into the orthorhombic form during melt-drawing. This

behaviour was investigated by *in situ* WAXD using synchrotron radiation,[52] which revealed that the structural transformation of amorphous chains induces transient crystallisation into the hexagonal form through disentanglement. Precise investigation of the amorphous phase is limited to a few spectroscopic techniques such as IR,[53–55] Raman[56,57] and NMR.[14,15,58–60] NMR spectroscopy has been applied to *in situ* measurements during deformation.[60–65] Gleason et al. investigated the effect of uniaxial deformation near the glass transition temperature on the chain mobility in the amorphous region of deuterated nylon 6.[62] Rault et al. studied the stress-induced crystallisation and melting of cross-linked rubber. Quantitative evaluation of chain entanglement or disentanglement has been analysed by the *in situ* NMR method.[66]

An in situ NMR measurement for evaluating molecular mobility during melt-drawing can be made by using a uniaxial cross-head extension device. Two cross-heads of this extension device move in opposite directions perpendicular to the magnetic field. In the usual variable-temperature system, hot air is blown from the bottom of the probe, which produces a temperature gradient in the sample. During drawing, this gradient leads to the distribution of the stress and strain in the receiver coil. In Figure 20 is shown the *in situ* probe for melt-drawing.[66] In this probe, hot air is applied perpendicular to the sample. Thus, the central region of the sample is always in a detection coil, which is located at the centre of the magnet.

From Carr-Purcell-Meiboom-Gill (CPMG) measurements, three amorphous components were obtained as rigid (shortest T_2), intermediate and mobile

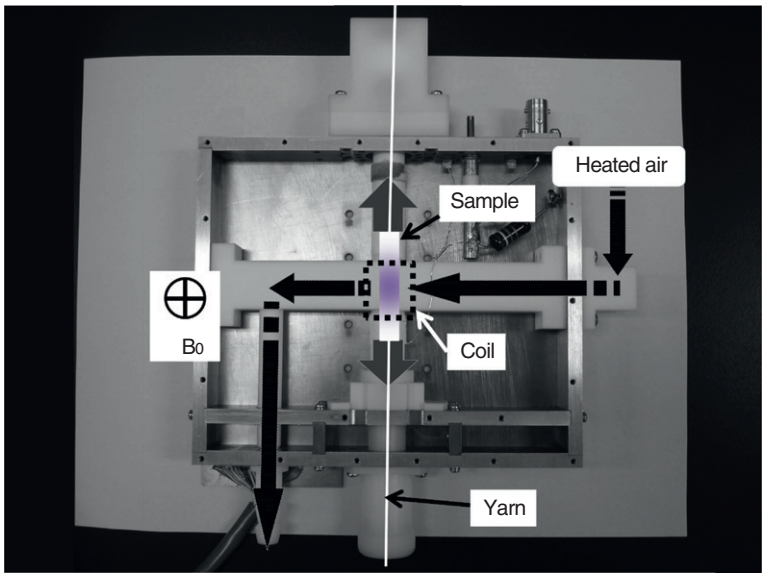

Figure 20 *In situ* NMR probe system. The direction of the magnetic field is through. The sample was set at the centre of a detection coil. Heated air was blown perpendicular to the drawing direction in the probe through a poly(tetrafluoroethylene) channel.

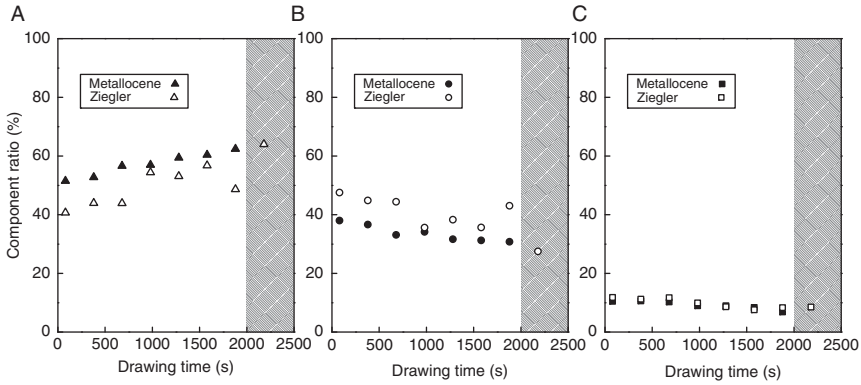

Figure 21 Changes in component ratio for metallocene (filled symbols) and Ziegler films (open symbols): (A) Mobile, (B) intermediate and (C) rigid amorphous components. The shaded area indicates the plateau stress region.

(longest T_2). For the change in T_2, the Ziegler film exhibits higher values for all components than the metallocene film. This indicates that the chain mobility for the Ziegler film is higher than that for the metallocene film. However, these values hardly change during melt-drawing for both films.

Figure 21 illustrates the changes in the component ratio of each component for the metallocene and Ziegler films during melt-drawing.[66] A difference in the component ratio between the metallocene and Ziegler films is observed for the intermediate and mobile amorphous components. Comparing the initial drawing stage, the mobile amorphous component is predominant for the metallocene film. In contrast, the intermediate amorphous component is predominant for the Ziegler film. With drawing, an increase in the mobile amorphous component and a decrease in the intermediate amorphous component are observed for both films. These opposite phenomena mean that structural transformation from intermediate to mobile amorphous components occurs during melt-drawing. In particular, this structural transformation is more significant for the Ziegler film. However, the rigid amorphous component hardly changes even for the component ratio during melt-drawing for both films. It is suggested that extensive disentanglement with chain slippage proceeds at the initial stage of melt-drawing for a Ziegler film with a broader molecular weight distribution.[67–69] The mobile amorphous component is attributed to the disentangled chains transformed from the prior intermediate amorphous component, considering that this component significantly increases at the same stage for the Ziegler film. In contrast, the intermediate amorphous component with less mobility than the mobile amorphous component can be construed as networked amorphous chains connected by entanglements and distributed homogeneously over the whole chain. The rigid amorphous component has much lower chain mobility, that is shorter T_2. Thus, this component consists of entanglements tightly confining each other.

Models for structural transformation of amorphous chains are proposed in Figure 22 based on the experiment results of these in situ NMR measurements.

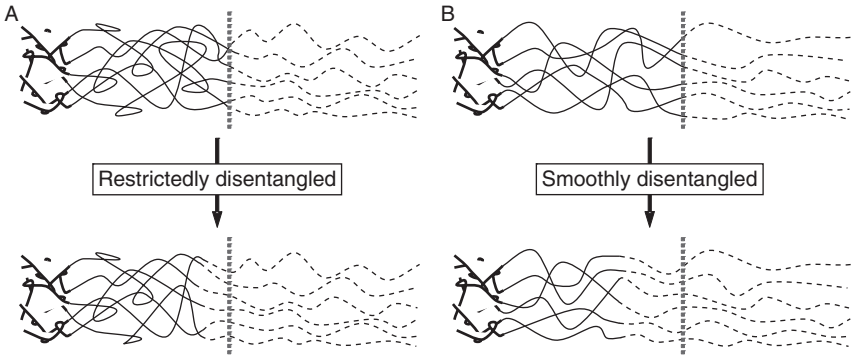

Figure 22 Models for structural transformation of amorphous chains for (A) metallocene and (B) Ziegler films. A bold, fine and dotted lines indicate rigid, intermediate, and mobile amorphous components, respectively. Top and bottom models represent the state before and after drawing, respectively. The vertical dotted lines indicate the boundary between intermediate and mobile amorphous components at the state before drawing. Chain shape and length for each component in each model reflect T_2 and the component ratio estimated from *in situ* NMR measurement. There is a small disentangled region for metallocene film (A) with lower chain mobility because disentanglement of the intermediate amorphous component is "restricted". In contrast, the corresponding region is larger for Ziegler film (B) with higher chain mobility due to "smooth" disentanglement of the intermediate amorphous component.

The rigid amorphous component with $T_2 \sim 1$ ms (dotted lines) can be defined as amorphous chains with tight entanglements that transfer the drawing stress well. The intermediate amorphous component with $T_2 \sim 5$ ms (fine lines) can be defined as amorphous chains with loose entanglements, and the mobile amorphous component with $T_2 \sim 15$ ms (bold lines) can be defined as disentangled amorphous chains. Significant structural transformation from intermediate into mobile amorphous components occurs during melt-drawing for the Ziegler film. Here, a Ziegler material with broader molecular weight distribution includes a larger amount of lower molecular weight component compared with a metallocene material. Consequently, the intermediate amorphous component for the Ziegler film has looser entanglements (Figure 22B) than that for the metallocene film (Figure 22A). Indeed, the Ziegler film exhibited slightly higher T_2s than the metallocene film for both intermediate and mobile amorphous components. That is, the broader molecular weight distribution of the Ziegler film enhances the chain mobility in both T_2 levels. Thus, chains disentangle more smoothly during melt-drawing for the Ziegler film (Figure 22B). This means that the continuity of molecular weight distribution for the Ziegler film induces the cooperation of the intermediate and mobile amorphous components during chain disentanglement. In contrast, a metallocene material with a narrower molecular weight distribution includes only a higher molecular weight component. Thus, disentanglement of the intermediate amorphous component is restricted due to lower chain mobility with entanglements, and structural transformation is less pronounced for the metallocene film (Figure 22A). No structural transformation of

the rigid amorphous component occurs during melt-drawing for either film due to the confinement of chains with tight entanglements.

4.2. Crystallisation mechanism of Nylon 46

So far, it was shown that the precise and perfect fit of ^{1}H pulse NMR FID can offer information about the relation between morphology with a large scale and the fine structure at the atomic level. Since polyethylene is composed of CH_2 units and only one kind of ^{1}H exists, ^{1}H NMR can give sufficient insight into considerations of the morphology. For more complicated polymers, high-resolution NMR combined with TEM and X-ray can also supply detailed information about dynamic processes in terms of functional groups in the polymer. For nylon 46, the combination NMR and TEM is applied in order to investigate the crystallisation mechanism.[69]

In Figure 23 is shown the TEM micrographs of the SGC and the melt-grown crystal (MGC) for nylon 46.[69] For SGC, the regular stacking of the lamellar crystals is clearly observed (Figure 23A). The lamellar thickness is uniform compared to the melt-crystallised samples. For MGC0m (where the number and alphabet after MGC means crystallisation time), the stacking of the lamellar crystal is not clear and the random arrangement of the curved lamellae with a short length is observed (Figure 23B). As the crystallisation time increases, many long lamellar crystals are arranged parallel and the lamellar stacking grows (Figure 23C).

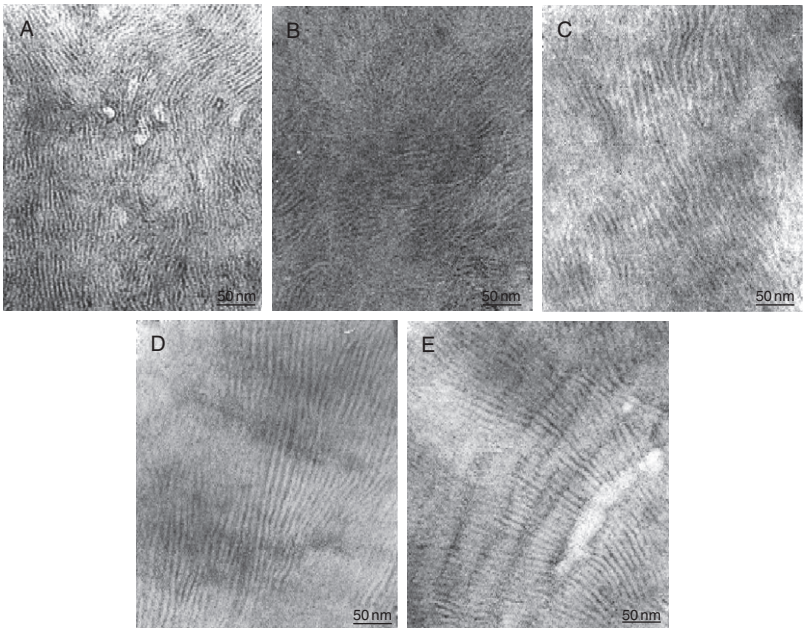

Figure 23 TEM micrographs of SGC and crystallized samples. (A) SGC, (B) MGC0m, (C) MGC1m, (D) MGC1h, (E) MGC24h.

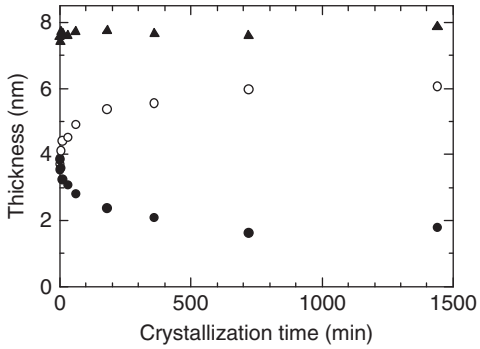

Figure 24 Crystallization time dependence of the thickness for the lamellae, the crystalline phase and the amorphous phase. ▲: lamellar, ○: crystalline phase, ●: amorphous phase.

A closer look at the micrographs revealed the change in thickness of the crystalline phase. In Figure 24 is shown the crystallisation time dependence of the thickness of the lamellae and crystalline and amorphous phases.[69] The lamellar thickness is the sum of the thicknesses of the crystalline and amorphous phases. As seen from Figure 24, the lamellar thickness is independent of the crystallisation time. On the other hand, the thicknesses of the crystalline and amorphous phases increase and decrease, respectively.

Figure 25 shows the ^{13}C CPMAS NMR spectrum of SGC nylon 46 together with the chemical structure. There are five chemically non-equivalent carbons in nylon 46. The carbonyl carbon peak appears at 173 ppm. Four methylene carbons, α_B, α_A, β_B and β_A, correspond to 42, 36, 27 and 26 ppm, respectively.[70]

As the crystallisation proceeds, the molecular mobility is also affected. In Figures 26A and B are shown the crystallisation time dependences of T_1 for the

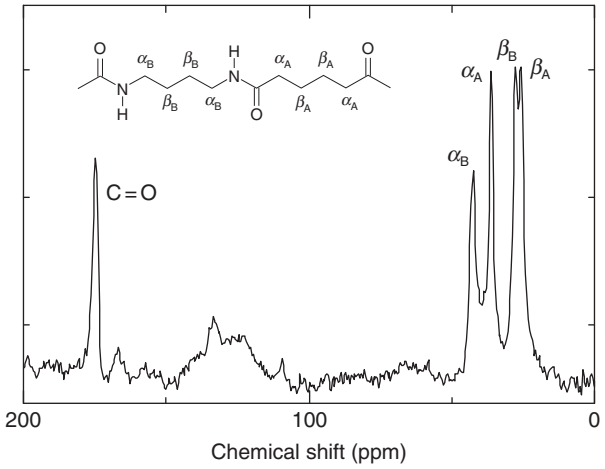

Figure 25 ^{13}C CPMAS NMR spectrum of SGC nylon 46.

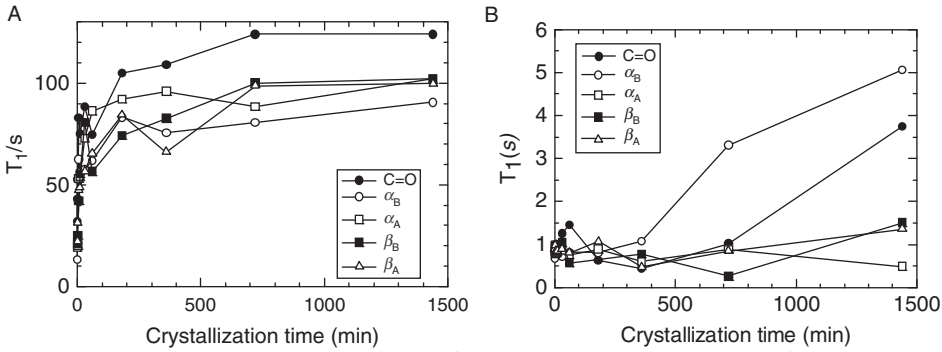

Figure 26 Crystallization time dependence of the spin–lattice relaxation time for nylon 46. (A) The crystalline phase; (B) the amorphous phase.

crystalline and amorphous phases, respectively. In Figure 26A, the T_1s of MGC0m are less than 35 s. As the crystallisation time increases, the T_1s of all the carbons rapidly increase for about 1 h and then become almost constant after 6 h. The T_1s of all the carbons for MGC24h become about 4 times greater than those for MGC0m. As T_1 decreases with the change in the molecular mobility based on the BPP theory for the solid polymers, the molecular mobility is restricted by the crystallisation.[25] The crystallisation time dependence of the T_1s is similar to the behaviour of crystallinity. This means that the molecular motion of the crystalline phase is restricted as soon as the stable crystalline structure is formed. In other words, after the crystallite reaches a certain size, the molecular mobility of the crystalline phase is fixed. In Figure 26B, the crystallisation time dependence of T_1 for the amorphous phase is shown. The T_1s for the amorphous phase are less than 5 s, which is much shorter than those for the crystalline phase, and means that the molecular mobility is high compared to that for the crystalline phase. The T_1s for all the carbons in the amorphous phase are about 1 s or less and do not change very much until 6 h. After crystallisation for 6 h, the T_1s of α_B and CO increased. This means that the molecular motion of the amorphous phase is restricted after the T_1s for the crystalline phase becomes constant. The fraction of the long T_1 increases with the crystallisation time, which is a behaviour similar to that of crystallinity. Therefore, the mobility of the amorphous phase is affected by the surrounding crystalline phase.

Spectra of crystalline and amorphous phases are separately observed by using the T_1 difference. The chemical shifts for the crystalline and amorphous phases are summarised in Table 4. The peak width for the amorphous phase is broader than those for the crystalline phase. The peak width is affected by the dipolar interaction and the distribution of chemical shift. For the dipolar interaction, the molecular mobility is the dominant factor for the peak broadening. As seen from the short ^{13}C T_1 observed in Figure 26B, the polymer chain is mobile in the amorphous phase. The peak broadening is caused by the reduced efficiency of high-power ^1H decoupling if the molecular motion is in the range of ^1H decoupling frequency. This peak broadening usually takes places above the glass transition temperature for the amorphous phase. As the glass transition temperature for nylon 46 is about

TABLE 4 ^{13}C NMR Chemical shiftsof methylene in nylon 46 for the crystalline and amorphous phases

Phase	^{13}C NMR chemical shift/ppm			
	α_B	α_A	β_B	β_A
Crystalline	42.6	36.1	27.5	25.7
Amorphous	39.9	36.7	27.0	27.0

60 °C, the dipolar interaction is not responsible for the large peak width for the amorphous phase in this case. The chemical shift is affected by the conformation of the polymer. In the amorphous phase, the polymer chain takes several conformers or makes rapid transitions between a number of conformational states. In this case, the distribution of the conformation contributes to the peak width of the amorphous phase.

The chemical shift of α_B for the crystalline phase appears at a lower field than that for the amorphous phase by about 2 ppm. In the crystalline phase, the conformation of nylon 46 is supposed to be the trans-zigzag conformation. It is known that the CH_2 carbons appear at a higher field by 4–6 ppm if a carbon atom three bonds away is in a gauche-conformation rather than in the trans-conformation (γ-effect).[71] There are two γ-positions for α_B methylene, that is α_B and α_A. As the NH–CO bond is rigid, α_A is thought to have the trans-conformation even in the amorphous phase. This is supported by the fact that the chemical shift of the carbonyl carbon is independent of the crystallisation time as described below. The chemical shift difference in α_B for the crystalline and amorphous phases is attributed to the conformational change around the β_B–β_B bond. In the amorphous phase, the β_B–β_B bond takes the gauche-conformation or makes the transition between the trans- and gauche-conformations. Since no chemical shift difference was observed for the α_A methylene, the β_A–β_A bond takes the trans-conformation both in the crystalline and amorphous phases. For the β_A and β_B methylenes, these peaks are split in two in the crystalline phase, but merged in the amorphous phase. If the bond that affects the chemical shift of the β_A and β_B methylenes is assumed to take the trans-zigzag conformation in the crystalline phase and the gauche-conformation in the amorphous phase, both methylene carbons appear at a lower field in the crystalline phase based on the γ-effect. This is the scenario for the β_B methylene. However, the β_A methylene at the crystalline phase appears at a higher field than that in the amorphous phase. It has been reported that the chemical shift of CO(amide) in polypeptides is displaced depending on the main chain conformation (dihedral angles ϕ and φ).[72] Since no chemical shift difference is observed for CO, the α_B–N and CO–α_A bonds take the trans-conformation both in the crystalline and amorphous phases. Therefore, the upfield shift in the crystalline phase is attributed to the conformational change around the β_A–α_A bond. As the conformation of this bond in the crystalline phase is assumed to be the trans-conformation based on the X-ray analysis, the conformation in the amorphous phase is thought to contain the

gauche conformation. The γ-position for the β_A methylene is not methylene, but CO, which may result in the upfield shift.

The chemical shift for the carbonyl carbon does not change with the crystallisation time. It has been demonstrated that the chemical shift for the carbonyl carbon is affected by the conformation and the hydrogen-bonding strength.[58] Therefore, the conformation near the carbonyl carbon and the hydrogen-bonding strength for the crystalline and amorphous phases are in a similar state. As the crystal structure of nylon 46 is composed of a stack of hydrogen-bonded sheets, the hydrogen bonding is formed even during the initial stage of the crystallisation and the distribution of the conformation and the hydrogen-bonding strength decreased with the growth of the crystalline phase. The distribution of the structure or the hydrogen-bond strength is reflected in the peak width. The half-height width of the carbonyl carbon decreases for 1 h and then gradually decreases. The half-height width of SGC is almost same as that of MGC24h.

Based on high-resolution solid-state NMR and TEM observation, the mechanism for the crystallisation of nylon 46 is summarised in Figure 27.[69] When the temperature of the melt sample decreased to the crystallisation temperature, hydrogen bond is formed with the nearby chains. At this stage, the size of the crystalline phase is small and the crystal structure is not energetically stable. The amorphous phase is mobile and the conformation of the amorphous phase contains the gauche conformation around the β_B–β_B bond. As the crystallisation proceeds, the crystal structure becomes stable and forms the hydrogen-bond sheet structure. At the same time, the crystalline phase grows by the conformational change in the amorphous phase. As the sliding of the main chain does not occur, the thickening of the lamellae does not take places. The thickness of the crystalline phase increases with the decrease in the amorphous phase thickness. During the final stage of the crystallisation, the mobility of the amorphous phase is restricted.

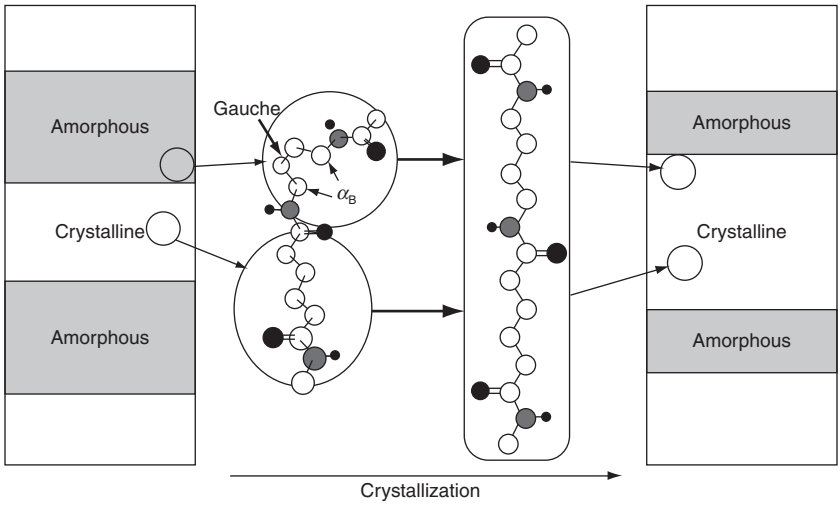

Figure 27 Crystallization mechanism of nylon 46.

5. CONCLUSIONS

Practical applications of NMR and other techniques such as microscopy and diffraction that supply information about the large-scale structure to the investigation for polymer morphology, structure and physical properties have been introduced. NMR has been thought to be an insensitive spectroscopic technique. Recent development of hardware has improved the stability, sensitivity and resolution of NMR, especially the solid-state NMR. The fine difference of the morphology and the large-scale structure of polymers do appear in the NMR signal. Careful and perfect fit or analysis of the NMR signal and the combination with other techniques that complement NMR's disadvantages certainly offer information on the nature of the polymer.

REFERENCES

1. I. Ando, M. Kobayashi, M. Kanekiyo, S. Kuroki, S. Ando, S. Matsukawa, H. Kurosu, H. Yasunaga and S. Amiya, NMR spectroscopy in polymer science, *in*: *Experimental Methods in Polymer Science*, T. Tanaka (ed.), Academic Press, San Diego, CA, 2000, p. 261.
2. I. Ando and T. Asakura, *Solid State NMR of Polymers*. Elsevier, Amsterdam, The Netherlands, 1998.
3. K. Schmidt-Rohr and H. W. Spiess, *Multidimensional Solid-State NMR and Polymers*. Academic Press, New York, 1994.
4. W. Klüver and W. Ruland, NMR-Studies of semicrystalline polymers using pulse techniques, *in: Prog. Colloid Polym. Sci.*, 1978, **64,** 255.
5. K. Bergmann, H. Schmiedberger and K. Unterforsthuber, *Colloid Polym. Sci.*, 1984, **262,** 283.
6. D. Dadayli, R. K. Harris, A. M. Kenwright, B. J. Say and M. M. Sunnetcioglu, *Polymer*, 1994, **35,** 4083.
7. E. W. Hansen, P. E. Kristiansen and B. Pedersen, *J. Phys. Chem. B*, 1998, **102,** 5444.
8. P. E. Kristiansen, E. W. Hansen and B. Pedersen, *J. Phys. Chem. B*, 1999, **103,** 3552.
9. P. E. Kristiansen, E. W. Hansen and B. Perdersen, *Polymer*, 2000, **41,** 311.
10. V. J. Loboda-Čačković, R. Hosemann and W. Wilke, *Kolloid Z. Z.*, 1969, **235,** 1263.
11. O. Phaovibul, J. Loboda-Čačković, H. Čačković and R. Hosemann, *Makromol. Chem.*, 1974, **2991,** 175.
12. R. Kitamaru, F. Horii and S.-H. Hyon, *J. Polym. Sci. Polym. Phys. Ed.*, 1977, **15,** 821.
13. K. Bergmann, *J. Polym. Sci. Polym. Phys. Ed.*, 1978, **16,** 1611.
14. R. Folland and A. Charlesby, *J. Polym. Sci. Polym. Lett. Ed.*, 1978, **16,** 339.
15. R. Folland and A. Charlesby, *Euro. Polym. J.*, 1979, **15,** 953.
16. H. Koch, R. Bachus and R. Kimmich, *Polymer*, 1980, **1009,** 21.
17. M. G. Brereton, I. M. Ward, N. Boden and P. Wright, *Macromolecules*, 1991, **2068,** 24.
18. D. C. Look, I. J. Lowe and J. A. Norhtby, *J. Chem. Phys.*, 1966, **44,** 3441.
19. A. M. Kenwright and B. I. Say, *in*: *NMR Spectroscopy of Polymers*, R. N. Ibbett (ed.), Chapman and Hall, London, 1993.
20. K. Bergmann, *Polym. Bull.*, 1981, **5,** 355.
21. J. P. Cohen-Addan, G. Feio and A. Peguy, *Polym. Commun.*, 1987, **28,** 252.
22. A. Abragam, *Principles of Nuclear Magnetism*. Oxford, Claredon, 1961.
23. G. E. Pake, *J. Chem. Phys.*, 1948, **16,** 327.
24. H. Uehara, T. Aoike, T. Yamanobe and T. Komoto, *Macromolecules*, 2000, **35,** 2640.
25. N. Bloembergen, E. M. Purcell and R. V. Pound, *Phys. Rev.*, 1948, **73,** 679.
26. R. J. L. Graff, G. Kortleve and C. G. Vonk, *J. Polym. Sci. Polym. Lett.*, 1970, **8,** 735.
27. G. A. H. Nooijen, *Euro. Polym. J.*, 1994, **30,** 11.
28. H. Uehara, T. Yamanobe and T. Komoto, *Macromolecules*, 2000, **33,** 4861.
29. F. G. Morin, G. Delmas and D. F. R. Gilson, *Macromolecules*, 1995, **28,** 3248.
30. T. Kanamoto, A. Tsuruta, K. Tanaka, M. Takeda and R. S. Porter, *Macromolecules*, 1988, **21,** 470.
31. P. Smith, P. J. Lemstra and H. C. Booij, *J. Polym. Sci. Polym. Phys. Ed.*, 1981, **19,** 877.

32. R. S. Porter and J. F. Johnson, *J. Appl. Polym. Sci.*, 1944, **1960,** 3.
33. R. S. Porter and J. F. Johnson, *Chem. Rev.*, 1966, **66,** 1.
34. J. S. Higgins and R. S. Stein, *J. Appl. Cryst.*, 1978, **11,** 346.
35. G. Hadziioannou, L. H. Wang, R. S. Stein and R. S. Porter, *Macromolecules*, 1982, **15,** 880.
36. G. Voigt and R. Kimmich, *Polymer*, 1980, **1001,** 21.
37. R. Kimmich and H. Koch, *Colloid Polym. Sci.*, 1980, **258,** 261.
38. I. Kamel and A. Charlesby, *J. Polym. Sci. Polym. Lett. Ed.*, 1981, **19,** 803.
39. J. P. Cohen-Addan and R. Dupeyre, *Polymer*, 1983, **24,** 400.
40. H. Uehara, H. Matsuda, T. Aoike, T. Yamanobe and T. Komoto, *Polymer*, 2001, **42,** 5893.
41. S. J. Spells and M. J. Hill, *Polymer*, 1991, **32,** 2716.
42. M. Engelsberg and I. J. Lowe, *Phys. Rev. B*, 1974, **10,** 822.
43. J. T. E. Cook, P. G. Klein, I. M. Ward, A. A. Brain, D. F. Farrar and J. Rose, *Polymer*, 2000, **41,** 8615.
44. N. E. Weeks, S. Mori and R. S. Porter, *J. Polym. Sci. Polym. Phys. Ed.*, 1975, **13,** 2031.
45. H. Uehara, M. Nakae, T. Kanamoto, O. Ohtsu, A. Sano and K. Matsuura, *Polymer*, 1998, **39,** 6127.
46. H. Uehara, A. Uehara, M. Kakiage, H. Takahashi, S. Murakami, T. Yamanobe and T. Komoto, *Macromolecules*, 2002, **35,** 2640.
47. Z. Bashir and A. Keller, *Colloid Polym. Sci.*, 1989, **267,** 116.
48. H. Uehara, M. Nakae, T. Kanamoto, A. E. Zachariades and R. S. Porter, *Macromolecules*, 1999, **32,** 2761.
49. M. Nakae, H. Uehara, T. Kanamoto, T. Ohama and R. S. Porter, *J. Polym. Sci. B Polym. Phys.*, 1999, **37,** 1921.
50. M. Nakae, H. Uehara, T. Kanamoto, A. E. Zachariades and R. S. Porter, *Macromolecules*, 2000, **33,** 2632.
51. M. Kakiage, M. Sekiya, T. Yamanobe, T. Komoto, S. Sasaki, S. Murakami and H. Uehara, *Polymer*, 2007, **48,** 7385.
52. H. Uehara, M. Kakiage, T. Yamanobe, T. Komoto and S. Murakami, *Macromol. Rapid Commun.*, 2006, **27,** 966.
53. S. Sasaki, K. Tashiro, M. Kobayashi, Y. Izumi and K. Kobayashi, *Polymer*, 1999, **40,** 7125.
54. J. Zhang, Y. Duan, H. Sato, H. Tsuji, I. Noda, S. Yan and Y. Ozaki, *Macromolecules*, 2005, **38,** 8012.
55. S. Watanabe, J. Dybal, K. Tashiro and Y. Ozaki, *Polymer*, 2010, **2006,** 47.
56. L. Kurelec, S. Rastogi, R. J. Meier and P. J. Lemstra, *Macromolecules*, 2000, **33,** 5593.
57. L. Brambilla and G. Zerbi, *Macromolecules*, 2005, **38,** 3327.
58. M. Ito, T. Kanamoto, K. Tanaka and R. S. Porter, *Macromolecules*, 1981, **14,** 1779.
59. H. Tanaka and T. Nishi, *J. Chem. Phys.*, 1986, **85,** 6197.
60. M. Takenaka, T. Yamanobe, T. Komoto, I. Ando, H. Sato and K. Sato, *J. Polym. Sci. B Polym. Phys.*, 1987, **25,** 2165.
61. L. S. Loo, R. E. Cohen and K. K. Gleason, *Macromolecules*, 1999, **32,** 4359.
62. L. S. Loo, R. E. Cohen and K. K. Gleason, *Science*, 2000, **288,** 116.
63. R. C. Hedden, H. Tachibana, T. M. Duncan and C. Cohen, *Macromolecules*, 2001, **34,** 5540.
64. T. Kameda and T. Asakura, *Polymer*, 2003, **44,** 7539.
65. J. Rault, J. Marchal, P. Judeinstein and P. A. Albouy, *Macromolecules*, 2006, **39,** 8356.
66. M. Kakiage, H. Uehara and T. Yamanobe, *Macromol. Rapid Commun.*, 2008, **29,** 1571.
67. M. Kakiage, T. Yamanobe, T. Komoto, S. Murakami and H. Uehara, *J. Polym. Sci. B Polym. Phys.*, 2006, **44,** 2455.
68. M. Kakiage, T. Yamanobe, T. Komoto, S. Murakami and H. Uehara, *Polymer*, 2006, **47,** 8053.
69. T. Yamanobe, H. Kurihara, H. Uehara and T. Komoto, *J. Mol. Struct.*, 2006, **829,** 80.
70. G. Schmack, R. Schreiber, W. S. Veeman, H. Hofmann and R. Beyreuther, *J. Appl. Polym. Sci.*, 1997, **66,** 377.
71. A. E. Tonelli and F. C. Schilling, *Acc. Chem. Res.*, 1981, **14,** 233.
72. H. Saito and I. Ando, *Ann. Rept. NMR Spectrosc.*, 1989, **21,** 210.

SUBJECT INDEX

R

S